AGH

AKADEMIA GÓRNICZO-HUTNICZA IM. STANISŁAWA STASZICA W KRAKOWIE

DZIEDZINA NAUK INŻYNIERYJNO-TECHNICZNYCH

DYSCYPLINA: INŻYNIERIA ŚRODOWISKA, GÓRNICTWO I ENERGETYKA

ROZPRAWA DOKTORSKA

Opracowanie modeli empirycznych do opisu pracy narzędzia wiercącego w laboratoryjnym wierceniu rdzeniowym

Autor: mgr Mitra Khalilidermani

Promotor rozprawy: Dr hab. inż. Dariusz Knez

Praca wykonana: Akademia Górniczo-Hutnicza w Krakowie

Wydział Wiertnictwa, Nafty i Gazu

Kraków, 2025

AGH UNIVERSITY OF SCIENCE AND TECHNOLOGY

FIELD OF ENGINEERING AND TECHNICAL SCIENCES

DISCIPLINE: ENVIRONMENTAL ENGINEERING, MINING AND ENERGY

DOCTORAL DISSERTATION

Development of Empirical Models to Describe Drilling Tool Performance in the Laboratory Core Drilling

Author: Mitra Khalilidermani

Supervisor: Dr hab. eng. Dariusz Knez

Completed at: AGH University of Krakow
Faculty of Drilling, Oil and Gas

Kraków, 2025

Abstract

In this dissertation, laboratory research is presented on four different Polish rock types to develop new empirical formulas for modelling rate of penetration (ROP) and mechanical specific energy (MSE) in the laboratory coring drilling tests. The investigations included coring drilling experiments as well as measurements of the physical and dynamic geomechanical properties of the subjected rocks.

Following experimental tests, the statistical method was used to quantify the impact of different operational and rock parameters on ROP and MSE. Parameters of weight on the bit (WOB), rotation per minute (RPM), rock's porosity, rock's density, compressional wave velocity, and core bit diameter were selected for inclusion in the ROP and MSE models.

Subsequently, dimensional analysis was employed to develop new formulas. As a result, the exponents of WOB, RPM, rock's porosity, rock's density, compressional wave velocity, bit's outer diameter, and the ratio of outer diameter to the inner diameter were computed as +1, +2, +1.7, -1, -1, -1, and -2. Consequently, a new equation was formulated for ROP modelling.

Leveraging measurements results and incorporating the developed ROP equation, a new MSE model was formulated. The new ROP and MSE formulations are easy to use and can be the basis for future research in the area of coring operations.

Streszczenie

W niniejszej rozprawie doktorskiej przedstawiono badania laboratoryjne czterech różnych polskich skał w celu opracowania nowych zależności empirycznych do modelowania chwilowej prędkości wiercenia (ROP) i mechanicznej energii właściwej (MSE) w laboratoryjnych testach wiercenia rdzeniowego. Badania obejmowały eksperymenty wiercenia rdzeniowego oraz pomiary fizycznych i dynamicznych właściwości geomechanicznych badanych skał.

Po przeprowadzeniu badań eksperymentalnych zastosowano metodę statystyczną do ilościowego określenia wpływu różnych parametrów operacyjnych i skał na ROP i MSE. Parametry takie jak nacisk na narzędzie wiercące (WOB), obroty (RPM), porowatość skały, gęstość skały, prędkość fali ultradźwiękowej i średnica koronki rdzeniowej zostały wybrane do uwzględnienia w modelach ROP i MSE.

Następnie zastosowano analizę wymiarową w celu opracowania nowych zależności. W rezultacie wykładniki dla WOB, RPM, porowatości skały, gęstości skały, prędkości fali ultradźwiękowej, średnicy zewnętrznej świdra oraz stosunku średnicy zewnętrznej do średnicy wewnętrznej obliczono jako +1, +2, +1,7, -1, -1, -1 i -2. W efekcie sformułowano nowe równanie do modelowania ROP.

Wykorzystując wyniki pomiarów i uwzględniając opracowane równanie ROP, sformułowano nowy model MSE. Nowe wzory ROP i MSE są łatwe w użyciu i mogą stanowić podstawę przyszłych badań w dziedzinie operacji rdzeniowych.

Acknowledgements

I gratefully acknowledge the invaluable assistance and thoughtful supervision of my advisor, Dr hab. eng. Dariusz Knez, Prof. AGH, throughout the entire course of this research. His insightful advice and constructive feedback have been essential to the successful completion of my PhD.

I am also profoundly grateful to Dr. Albert Złotkowski and Dr. Mohammad Zamani Ahmad Mahmoudi for their expert guidance and invaluable help, which have significantly contributed to this research. Their support and encouragement have been deeply appreciated.

Lastly, I extend my appreciation to Piotr Mytnik, for his help in the laboratory experiments. His assistance has been incredibly meaningful in the completion of this work.

List of contents

List of Figures

List of Tables

Chapter 1:

Introduction

Drilling into the Earth's subsurface is a critical component of modern engineering and resource extraction industries, including petroleum engineering, geothermal development, mineral exploration, and geotechnical investigation. Despite significant advancements in drilling systems and instrumentation, predicting drilling performance remains a complex task due to the intricate interplay between mechanical inputs and the inherent variability of geological formations. This complexity is amplified in heterogeneous lithologies, where rock properties such as porosity, density, and stiffness can vary considerably within short spatial intervals. In this context, the ability to accurately forecast drilling behavior becomes vital not only for operational efficiency but also for cost control, risk reduction, and overall wellbore stability.

Two fundamental indicators govern the evaluation of drilling efficiency: ROP and the MSE. ROP measures how rapidly the drill bit penetrates into the rock, while MSE quantifies the energy consumed per unit volume of rock removed. Together, they reflect the mechanical interaction of the rock–bit system. However, existing models for ROP and MSE often fall short in field applicability. Many rely heavily on idealized assumptions or exclude rock-specific variables, leading to oversimplified predictions.

For instance, earlier models, such as Bourgoyne and Young's ROP model often excluded key rock properties like porosity or relied on empirical constants derived from limited field conditions (Bourgoyne and Young, 1974). Similarly, Teale's MSE equation, while foundational, does not account for variations in rock properties such as porosity, density, and mechanical stiffness, which significantly influence energy consumption during drilling operations (Teale, 1965). These limitations reduced their adaptability and predictive accuracy, especially when applied to lithologically diverse formations.

Additionally, some ROP and MSE models lack dimensional consistency. For instance, Bilim and Karakaya (2021) developed an empirical ROP model using laboratory experiments. In the model, parameters of rock's density and porosity were combined linearly without applying dimensional analysis. This resulted in a model where terms with incompatible units were added together, violating the principle of dimensional consistency.

Furthermore, some models rely on input variables like rock's uniaxial compressive strength (UCS) and confined compressive strength (CCS), which are often unavailable or costly to obtain during real-time operations. As an illustration, Basarir et al. (2014) established an empirical ROP model by formulating ROP as a second-degree function of UCS. While the model showed reasonable predictive capability within the tested range, its practical applicability is limited by its reliance on UCS, a parameter that is often difficult, time-consuming, and costly to measure during real-time drilling operations. The model also lacked dimensional consistency as the unit of ROP is m/s, while the second-degree term of UCS has units of Pa^2.

Another shortcoming in the relevant literature review is that many researchers have dedicated their efforts to characterizing ROP and MSE in rotary and percussive drilling activities, and less attention has been given to coring drilling operations. Coring operations, which aim to retrieve intact rock samples rather than simply excavate material, involve different mechanical dynamics and bit–rock interactions. Unlike standard drill bits that grind or crush rock over a broad surface, coring bits cut annular hollows and generate a cylindrical core, resulting in a more concentrated contact area and different stress distribution at the cutting interface. As a result, models developed for conventional rotary or percussive drilling may not accurately capture the performance metrics of coring processes. This gap highlights the need for specialized models that consider the unique operational and mechanical characteristics of coring bits.

To address the above-mentioned limitations, this PhD research establishes a dimensionally consistent, statistically supported framework for ROP and MSE prediction in coring drilling operations. The framework emphasizes the use of readily measurable parameters to enhance model applicability in real-time environments. It also aims to improve drilling efficiency by providing more accurate and reliable performance results across varying geological conditions.

The primary objectives of this research are:

1) To quantify the impact of different operational parameters and rock properties with ROP and MSE.
2) To formulate new empirical models for ROP and MSE that are dimensionally consistent and based on simply measurable parameters.

The proposed models are developed through a combination of controlled laboratory experiments and analytical techniques, allowing for a clear understanding of how variables such as weight on the bit (WOB), rotation speed, porosity, density, etc. interact to influence drilling performance.

The thesis is that drilling performance is governed by the combined effects of operational parameters and rock properties.

Rocks' physical and mechanical features such as rock's density, bulk modulus, Young's modulus, P-wave velocity, etc. were expected to exhibit an inverse relationship with ROP, as stiffer and denser rocks typically resist penetration more effectively. Furthermore, rock's porosity, due to its influence on the rock brittleness and fragmentation, was conceived to positively correlate with ROP.

Regarding MSE, it was postulated that higher WOB and RPM would reduce the energy required per unit volume of rock removed (i.e., lower MSE), while higher density and stiffness parameters, e.g. bulk modulus, Young's modulus, and P-wave velocity, would increase MSE due to greater resistance and energy absorption during drilling.

The above-mentioned theses served as the conceptual foundation for both the experimental designation and the development of new predictive models. These theses provided a logical framework that guided data interpretation and facilitated the validation of the new formulations introduced in this study. This thesis-driven approach enhanced the scientific rigor and credibility of the developed ROP and MSE models.

To test those theses, a methodology consisting of experimental and analytical evaluations was established. The experimental tests were performed through conducting a total number of 64 drilling tests. The measurements from the experimental tests were then used in the analytical part to formulate new ROP and MSE models.

The experimental tests were conducted on rock samples obtained from four distinct geological formations in southern Poland: Szydłowiec–Śmiłów sandstone, Wola Komborska sandstone, Tumlin sandstone, and Morawica marble. Firstly, large slabs from each formation were transported to the Drilling and Geoengineering Laboratory at AGH University of Krakow. These slabs were then cut, and cylindrical core samples were extracted using a coring drilling machine.

The Szydłowiec–Śmiłów sandstone samples were obtained from the Śmiłów quarry near Szydłowiec in the Świętokrzyskie region. They were characterized by well-sorted, rounded grains and silica-based contact cement (Waśkowska et al., 2014). The Wola Komborska sandstone samples were collected from the Wola Komborska deposit. They were classified as Istebna sandstone, typically grey, medium-grained, and associated with the Silesian nappe of the Flysch Carpathians (Strzeboński, 2015). The Tumlin sandstone samples were taken from the upper stratigraphic section of the Tumlin deposit, and belonged to the Triassic sedimentary cover (Gradziński and

Uchman, 1994). They were orange-colored, well-sorted, and composed of rounded grains with silica cement. The Morawica marble samples were taken from the mines close to Morawica which are situated in geological units of the Carpathian Foredeep, typically linked to hydrocarbon-bearing structures (Słonka and Krzywiec, 2020). The samples had signs of digenetic and low-grade metamorphic alteration.

Selecting samples from those four different formations provided the research with a wide spectrum of rocks' porosity, density, and mechanical parameters. Consequently, the evaluation of the ROP and MSE models under diverse geological conditions was enabled. All coring drilling experiments were performed using a bit with outer and inner diameters respectively equal to 44 mm and 38 mm under systematically varied RPM and WOB levels. Apart from those drilling tests, the rocks' physical and dynamic mechanical properties were measured through standardized laboratory equipment such as a saturation apparatus, a tri-axial compression test machine as well as an acoustic wave propagation apparatus.

For implementation of the experimental tests, several simplifying assumptions were made. It was assumed that pore pressure was negligible during laboratory drilling, as all tests were performed under near-atmospheric conditions (~0.1 MPa). Moreover, bit wear was considered insignificant due to the short duration of each test. Furthermore, temperature variation, thermal effects, fluid-rock interactions, mud circulation, and down-hole vibrations were not considered, as these were outside the scope of controlled laboratory environments. These assumptions, while limiting in scope, were essential for building reliable, first-principle models and avoiding confounding variables.

In addition to the above-mentioned assumptions, it must be emphasized that all conclusions drawn from the experimental and analytical evaluations are valid only within the scope of the tested lithologies and laboratory conditions. Specifically, the formulations developed in this research are based on sandstones and marble obtained from southern Poland, and their applicability to other lithological types remains to be validated. The experiments were also carried out on small cylindrical core samples under controlled boundary conditions, which may not fully replicate the scale, heterogeneity, and dynamic stresses present in field drilling operations. Consequently, while the models provide a robust mechanistic framework, their predictive capability should be interpreted as conditional upon these constraints, and future studies are required to confirm their validity across broader geological and operational contexts.

It was also assumed that the rock samples were homogeneous and isotropic at the scale of testing. In reality, natural rocks often exhibit heterogeneities such as bedding planes, micro-fractures, mineralogical variations, or anisotropy in mechanical properties. These features may significantly influence drilling response in field-scale conditions. However, for the purposes of this research, the laboratory core samples were treated as mechanically uniform, which allowed for more consistent interpretation of drilling performance and model development.

The analytical methodology adopted in this research involved statistical and dimensional analyses. Pearson's correlation coefficient technique was used to statistically assess the relations between input parameters and the two target variables, i.e. ROP and MSE. The computed correlation coefficients served as the basis for variable selection and sensitivity prioritization. Subsequently, the dimensional analysis technique was applied to derive physically consistent equations using three key formulation criteria: 1) only input parameters that are easily measurable in the field or laboratory must be selected to ensure practical implementation. 2) as far as possible, only a minimal set of essential variables should be used in order to avoid redundancy and enhance the clarity of the model. 3) dimensional consistency must be enforced to ensure physical validity and universal applicability of the equations.

Through the applied experimental and analytical methodology, a new empirical ROP model (See (Eq. 6.16)) was established. Such a new model incorporated WOB, RPM, rock's porosity, rock's density, P-wave velocity, core bit outer diameter, and the ratio of bit's outer diameter to inner diameter. Interestingly, it yielded a strong match with the experimental data. The ROP increased linearly with WOB and approximately quadratically with RPM, while increasing rock's density, P-wave velocity, and bit's outer diameter reduced the penetration rate linearly. Furthermore, rock's porosity and the ratio of bit's outer diameter to inner diameter showed a non-linear influence on ROP, with a fitted exponents of approximately 1.7 and -2, respectively.

Furthermore, based on the newly developed ROP model, a novel MSE model (See (Eq. (6.28)) was also formulated for coring drilling operations. The drilling tests also revealed that the MSE of coring operation is almost entirely derived from the rotary mechanism. As a result, the total MSE was defined solely in terms of the rotary energy, which itself was a function of ROP. By integrating the new ROP equation into the MSE formulation, the resulting expression linked MSE not only to operational parameters but also to rock-specific properties. As a result, the predictive accuracy and applicability of the novel MSE models were markedly enhanced.

The validation of the developed ROP and MSE models was carried out across all four rock types, individually and collectively, using statistical comparisons between real and predicted values. The ROP model demonstrated a coefficient of determination (R^2) of 0.98, and a mean absolute percentage error (MAPE) of 28%, confirming its ability to capture the variations in drilling performance with minimal deviation. The MSE model also achieved robust results, with R^2=0.95 and MAPE=30%, demonstrating that integrating rock-specific parameters significantly enhances its predictive power. The consistency of these results across different lithologies shows the generalizability and reliability of the proposed mathematical ROP and MSE models in coring drilling operations.

It was proved that drilling performance is the outcome of a balanced interaction between operational parameters and intrinsic rock characteristics. While increases in WOB and RPM reliably enhanced penetration, this effect was moderated by the physical properties of the formation. Denser, stiffer rocks with higher P-wave velocities resisted penetration more effectively, while porous rocks facilitated fragmentation and improved bit penetration. This demonstrated that neither operational inputs nor rock properties alone can adequately explain drilling behavior; only their combined influence provides a reliable basis for performance evaluation.

It was also proved that incorporating wave-propagation properties of rock, particularly P-wave velocity, can provide a reliable proxy for stiffness effects in drilling performance models. By embedding this parameter into the formulations, the research demonstrated that rock mechanical resistance can be captured effectively without relying on laboratory-intensive strength tests. This not only enhanced predictive precision but also offered a practical path for applying the models in real-time field operations.

The study also proved that in coring operations, the contribution of the percussive mechanism to MSE is negligible when compared with the rotary mechanism. This finding clarified that energy consumption during coring is overwhelmingly governed by rotary action. As a result, MSE can be formulated solely on the basis of rotary parameters, simplifying the predictive framework.

It was also proved that predictive models are substantially strengthened when they are formulated on sound physical principles. Ensuring dimensional consistency and limiting the framework to parameters that are both measurable and non-redundant resulted in equations that are not only scientifically coherent but also adaptable to diverse drilling contexts. This showed that rigorous formulation standards provide more dependable insights than empirical curve-fitting approaches.

Compared to previous models in the literature, the proposed ROP and MSE models offers improved predictive accuracy by including rock-specific properties that were often overlooked in the past. Moreover, their dimensional consistency and reliance on measurable parameters make them reliable and applicable in diverse drilling scenarios.

What distinguishes this study from previous efforts is its commitment to dimensional coherence, as well as careful selection of non-redundant and measurable input parameters, and its emphasis on experimental validation. As already mentioned, many existing ROP and MSE models either have overlooked rock-specific properties or rely on complex input variables that are impractical for field use. Furthermore, some of them are inconsistent dimensionally. The aforesaid examples were Bourgoyne and Young's ROP model, Teale's MSE model, Bilim and Karakaya' ROP model, and Basarir et al.'s ROP model. This PhD research addressed that gap by developing two new ROP and MSE models that are both theoretically robust and practically applicable. The proposed models are dimensionally consistent and integrate measurable, non-redundant parameters from both operational (drilling) conditions and rocks' properties.

The findings of the current research are highly applicable to any coring drilling initiative where rock type and operational inputs vary. The applicable projects are drilling of hydrocarbon wells, geothermal boreholes, CO_2 injection wells, underground storage systems, etc. The novel two formulations are applicable for real-time drilling optimization, performance forecasting, or tool selection by leveraging data that are already available through standard field logging or laboratory testing. Furthermore, the methodological framework developed herein can serve as a template for future drilling investigations, heightening its robustness in drilling efficiency prediction and optimization. However, further validation under field conditions is required before broad application.

Building on the outcomes of this study, future research should aim to extend the developed ROP and MSE models beyond laboratory settings by validating them under real field conditions, where factors such as formation pore pressure, rock- fluid interaction, and operational variability come into play. Additionally, expanding the model framework to include other lithological variables, e.g. rock abrasiveness, mineral composition, or micro-fracture density, could refine predictive accuracy across even more diverse geological formations. These directions would not only improve model robustness but also pave the way for smarter, automated drilling optimization systems in both conventional and unconventional resource development.

In sum, this dissertation delivers an integrated exploration of how operational parameters and rock properties jointly affect drilling performance, expressed through two key indicators: ROP and MSE. The findings offer two new formulations that bridge theoretical rigor and field utility, paving the way for more intelligent, efficient, and adaptive drilling practices across various sectors of subsurface engineering. By enabling more accurate prediction of coring drilling performance based on readily measurable parameters, the proposed models contribute to reducing operational uncertainty, optimizing equipment lifespan, and minimizing non-productive time in drilling operations.

Based on the conducted PhD research, the following new achievements were obtained:

3) A new dimensionally consistent empirical ROP formulation (see Eq. (6.16)) was developed for coring drilling operations.
4) A new dimensionally consistent empirical MSE formulation (see Eq. (6.28)) was established for coring drilling operations.
5) P-wave velocity was directly incorporated as a measurable real-time drilling parameter in the newly developed ROP and MSE formulations.

Chapter 2:

Contributing Factors on Drilling Efficiency

Efficiency is a critical metric in drilling operations, directly influencing operational costs, safety, and project timelines. Achieving high efficiency requires a careful balance of various parameters that interact dynamically with geological conditions, equipment limitations, and operational goals. This chapter explores key contributing factors that affect drilling efficiency, categorized into operational, hydraulic, geological, mechanical and practical factors.

2.1. Operational drilling parameters

2.1.1. Rotary Speed

Rotary speed refers to the revolutions per minute of the drill bit, and significantly influences the rate of penetration. High RPM can enhance ROP in softer formations but may lead to excessive wear in harder rock, especially for fixed cutter bits like PDCs. Optimal rotary speed balances penetration rate with tool longevity. Beyond optimal RPM, higher speeds can cause excessive friction, heat, or bit balling, which can actually reduce ROP (Bourgoyne et al., 1986). Additionally, RPM must be optimized to prevent harmful vibrations and stick-slip motion, which can damage downhole tools and reduce drilling efficiency (Rabia, 1985).

When considering the optimal RPM for drilling operations, several practical considerations should be addressed. Firstly, the type of formation is crucial; softer formations can sustain higher RPMs, whereas harder formations necessitate lower speeds to avoid damaging the drill bit. Secondly, the choice of bit plays a significant role; PDC bits typically operate at higher RPMs compared to roller cone bits. Furthermore, if downhole motors are employed, their RPM needs to be embedded within real-time control frameworks. Monitoring through real-time telemetry from MWD (Measurement While Drilling) and RSS (Rotary Steerable Systems) tools provides essential data for dynamically optimizing RPM throughout the drilling process (Mitchell and Miska, 2011).

2.1.2. Torque

Torque is the rotational force imposed on the drill bit during the drilling process, essential for effective penetration into the formation. It is a measure of the twisting force that enables the drill bit to cut through rocks as it rotates. In International System of Units (SI), torque is expressed in units of Newton.meters (N·m) (Mitchell and Miska, 2011). It is closely tied to the formation being drilled. For example, harder rock formations may require higher torque to maintain efficient cutting, whereas softer formations may require less torque (Mitchell and Miska, 2011).

The required torque to rotate a drill bit is provided by the drilling rig's power source, which can include electric motors, diesel engines, or other types of internal combustion engines. Those power sources deliver the necessary rotational force to the drill string, which is then transmitted to the drill bit to facilitate the cutting process (Hopmann and Algrain, 2003).

The torque has a direct relationship with the drill bit's angular velocity, forming a key dynamic in drilling operations. In general, the torque required for drilling can be influenced by both the force applied to the bit and the speed at which the bit rotates. By increasing the torque or reducing the angular velocity, operators can influence the efficiency and performance of the drilling process.

Mathematically, the relationship between torque, power, and angular velocity can be expressed as follows (Shigley et al., 1985):

$$T = \frac{P}{\omega} \tag{2.1}$$

Where T is torque (N.m), P is power of drilling machine (W), and ω is the angular velocity (rad/s).

Managing torque effectively is critical for optimizing drilling performance and ensuring the longevity of drilling equipment. Torque must be carefully balanced with other parameters, such as WOB and RPM, to maintain a steady and efficient drilling process. Excessive torque can result in problems such as increased wear on the drill bit, potential damage to the drill string, or even stuck pipe incidents, whereas insufficient torque may cause inefficient cutting and slower penetration rates (Mitchell and Miska, 2011).

2.1.3. WOB

WOB is a critical parameter in drilling operations that measures the axial load exerted on the drill bit during drilling. Such a force is primarily generated from the weight of the drill strings transmitted to the drill bit working at the bottom-hole (Trenchlesspedia, 2023).

The WOB is pivotal for efficient drilling as it affects the rate of penetration (ROP) and overall drilling performance. Optimal WOB ensures effective engagement of the drill bit with the formation, facilitating smoother and faster drilling processes while minimizing the risk of equipment damage. Adjustments to WOB are typically achieved by adding or removing drill collars or adjusting the drilling fluid density (Bani Mustafa et al., 2021).

The required WOB varies based on geological conditions such as formation hardness, abrasiveness, and lithology. Harder formations necessitate higher WOB to penetrate effectively, whereas softer formations require less WOB to avoid excessive bit wear and potential damage (Great Drill Bit, 2022)

WOB is monitored and adjusted in real-time using instrumentation on the drilling rig, allowing operators to optimize drilling parameters for maximum efficiency and equipment longevity (Mitchell and Miska, 2011). Improper WOB management can lead to detrimental effects such as premature bit wear, reduced drilling efficiency, and potential equipment failures. Excessive WOB can cause accelerated wear and fatigue on the drill bit (Bourgoyne et al., 1986; Mitchell and Miska, 2011).

Therefore, controlling WOB is essential for optimizing drilling operations, ensuring both productivity and equipment integrity. By carefully managing WOB based on geological conditions and real-time monitoring, drilling operators can enhance overall drilling performance and extend the lifespan of drilling equipment.

2.1.4. Drill Bit Selection

Drill bit selection is a fundamental aspect of drilling optimization, directly influencing ROP, bit longevity, and overall operational expenditure. The choice of bit must be tailored to the specific formation characteristics, taking into account factors such as rock hardness, abrasiveness, and heterogeneity. Common bit types include roller cone bits, which are versatile and suitable for soft to medium formations; polycrystalline diamond compact (PDC) bits, favored for their high ROP and durability in homogeneous formations; and natural diamond bits, which excel in extremely hard or abrasive formations. A well-matched bit not only improves drilling efficiency but also minimizes wear and reduces the frequency of bit trips, thereby cutting down on non-productive time (Wamsley and Ford, 2006).

2.1.5. Drill bit diameter

Bit diameter is a geometric characteristic of a drilling system and directly influences both the mechanics of rock fragmentation and the overall efficiency of drilling operations. The bit's diameter dictates the size of the hole being created and consequently the volume of rock that must be removed per unit length of penetration. As the diameter increases, the surface area contacting the rock also increases, thereby expanding the rock removal zone and requiring more energy for effective penetration. This increased contact area alters the stress distribution beneath the bit, which in turn affects chip formation, bit wear, and the torque required to maintain a consistent rotational speed.

In drilling operations, bit diameter also impacts other operational factors such as fluid circulation, cuttings transport, and bottom hole cleaning. A larger bit often requires more efficient circulation systems to prevent clogging and maintain consistent drilling performance. Therefore, the bit diameter does not only influence the energy transfer and mechanical interaction rock–bit contact area but also affects the efficiency of auxiliary systems that support the drilling process. Regarding MSE, which is described as the energy necessary for breaking and removing one unit volume of rock, an increase in bit diameter typically leads to higher MSE. This is because the larger rock contact area demands more force to initiate and propagate fractures, particularly under constant WOB and torque. Essentially, with greater bit diameter, more energy is expended per volume drilled, raising the specific energy index (Lu et al., 2021).

2.2. Hydraulic factors

2.2.1. Drilling fluid properties

Drilling fluids, commonly referred to as mud, serve several critical functions during drilling operations, including lubricating and cooling the drill bit, removing cuttings from the wellbore, and maintaining wellbore pressure control. To perform these roles effectively, the fluid must possess key properties including: 1) appropriate density to balance formation pressure; 2) viscosity and gel strength to suspend and transport cuttings; 3) filtration control to minimize fluid loss and prevent formation damage; and 4) chemical compatibility to avoid adverse reactions with formation fluids. Properly engineered drilling fluids are necessary for guaranteeing the efficiency of drilling operations (Amanullah and Al-Arfaj, 2011; Bourgoyne et al., 1986).

2.2.2. Flow rate

Flow rate is a highly potent factor in drilling operations as it directly influences cuttings transport, bit cooling, and wellbore pressure management. Maintaining an optimal circulation rate is essential for achieving hydraulic efficiency, which ensures that drilled cuttings are effectively carried to the surface, reducing the likelihood of cuttings accumulation and associated issues such as stuck pipe. A well-regulated flow rate contributes to effective hole cleaning which is vital for maintaining drilling performance and preventing costly non-productive time (Amanullah and Al-Arfaj, 2013; Bourgoyne et al., 1986).

2.2.3. Hydraulic power (HP)

Hydraulic power (HP) is a measure of the energy transmitted by the drilling fluid to the drill bit, playing a vital role in enhancing bit cleaning, cooling, and penetration efficiency (Bourgoyne et al., 1986). It is calculated using the flow rate, pressure, and hydraulic efficiency of the circulating fluid system. The general formula is (Ramsey, 2019):

$$HP = \frac{p \times Q}{1000} \tag{2.2}$$

Where HP represents hydraulic power (kW), p indicates pressure (Pa), and Q stands for the flow rate (m^3/s). A higher hydraulic power improves the jet impact force at the bit nozzles, which helps break rock more effectively and improves cuttings removal, ultimately boosting drilling performance and reducing wear on the bit (Rabia, 1985).

2.2.4. Bit nozzle configuration

Nozzle design is of fundamental importance in optimizing the hydraulic performance of a drill bit by controlling how drilling fluid is delivered to the cutting structure. Proper nozzle configuration, including the number, size, and orientation of the nozzles, significantly improves hydraulic efficiency, enhances debris evacuation, and ensures effective bit cooling. By directing high-velocity fluid jets precisely to the cutter face and the bottom of the hole, nozzles aid in breaking down rock more efficiently and transporting cuttings further from the drill bit.

The choice of nozzle size must be tailored to formation characteristics and bit type to achieve the desired jet impact force (Mitchell and Miska, 2011; Song et al., 2022). Even small changes in nozzle diameter can have a significant effect on the force delivered by the fluid jet. Therefore, optimizing nozzle design is essential to maximize bit performance, minimize bit balling, and ensure efficient drilling under varying formation conditions.

2.2.5. Hole cleaning

Effective hole cleaning is critical to maintaining drilling performance, as poor removal of cuttings can reduce ROP, increase the risk of stuck pipe, and compromise wellbore stability. The efficiency of hole cleaning is influenced by several operational and design factors, including drilling fluid velocity, rheological properties, annular geometry, and the drill pipe's rotation. To evaluate hole cleanliness quantitatively, Hole Cleaning Efficiency (HCE) represents the fraction of cuttings actually carried out of the wellbore compared to the theoretical maximum rate, where all produced cuttings are removed instantaneously. This is expressed mathematically as follows (Wang et al., 2022):

$$HCE = \left(\frac{AFR}{IFR}\right) \times 100\% \tag{2.3}$$

Where AFR (Actual Flow Rate) represents the average mass rate at which cuttings exit the well (kg/s), and IFR (Ideal Flow Rate) represents the theoretical mass rate of cuttings generated at the bit based on the rate of penetration (kg/s). A higher HCE value indicates more efficient cuttings transport, which is essential for reducing downhole problems and ensuring smooth drilling operations, especially in inclined or horizontal sections (Hu et al., 2024).

2.3. Geological characteristics

2.3.1. Porosity

Porosity is a key property in formation evaluation and refers to the proportion of void spaces (pores) within a rock. These voids can store fluids such as oil, gas, or water, making porosity critical for assessing the reservoir potential of a formation. Porosity also influences the mechanical strength of rocks. Higher porosity usually correlates with lower strength and reduced resistance to drilling forces.

Porosity can be expressed as the proportion of void space volume to the total volume of the rock sample, usually expressed as a percentage (Zhang, 2019):

$$\varphi = \frac{V_V}{V} \times 100 \qquad (2.4)$$

Here φ represents porosity (dimensionless), V_V indicates the volume of pores (voids), and V stands for the total volume of the rock sample (m^3). Porosity varies significantly among different rock types. For example, unconsolidated clays can have porosities as high as 55%, while dense crystalline rocks may have porosities close to 0% (Asanlou, 1991). In general, porosity decreases with increasing depth due to compaction and pressure, which reduce the volume of the pore spaces.

2.3.2. Rock's density

Rock's density expresses the mass present in each unit of rock volume, and is directly related to its mineral composition and degree of compaction. Higher rock's density often correlates with increased strength and hardness, making drilling more challenging and reducing the ROP. Conversely, lower-density formations are generally easier to drill, allowing for faster progress and reduced bit wear.

From a drilling engineering perspective, understanding rock's density is essential for selecting appropriate drilling factors, like type of bit, WOB, and RPM. It also serves a key role in evaluating formation pressure and designing drilling mud systems. The basic equation for density is as follows (Flood, 2023):

$$\rho = \frac{M}{V} \tag{2.5}$$

Where ρ indicates the rock's density (kg/m^3), M shows the rock's mass (kg), and V demonstrates the volume of the rock sample (m^3).

Measurements of rock's density are usually given in kg/m^3 or g/cm^3. However, it is sometimes compared to the density of water to give a dimensionless value known as specific gravity as follows (Roseke Engineering Ltd., 2013).

$$SG = \frac{\rho}{\rho_w} = \frac{\gamma}{\gamma_w} \tag{2.6}$$

where SG is rock's specific gravity (dimensionless), ρ stands for the density of the rock (kg/m^3), ρ_w shows density of water (usually 1000 kg/m^3 at standard conditions), γ represents the specific rock's weight (N/m^3), and γ_w is specific water's weight (N/m^3). Rock's specific gravity is a useful normalized value that simplifies calculations in some engineering applications since it is dimensionless.

2.3.3. Pore pressure

Pore pressure refers to the pressure exerted by pore fluids, e.g. water, oil, and gas, trapped within the pore spaces of formations below the Earth's surface. It is a fundamental parameter in drilling operations because it influences wellbore stability, drilling fluid design, and overall well control. Pore pressure usually increases as depth increases, driven by the load of overlying strata and contained fluids; this is known as normal pore pressure. However, in many cases, abnormal (over pressured) or subnormal pressure zones are encountered, which can complicate drilling operations if not properly anticipated (Zhang, 2019).

Understanding pore pressure is crucial for selecting the appropriate mud weight to *maintain* a safe and stable wellbore. If the mud pressure is too low (underbalanced), formation fluids may enter the wellbore, causing kicks or blowouts. If it's too high (overbalanced), it can fracture the formation, leading to lost circulation. Pore pressure prediction is typically done using seismic data, offset well logs, and drilling parameters. Proper assessment and management of pore pressure help ensure safe, efficient, and cost-effective drilling operations (Zhang, 2019).

Pore pressure significantly influences drilling efficiency parameters including ROP and MSE. When pore pressure is high, the effective stress on the rock is reduced, making the formation easier to drill. This typically leads to an increase in ROP, as the drill bit encounters less resistance. Conversely, in low pore pressure zones, rocks are more compact and harder, resulting in slower drilling rates. However, if pore pressure is very high, it necessitates the use of heavier drilling mud to maintain well control, which can suppress ROP by increasing the downhole pressure and reducing the pressure differential that drives efficient rock failure (Yin et al., 2022).

From an MSE perspective, pore pressure affects the energy required to break rock. High pore pressure zones, when managed with optimal mud weight, can lead to lower MSE due to the reduced rock strength, meaning the bit uses less energy to remove each unit of rock. But if mud weight is excessively high to overbalance formation pressure, the increased confinement on the rock raises MSE, decreasing drilling efficiency. Therefore, accurate pore pressure prediction and management are critical to balancing mud weight, maximizing ROP, and minimizing MSE (Yin et al., 2022).

2.4. Mechanical properties

2.4.1. Young's modulus

Young's modulus (or modulus of elasticity) is an essential mechanical parameter that characterizes the stiffness of a material. It describes how much a material deforms under applied stress within the elastic (non-permanent) deformation region. Young's modulus plays a vital role in wellbore stability, fracture propagation analysis, hydraulic fracturing design, and casing designation. It can be determined through laboratory compression tests on core rock samples providing a static modulus that reflects actual mechanical behavior under slow loading conditions. Alternatively, a dynamic Young's modulus can be estimated using sonic log data by combining rock density with compressional and shear wave velocities. While dynamic values are easier to obtain in situ, static measurements are generally more accurate for mechanical design purposes.

Young's modulus describes the linear relationship between axial stress and axial strain in the elastic region of the stress–strain curve, and can be written as (Zhang, 2019):

$$E = \frac{\sigma_{axial}}{\epsilon_{axial}} \tag{2.7}$$

Where E represents Young's modulus (N/m²), σ_{axial} is axial stress (Pa), and ϵ_{axial} is axial strain.

Young's modulus is related to other elastic moduli as follows (Fjaer et al., 2008):

$$E = 2G(1 + v) \tag{2.8}$$

$$E = 3K(1 - 2v) \tag{2.9}$$

Where G represents share modulus (N/m²), v shows Poisson's ratio (dimensionless), and K represents bulk modulus (N/m²). These relationships are useful when only some elastic constants are known and others need to be derived.

2.4.2. Poisson's ratio

When a rock sample is subjected to axial stress (such as tension or compression), its length changes in the direction of the force, but also contracts or expands in the perpendicular directions. Poisson's ratio is defined as follows (Wang, 2000):

$$v = -\frac{\epsilon_{lateral}}{\epsilon_{axial}} \tag{2.10}$$

In the above equation, v indicates the Poisson's ratio, $\epsilon_{lateral}$ corresponds to the strain occurring in the direction perpendicular to the applied load, and ϵ_{axial} represents the strain in the axial (loading) direction. The negative sign accounts for the fact that lateral strain is usually in the opposite direction of the axial strain (e.g., if a material is stretched, it gets thinner) (Wang, 2000). A higher Poisson's ratio indicates greater lateral deformation when compressed, which can significantly affect how stress is redistributed in the formation and how fractures behave (Zhang, 2019).

2.4.3. Bulk modulus

Bulk modulus is a fundamental elastic property that measures the rock's resistance to uniform compression. It quantifies how much the rock's volume decreases under applied external pressure. In the context of geological formations, bulk modulus mainly reflects the compressibility of rock, and is crucial in evaluating how subsurface formations respond to stress, especially during drilling, production, and reservoir deformation processes.

The magnitude of bulk modulus depends on several factors, including the mineral composition, grain structure, porosity, and the absence or presence of fluids in the pore spaces. It is expressed mathematically as follows (Hart and Wang, 1995):

$$K = -V\frac{\delta\sigma}{\delta V} \tag{2.11}$$

In the above equation, K represents the bulk modulus (Pa), and V stands for the initial volume of the rock (m^3). Note that $\frac{\delta\sigma}{\delta V}$ quantifies the variation of stress per unit change in volume. The negative sign indicates that as pressure rises, the volume of the rock decreases. A higher bulk modulus signifies a stiffer, less compressible material.

2.4.4. Shear modulus

Shear modulus is an important elastic parameter that represents a material's resistance to deformation under shear stress. In geological formations, it reflects how rocks respond to forces that cause layers or particles within them to slide. This property is especially relevant when analyzing deformation around wellbores, fault movement, and stress redistribution during drilling or reservoir production. Shear stress acts tangentially to the rock surface, and when applied, it causes the rock to experience shear strain, or angular distortion. Fundamentally, shear modulus is expressed as the proportion of the applied shear stress (τ_{xy}) to the resulting shear strain (ϵ_{xy}) as follows (Nic et al., 2005):

$$G = \frac{\tau_{xy}}{\epsilon_{xy}} \tag{2.12}$$

Where G stands for the shear modulus (Pa), τ_{xy} represents the applied shear stress (Pa), and ϵ_{xy} displays shear strain (dimensionless).

A higher shear modulus indicates a more rigid and resistant rock, while lower values suggest greater shear deformability. It is also closely associated with other elastic properties, like Poisson's ratio and bulk modulus. When both of these are known, the shear modulus can be estimated using the following relation (Rice, 1998):

$$G = 3K\frac{1-2v}{2+2v} \tag{2.13}$$

2.4.5. Rock's UCS

UCS represents the maximum axial stress a rock specimen can withstand under unconfined conditions—that is, without any lateral pressure. UCS is widely used in rock mechanics and drilling engineering to assess formation strength, select drilling parameters, and design wellbore stability models. It is particularly useful due to its simplicity and cost-effectiveness in laboratory testing, typically performed on cylindrical core samples under controlled loading. The UCS value strongly correlates with rock type, mineral composition, porosity, and cementation.

UCS is commonly expressed in units of MPa and often serves as a reference point for estimating other mechanical properties, such as cohesion and tensile strength, using empirical correlations. For formations where core data is unavailable, UCS can also be indirectly estimated from well logs or drilling parameters such as ROP, torque, and WOB (Jaeger et al., 2007; Zoback, 2007).

2.5. Practical factor

Drilling efficiency is also influenced by practical factors, including environmental, weather-related, and human factors (Skalle, 2015). Geographical conditions such as terrain complexity can affect penetration rates and equipment wear, while extreme weather—like storms, high winds, or temperature extremes—can delay operations and compromise equipment performance. Additionally, logistical challenges in remote areas and the need for additional precautions in complex formations further impact drilling speed and safety.

Equally important are the professionalism of workers and the quality of equipment used. Skilled engineers and trained personnel ensure better planning, faster problem resolution, and fewer operational errors, all of which reduce non-productive time. Modern, well-maintained rigs and advanced technologies significantly enhance drilling performance, while delays in supply chains or strict regulatory compliance can either slow down or stabilize operations depending on management effectiveness. Together, these factors define how efficiently a drilling project can be executed (Rabia, 1985).

Chapter 3:

State-of-the-Art

In the past decades, a variety of empirical and AI-based models have been developed for ROP and MSE predictions. The empirical ones are primarily based on the field drilling data or laboratory drilling experiments. Those models often utilize linear regression techniques to correlate ROP and MSE with other variables. In contrast, data-driven models predict ROP values by employing AI and computer techniques (Khalilidermani and Knez, 2022). A detailed overview of recent advances and state-of-the-art studies on ROP and MSE within drilling operations is presented in this chapter. The investigations are categorized into two main areas: empirical studies and artificial intelligence-based approaches.

3.1. ROP state-of-the-art

3.1.1. ROP empirical models

Drilling engineers are constantly exploring new ways for enhancing the precision of ROP prediction. Current ROP models often overlook certain factors, and there is ongoing discussion about how these models can be further enhanced. These topics are of great interest to drilling engineers, who are focused on reducing both the overall cost and time required for drilling operations.

Drilling is widely recognized as one of the most costly methods to exploit underground valuable resources such as hydrocarbons, metals, and groundwater (De Oliveira et al., 2021). To minimize the costs and duration of drilling operations, engineers typically focus on optimizing either ROP or MSE. The term of MSE reflects the energy necessary to break the rock. On the other side, ROP represents the rate of drilling progress (Bourgoyne et al., 1986).

The term of ROP was initially introduced by Maurer (Maurer, 1962), followed by Teale's introduction of the MSE concept in 1965 (Teale, 1965). Since then, numerous researchers have worked to improve these foundational concepts by incorporating additional parameters into the initial models.

The existing ROP models are basically divided into two sorts: empirical and data-driven models. Similarly, MSE models are generally categorized into two forms: data-driven and empirical models. From a mathematical viewpoint, ROP is expressed as the division of the length of the drilled rock to the time of drilling operation. A variety of factors influence ROP (Bourgoyne and Young, 1974), and those parameters are categorized as controllable or uncontrollable. Controllable parameters such as RPM, WOB, and torque, are adjusted by the drilling crew (Youcefi et al., 2020). Conversely, uncontrollable parameters, e.g. rock density and porosity, are unchangeable as a result of geological constraints (Edalatkhah et al., 2010).

Given that ROP directly impacts both the cost and duration of drilling operations, its optimization has been a focal point for many researchers and companies. However, optimizing ROP is a complex task due to the intricate relationships between ROP and the various factors affecting it (Perrin et al., 1997; Bond, 1990; Rabia, 1985; Pathankar and Misra, 1976; Tandanand and Unger, 1975; Paone et al., 1969; Protodyakonov, 1963). As a result, multiple attempts have been made to develop predictive models that provide optimal results.

Initial investigations focused on the development of empirical ROP models based on laboratory experiments. In 1959, Graham and Muench proposed an approach to optimize ROP (Graham and Muench, 1959). They proposed an empirical formula linking ROP with bit life. Maurer followed with a mathematical model for predicting ROP for roller-cone drill bits (Maurer, 1962). Afterwards, Galle and Wood further developed this by using regression analysis to ascertain an empirical relationship between RPM and WOB (Galle and Woods, 1963). Bingham modified Maurer's model, focusing on low RPM and WOB values (Bingham, 1965).

In 1965, Teale introduced an empirical model correlating ROP with MSE. In other words, the model was capable of linking ROP to the energy needed in the process of removing a unit volume of rock by drilling (Teale, 1965). Eckel, in 1967, conducted micro-bit experiments to improve ROP predictions in drilling operations (Eckel, 1967).

A landmark in empirical ROP modeling was the work done by Bourgoyne and Young in 1974, which included multiple drilling factors and became a widely used optimization method in real-time drilling operations (Bourgoyne and Young, 1974). Afterwards, Warren introduced a model in 1981 (Warren, 1981), followed by a refined version in 1984 (Warren, 1984). Many other researchers have since contributed to the evolution of empirical ROP models (Maidla and Ohara, 1991; Hareland and Rampersad, 1994; Motahhari et al., 2010; Hareland et al., 2010; Alum and Egbon, 2011; Al-Betairi et al., 1988).

In parallel with empirical models, several researchers utilized artificial intelligence (AI) algorithms for ROP prediction. During drilling, large amounts of data are collected. This data often contains uncertainties and hidden correlations, which AI techniques can effectively detect (Moazzeni and Khamehchi, 2020). Recent studies suggest that AI-based models are becoming one of the most reliable methods for predicting ROP (Bataee et al., 2014; Kahraman, 2016; Hegde et al., 2017; Jahanbakhshi et al., 2012). A large number of previous studies have applied AI to enhance ROP estimations (Mantha and Samuel, 2016; Hegde and Gray, 2017; Anemangely et al., 2018; Elkatatny, 2019; Abdulmalek et al., 2018; Stelzer, 2007; Hegde et al., 2018; Yavari et al., 2018; Gan et al., 2019; Dunlop et al., 2011; Sobhi et al., 2022).

Except petroleum engineering, ROP models have been also applied through the mining operations, where drilling is mainly carried out for coring rock samples and shallow blasting holes. While ROP is essential for oil and gas drilling, where the depth is much greater, ROP remains a critical parameter in mining operations as well (Niyazi, 2011; Kuesel et al., 2012; Howarth, 1986; Hoseinie et al., 2008; Kumar and Murthy, 2014a; Kumar and Murthy, 2014b). Drilling for groundwater wells and coal bed methane extraction, as well as for extraterrestrial purposes, also rely on accurate ROP optimization (Khalilidermani et al., 2021; Knez and Khalilidermani, 2021).

Thus, ROP optimization is highly critical for ensuring the success and profitability of drilling projects in the oil and gas industry, mining sites, groundwater wells, and beyond. Drilling technology is inherently multidisciplinary, drawing on various fields such as geology, petroleum engineering, mechanical engineering, and computer science to enhance efficiency and reduce costs.

Khalilidermani and Knez stated that there is a need for development of a rock-type-based classification standard for input parameters, given that uncontrollable factors arise from geological uncertainties (Khalilidermani and Knez, 2023). For example, rock abrasiveness is highly important in ROP prediction for sandstone formations while it is almost irrelevant (ineffective) for salt layers. Conversely, rock creep is a determining factor for salt rocks but not for sandstone. Such a classification standard might minimize the number of geological parameters required for reliable ROP modeling across different formations.

To improve ROP models, it is essential to identify all manageable and unmanageable parameters (Anemangely et al., 2018). Unmanageable parameters, primarily arising from geological uncertainty, are often underrepresented in oil and gas ROP models, although they are more thoroughly considered in mining ROP models. In contrast, manageable parameters, e.g. WOB can be optimized on the drilling site to improve ROP in oil and gas applications. However, less attention has been paid to these parameters in the mining industry.

Figure 3.1 illustrates the variation of ROP with WOB. Below the threshold formation stress (point a), no significant ROP is achieved. However, as WOB increases, ROP increases linearly until a certain point (point b). Beyond point b, if WOB is raised up to point c, ROP increases more steeply which indicates greater drilling efficiency. After point c, if higher WOB is applied, ROP reaches its maximum value (point d). Beyond point d, further increases in WOB may lead to reduced ROP due to inefficient bottom-hole cleaning, as a large volume of cuttings hampers fluid flow and drilling efficiency (Hossain and Al-Majed, 2015; Abdulmalek et al., 2018).

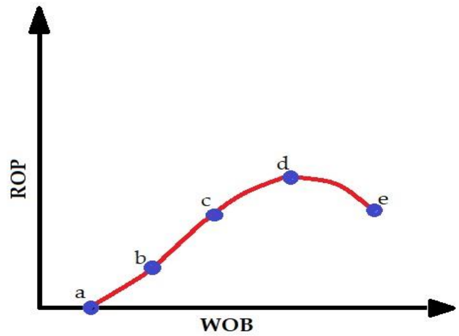

Figure 3.1 Variation of ROP vs. WOB.

Maurer introduced the first fundamental empirical formulation for ROP prediction (Maurer, 1962). That model included key variables like rock strength, RPM, WOB, and drill bit diameter. Maurer's model is as follows (Maurer, 1962):

$$ROP = \frac{K''}{S^2}\left(\frac{WOB \times g}{D} - \frac{WOB_0 \times g}{D}\right)^2 RPM \tag{3.1}$$

Here, K'' represents the proportionality coefficient (dimensionless), g depicts the gravitational acceleration (m/s^2), WOB stands for the weight on the bit (kg), D refers to the diameter of drill bit (m), RPM indicates the rotational velocity (rev/s), WOB_0 indicates the threshold WOB (kg). Moreover, S denotes the compressive strength of the formation (Pa).

The subsequent ROP formulation was proposed by Galle and Woods as follows (Galle and Woods, 1963):

$$ROP \propto \left(\frac{1}{0.02357\, {h_f}^2 + 0.1524 h_f + 1}\right)^{b_7} \tag{3.2}$$

Where, h_f represents the fractional bit tooth dullness (m). Furthermore, b_7 is an exponent (dimensionless) which can be assumed equal to 0.5.

Bingham proposed another ROP predictive model expressed as follows (Bingham, 1965):

$$ROP = K' \left(\frac{WOB \times g}{d_{bit}}\right)^{b_5} RPM \tag{3.3}$$

In this equation, b_5 represents the WOB exponent (dimensionless). Additionally, K' is a proportionality constant that incorporates the rock strength into the formula.

In 1974, Bourgoyne and Young developed one of the most applicable ROP predictive models. The model was expressed as follows (Bourgoyne and Young, 1974):

$$ROP = f_1 \times f_2 \times f_3 \times f_4 \times f_5 \times f_6 \times f_7 \times f_8 \tag{3.4}$$

Where

$$f_1 = exp^{2.303 \times a_1} \tag{3.5}$$

$$f_2 = exp^{2.303 \times a_2 \times (3048 - TVD)} \tag{3.6}$$

$$f_3 = exp^{2.303 \times a_3 \times TVD^{0.69} \times (g_p - 1.017)} \tag{3.7}$$

$$f_4 = exp^{2.303 \times a_4 \times TVD \times (g_p - ECD)} \tag{3.8}$$

$$f_5 = \left[\frac{\left(\frac{WOB \times g}{D}\right) - \left(\frac{WOB \times g}{D}\right)_{threshold}}{4 - \left(\frac{WOB \times g}{D}\right)_{threshold}}\right]^{a_5} \tag{3.9}$$

$$f_6 = \left(\frac{RPM}{60}\right)^{a_6} \tag{3.10}$$

$$f_7 = exp^{-a_7 \times h_f} \tag{3.11}$$

$$f_8 = \left(\frac{F_{Jet}}{1000}\right)^{a_8} \tag{3.12}$$

In above equations, a_1, a_2, a_3,..., a_8 are constants which are ascertained by using actual drilling measurements. Additionally, TVD represents the true vertical depth (m), g_p indicates the gradient of pore-fluid pressure (MPa/m), ECD depicts equivalent circulating density (kg/m^3), the *threshold* subscript refers to the threshold WOB and bit diameter, h_f demonstrates the fractional bit tooth dullness (m), and F_{Jet} shows the mud motion force beneath the bit (N).

In another laboratory investigation, Reza and Alcocer deployed the dimensional analysis technique to formulate a nonlinear ROP model. In that research, regression analysis was adopted to extract correlation between ROP and other parameters. The resulting ROP equation is expressed as (Reza and Alcocer, 1986):

$$\frac{ROP}{RPM \times d_{bd}} = 0.33[\frac{RPM \times {d_{bd}}^2}{v'}]^{0.43}[\frac{RPM \times {d_{bd}}^3}{Q}]^{-0.68}[\frac{H \times d_{bd}}{WOB \times g}]^{-0.91}[\frac{\Delta p \times d_{bd}}{WOB \times g}]^{-0.15} \quad (3.13)$$

where, d_{bd} (m) is the bearing's diameter, v' (m^2/s) depicts mud's kinematic viscosity, Q (m^3/s) shows the flow rate of mud, Δp (Pa) illustrates the pressure differential between the drilling mud and the pore fluids, and H (Pa) indicates the rock hardness.

The "Perfect-Cleaning Model," introduced by Warren (1981), incorporated variables such as diameter of bit, WOB, RPM, and rock strength. The equation for this model was expressed as:

$$ROP = 1/(\frac{a' \times S^2 \times D^3}{RPM^{b'}(WOB \times g)^2} + \frac{b'}{RPM \times D}) \quad (3.14)$$

where, a' and b' stand for two coefficients which both are dimensionless, and S shows the strength of rock (Pa). This model is limited in that it does not incorporate the effect of cuttings removal. As a solution, Warren introduced the "Imperfect-Cleaning Model." This enhanced version incorporated cuttings removal that is dependent on mud's viscosity and density, along with the jet's impact force. As a result, the new model proved to be more applicable than its predecessor. The model is expressed by the following formula (Warren, 1984):

$$ROP = 1/(\frac{a' \times S^2 \times D^3}{RPM^{b'}(WOB \times g)^2} + \frac{b'}{RPM \times D} + \frac{c' \times D \times \gamma_f \times \mu}{F_{jet}}) \quad (3.15)$$

where, c' stands for a dimensionless constant, γ_f shows the fluid specific gravity (N/m^3), μ illustrates the drilling fluid's dynamic viscosity (Pa.s), and F_{jet} stands for the effect of jet force (N). The units of the rest of parameters are similar to the previously mentioned equations.

Hareland and Rampersad (1994) modified Warren's imperfect cleaning model by introducing the effect of bit wear, which they represented through a wear function, W_f, defined as:

$$ROP = W_f/[f_c(P_e)\left(\frac{a' \times S^2 \times D^3}{RPM^{b'}(WOB \times g)^2} + \frac{b'}{RPM \times D} + \frac{c' \times D \times \gamma_f \times \mu}{F_{jet}}\right)] \tag{3.16}$$

where, W_f manifests the bit wear function (unitless), and P_e stands for the effective pressure (Pa). Moreover, f_c represents the chip hold down function. It is noteworthy that some other researchers such as Bourgoyne and Young, Reza and Alcocer, and Osgouei formulated bit wear in their investigations. However, their detailed explanations are excluded here to maintain clarity and avoid excessive detail.

Osgouei proposed another significant empirical ROP model (Osgouei, 2007). The basis of his model was the Bourgoyne and Young's ROP model. Osgouei introduced three new factors, namely f_9', f_{10}', and f_{11}', which incorporated the well cleaning factors for directional, horizontal, and vertical wells. The model was also applicable for both PDC and roller cone bits. The corresponding ROP model was as follows (Osgouei, 2007):

$$ROP = f_1' \times f_2' \times f_3' \times f_4' \times f_5' \times f_6' \times f_7' \times f_8' \times f_9' \times f_{10}' \times f_{11}' \tag{3.17}$$

$where,$

$$f_1' = e^{a_1} \tag{3.18}$$

$$f_2' = e^{a_2 \times (2682.24 - TVD)} \tag{3.19}$$

$$f_3' = e^{a_3 \times TVD^{0.69} \times (g_p - 1078.2)} \tag{3.20}$$

$$f_4' = e^{a_4 \times TVD \times (g_p - ECD)} \tag{3.21}$$

$$f_5' = \left[\frac{\frac{WOB}{D}}{\left.\frac{WOB}{D}\right|_{threshold}}\right]^{a_5} \tag{3.22}$$

$$f_6' = \left(\frac{RPM}{RPM_c}\right)^{a_6} \tag{3.23}$$

$$f_7' = e^{-a_7\, h_f} \tag{3.24}$$

$$f_8' = \left(\frac{F_{Jet}}{F_{Jc}}\right)^{a_8} \tag{3.25}$$

$$f_9' = \left(\frac{A_{bed}/A_{well}}{0.2}\right)^{a_9} \tag{3.26}$$

$$f_{10}' = \left(\frac{V_{Actual}}{V_{Critical}}\right)^{a_{10}} \tag{3.27}$$

$$f_{11}' = \left(\frac{C_c}{100}\right)^{a_{11}} \tag{3.28}$$

In the above equation, the constants a_1, a_2, a_3, …, and a_{11} are determined using actual drilling data. Additionally, RPM_c (rev/s) represents the critical RPM, which should be estimated based on the drilling string characteristics, type of the bits, and the geological information of the drilling site. The parameter F_{Jc} is critical jet force (N), and relies on the bit type used, drilling fluid's properties, as well as the pressure of the pump. Furthermore, h_f indicates the dimensionless fractional tooth dullness constant. The variable V_{Actual} refers to the volume of cuttings (m^3), while $V_{critical}$ indicates the critical volume for cuttings removal (m^3). Moreover, C_c stands for the constant for cuttings concentration. In addition, parameters A_{bed} and A_{well} represent the cuttings bed area and the wellbore area (m^2), respectively.

As previously stated, various researchers have worked to enhance the ROP models by incorporating new contributing parameters. That is why the empirical ROP models have seen ongoing enhancements, from Maurer's model to Osgouei's model. A summary of the different factors (including controllable and uncontrollable) used in the mentioned empirical models of ROP is provided in Table 3.1. According to the information in this table, the overall frequency of each included factor was determined, as shown in Figure 3.1.

Table 3.1 Parameters taken into account in the current empirical ROP Models.

Year	Author(s)	Controllable Parameters										Uncontrollable Parameters				
		WOB	RPM	D	h_f	F_{Jet}	TVD	μ	W_f	ρ_m	Q	S	H	p_p	C_c	A_{well}
1962	Maurer	Yes	Yes	Yes	No	No	No	No	No	No	No	Yes	No	No	No	No
1963	Galle and Woods	No	No	No	Yes	No	No	No	No	No	No	No	No	No	No	No
1965	Bingham	Yes	Yes	Yes	No	No	No	No	No	No	No	Yes	No	No	No	No
1974	Bourgoyne and Young	Yes	Yes	Yes	Yes	Yes	Yes	No	Yes	Yes	No	Yes	No	Yes	No	No
1981	Warren	Yes	Yes	Yes	No	No	No	No	No	No	No	Yes	No	No	No	No
1984	Warren	Yes	Yes	Yes	No	Yes	No	Yes	No	Yes	No	Yes	No	No	No	No
1986	Reza and Alcocer	Yes	Yes		Yes			Yes	Yes	Yes	Yes	No	Yes	Yes	No	No
1994	Hareland and Rampersad	Yes	Yes	Yes	Yes	Yes	No	Yes	Yes	Yes		Yes	Yes	No	No	No
2007	Osgouei	Yes	Yes	Yes	Yes	Yes	Yes	Yes	Yes	Yes		Yes	Yes	Yes	Yes	Yes
2022	Miska et al.	Yes	Yes	Yes	No	No	No	No	No	No	No	Yes	Yes	No	No	No

Figure 3.2 shows proportion of both manageable and unmanageable parameters in major empirical ROP models. According to this illustration, only 23% of these factors fall into the uncontrollable category. Therefore, compared to manageable parameters, uncontrollable parameters need to be more incorporated into future ROP models.

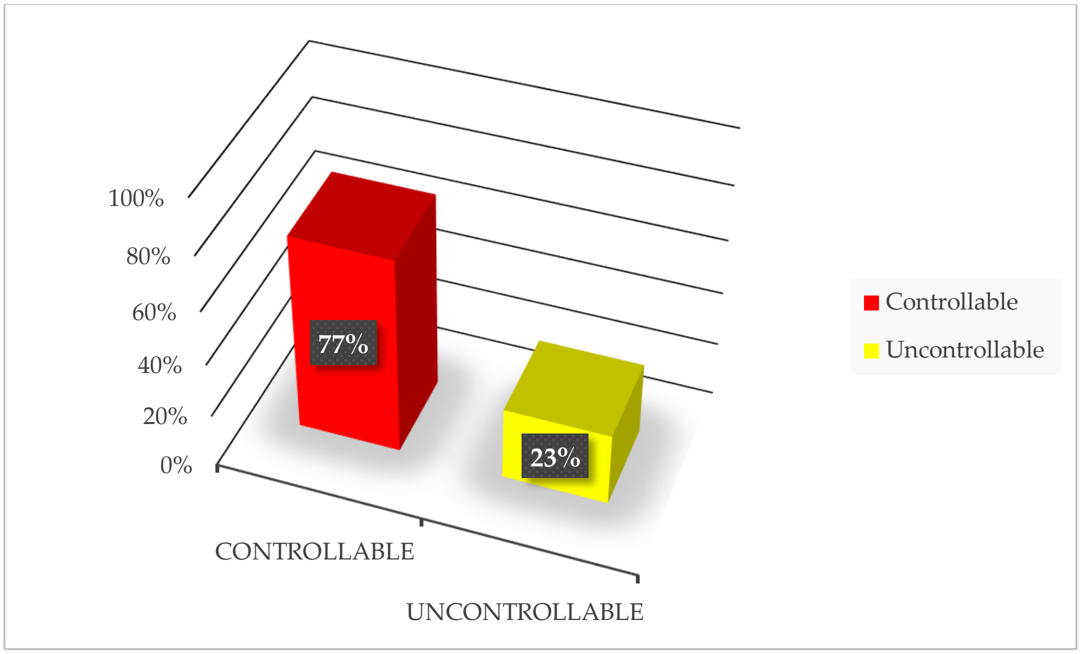

Figure 3.2 The proportion of inclusion of various controllable and uncontrollable parameters in the major existing models of ROP.

Besides the influencing factors, the relevance and usability of each ROP model are critically important as well. In drilling engineering, cutting tools or bits are generally categorized into two primary categories: fixed cutter bits and roller cone bits. The type of bit can significantly affect ROP. As an example, roller cone bits typically have the highest initial ROP, particularly those with significant offset and extended teeth. Such drill bits are well-suited for use in soft geological structures, but the corresponding ROP values decline as the bit advances into the denser rock layers (Abdulmalek et al., 2018). In contrast, fixed cutter bits employ a wedging action to fragment the rock method. As a result, the cutting angle at the bit bottom and the blade count have a significant impact on the ROP.

Table 3.2 presents the use of ROP models by bit category and highlights that empirical models are predominantly tailored to roller cone drill bits. It is noteworthy that just two models that were introduced by Reza and Alcocer and Osgouei, are applicable to both fixed cutter bits and roller cone bits.

Table 3.2 The relevance of empirical models of ROP in relation to the type of bit.

Year	**Author(s)**	**Bit type**	
		Roller cone bit	**Fixed cutter bit**
1962	Maurer	Yes	No
1963	Galle and Woods	Yes	No
1965	Bingham	No	Yes
1974	Bourgoyne and Young	Yes	No
1981	Warren	Yes	No
1984	Warren	Yes	No
1986	Reza and Alcocer	Yes	Yes
1994	Hareland and Rampersad	No	Yes
2007	Osgouei	Yes	Yes

The aforementioned ROP models have been mostly established for drilling of hydrocarbon production wells. Yet there is still a significant research gap to develop ROP models for coring operations. In coring operations, while increasing the ROP is generally desirable to reduce drilling costs and time, it is crucial to strike a balance between speed and core sample quality. A higher ROP may decrease drilling time but could also result in lower-quality cores, which is problematic if accurate geological data is needed. Coring operations are typically slower than conventional drilling due to the additional steps involved, such as handling and retrieving the cores, which further reduce ROP. As a result, optimizing ROP in coring requires careful consideration of factors such as the rock formation, bit type, drilling parameters, and the desired core quality.

The development of reliable ROP models tailored specifically for core bits remains a relatively underexplored area, despite its critical importance in optimizing core drilling operations. While numerous studies have addressed ROP and drilling efficiency in broader contexts, only a limited number of investigations focused explicitly on the unique dynamics of core bits, which involve distinct geometries and operational challenges.

Detournay et al. established a theoretical framework for understanding the drilling dynamics of coring bits, focusing on the interaction between key drilling factors like RPM, torque, WOB, and ROP. The study provided a great framework that incorporated core bit geometry and annular cutting mechanism. In that study, the depth of cut with each full rotation was defined as follows (Detournay et al., 2008):

$$d_c = \frac{2\pi ROP}{\omega} \tag{3.29}$$

Where ω is angular velocity (rad/s), and d_c represents the depth of cut during each complete rotation. This parameter provides insight into the efficiency of energy transfer during drilling, emphasizing the impact of rotational dynamics on ROP. To specify the model for coring bits, WOB and T were formulated as follow (Detournay et al., 2008):

$$\beta = \frac{WOB}{(\frac{D}{2})(1-\gamma')} \tag{3.30}$$

$$\zeta = \frac{2T}{(\frac{D}{2})^2(1-\gamma'^2)} \tag{3.31}$$

Here, β represents the normal force applied along each unit length of a two-dimensional cutter (N/m), ζ indicates shear force applied along each unit length of a two-dimensional cutter (N/m), D donates the diameter of bit (m), and γ' represents the proportion between the inner and outer diameter of bit.

Moreover, in that study, the drilling response was categorized into three distinct phases including:

- Friction-dominated phase: at shallow depths of cut, frictional forces between the bit and rock dominate, resulting in lower penetration efficiency.
- Optimal cutting phase: energy utilization is maximized as contact forces are fully mobilized, achieving efficient penetration.
- Overloading phase: excessive WOB or inadequate hole cleaning leads to diminished efficiency and potential tool wear.

Adapting Detournay's model to core bits involves addressing unique operational challenges. In better words, the proposed model, while effective in describing the drilling dynamics of core bits, presents certain limitations when applied in practical scenarios. One major drawback is the challenge of maintaining core quality. For instance, the model assumes ideal conditions for bottom-hole cleaning, which may not align with real-world operations. Inefficient removal of cuttings from the annular zone can lead to regrinding of debris, increased energy consumption, and reduced ROP. This drawback underscores the need for integrating additional parameters or adaptive control mechanisms into the model to better address these practical challenges.

In another study performed by Bilim and Karakaya, an ROP model was developed for core drilling operations. The model incorporated rock properties including porosity and density, along with the applied WOB (Bilim and Karakaya, 2021). To construct this model, the authors conducted core drilling tests on different rock types subjected to distinct WOBs. They also characterized the rocks by measuring key physical properties, specifically porosity and density, which strongly influence drilling performance. Porosity was considered because higher porosity typically reduces rock strength, making drilling easier, while density was included because denser rocks tend to resist penetration more. The applied dataset including ROP, porosity, density, and WOB formed the foundation for deriving their predictive model.

The model revealed that porosity positively correlates with ROP, while density negatively correlates, aligning with the mechanical properties of rocks. WOB was shown to increase ROP, although the effect may plateau at very high forces. By validating the model against their experimental data, the authors demonstrated that it could reliably predict ROP within the tested range of rock properties and drilling conditions. This approach highlighted the importance of integrating rock characteristics and operational parameters to optimize drilling performance. The corresponding ROP model was as follows (Bilim and Karakaya, 2021):

$$ROP = -0.000795\rho + 0.2\varphi + 2987 \tag{3.32}$$

Where, ρ represents density (kg/m^3) and φ stands for porosity.

Basarir et al. created an empirical ROP model for diamond drilling based on rock's UCS. They proposed a quadratic model for POR expressed as follows (Basarir et al., 2014):

$$ROP = -6.505 + 0.342\ UCS + 0.003UCS^2 \tag{3.33}$$

Where UCS represents the magnitude of rock's unconfined compression strength (MPa). This model highlights a relationship where ROP initially increases with UCS before plateauing or decreasing at higher values, reflecting the mechanical behavior of rocks under drilling conditions.

3.1.2. ROP AI-based models

Although ROP empirical models are robust, they may produce unreliable outcomes because they fail to consider all influencing factors (Mendes et al., 2007; Hamrick, 2011; Paiaman et al., 2009; Sultan and Al-Kaabi, 2002; Amar and Ibrahim, 2012; Abtahi, 2011; Gong et al. 2024). As a result, many researchers have explored the use of AI techniques in ROP modeling (Allawi et al., 2025; Mohammadinia et al., 2025; Huang et al., 2025; Gupta and Bhui, 2025; Ma et al., 2024; Bahari and Baradaran, 2009; Anemangely et al., 2017). Throughout the drilling process, a large volume of information is collected every day. This has led some experts and researchers in petroleum engineering to turn to AI approaches to predict ROP. The use of AI algorithms allows engineers to comprehensively analyze the collected information and derive useful perspectives. These techniques have been applied in various drilling-related challenges (Elkatatny, 2018; Minghui et al., 2016; Dupriest and Koederitz, 2005; Bello et al., 2016; Pollock et al., 2018).

To date, numerous AI methods have been employed for ROP modeling, with most studies utilizing Artificial Neural Networks (ANNs) algorithms. Additionally, a diverse set of input variables have been incorporated into those models.

ANNs mimic the way the brain processes information through biological neurons to learn features (Angelini and Ludovici, 2009; Monjezi and Dehghani, 2008Each artificial neural network is organized into an input layer, one or more hidden (intermediate) layers, and an output layer, with neurons serving as the basic structural components of every layer. Transfer functions are used to create links between these layers, followed by appropriate algorithms for training the model (Lippmann, 1987). The links between the neurons are associated with biases and weights (Hinton et al., 2006). The ANN algorithm involves two primary stages: training as well as testing. In the training phase, the hidden layer conveys the input factors onward to the output layer. In the testing phase, the forecasted ROP values are compared with actual ROP values measured in the field. Generating "black box" models is one of the major limitations of the ANN algorithm, making it difficult to understand the process by which the results are derived. Additionally, a significant number of parameters need to be configured in the ANN to avoid overtraining (Ahmed et al., 2018).

ROP prediction was first investigated using ANN by Bilgesu et al. (1997). Following this, Anemangely et al. developed two hybrid ANN-based methods for the formulation of a practical ROP model (Anemangely et al., 2018). Elkatatny also developed an ANN-based model, achieving highly accurate results (Elkatatny, 2019). Jahanbakshi et al. created an ANN model for predicting ROP in petroleum wells, which was identified as a highly dependable predictor able to produce accurate predictions. Other researchers applied different ANN structures, including Back Propagation Neural Networks (BPNN) (Jahanbakhshi et al., 2012) and Extreme Learning Machines (ELM) (Mahdi, 2020; Shi et al., 2016) for predicting ROP. The ELM technique was found to be more accurate than traditional ANN models (Mahdi, 2020; Shi et al., 2016).

In addition to the ANN approach, Support Vector Machine (SVM) algorithms were successfully employed to model ROP. In machine learning, SVM is recognized as a supervised algorithm commonly applied to classification and regression tasks. In regression applications, it utilizes a ε-insensitive loss function. In a study, the performance of SVM against BPNN was compared for ROP prediction. Findings revealed that SVM outperformed BPNN (Bodaghi et al., 2015). The SVM method was also utilized by Abdulmalek et al. for predicting ROP (Abdulmalek et al., 2018). Moreover, other SVM-based methods, like Least Squares Support Vector Regression (LS-SVR), were utilized to forecast ROP values. A study by Ahmed et al. assessed the relative performance of SVM, ELM, ANN, and LS-SVR algorithms in forecasting ROP within Niger Delta onshore drilling operations (Ahmed et al., 2018). The results showed that SVM and LS-SVR models outperformed the ELM and ANN models, but the testing process for SVM and LS-SVR was significantly longer (Shi et al., 2016).

Hegde et al. compared two types of ROP models including data-driven and empirical models; they concluded that the models obtained by data-driven methods offer better ROP predictions (Hegde et al., 2017). They pointed out that the primary drawbacks of empirical models are their reliance on empirical constants and lower precision in ROP value predictions. Additionally, many empirical models fail to account for factors such as mud properties, bit properties, and bit hydraulics. On the other hand, data-driven models have two key advantages: they do not require empirical constants, and the input data are actual Measured-While-Drilling (MWD) data collected from the drilling sites.

Arehart utilized neural networks to predict the level of bit wear during drilling, using input variables like ROP, WOB, RPM, torque, and hydraulic horsepower (Arehart, 1990). The model provided reasonably accurate predictions, though it was noted that additional data was required to better capture the relationship between the bit wear and variables. In a similar manner, Gidh et al. also employed neural networks to predict drill bit wear and subsequently applied the obtained results to improve ROP predictions (Gidh et al., 2012).

Bilgesu et al. developed a neural network-based approach to estimate ROP, utilizing a dataset of 8000 readings gathered from a rig floor simulation system (Bilgesu et al., 1997). The data consisted of parameters such as WOB, RPM, torque, rock drill-ability, mud pump rate, and bit characteristics. Amar and Ibrahim also employed neural networks to predict ROP, utilizing some parameters including WOB, tooth wear, ECD, Reynolds number, RPM, depth, and pore fluid pressure gradient (Amar and Ibrahim, 2012).

Almomen et al. developed and validated an ANN model for predicting ROP in unconventional reservoirs, achieving high accuracy with over 58,000 data points. The optimized ANN and derived empirical correlation show strong predictive performance, supporting better drilling efficiency and decision-making under challenging reservoir conditions (Almomen et al., 2024).

Hybrid approaches that integrate physics-based models with machine learning have recently gained popularity for predicting rate of penetration (ROP), demonstrating notably high accuracy (Bai et al., 2024). As an illustration, Jiao et al. applied a hybrid method using 5,655 field data recordings to enhance ROP prediction in the Tarim Basin. Their evaluation of different techniques revealed that residual modeling delivered the best performance (R^2 = 0.9936), offering both high predictive accuracy and interpretability, and thus serving as a valuable tool for drilling optimization (Jiao et al., 2024).

Although numerous AI algorithms have been applied for ROP prediction, choosing the most effective algorithm is challenging, specifically since there is no standard procedure for selecting the best algorithm. For example, while linear regression involves minimal computational complexity, it is unreliable in the presence of delimited parameters (Noshi and Schubert, 2018). On the other hand, the accuracy of Decision Tree models remains reliable, even with noisy or outlier-affected data, but they may suffer from overfitting. To address this issue some researchers such as Meng et al. introduced AI models like neural basis model (NBM) for ROP prediction which is a safer and more practical alternative to black-box AI models in drilling operations (Meng et al., 2024).

Additionally, the quantity and nature of the input variables to the AI models vary significantly between the conducted studies. Even with the selection of the best-performing AI algorithm, determining the ideal number of input parameters continues to be difficult. The category of input features can substantially influence the precision of AI-based predictions (Mostafaei et al., 2022). Drilling activities are conducted in formations with diverse geological units, such as sandstone, shale, and limestone. Thus, the lithology of the project site can greatly influence the input variables' selection. Moreover, geological variables may fluctuate significantly by depth, leading to the existence of irregular data points or noise. As a result, the ability of the chosen AI approach to handle such issues should be considered. Noisy data tends to have a stronger effect on statistical regression methods than on neural networks. The SVM-based models are generally less sensitive to noise than neural networks.

Akin and Karpuz developed an artificial neural networks (ANNs) ROP model for coring bits (Akin and Karpuz, 2008). The model was trained with data obtained from various drilling projects, incorporating factors like depth, rock properties and operational parameters. However, the developed model was not directly applicable to all bit types without re-training or significant modification of the model.

3.2. MSE state-of-the-art

3.2.1. MSE empirical models

In petroleum engineering, except maximizing ROP, minimizing energy consumption is also vital for reducing the total drilling costs. To achieve this, MSE models have been extensively formulated so far (Chen et al., 2018). MSE is very practical for optimizing the drilling activity, as it is practical to identify areas with high drilling efficiency or inefficiency (Macpherson 2025; Wiśniowski et al., 2015). MSE can be defined in simple terms as follows (Rafatian et al., 2010):

$$MSE = Input\ Energy/Volume\ of\ Rock\ Cut \tag{3.34}$$

Teale proposed the first MSE model. The following equation represents the mathematical expression of that model (Teale, 1965):

$$MSE = \frac{WOB \times g}{A} + \frac{2 \times \pi \times RPM \times T}{A \times ROP} \tag{3.35}$$

Rabia proposed a straightforward model for computing the consumed specific energy during drilling, as follows (Rabia, 1985):

$$E_S = \frac{WOB \times g \times RPM}{3 \times D \times ROP} \tag{3.36}$$

where, E_S stands for the drilling specific energy (Pa), and D shows the diameter of bit (m).

Later, in 1992, Pessier and Fear enhanced Rabia's model by using the MSE term instead of E_S. The corresponding model was as follows (Pessier and Fear, 1992):

$$MSE = g \times WOB \times \left(\frac{1}{A} + \frac{0.22 \times \mu_b \times RPM}{D \times ROP}\right) \tag{3.37}$$

where μ_b stands for the friction coefficient between the rock and drill bit (dimensionless). Generally, for tricone bits the value of μ_b is assumed to be 0.25 while for PDC bits it is 0.5.

Some studies have associated MSE factor with the rock's CCS to assess drilling efficiency. The relationship between rock's CCS and MSE might be expressed in empirical terms as (Minghui et al., 2016):

$$E_m = \frac{CCS}{MSE} \times 100 \tag{3.38}$$

Where E_m represents the drilling's mechanical efficiency (dimensionless).

Dupriest and Koederitz incorporated the parameter E_m into their MSE model (Dupriest and Koederitz, 2005). They incorporated the concept of mechanical efficiency into Teale's MSE model assuming E_m typically falls within the range of 30%-40% of MSE (Rafatian et al., 2010). Their model is represented by the following relationship (Dupriest and Koederitz, 2005):

$$MSE = E_m \left(\frac{WOB \times g}{A} + \frac{2 \times \pi \times RPM \times T}{A \times ROP} \right) \tag{3.39}$$

Armenta conducted a study to explore a relationship between drilling performance and the rock's UCS (Armenta, 2008). Therefore, through laboratory testing, a great attempt was made to identify whether a meaningful correlation could be established between UCS and MSE. It was stated that the rock's UCS may not be a suitable indicator for evaluating MSE during drilling. It was observed that MSE values are often significantly higher than UCS values, making it difficult to define a clear relationship between the two parameters. Additionally, it was noted that MSE values might also exceed the rock's UCS at the bottom of the wellbores (Chen et al., 2018). It is noteworthy to mention that it is possible to estimate UCS by MSE. By incorporating pore pressure and bottom-hole pressure, the modified MSE (MMSE) shows alignment with resistivity logs and enhances the prediction of drilling efficiency. This indicates that MMSE could somehow act as a substitute for UCS estimation, supporting more accurate pore pressure evaluation and advancing drilling automation (Sahood et al., 2024).

The direction of drilling also significantly impacts the stresses applying on the drill-bit as it penetrates deeper. Chen et al. developed an outstanding empirical MSE model which was applicable for all drilling directions including vertical, horizontal, and inclined boreholes (Chen et al., 2018). According to that model, WOB as well as torque are highly determining in MSE evaluation. The corresponding model was formulated as follows (Chen et al., 2018):

$$MSE = E_m \times g \times WOB_b \left(\frac{1}{A} + \frac{0.222 \times \mu_b \times RPM}{D \times ROP}\right) \tag{3.40}$$

where,

$$WOB_b = WOB \times e^{-\mu_s \gamma_b} \tag{3.41}$$

Where WOB_b is the weight on the bit at the bottom-hole (kg). Additionally, μ_s represents the coefficient of drill string sliding (dimensionless), and parameter γ_b stands for the unitless bottom-hole inclination constant.

Miska et al. proposed an MSE model based on the relationship between the torque exerted by the drill bit, the depth of penetration, and the bit's cross-sectional area. The corresponding MSE model was as follows (Miska et al., 2022):

$$MSE = \frac{T}{d_c A} \tag{3.42}$$

Where T represents the torque (N.m), d_c stands for the depth of cutting (m), and A depicts the bit's cross-sectional area (m^2). The parameter d_c was formulated as follows (Miska et al., 2022):

$$d_c = \frac{c_1 \times \boldsymbol{\mu_b} \times WOB \times g \times E_f}{CCS} \tag{3.43}$$

Where parameter c_1 is a constant determined by the specific geometric characteristics of the drill bit (dimensionless), μ_b stands for the friction coefficient between the rock and drill bit (dimensionless), E_f shows the drilling efficiency (dimensionless), and CCS is confined compression strength of rock (Pa).

Moreover, an ROP model was developed as follows (Miska et al., 2022):

$$ROP = 2\pi N d_c = 2\pi N \frac{c_1 \times \mu \times WOB \times g \times E_f}{CCS} \tag{3.44}$$

Where, N is the normal force exerted by the drill bit (N) computed as follows (Miska et al., 2022):

$$\mu = \frac{F}{\mu_b} \tag{3.45}$$

Where F depicts the frictional force at the interface of rock and bit (N). Note that this model is derived theoretically under the assumption that certain parameters including μ_b, E_f, CCS are known and available.

The aforementioned empirical models encompass some of the most widely applicable MSE models. As observed, those models were gradually refined over time. Nevertheless, yet there are some research gaps that need to be addressed. In general, the input variables in MSE models are associated with two main origins including the operational parameters and rock's characteristics. As an illustration, the MSE models developed by Teale and Rabia chiefly incorporated the operational factors in MSE formulations. The main drawbacks of both models was that they did not include the impact of formation characteristics in the MSE formulations.

Several researchers sought to enhance MSE predictive models particularly by incorporating additional parameters related to rock properties. One of the notable efforts in this regard was conducted by Armenta (Armenta, 2008). It was attempted to correlate the UCS of rocks with the MSE quantities. Although this work was considered pioneering and unique at the time, the subsequent experiments revealed that there is no consistent or direct relationship between UCS and MSE. This discrepancy arises from the fact that UCS alone cannot serve as a reliable indicator of rock drill-ability. As a matter of fact, several other critical factors, e.g. porosity, density, anisotropy, chemical composition, type of pore fluid, hardness, and abrasiveness, also significantly influence MSE. Hence, while UCS may reflect the general hardness of the rock, it fails to capture the full spectrum of variables that affect drilling performance. The limitation of current models in integrating an optimal combination of rock parameters remains an unresolved issue. In this doctoral dissertation, one of the main objectives is to address this research gap by incorporating a broader range of rock characteristics into MSE-based predictive models.

These parameters mainly include the rock's mechanical properties and fundamental physical attributes, such as density and porosity.

Although the initial use of the MSE concept was primarily focused on optimizing drilling operations, its applications have since expanded to include a variety of important tasks (Dupriest et al., 2023) such as estimating formation properties, designing bits and cutters, and estimating formation pore pressure (Khalilidermani and Knez, 2022). In the following paragraphs, those novel applications are briefly elaborated to provide the latest advancements in this research area.

The MSE concept can be used to estimate formation properties (Peña-Gutiérrez and Sabirov., 2024). In 2020, Trivedi et al. estimated the CCS of some rocks using a predictive MSE program (Trivedi et al., 2020). Their MSE model incorporated drilling-related dysfunctions including drill string vibration, drilling fluid engine dynamics, and frictional losses in the drill string. The authors concluded that it is feasible to extract an empirical correlation between the CCS of rocks and MSE values using two supplementary factors: Hydraulic Specific Energy (HSE) together with the Vibration Specific Energy (VSE). The HSE term indicated the hydraulic impact load on the rock, and the VSE term represented the energy losses during the vibration mechanism. Klib et al. (2022) also introduced new processes for CCS estimation based on MSE.

Additionally, the MSE concept is applicable in the designation of bits and cutters. Through trial-and-error approaches and advanced numerical modellings, the rock cutting process and bit performance can be thoroughly analyzed. The goal of these investigations is bit (or cutter) designation which minimizes the amount of MSE required to effectively fragment the rock. These studies have primarily focused on PDC bit/rock or PDC cutter/rock interactions (Chen et al., 2021). Amongst those models, the PDC cutter/rock interaction model established by Miedema served as a foundational model for later research (Miedema, 1987). This model was designed to assess the interaction between PDC cutters and different rocks. The model utilized the concept of equilibrium of forces to estimate the forces of cutting and MSE quantities.

The concept of MSE has also been used to assess the pore pressure within the formation. Removing a single unit of rock volume requires energy that is affected by in-situ strength of rock and the pressure variation exerted. For instance, Majidi et al.

proposed a technique for estimating pore fluid pressure by combining in-situ rock properties and subsurface drilling mechanics via drilling efficiency (DE) and MSE terms (Majidi et al., 2017). The method utilized MSE for pore pressure prediction, integrating torque and WOB to include the consumed drilling energy. It was reported that the MSE-based pore pressure prediction method yielded results that aligned very suitably with traditional petrophysical estimations techniques.

3.2.2. MSE AI-based models

The AI techniques have been frequently deployed for MSE prediction. The vast volume of MWD information can effectively be imported into different AI algorithms (Bello et al., 2016). The SVM technique, ANN approach, and generic algorithms (GA) have been the most widely applied AI techniques for MSE prediction (Tian et al., 2023; Holdaway, 2014; Goebel et al., 2014). Nowadays, data-driven MSE models are being used more and more because they can quickly incorporate a wide range of drilling parameters. Some of the more fascinating instances of this kind of models are described in this section.

To forecast the features of the underlying geological formations belonging to an oil field in southern Iran, Anemangely et al. developed a model for MSE based on data-driven methods in 2018 (Anemangely et al., 2018). These rock characteristics included Poisson's ratio, internal friction angle, UCS, and CCS. They used MLP neural networks to achieve this. Their results demonstrated how well the applied AI techniques could anticipate the characteristics of the rock and MSE. It was stated that the predictions could be affected by the type of input data. In fact, they found that when the goal is to estimate the internal friction angle, UCS, and CCS, utilizing AI approaches yields accurate results. The Poisson ratio forecast, however, did not perform as well as other characteristics.

In 2018, Hegde and Gray used the random forest algorithm to create an MSE model (Hegde and Gray, 2017). They developed their model using drilling real-time data, including mud flow rate, rotation speed, WOB, and formation strain. They claimed that they could reduce the bit's torque by up to 7% and raise the ROP by up to 20% using the new MSE model. As a result, they came to the conclusion that the data-driven MSE model helped the bit lasts longer and have less downtime. A similar study was conducted by Hassan et al. who optimized the ROP using torque and MSE (Hassan et al., 2018).

In a different study, Hamlawi et al. introduced a new MSE model based on data-driven methods to estimate the ideal RPM and WOB values, allowing for real-time drilling efficiency optimization (Hamlawi et al., 2021). The MSE model served as a tool for advising on improving penetration rates and extending the lifespan of drilling equipment. The model was capable of predicting potential drilling issues and notifying the drilling team about possible undesirable events. They concluded that the AI-based MSE models can significantly reduce bit wear, the cost of replacing bits, fuel usage, non-productive time (NPT), along with overall operational days.

Liang et al. employed the SVM technique for developing an MSE model for identifying lithological composition in front of the drill bit (Liang et al., 2022). They developed multiple SVM models applying various types of raw data. It was found that the MSE concept could effectively recognize lithology with an accuracy exceeding 90%. The SVM method's main strength lay in its ability to handle large amounts of noisy data with outliers.

A deep learning technique, based on the MSE concept, was introduced by Arnø et al. to classify formations being drilled at the bit's depth in real time (Arnø et al., 2021). Once the model was trained and validated, its ability to classify various formations was tested and found to be highly successful. The model quickly identified the type of layers at different boundaries, allowing operators to be rapidly alerted when the drill bit began penetrating a new formation.

Chapter 4:

Methodology

The methodology of this research consists of two main parts: laboratory and analytical. This research follows a two-part methodology: laboratory experimentation and analytical evaluation. The laboratory part (Section 4.1) involves physical and mechanical measurements of rock samples, while the analytical part (Section 4.2) applies statistical and analytical techniques to establish relationships between drilling performance metrics.

The laboratory part started with sample preparation, including cutting, drilling, and smoothing rock cylindrical cores, followed by density and porosity measurements. A drilling machine was used to measure ROP and MSE based on controlled experiments. Additionally, rocks' mechanical properties including UCS and dynamic elastic parameters (Poisson's ratio, Young's modulus, bulk modulus, and shear modulus) were obtained through a tri-axial compression machine and an acoustic velocity measurement (AVS) apparatus, respectively.

The analytical part employed Pearson's correlation coefficient technique to identify the most influential rock properties and drilling parameters affecting ROP and MSE. Basically, this statistical approach quantifies the linear relationship between variables, guiding the selection of key parameters for the analytical analysis part.

Following this, dimensional analysis was utilized to derive empirical equations for ROP and MSE formulation. This technique ensured that the developed ROP and MSE models: 1) maintained dimensional consistency, 2) relied on the most essential and measurable parameters, and 3) provided accurate results. The empirical correlations obtained through dimensional analysis formed the basis for predictive modeling, which is elaborated in subsequent chapters.

Together, the laboratory and analytical methodologies provide a comprehensive framework for analyzing the influence of rock characteristics and drilling variables on drilling efficiency (ROP and MSE), contributing to improved drilling optimization.

4.1. Laboratory part

The laboratory measurements process included two segments: 1) Drilling tests; 2) Rock mechanical tests. In what follows, the methodology of both tests as well as the applied laboratory equipment are described. All applied laboratory equipment were available in the laboratory of the Department of Drilling and Geoengineering at AGH University of Krakow.

4.1.1. Drilling tests

The drilling tests were done on four rock type including Szydłowiec-Śmiłów sandstone, Wola Komborska sandstone, Tumlin sandstone, and Morawica marble. Samples of Szydłowiec–Śmiłów sandstone were collected from the Śmiłów quarry near Szydłowiec in the Świętokrzyskie region. The Wola Komborska sandstone, classified as Istebna sandstone, originated from the Wola Komborska deposit. Tumlin sandstone was extracted from the upper stratigraphic levels of the Tumlin deposit, located to the north of Krakow, Poland. Morawica marble samples were also gathered from the northern area of Krakow.

To perform the drilling tests, firstly a large piece of each rock type was taken from the site, and then, transferred to the laboratory. Afterwards, using a cutting machine, those rock pieces were cut to the smaller slabs. Figure 4.1 shows the applied cutting machine. This machine is basically used for the initial cutting of large pieces of rocks. The operating procedure involves placing a rock piece in front of the machine's circular blade. Upon activating the motor, the circular blade cuts the rock piece into smaller pieces. During the cutting process, water is sprayed onto the blade through a nozzle to prevent the blade wear and tear.

Figure 4.1 Cutting machine.

In the subsequent step, the drilling tests were performed on the obtained rock slabs. The two main objectives of performing the drilling tests were:

- Measuring the drilling parameters, e.g. ROP and MSE, for different rock types.
- Taking core samples for conducting rock physical and mechanical tests.

To perform the drilling tests, firstly, a rock slab was positioned beneath the coring drill bit of the drilling machine. Figure 4.2(a) illustrates the drilling machine, while Figure 4.2(b) shows the coring drill bit. The drill machine was manufactured by Syderic Company. Syderic is a French manufacturer specializing in the production of drilling and milling machines. Their equipment is well-regarded for precision and durability, commonly utilized in metalworking and drilling machines applications. In this research, all drilling tests were performed using a diamond coring drill bit which was 135 mm in length. Additionally, the outer and inner diameters of the coring bit were 44 mm and 38 mm, respectively. Thus, the ratio of outer diameter to the inner diameter of the coring bit was approximately equal to 1.16.

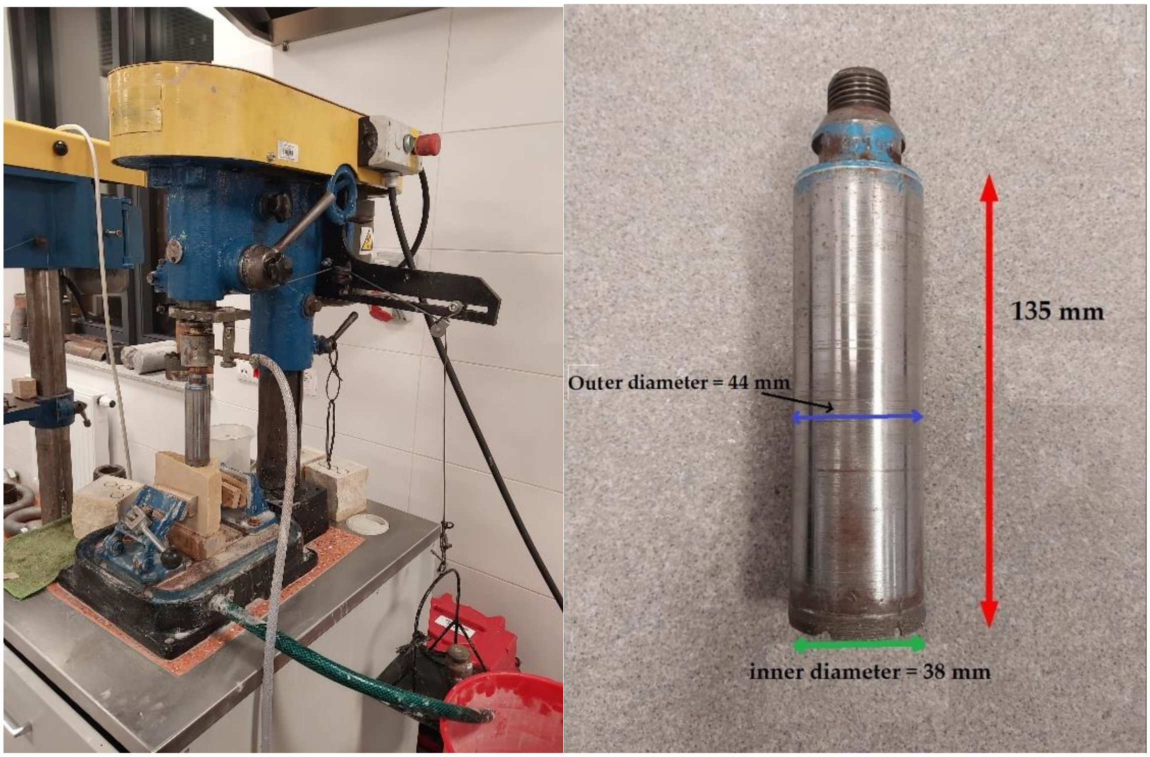

Figure 4.2 a) Drilling machine; b) coring diamond drill bit.

Once the rock slab was positioned beneath the drill bit, the drilling machine was turned on. It is also worth mentioning that water was continually poured on the rock-bit interface to prevent bit wear, and transport the rock debris out of the hole during the drilling process.

Subsequent to this stage, the WOB and RPM were set; the drilling tests were carried out under following combinations of WOB and RPM:

- *WOB*: 4 kg, 8kg, 12 kg, and 16 kg for three sandstones, and 8 kg, 12 kg, 16 kg, and 20 kg for Morawica marble (It is noteworthy that the WOB applied on the dolomite could not set as 4 kg because it was insufficient for drilling the rock).
- *RPM*: 450 REV/min, 977 REV/min, 1636 REV/min, and 2634 REV/min for all rock types.

In total, 64 drilling tests were conducted which also resulted in taking 64 cylindrical core samples. As there were 4 different rock types, 16 core samples were taken for each rock type. When a specific drilling test finished, the corresponding drilling time and the drilling depth (hole depth) were measured. The depth of the hole was measured with a caliper with an accuracy of 0.1 mm. Subsequently, the corresponding ROP was calculated by dividing the drilling depth to the drilling time as follows:

$$ROP = \frac{h}{t} \tag{4.1}$$

Where h represents the drilling depth (m), and t indicates drilling time (s).

After that, having the electric power of the drilling machine, drilling time, and the cut volume of the rock sample, the corresponding MSE was computed as follows:

$$MSE = \frac{E}{V_{net}} \tag{4.2}$$

Where, E represents the electrical energy consumed by the drilling machine (J), and V_{net} indicates the net removed volume of the rock (m^3) by coring bit. The consumed electrical energy was calculated as follows:

$$E = P \times t \tag{4.3}$$

Where P represents the electric power of the drilling machine. That power was equal to 400 Watts. Additionally, the parameter V_{net} was determined as follows:

$$V_{net} = h \times A_{net} \tag{4.4}$$

Where

$$A_{net} = \frac{\pi}{4} D^2 \times (1 - \frac{1}{\lambda^2}) \tag{4.5}$$

Where A_{net} represents the area of the non-hollow cross section of the coring bit. Moreover, D represents the outer diameter of the coring bit, and λ represents the ratio of outer diameter to the inner diameter of the coring bit. As earlier mentioned, the outer diameter of the coring bit was 44 mm, and the value of λ was approximately equal to 1.16. Hence, using Eq. (4.5), the value of A_{net} is calculated as 0.000386 m^2.

Using the procedure outlined above, the first main objective, i.e. measuring the drilling parameters for different rock types, was successfully achieved. Subsequently, core samples were taken and utilized to assess their physical and mechanical properties, which will be detailed in the following subsection.

4.1.2. Rock physical and mechanical tests

During the drilling tests, 64 core samples were collected, with 16 samples obtained from each rock type. Variations among the 16 samples were expected due to potential inhomogeneities, such as cracks, irregular voids, and minor mineralogical differences. Consequently, the physical and mechanical properties of all 16 core samples were measured for all four types of rock.

To measure the physical and mechanical parameters of core samples, various devices were utilized. The following procedure was performed for each core sample:

1) Firstly, each core sample was cut to the desired length, and then, its lateral sides were smoothed using a specific cutting-smoothing apparatus. This apparatus is illustrated in Figure 4.3. The lateral sides of the core samples were smoothed to ensure that they were free of any roughness or asymmetry affecting the results during the conduction of physical and mechanical tests.

Figure 4.3 Cutting-smoothing apparatus.

2) After shaping the rock samples to the required dimensions, their weights were determined using a balance. With both the measurements of their dimension and recorded weight, the volume and density of each sample were calculated. To ensure accuracy, multiple measurements were taken, and any inconsistencies were noted. The density of each rock sample needed to be measured, as it is an essential parameter for calculating rock's dynamic elastic moduli.

3) In the next step, an acoustic wave propagation instrument (AVS) was deployed to measure the dynamic elastic characteristics of the rock samples (Figure 4.4). The dynamic tests were utilized as the equivalent static instruments were not available in the laboratory. The AVS instrument, model AVS 1000, was manufactured by the French company VINCI, known for producing high-quality laboratory devices. With a strong reputation for reliability and precision, VINCI devices are widely used in various industries, including construction, engineering, and geology, ensuring accurate and dependable results in laboratory testing.

Figure 4.4 AVS instrument.

Using the AVS instrument, four primary dynamic elastic parameters were measured for each core sample: Poisson's ratio, bulk modulus, shear modulus, and Young's modulus. To obtain these measurements, the core sample was first placed in the core holder. A compressional wave together with two shear waves were then transmitted through the sample from one side to the other. The characteristics of the transmitted waves, e.g. time of flight, were displayed on an oscilloscope screen. Having the time of flight for each transmitted wave and the length of the core sample, the velocity of each wave was calculated.

Afterwards, the following formulas were utilized to calculate the dynamic elastic parameters of the samples:

$$v_{dyn} = \frac{\frac{1}{2}-\left(V_s/V_p\right)^2}{1-\left(V_s/V_p\right)^2} \tag{4.6}$$

$$E_{dyn} = \rho \frac{V_p^2(1+v_{dyn})(1-2v_{dyn})}{(1-v_{dyn})} \tag{4.7}$$

$$K_{dyn} = \rho({V_p}^2 - \frac{4}{3}{V_s}^2) \tag{4.8}$$

$$G_{dyn} = \rho V_s^2 \tag{4.9}$$

In Eqs. (4.6-4.9), v_{dyn}, E_{dyn}, K_{dyn}, and G_{dyn} represent the dynamic Poisson's ratio, dynamic Young's modulus, dynamic bulk modulus, and dynamic shear modulus, respectively. Additionally, V_P and V_s respectively indicate the compressional and shear wave velocity. The rock's density is represented by the symbol ρ.

It is important to note that two types of S-waves were propagated through the specimens: S1-wave and the S2-wave. When the rock specimen was isotropic, the velocities of the S1 and S2 waves were nearly identical. However, if the velocities differed, it indicated the presence of anisotropy in the specimen's structure. According to the results of the conducted experiments, the velocities of the S1-wave and S2-wave were consistently found to be equal, suggesting that the specimens were isotropic.

Since the velocities of acoustic waves in rocks are influenced by the stresses acting on them, lateral and axial pressures were applied during each test in intervals of 5 MPa, up to a maximum of 70 MPa. The stress was applied on the rock sample through a hand-operated pump jack. For each rock sample, the parameters of V_P, V_s, v_{dyn}, E_{dyn}, K_{dyn}, and G_{dyn} were measured under 14 loading conditions, corresponding to hydrostatic stresses applied at intervals of 5 MPa, beginning at 5 MPa and reaching 70 MPa. The final value for V_P, V_s, v_{dyn}, E_{dyn}, K_{dyn}, and G_{dyn} for each rock sample was then calculated were then calculated by averaging the results from these 14 measurements.

It should be mentioned that the maximum hydrostatic stress applied on the core samples in AVS instrument was determined using a triaxial compression testing machine. This machine is shown in Figure 4.5. Using this device, the Uniaxial Compression Strength (UCS) of all rock types were determined. By having the UCS of each rock type, the maximum hydrostatic pressure for the AVS test was determined. Although, rocks have less resistance under uniaxial pressure conditions, but as a precaution and to prevent the sample from collapsing in the AVS chamber during testing, the average UCS of the rock was considered as the maximum allowable hydrostatic pressure allowed for the AVS test.

Figure 4.5 Triaxial compression testing machine.

4) After completing the AVS tests, the samples were placed in an oven to remove any moisture. They were kept in the oven at 90°C for 72 hours to ensure complete drying. Once removed from the oven, the dry masses of the samples were measured. Subsequently, the samples were saturated with distilled water. Figure 4.6 illustrates the saturation device used, which was manufactured by the French company VINCI. The saturation process began by placing the samples inside the chamber of the device. A vacuum pump was then used to remove the air and water from the chamber. Once the air and water was completely evacuated, the water inlet valve was opened to allow water to flow into the chamber. Then, using a manual lever, the pressure inside the chamber was gradually raised. The samples remained in the chamber under 14 MPa for 48 hours to reach complete saturation. After that, the samples were taken out, and their saturated weight were measured. Having the dry and saturated masses of each rock sample, the porosity of all the samples was determined.

Figure 4.6 Saturation device.

4.2. Analytical part

The second part of the methodology involved analytical approaches aimed at achieving the following goals:

1) Quantifying the correlations between various contributing factors and ROP and MSE.
2) Developing empirical formulations linking ROP and MSE to the most influential parameters.

To reach the first goal, Pearson's correlation coefficient technique was utilized. Developed by the British mathematician Karl Pearson (1857-1936), this technique statistically determines the degree and orientation of linear relation between two arbitrary parameters.

To reach the second goal, dimensional analysis approach was utilized. Dimensional analysis is a powerful technique that allows for the derivation of mathematical relationships by analyzing the dimensions of the quantities involved. Both Pearson's correlation coefficient and dimensional analysis techniques are elaborated in the following subsections.

4.2.1. Pearson's correlation coefficient technique

A standard statistical tool for exploring the relationship between two arbitrary variables is Pearson's correlation coefficient technique. This method is particularly useful in drilling data analysis, where understanding the influence of different parameters on ROP and MSE is crucial for optimizing drilling efficiency. This approach enables drilling engineers to identify the most influential parameters on ROP and MSE values, thereby improving ROP and MSE predictive models.

To quantify the relationship between two arbitrary variables of x and y, the Pearson's method calculates a correlation coefficient between two parameters. Such a correlation coefficient is formulated as follows (Rodgers and Nicewander, 1998):

$$r = \frac{\Sigma(x_i - \bar{x})(y_i - \bar{y})}{\sqrt{\Sigma(x_i - \bar{x})^2}\sqrt{\Sigma(y_i - \bar{y})^2}} \tag{4.10}$$

Where, r indicates the Pearson's correlation coefficient; Furthermore, x and y represent the two arbitrary variables. In addition, $\bar{x}$ and $\bar{y}$ indicate the means of x and y, respectively. Moreover, x_i corresponds to the i-th observation of variable x, while y_i denotes the variable y at the same data point.

The value of r lies within the range of $-1 \leq r \leq +1$. As it approaches +1, the positive linear association between x and y is stronger. On the other hand, the closer it is to -1, the stronger the negative linear association. As r is closer to 0, it indicates a weaker or more non-linear relationship between two parameters.

In the current research, the values of *r* were calculated for different rock's and drilling parameters, and ROP and MSE. Based on the obtained results, the most influential rock properties and drilling variables affecting ROP and MSE values were identified.

4.2.2. Dimensional Analysis

Dimensional analysis is a fundamental mathematical technique used to derive empirical relationships between different variables by analyzing their fundamental units. This approach is particularly valuable in drilling engineering, as it enables the development of ROP and MSE mathematical models by incorporating key drilling parameters and rocks' properties. By ensuring dimensional consistency, this method facilitates the identification of relationships among different variables.

Once the most influential parameters affecting the drilling process were identified using Pearson's correlation technique, dimensional analysis was applied to derive empirical equations for ROP and MSE. These equations were formulated to satisfy the following fundamental criteria:

1. The selected parameters must be practical and straightforward to measure in real-world drilling operations.
2. The equations should incorporate only the essential parameters necessary to ensure accurate and reliable estimations of ROP and MSE.
3. The derived empirical equations must be dimensionally consistent.

4.2.3. Model evaluation and validation strategy

The final step of this research involves evaluating how well the developed models replicate actual drilling performance. To achieve this, the experimentally measured values of ROP and MSE are compared against the values generated by the newly developed formulations. The degree of agreement between measured and estimated results provides a direct indication of the models' reliability under laboratory conditions.

Validation is carried out through both visual and statistical techniques. On the qualitative side, graphical comparisons such as scatter plots are used to illustrate the closeness of fit between experimental data and model estimations. On the quantitative side, widely accepted statistical evaluation metrics such as R^2, MAPE, and mean root mean square error (RMSE) are deployed to provide a rigorous assessment of predictive accuracy. Together, these methods ensure that the performance of the models is evaluated from multiple perspectives, reinforcing the robustness of the conclusions drawn in later chapters. Based on the above-mentioned criteria, two empirical equations were obtained for ROP and MSE. Those equations are comprehensively described in Chapter 7.

.

Chapter 5:
Laboratory Measurements

5.1. Coring tests

As mentioned in the previous chapter, 64 coring tests were undertaken systematically to analyze the influence of drilling parameters on core drilling performance. As a result, 64 core samples were taken. Figure 5.1 presents the collected core samples categorized by rock type. To provide further insight, Figures 5.2 through 5.5 display vertical and cross-sectional views, accompanied by close-up images of the mineralogical texture and grain structure for each rock type.

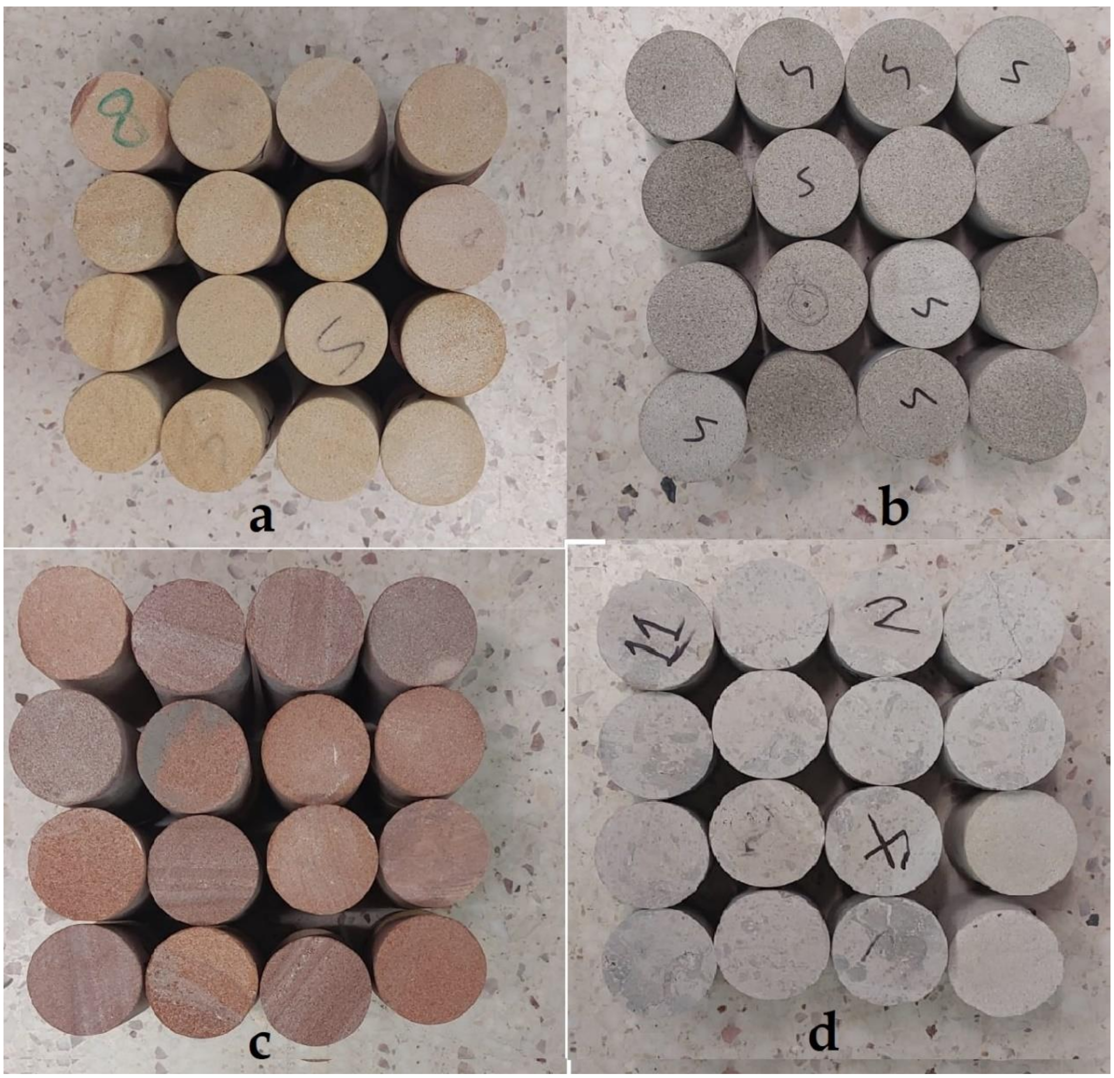

Figure 5.1 Core samples obtained from drilling tests on: a) Szydłowiec–Śmiłów sandstone; b) Wola Komborska; c) Tumlin sandstone; and d) Morawica marble.

Figure 5.2 Vertical and cross-sectional views with close-up of mineralogical texture and grain structure of Szydłowiec–Śmiłów sandstone.

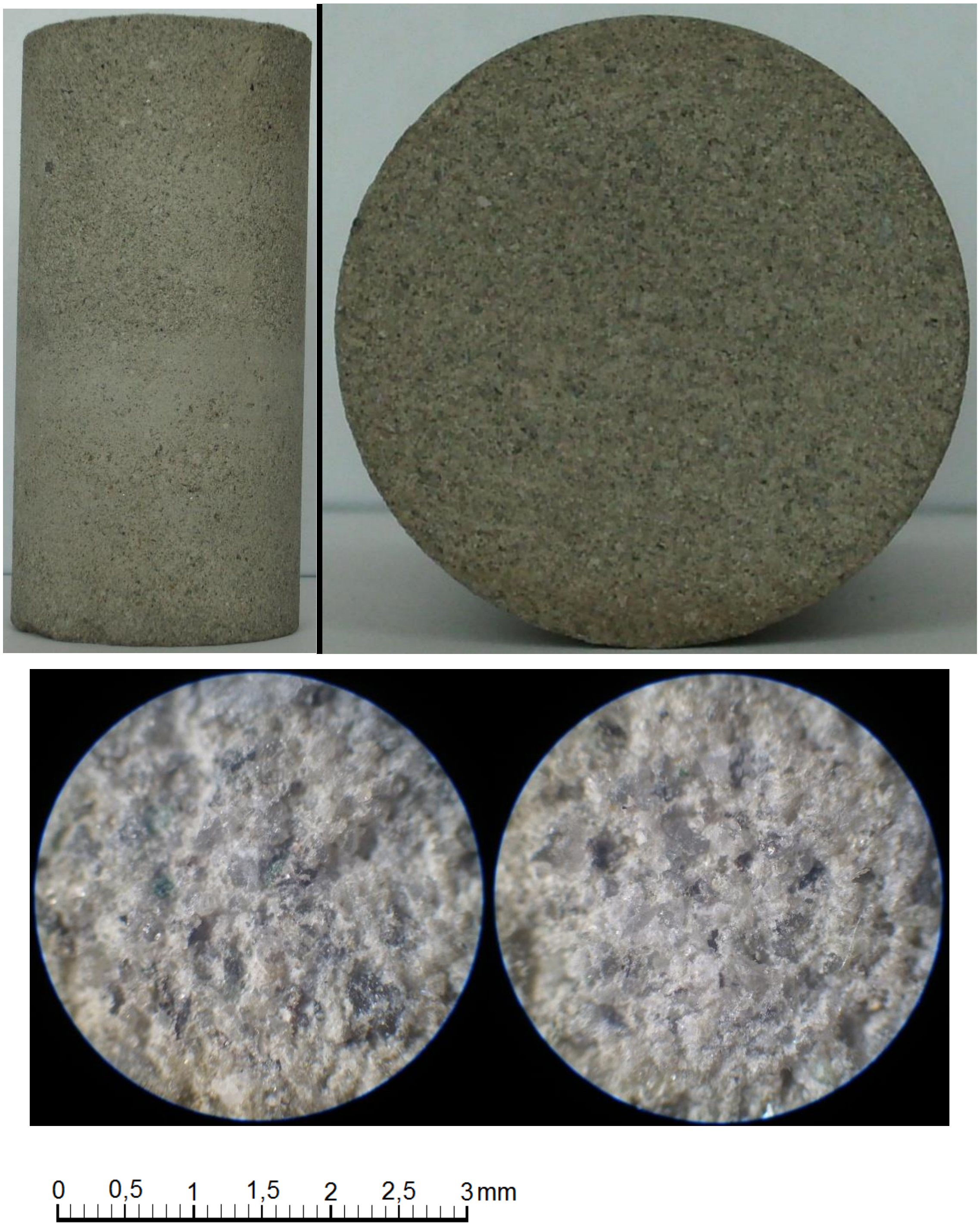

Figure 5.3 Vertical and cross-sectional views with close-up of mineralogical texture and grain structure of Wola Komborska sandstone.

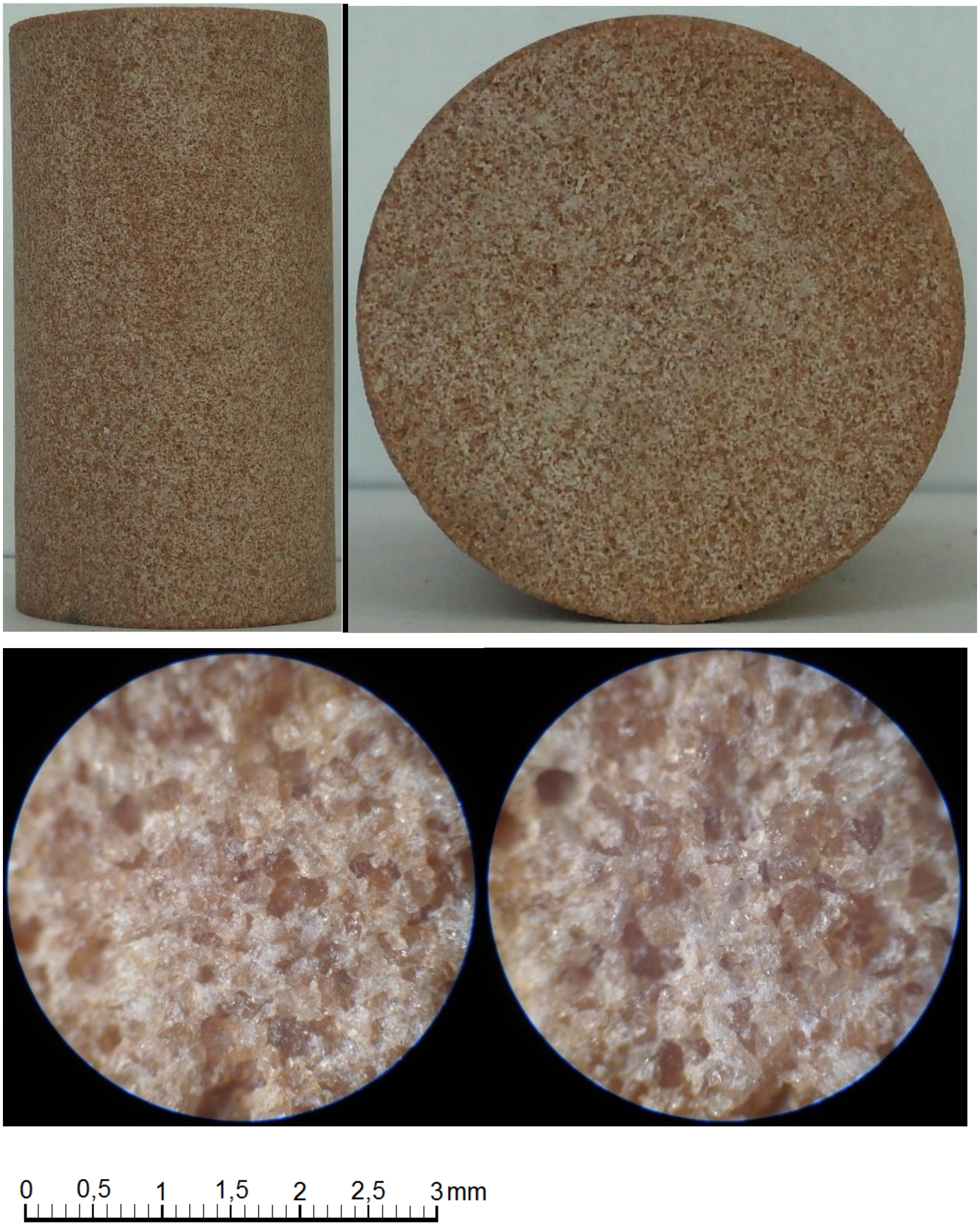

Figure 5.4 Vertical and cross-sectional views with close-up of mineralogical texture and grain structure of Tumlin sandstone.

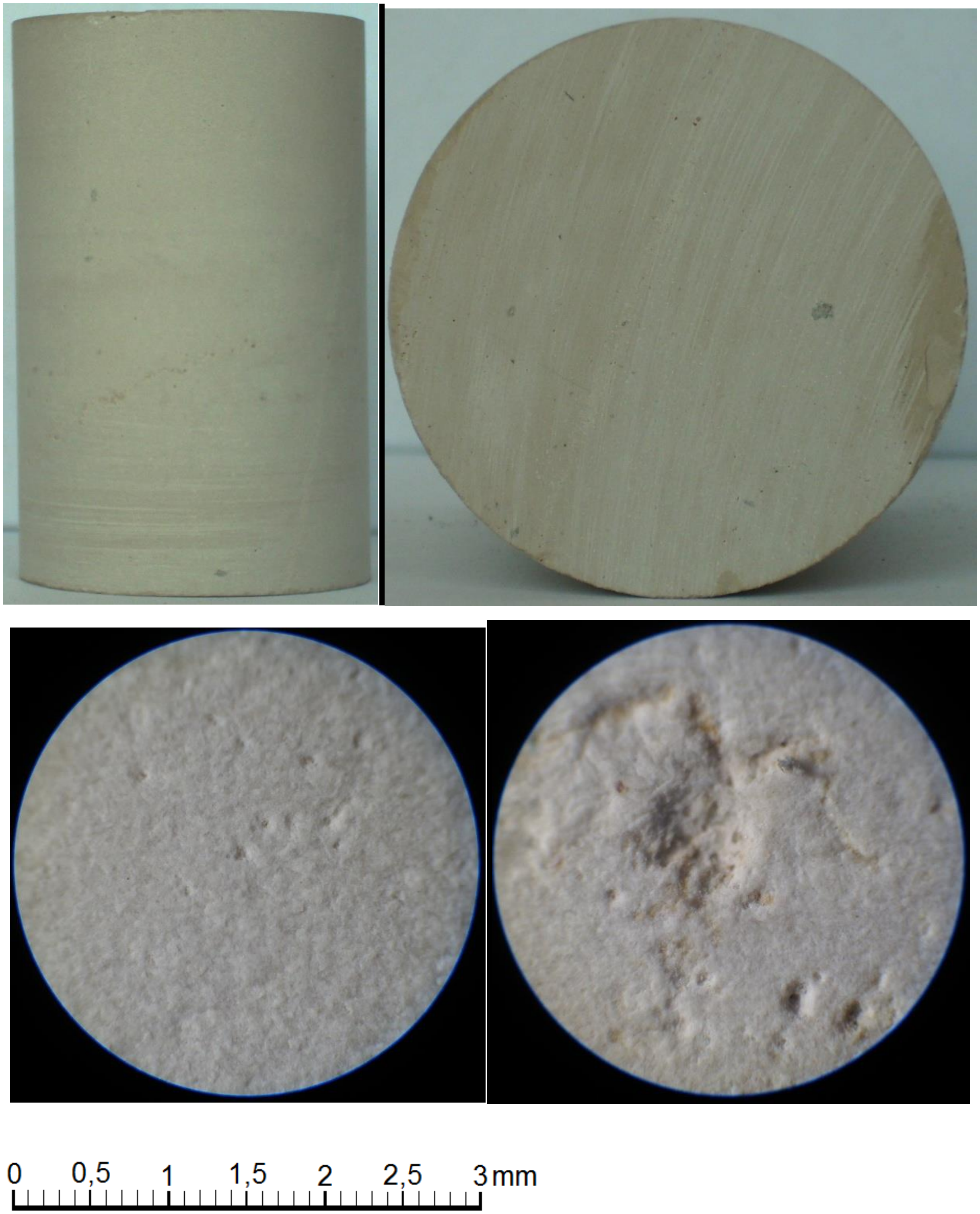

Figure 5.5 Vertical and cross-sectional views with close-up of mineralogical texture and grain structure of Morawica marble.

As illustrated in Figure 5.1, for each of four rock types, 16 cores were obtained under varying conditions of RPM and WOB. Table 5.1 presents the combinations of RPM and WOB used in the 16 core drilling tests conducted for each rock type.

Table 5.1 The applied RPM and WOB in different drilling coring tests for different rock types.

Test order	**RPM (REV/s)**	**WOB (kg)**	
	All four rock types	Sandstone rocks	Morawica marble
1	7.50	4	8
2	7.50	8	12
3	7.50	12	16
4	7.50	16	20
5	16.28	4	8
6	16.28	8	12
7	16.28	12	16
8	16.28	16	20
9	27.30	4	8
10	27.30	8	12
11	27.30	12	16
12	27.30	16	20
13	43.90	4	8
14	43.90	8	12
15	43.90	12	16
16	43.90	16	20

Each test was defined by a specific combination of RPM and WOB. Four rotational speeds were selected: 7.50, 16.28, 27.30, and 43.90 REV/s. For each RPM, four different WOB values were applied: 4, 8, 12, and 16 kg. It should be noted that for Morawica Marble, the corresponding WOB values were slightly higher—8, 12, 16, and 20 kg—reflecting its higher mechanical strength compared to the sandstone rocks.

As 16 unique test conditions were defined for each rock type, a total of 64 core drilling tests were performed. This experimental design allowed for a comprehensive evaluation of the effects of RPM and WOB for different rock types. The results of the coring tests for Szydłowiec-Śmiłów sandstone, Wola Komborska sandstone, Tumlin sandstone, and Morawica Marble are summarized in Tables 5.2 to 5.5, respectively. Each table presents the recorded parameters, including RPM, WOB, drilling time, drilled length, rate ROP, drilled volume, energy consumption, MSE, and torque.

Table 5.2 The measurements of drilling coring tests on Szydłowiec-Śmiłów sandstone

Test number	RPM (REV/s)	WOB (kg)	Drilling time (s)	Drilled length (m)	ROP (m/s)	A_{net} (m^2)	V_{net} (m^3)	Energy (J)	MSE (J/m^3)	MSE (MPa)	Torque (N.m)
1	7.5	4	597	0.05	0.00008	0.000386	1.93208E-05	238800	12359739971	12360	509.55
2	7.5	8	300	0.068	0.00023	0.000386	2.62763E-05	120000	4566856330	4567	509.55
3	7.5	12	150	0.057	0.00038	0.000386	2.20257E-05	60000	2724089741	2724	509.55
4	7.5	16	124	0.05	0.00040	0.000386	1.93208E-05	49600	2567182171	2567	509.55
5	16.3	4	155	0.074	0.00048	0.000386	2.85948E-05	62000	2168228185	2168	234.70
6	16.3	8	128	0.064	0.00050	0.000386	2.47306E-05	51200	2070308203	2070	234.70
7	16.3	12	35	0.068	0.00194	0.000386	2.62763E-05	14000	532799905.1	533	234.70
8	16.3	16	24	0.062	0.00258	0.000386	2.39578E-05	9600	400704813.4	401	234.70
9	27.3	4	114	0.072	0.00063	0.000386	2.78219E-05	45600	1638993994	1639	139.99
10	27.3	8	53	0.074	0.00140	0.000386	2.85948E-05	21200	741394153.7	741	139.99
11	27.3	12	20	0.065	0.00325	0.000386	2.5117E-05	8000	318508954.3	319	139.99
12	27.3	16	16	0.07	0.00438	0.000386	2.70491E-05	6400	236606651.8	237	139.99
13	43.9	4	15	0.07	0.00467	0.000386	2.70491E-05	6000	221818736	222	87.05
14	43.9	8	11	0.078	0.00709	0.000386	3.01404E-05	4400	145983270.7	146	87.05
15	43.9	12	8	0.07	0.00875	0.000386	2.70491E-05	3200	118303325.9	118	87.05
16	43.9	16	7	0.092	0.01314	0.000386	3.55503E-05	2800	78761725.11	79	87.05

Table 5.3 The measurements of drilling coring tests on Wola Komborska sandstone

Test number	RPM (REV/s)	WOB (kg)	Drilling time (s)	Drilled length (m)	ROP (m/s)	A_{net} (m^2)	V_{net} (m^3)	Energy (J)	MSE (J/m^3)	MSE (MPa)	Torque (N.m)
17	7.5	4	5500	0.076	0.00001	0.000386	2.93676E-05	2200000	74912467865	74912	509.55
18	7.5	8	2480	0.0765	0.00003	0.000386	2.95608E-05	992000	33557936882	33558	509.55
19	7.5	12	1754	0.079	0.00005	0.000386	3.05269E-05	701600	22983041695	22983	509.55
20	7.5	16	1185	0.067	0.00006	0.000386	2.58899E-05	474000	18308322540	18308	509.55
21	16.3	4	950	0.07	0.00007	0.000386	2.70491E-05	380000	14048519948	14049	234.70
22	16.3	8	560	0.0715	0.00013	0.000386	2.76287E-05	224000	8107500654	8108	234.70
23	16.3	12	224	0.075	0.00033	0.000386	2.89812E-05	89600	3091660250	3092	234.70
24	16.3	16	137	0.068	0.00050	0.000386	2.62763E-05	54800	2085531057	2086	234.70
25	27.3	4	772	0.0645	0.00008	0.000386	2.49238E-05	308800	12389751415	12390	139.99
26	27.3	8	351	0.066	0.00019	0.000386	2.55034E-05	140400	5505137721	5505	139.99
27	27.3	12	180	0.073	0.00041	0.000386	2.82084E-05	72000	2552434771	2552	139.99
28	27.3	16	100	0.077	0.00077	0.000386	2.9754E-05	40000	1344355976	1344	139.99
29	43.9	4	251	0.0675	0.00027	0.000386	2.60831E-05	100400	3849239696	3849	87.05
30	43.9	8	146	0.074	0.00051	0.000386	2.85948E-05	58400	2042331065	2042	87.05
31	43.9	12	75	0.069	0.00092	0.000386	2.66627E-05	30000	1125167502	1125	87.05
32	43.9	16	45	0.076	0.00169	0.000386	2.93676E-05	18000	612920191.6	613	87.05

Table 5.4 The measurements of drilling coring tests on Tumlin sandstone

Test number	RPM (REV/s)	WOB (kg)	Drilling time (s)	Drilled length (m)	ROP (m/s)	A_{net} (m^2)	V_{net} (m^3)	Energy (J)	MSE (J/m^3)	MSE (MPa)	Torque (N.m)
33	7.5	4	4960	0.054	0.00001	0.000386	2.08665E-05	2E+06	95080821167	95081	509.55
34	7.5	8	1057	0.054	0.00005	0.000386	2.08665E-05	422800	20262183059	20262	509.55
35	7.5	12	705	0.055	0.00008	0.000386	2.12529E-05	282000	13268793482	13269	509.55
36	7.5	16	487	0.055	0.00011	0.000386	2.12529E-05	194800	9165819043	9166	509.55
37	16.3	4	704	0.054	0.00008	0.000386	2.08665E-05	281600	13495342359	13495	234.70
38	16.3	8	254	0.051	0.00020	0.000386	1.97072E-05	101600	5155473368	5155	234.70
39	16.3	12	258	0.06	0.00023	0.000386	2.3185E-05	103200	4451162636	4451	234.70
40	16.3	16	155	0.054	0.00035	0.000386	2.08665E-05	62000	2971275661	2971	234.70
41	27.3	4	413	0.049	0.00012	0.000386	1.89344E-05	165200	8724870283	8725	139.99
42	27.3	8	185	0.048	0.00026	0.000386	1.8548E-05	74000	3989656433	3990	139.99
43	27.3	12	136	0.048	0.00035	0.000386	1.8548E-05	54400	2932936621	2933	139.99
44	27.3	16	96	0.048	0.00050	0.000386	1.8548E-05	38400	2070308203	2070	139.99
45	43.9	4	138	0.047	0.00034	0.000386	1.81615E-05	55200	3039388638	3039	87.05
46	43.9	8	103	0.047	0.00046	0.000386	1.81615E-05	41200	2268529201	2269	87.05
47	43.9	12	57	0.043	0.00075	0.000386	1.66159E-05	22800	1372181018	1372	87.05
48	43.9	16	50	0.0435	0.00087	0.000386	1.68091E-05	20000	1189832300	1190	87.05

Table 5.5 The measurements of drilling coring tests on Morawica Marble.

Test number	RPM (REV/s)	WOB (kg)	Drilling time (s)	Drilled length (m)	ROP (m/s)	A_{net} (m^2)	V_{net} (m^3)	Energy (J)	MSE (J/m^3)	MSE (MPa)	Torque (N.m)
49	7.5	8	3102	0.02	0.000006	0.000386	7.72832E-06	1E+06	1.60552E+11	160552	509.55
50	7.5	12	6201	0.064	0.000010	0.000386	2.47306E-05	2E+06	1.00297E+11	100297	509.55
51	7.5	16	4987	0.065	0.000013	0.000386	2.5117E-05	2E+06	79420207750	79420	509.55
52	7.5	20	4852	0.065	0.000013	0.000386	2.5117E-05	2E+06	77270272308	77270	509.55
53	16.3	8	1200	0.05	0.00004	0.000386	1.93208E-05	480000	24843698434	24844	234.70
54	16.3	12	625	0.05	0.00008	0.000386	1.93208E-05	250000	12939426268	12939	234.70
55	16.3	16	481	0.053	0.00011	0.000386	2.048E-05	192400	9394511751	9395	234.70
56	16.3	20	458	0.055	0.00012	0.000386	2.12529E-05	183200	8620010517	8620	234.70
57	27.3	8	600	0.038	0.00006	0.000386	1.46838E-05	240000	16344538443	16345	139.99
58	27.3	12	280	0.058	0.00021	0.000386	2.24121E-05	112000	4997295662	4997	139.99
59	27.3	16	221	0.05	0.00023	0.000386	1.93208E-05	88400	4575381128	4575	139.99
60	27.3	20	216	0.054	0.00025	0.000386	2.08665E-05	86400	4140616406	4141	139.99
61	43.9	8	280	0.047	0.00017	0.000386	1.81615E-05	112000	6166875498	6167	87.05
62	43.9	12	172	0.055	0.00032	0.000386	2.12529E-05	68800	3237209190	3237	87.05
63	43.9	16	113	0.057	0.00050	0.000386	2.20257E-05	45200	2052147605	2052	87.05
64	43.9	20	108	0.06	0.00056	0.000386	2.3185E-05	43200	1863277383	1863	87.05

For Szydłowiec-Śmiłów sandstone, the results showed that increasing RPM and WOB consistently improved drilling performance. Specifically, higher operational parameters led to significantly reduced drilling times and enhanced ROP values. For example, at 7.5 rev/s and 4 kg WOB, the ROP was very low (approximately 0.00008 m/s), while at 43.9 rev/s and 16 kg WOB, the ROP increased markedly to approximately 0.01314 m/s. Concurrently, MSE values dropped from over 12,000 MPa to around 79 MPa, indicating more efficient drilling. These trends highlight that Szydłowiec-Śmiłów sandstone, being relatively soft, responded positively to increases in both RPM and WOB, achieving optimal drilling conditions at higher energy inputs.

The performance on Wola Komborska sandstone followed a similar pattern but with some distinctions. Although increased RPM and WOB again resulted in reduced drilling times and higher ROPs, the absolute values of MSE were notably higher than those observed for Szydłowiec-Śmiłów sandstone. Even under the most favorable conditions (43.9 rev/s and 16 kg WOB), MSE values for Wola Komborska sandstone remained around 613 MPa. This reflects the higher mechanical strength of Wola Komborska sandstone compared to Szydłowiec-Śmiłów sandstone and suggests that more energy was required to achieve comparable drilling rates.

Tumlin sandstone presented an intermediate behavior between Szydłowiec-Śmiłów and Wola Komborska sandstones. Initial drilling at low RPMs and WOBs resulted in very high MSE values, exceeding 95,000 MPa under the most unfavorable conditions. However, as RPM and WOB increased, MSE decreased significantly, reaching values as low as 1,190 MPa at 43.9 rev/s and 16 kg WOB. The ROP also improved accordingly. This pattern underscores the importance of operational parameters in overcoming initial drilling resistance in moderately hard rocks.

Drilling through Morawica Marble proved to be the most challenging. Despite applying higher WOB values (ranging from 8 kg to 20 kg, in contrast to 4 kg to 16 kg for the other rocks), Morawica Marble exhibited the highest drilling resistance, reflected in both prolonged drilling times and consistently high MSE values. Even under the highest RPM and WOB conditions, the MSE for Morawica Marble remained above 1,800 MPa, and ROP values were comparatively low. These results confirm that Morawica Marble possesses the greatest mechanical strength and toughness among the rocks tested.

The analysis for all four rock types reveals that increasing RPM and WOB generally enhances drilling performance by increasing ROP and reducing MSE. However, the extent of this improvement varies mainly depending on the rock's mechanical characteristics. Softer rocks such as Szydłowiec-Śmiłów sandstone show dramatic efficiency gains at higher operational parameters, while harder rocks like Morawica Marble demonstrate limited improvement, even under aggressive drilling conditions.

5.2. Physical tests

Once the core drilling tests were completed and the corresponding drilling parameters recorded, the obtained core samples were subjected to physical testing. These tests were performed, mainly with the purpose of identifying the porosity and density of the core samples collected from the drilling experiments. A total of 64 core samples were obtained, representing the rocks drilled during the coring tests. The results of the physical tests for Szydłowiec-Śmiłów sandstone, Wola Komborska sandstone, Tumlin sandstone, and Morawica Marble are summarized in Tables 5.6 to 5.9, respectively. Each table presents key measurements, including core length, dry mass, saturated mass, porosity, and density. The diameter of all core samples was 38 mm.

Table 5.6 Physical characteristics of 16 coring samples of Szydłowiec-Śmiłów sandstone.

Core Code	Length (m)	Mass (kg)	Density (kg/m³)	Porosity (%)
S1	0.042	0.09699	2037	21.76
S2	0.042	0.10019	2130	20.64
S3	0.043	0.10021	2080	20.76
S4	0.042	0.09743	2046	21.07
S5	0.042	0.09968	2119	21.92
S6	0.042	0.10101	2122	21.30
S7	0.042	0.09989	2098	20.58
S8	0.043	0.10000	2076	21.28
S9	0.042	0.10007	2102	21.80
S10	0.040	0.09802	2162	20.95
S11	0.044	0.10501	2105	22.14
S12	0.042	0.09938	2087	20.75
S13	0.042	0.09413	1977	21.59
S14	0.042	0.09504	2020	22.45
S15	0.044	0.10410	2087	21.57
S16	0.045	0.10664	2091	20.98

Table 5.7 Physical characteristics of 16 coring samples of Wola Komborska sandstone.

Core Code	Length (m)	Mass (kg)	Density (kg/m³)	Porosity (%)
W1	0.047	0.12398	2327	13.06
W2	0.042	0.11098	2331	12.52
W3	0.041	0.10765	2316	12.42
W4	0.048	0.12593	2314	12.42
W5	0.047	0.12241	2298	12.84
W6	0.0435	0.11449	2322	12.98
W7	0.047	0.12269	2303	9.80
W8	0.042	0.11036	2318	12.60
W9	0.042	0.11179	2348	12.77
W10	0.042	0.11149	2342	11.99
W11	0.045	0.11929	2339	12.82
W12	0.042	0.11065	2324	12.25
W13	0.044	0.11576	2321	12.89
W14	0.046	0.12057	2312	12.50
W15	0.047	0.12353	2319	13.10
W16	0.042	0.11068	2325	12.71

Table 5.8 Physical characteristics of 16 coring samples of Tumlin sandstone.

Core Code	Length (m)	Mass (kg)	Density (kg/m³)	Porosity (%)
T1	0.046	0.11439	2194	14.61
T2	0.048	0.12300	2261	14.48
T3	0.041	0.10346	2226	14.03
T4	0.043	0.10764	2208	15.12
T5	0.051	0.12877	2227	13.23
T6	0.0495	0.12459	2220	13.74
T7	0.045	0.11773	2308	11.41
T8	0.0405	0.10503	2288	11.96
T9	0.04	0.10412	2296	11.53
T10	0.043	0.11425	2344	11.43
T11	0.051	0.13928	2409	8.65
T12	0.044	0.11869	2380	9.38
T13	0.044	0.12027	2411	10.39
T14	0.048	0.13020	2393	8.53
T15	0.044	0.12000	2406	9.00
T16	0.048	0.13200	2426	8.23

Table 5.9 Physical characteristics of 16 coring samples of Morawica Marble.

Core Code	Length (m)	Mass (kg)	Density (kg/m³)	Porosity (%)
M1	0.043	0.12453	2555	5.31
M2	0.039	0.11388	2576	5.20
M3	0.044	0.12771	2561	5.47
M4	0.047	0.13595	2552	5.54
M5	0.039	0.11385	2575	4.59
M6	0.042	0.12239	2571	5.27
M7	0.045	0.13042	2557	5.35
M8	0.0415	0.12102	2573	5.27
M9	0.043	0.12330	2530	6.26
M10	0.04	0.11778	2598	6.48
M11	0.047	0.13579	2549	5.86
M12	0.042	0.12308	2585	5.88
M13	0.041	0.11820	2543	5.47
M14	0.042	0.12227	2568	5.67
M15	0.041	0.11944	2570	5.66
M16	0.043	0.12648	2595	5.38

Based on Tables 5.6-5.9, the average values of porosity and density for different core samples was calculated. Figure 5.6 depicts a comparative diagram of those values.

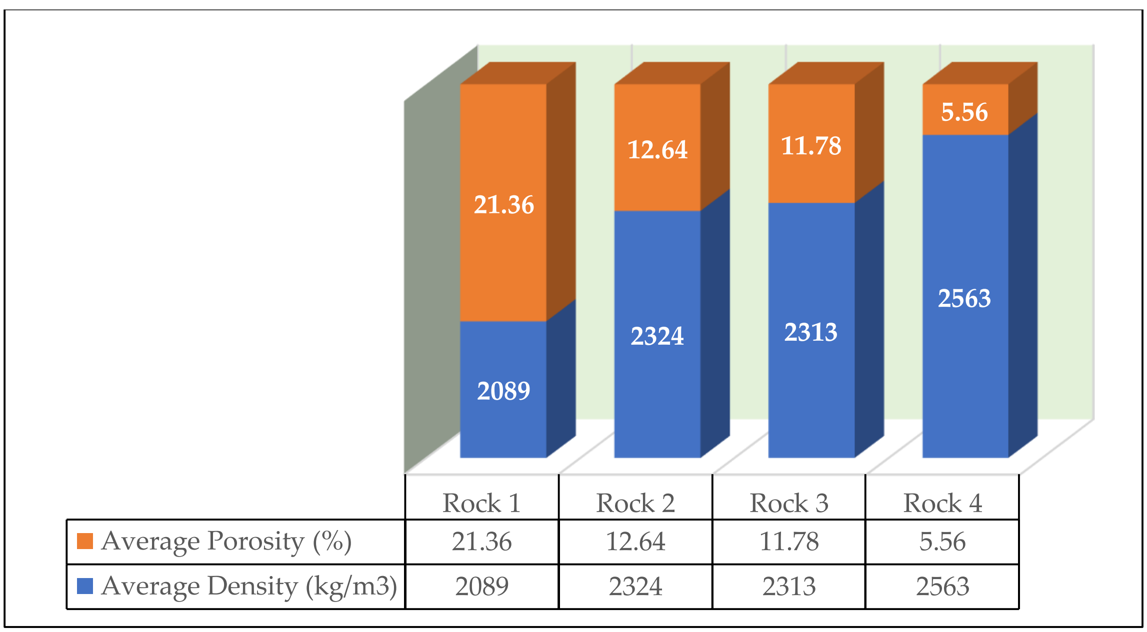

Figure 5.6 The average values of porosity and density for all four rock types.

Therefore, according to Tables 5.6-5.9, and Figure 5.1, the following key points can be stated:

For Szydłowiec-Śmiłów sandstone, the density of the samples ranged between approximately 1977 kg/m³ and 2162 kg/m³, with an average density of 2089 kg/m³. The porosity values varied from 20.58% to 22.45%, with an average porosity of 21.36%. These results indicate that Szydłowiec-Śmiłów sandstone is relatively porous and low in density. The consistency of the physical properties across samples suggests a homogeneous rock texture.

Wola Komborska sandstone exhibited higher density values, generally ranging between 2298 kg/m³ and 2348 kg/m³, with an average density of 2324 kg/m³. The porosity values were lower compared to Szydłowiec-Śmiłów sandstone, ranging from 9.80% to 13.10%, with an average porosity of 12.64%. This higher density and lower porosity confirm that Wola Komborska sandstone is denser and less porous, which aligns with its observed greater mechanical strength during drilling.

The results for Tumlin sandstone showed a slightly wider variation in physical properties. Densities ranged from 2194 kg/m³ to 2426 kg/m³, with an average density of 2313 kg/m³. Porosity values ranged between 8.23% and 15.12%, with an average porosity of 11.78%. Lower porosity samples were associated with higher density, suggesting heterogeneity in the rock's microstructure, which may influence its drilling performance.

Among all rock types, Morawica Marble demonstrated the highest density and the lowest porosity. The density values ranged from 2530 kg/m³ to 2598 kg/m³, with an average density of 2563 kg/m³. Porosity values varied between 4.59% and 6.48%, with an average porosity of 5.56%. These characteristics confirm that Morawica Marble is the most compact and least porous among the studied rocks, which is consistent with its greater resistance to drilling observed in previous tests.

Overall, the physical characterization results provided important insights into the intrinsic properties of the rocks tested. In general, a direct relationship was observed between rock density and mechanical resistance, as well as an inverse relationship between porosity and drilling ease. Rock types with lower density and higher porosity (e.g., Szydłowiec-Śmiłów sandstone) demonstrated easier drilling conditions, while those with higher density and lower porosity (e.g., Morawica Marble) exhibited greater resistance to drilling. These findings reinforce the critical role of understanding rock physical properties in optimizing drilling strategies and predicting drilling performance in various geological formations.

5.3. UCS tests

To obtain an early perspective about the strength of different rock types, the UCS tests were performed. In general, higher UCS values typically reflect a stronger, more resistant rock matrix, which directly correlates with reduced drillability and increased energy requirements during drilling operations. In contrast, lower UCS values suggest weaker and more deformable rocks, which are generally easier to drill. To conduct the UCS tests, for each rock type, five cylindrical specimens were prepared and subjected to uniaxial pressure loading. Figure 5.7 depicts those core samples. Table 5.10 also demonstrates the raw data of UCS measurements for all rock specimens.

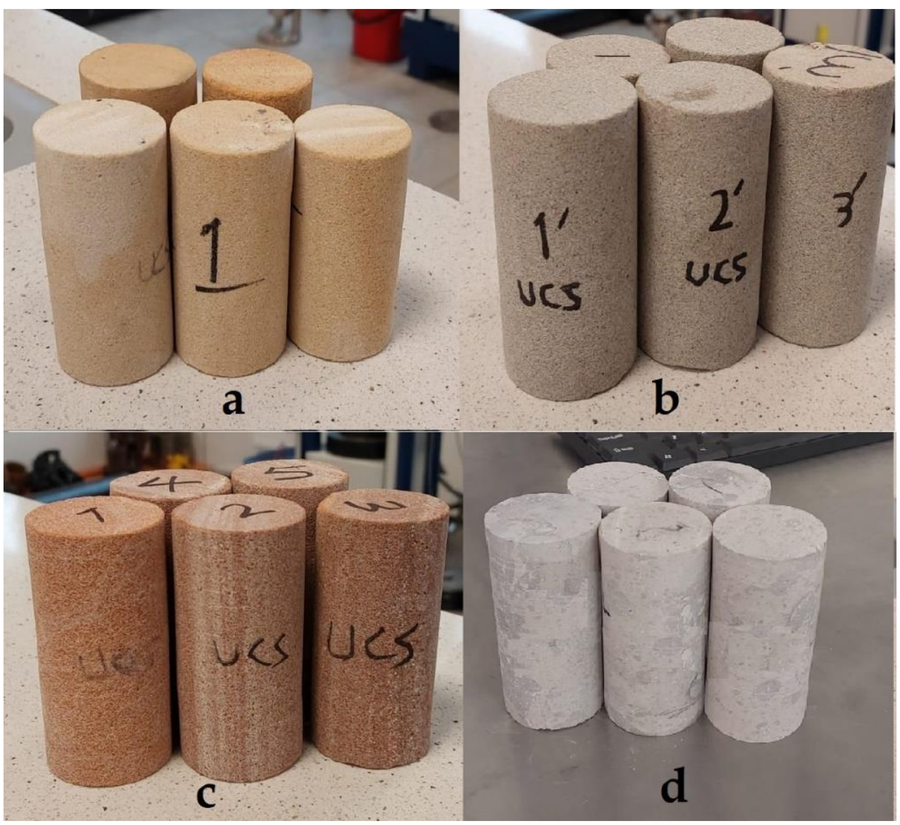

Figure 5.7 Core samples used for UCS measurement tests: a) Szydłowiec–Śmiłów sandstone; b) Wola Komborska; c) Tumlin sandstone; and d) Morawica marble

Table 5.10 The UCS results for different rock types.

Rock type	Specimen code	Diameter (mm)	Length (mm)	UCS (MPa)
Szydłowiec-Śmiłów sandstone	SS1	38	76	38.8
	SS2	38	76	47.2
	SS3	38	76	39.3
	SS4	38	76	45.2
	SS5	38	76	40.3
Wola Komborska sandstone	WS1	38	76	61.2
	WS2	38	76	51.1
	WS3	38	76	56.3
	WS4	38	76	54.6
	WS5	38	76	49.6
Tumlin sandstone	TS1	38	76	59.4
	TS2	38	76	103.4
	TS3	38	76	71.5
	TS4	38	76	85.4
	TS5	38	76	92.5
Morawica Marble	MS1	38	76	105.1
	MS2	38	76	115.2
	MS3	38	76	100.4
	MS4	38	76	95.8
	MS5	38	76	90.3

To analyze the data provided in Table 5.10, the average UCS and variation range of UCS for different rock types have been depicted in Figures 5.8 (a) and 5.8 (b).

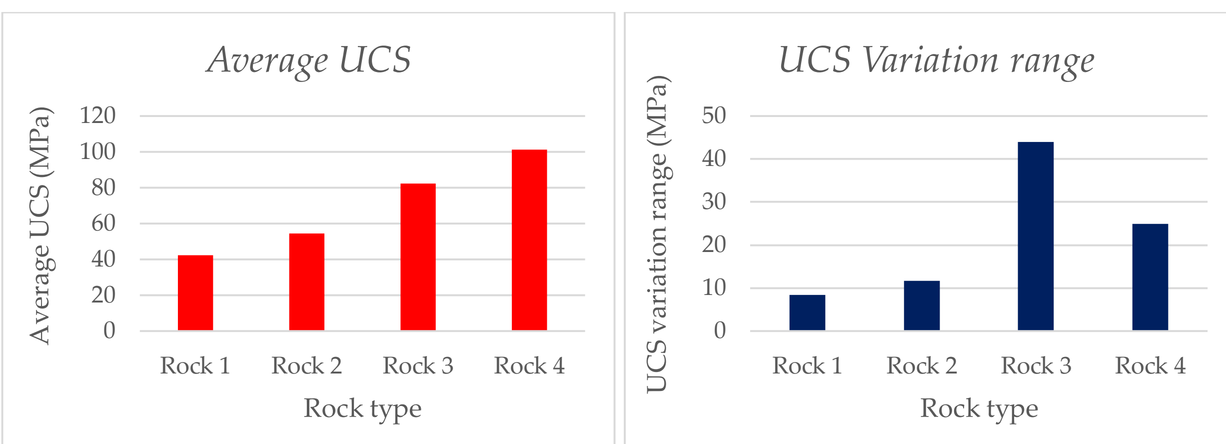

Figure 5.8 a) The average value of UCS for all four rock types; b) The UCS variation range for different specimens of all four rock types.

As it can be observed, Szydłowiec-Śmiłów sandstone exhibited the lowest average UCS of 42.2 MPa, indicating it is the weakest among the tested rocks and most susceptible to deformation under uniaxial loading. Wola Komborska sandstone showed a moderate average UCS of 54.6 MPa, suggesting improved strength likely due to its higher density and lower porosity compared to Szydłowiec-Śmiłów sandstone. Tumlin sandstone recorded a high average UCS of 82.4 MPa, reflecting strong internal bonding typical of well-cemented sandstones. Finally, Morawica Marble demonstrated the highest average UCS at 101.4 MPa, confirming it as the most competent and mechanically resistant rock, consistent with its dense, crystalline marble structure.

Furthermore, as illustrated in Figure 5.8 (b), Szydłowiec-Śmiłów sandstone showed a narrow UCS variation range of 8.4 MPa (from 38.8 to 47.2 MPa), indicating a relatively homogeneous and consistent material structure. Wola Komborska sandstone had a slightly wider range of 11.6 MPa (49.6 to 61.2 MPa), suggesting moderate variability, possibly due to subtle differences in grain structure or cementation. Tumlin sandstone exhibited a notably wide variation of 44.0 MPa (59.4 to 103.4 MPa), reflecting significant heterogeneity within the sandstone samples, which may arise from variations in porosity or mineral composition. Morawica Marble, showed a UCS variation range of 24.9 MPa (90.3 to 115.2 MPa), indicating relative internal heterogeneity. From the drilling perspective, a narrow UCS variation range implies a uniform material structure, leading to more predictable behavior under stress, while a wider range may indicate variations in cementation, grain size, or mineral composition, which can result in inconsistent performance during drilling.

5.4. AVS tests

After conducting the physical tests, all core samples were subjected to acoustic wave propagation experiment. Those experiments were performed to measure the rocks' dynamic mechanical parameters to evaluate their geomechanical behavior and potential implications for drill-ability. Measurements included velocities of compressional wave, shear wave, Young's modulus, shear modulus, Poisson's ratio, and bulk modulus. The corresponding results of those experiments for Szydłowiec-Śmiłów sandstone, Wola Komborska sandstone, Tumlin sandstone, and Morawica Marble are presented in Tables 5.11 to 5.14, respectively.

Table 5.11 Dynamic mechanical properties of 16 core samples of Szydłowiec-Śmiłów sandstone.

Core Code	Vp (m/s)	Vs (m/s)	v_{dyn}	E_{dyn} (MPa)	K_{dyn} (MPa)	G_{dyn} (MPa)
S1	1678	779	0.37	3675	4348	1353
S2	1659	797	0.35	3898	4216	1451
S3	1685	792	0.36	3826	4383	1414
S4	1687	794	0.36	3736	4240	1384
S5	1691	844	0.34	4373	4256	1649
S6	1696	820	0.35	4138	4350	1547
S7	1694	813	0.35	4012	4332	1494
S8	1724	842	0.35	4267	4385	1599
S9	1757	841	0.36	4305	4667	1604
S10	1689	819	0.35	4196	4405	1568
S11	1682	787	0.36	3821	4425	1411
S12	1693	806	0.36	3915	4342	1452
S13	1626	788	0.35	3567	3759	1332
S14	1691	807	0.36	3814	4164	1419
S15	1726	830	0.35	4180	4463	1560
S16	1652	784	0.36	3776	4220	1399

Table 5.12 Dynamic mechanical properties of 16 core samples of Wola Komborska sandstone.

Core Code	Vp (m/s)	Vs (m/s)	v_{dyn}	E_{dyn} (MPa)	K_{dyn} (MPa)	G_{dyn} (MPa)
W1	3866	1307	0.44	11913	30368	4153
W2	3637	1241	0.43	10743	26867	3748
W3	3663	1224	0.44	10404	27110	3625
W4	3719	1262	0.44	10980	27698	3830
W5	3729	1286	0.43	11311	27575	3952
W6	3732	1319	0.43	11997	27746	4202
W7	3678	1304	0.43	11665	26699	4088
W8	3770	1283	0.44	11390	28641	3973
W9	3776	1299	0.43	11794	28827	4120
W10	3660	1273	0.43	11390	27112	3984
W11	3716	1254	0.44	10987	28122	3830
W12	3696	1334	0.43	12280	27044	4312
W13	3666	1288	0.43	11464	26878	4012
W14	3671	1273	0.43	11200	26953	3915
W15	3773	1291	0.43	11516	28547	4020
W16	3683	1273	0.43	11219	27281	3920

Table 5.13 Dynamic mechanical properties of 16 core samples of Tumlin sandstone.

Core Code	Vp (m/s)	Vs (m/s)	v_{dyn}	E_{dyn} (MPa)	K_{dyn} (MPa)	G_{dyn} (MPa)
T1	3626	1677	0.36	18679	22810	6853
T2	3114	1466	0.36	14192	16391	5252
T3	2966	1379	0.36	11683	13900	4319
T4	3116	1326	0.39	10832	16263	3901
T5	3610	1717	0.36	17835	20360	6613
T6	3451	1673	0.35	17163	18200	6420
T7	3580	1700	0.36	18562	20912	6874
T8	2934	1363	0.36	11725	13974	4334
T9	2873	1327	0.36	11193	13526	4127
T10	3210	1497	0.36	14858	17411	5484
T11	3238	1526	0.36	15804	17894	5866
T12	3644	1673	0.37	18398	22750	6749
T13	3620	1674	0.37	18559	22682	6813
T14	3382	1632	0.35	17693	18979	6605
T15	3114	1466	0.36	14192	16391	5252
T16	3626	1677	0.36	18679	22810	6853

Table 5.14 Dynamic mechanical properties of 16 core samples of Morawica Marble.

Core Code	Vp (m/s)	Vs (m/s)	v_{dyn}	E_{dyn} (MPa)	K_{dyn} (MPa)	G_{dyn} (MPa)
M1	3140	1412	0.37	14184	18531	5170
M2	2967	1339	0.37	12876	16635	4700
M3	3033	1375	0.37	13465	17204	4920
M4	3233	1459	0.37	15121	19549	5518
M5	2911	1309	0.37	12297	16049	4483
M6	3059	1369	0.38	13431	17751	4891
M7	3149	1422	0.37	14401	18599	5255
M8	2982	1347	0.37	12998	16763	4745
M9	3036	1371	0.37	13231	17091	4829
M10	2982	1345	0.37	13101	16953	4782
M11	3149	1419	0.37	14290	18559	5212
M12	3131	1411	0.37	14391	18616	5254
M13	2874	1310	0.37	12111	15286	4431
M14	2907	1318	0.37	12415	15852	4536
M15	2982	1346	0.37	12952	16760	4727
M16	3070	1385	0.37	13888	17953	5069

According to the data provided in Tables 5.11-5.14, the average values of those dynamic mechanical parameters were calculated and depicted in Figure 5.9.

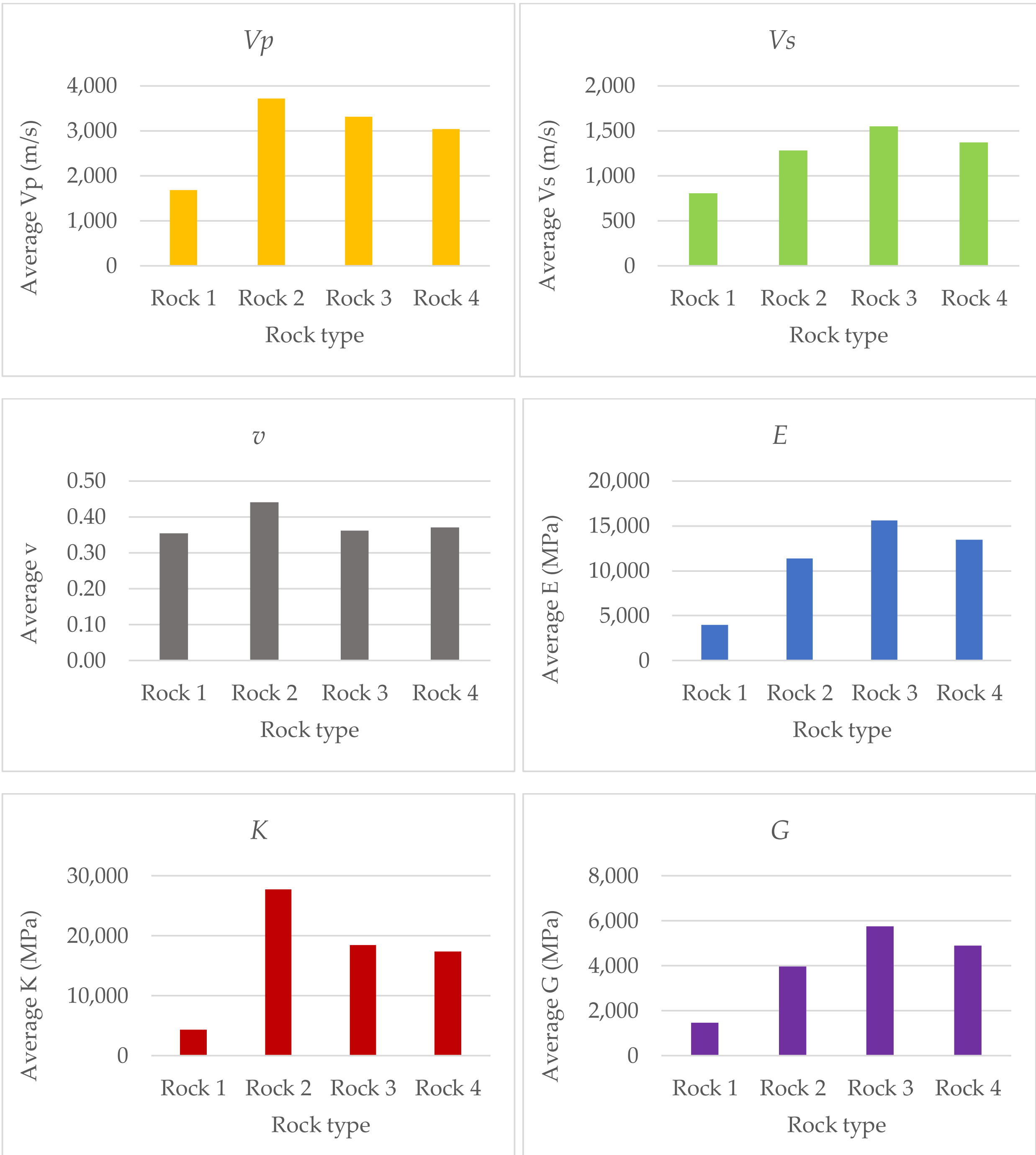

Figure 5.9 The average values of dynamic mechanical properties of different rock types.

According to Figure 5.9, Szydłowiec-Śmiłów sandstone showed the lowest acoustic velocities and elastic moduli values, suggesting a weak, less consolidated formation. This rock is expected to be easily drillable due to its ductile behavior and low stiffness, which is reflected in its high ROP and low MSE in the field. Furthermore, Wola Komborska sandstone presented a unique profile with a high bulk modulus and Poisson's ratio. These properties imply resistance to volumetric deformation and increased ductility, possibly due to matrix-rich composition. Although stiff, its ductility likely moderates the energy required for drilling, resulting in a moderate ROP and MSE.

The dynamic mechanical properties of Tumlin sandstone and Morawica Marble are closely aligned, exhibiting high compressional and shear wave velocities, along with elevated Young's, bulk, and shear moduli. These characteristics indicate stiff and brittle behavior, suggesting that both rocks should present significant resistance to deformation. These measurements suggest that both rocks are mechanically stiff and brittle. However, despite their similar laboratory-measured stiffness, Morawica Marble, identified as marble, exhibits lower ROP and higher MSE during drilling compared to Tumlin sandstone, which is a sandstone. This discrepancy can be justified when considering their density, porosity, heterogeneity level, and UCS values (see Figures 5.8 and 5.9).

Marble (Morawica Marble) is the most compact and least porous of all the tested rocks, with an average density of 2563 kg/m^3 and porosity of only 5.56%, indicating a tightly crystalline, interlocked grain structure that resists mechanical failure. In contrast, the sandstone (Tumlin sandstone) shows an average density of 2313 kg/m^3 and porosity of 11.78%, reflecting a more variable and often more drillable framework, particularly in samples with lower cementation or the presence of micro-fractures. These factors allow sandstone to fracture and chip more effectively, explaining its relatively higher ROP and lower MSE despite similar elastic moduli.

These observations affirm that while dynamic elastic properties are essential for understanding stiffness and wave behavior, actual drill-ability is strongly influenced by rock type, microstructure, mineralogy, and physical properties such as density and porosity. The later comparison between sandstone and marble, in particular, reveals the importance of integrating geological context with mechanical measurements to accurately predict drilling performance in diverse lithologies.

Chapter 6
Analytical Analysis

6.1. Analysis procedure

This chapter presents the analytical component of the research, which complements the laboratory findings by statistically and mathematically analyzing the relationships between drilling efficiency performance (ROP and MSE) and rocks' properties and drilling parameters. The primary objectives are to (1) identify the most influential variables affecting drilling efficiency, and (2) develop empirical equations for predicting ROP and MSE based on measurable parameters. In what follows, the applied analysis procedure is comprehensively elaborated.

6.1.1. Statistical Analysis

Pearson's correlation coefficient was employed to statistically quantify the linear relationships between ROP and MSE and contributing factors including rocks' porosity, density, dynamic elastic moduli, WOB and RPM. This method quantifies the degree as well as the directionality of the linear correlation between two continuous variables by calculating a value, r, which is called Pearson's correlation coefficient. It is noteworthy that the corresponding formula has been already written in Methodology chapter, Eq. (4.10).

The value of r varies between−1 to +1, where the values of the coefficient r reveal strong positive linear dependence when close to +1 and strong negative dependence when close to −1, while values near zero suggest weak or no linear correlation. This statistical approach facilitates the identification of the variables that most strongly influenced drilling performance, thereby guiding the selection of parameters for empirical modeling.

To perform the analysis, firstly, Table 6.1 encompassing all experimental raw data was created. In fact, Table 6.1 was a combination of main measured parameters already presented in Tables 5.2-5.9 and 5.11-5.13. This table is shown below. The main included parameters are WOB, RPM, ROP, MSE, density, porosity, compressional wave velocity, shear wave velocity, dynamic Poisson's ratio, dynamic Young's modulus, dynamic bulk modulus, and dynamic shear modulus.

Table 6.1 The main measured parameters used in Pearson's correlation coefficient analysis.

Rock type	sample	*RPM* (REV/s)	*WOB* (kg)	*ROP* (m/s)	*MSE* (MPa)	ρ (Kg/m^3)	φ (-)	*Vp* (m/s)	*Vs* (m/s)	v_{dyn} (-)	E_{dyn} (MPa)	K_{dyn} (MPa)	G_{dyn} (MPa)
Szydłowiec-Śmiłów sandstone	1	7.50	4	0.00008	12360	2037	0.22	1678	779	0.37	3675	4348	1353
	2	7.50	8	0.00023	4567	2130	0.21	1659	797	0.35	3898	4216	1451
	3	7.50	12	0.00038	2724	2080	0.21	1685	792	0.36	3826	4383	1414
	4	7.50	16	0.00040	2567	2046	0.21	1687	794	0.36	3736	4240	1384
	5	16.28	4	0.00048	2168	2119	0.22	1691	844	0.34	4373	4256	1649
	6	16.28	8	0.00050	2070	2122	0.21	1696	820	0.35	4138	4350	1547
	7	16.28	12	0.00194	533	2098	0.21	1694	813	0.35	4012	4332	1494
	8	16.28	16	0.00258	401	2076	0.21	1724	842	0.35	4267	4385	1599
	9	27.30	4	0.00063	1639	2102	0.22	1757	841	0.36	4305	4667	1604
	10	27.30	8	0.00140	741	2162	0.21	1689	819	0.35	4196	4405	1568
	11	27.30	12	0.00325	319	2105	0.22	1682	787	0.36	3821	4425	1411
	12	27.30	16	0.00438	237	2087	0.21	1693	806	0.36	3915	4342	1452
	13	43.90	4	0.00467	222	1977	0.22	1626	788	0.35	3567	3759	1332
	14	43.90	8	0.00709	146	2020	0.22	1691	807	0.36	3814	4164	1419
	15	43.90	12	0.00875	118	2087	0.22	1726	830	0.35	4180	4463	1560
	16	43.90	16	0.01314	79	2091	0.21	1652	784	0.36	3776	4220	1399

Table 6.1. Continued.

Rock type	sample	RPM (REV/s)	WOB (kg)	ROP (m/s)	MSE (MPa)	ρ (Kg/m³)	φ (-)	Vp (m/s)	Vs (m/s)	v_{dyn} (-)	E_{dyn} (MPa)	K_{dyn} (MPa)	G_{dyn} (MPa)
Wola Komborska sandstone	1	7.50	4	0.00001	74912	2327	0.13	3866.11	1306.59	0.44	11913	30368	4153
	2	7.50	8	0.00003	33558	2331	0.13	3636.67	1241.01	0.43	10743	26867	3748
	3	7.50	12	0.00005	22983	2316	0.12	3662.61	1224.44	0.44	10404	27110	3625
	4	7.50	16	0.00006	18308	2314	0.12	3719.09	1261.54	0.44	10980	27698	3830
	5	16.28	4	0.00007	14049	2298	0.13	3729.14	1285.90	0.43	11311	27575	3952
	6	16.28	8	0.00013	8108	2322	0.13	3732.16	1318.79	0.43	11997	27746	4202
	7	16.28	12	0.00033	3092	2303	0.10	3677.82	1303.79	0.43	11665	26699	4088
	8	16.28	16	0.00050	2086	2318	0.13	3770.35	1283.31	0.44	11390	28641	3973
	9	27.30	4	0.00008	12390	2348	0.13	3775.56	1298.63	0.43	11794	28827	4120
	10	27.30	8	0.00019	5505	2342	0.12	3659.85	1273.50	0.43	11390	27112	3984
	11	27.30	12	0.00041	2552	2339	0.13	3716.48	1253.87	0.44	10987	28122	3830
	12	27.30	16	0.00077	1344	2324	0.12	3695.80	1334.09	0.43	12280	27044	4312
	13	43.90	4	0.00027	3849	2321	0.13	3666.24	1287.55	0.43	11464	26878	4012
	14	43.90	8	0.00051	2042	2312	0.13	3671.28	1273.33	0.43	11200	26953	3915
	15	43.90	12	0.00092	1125	2319	0.13	3772.96	1290.97	0.43	11516	28547	4020
	16	43.90	16	0.00169	613	2325	0.13	3682.72	1273.17	0.43	11219	27281	3920

Table 6.1. Continued.

Rock type	sample	RPM (REV/s)	WOB (kg)	ROP (m/s)	MSE (MPa)	ρ (Kg/m³)	φ (-)	Vp (m/s)	Vs (m/s)	v_{dyn} (-)	E_{dyn} (MPa)	K_{dyn} (MPa)	G_{dyn} (MPa)
Tumlin sandstone	1	7.50	4	0.00001	95081	2194	0.15	3625.57	1676.57	0.36	18679	22810	6853
	2	7.50	8	0.00005	20262	2261	0.14	3113.63	1465.77	0.36	14192	16391	5252
	3	7.50	12	0.00008	13269	2226	0.14	2965.64	1378.89	0.36	11683	13900	4319
	4	7.50	16	0.00011	9166	2208	0.15	3116.02	1325.96	0.39	10832	16263	3901
	5	16.28	4	0.00008	13495	2227	0.13	3609.92	1716.85	0.36	17835	20360	6613
	6	16.28	8	0.00020	5155	2220	0.14	3450.96	1672.50	0.35	17163	18200	6420
	7	16.28	12	0.00023	4451	2308	0.11	3580.01	1699.75	0.36	18562	20912	6874
	8	16.28	16	0.00035	2971	2288	0.12	2934.01	1363.28	0.36	11725	13974	4334
	9	27.30	4	0.00012	8725	2296	0.12	2873.48	1326.50	0.36	11193	13526	4127
	10	27.30	8	0.00026	3990	2344	0.11	3210.27	1497.07	0.36	14858	17411	5484
	11	27.30	12	0.00035	2933	2409	0.09	3238.02	1526.40	0.36	15804	17894	5866
	12	27.30	16	0.00050	2070	2380	0.09	3643.55	1672.79	0.37	18398	22750	6749
	13	43.90	4	0.00034	3039	2411	0.10	3620.40	1673.87	0.37	18559	22682	6813
	14	43.90	8	0.00046	2269	2393	0.09	3381.69	1631.55	0.35	17693	18979	6605
	15	43.90	12	0.00075	1372	2406	0.09	3113.63	1465.77	0.36	14192	16391	5252
	16	43.90	16	0.00087	1190	2426	0.08	3625.57	1676.57	0.36	18679	22810	6853

Table 6.1. Continued.

Rock type	sample	RPM (REV/s)	WOB (kg)	ROP (m/s)	MSE (MPa)	ρ (Kg/m^3)	φ (-)	Vp (m/s)	Vs (m/s)	v_{dyn} (-)	E_{dyn} (MPa)	K_{dyn} (MPa)	G_{dyn} (MPa)
Morawica Marble	1	7.50	8	0.00001	160552	2555	0.05	3140.22	1412.03	0.37	14184	18531	5170
	2	7.50	12	0.00001	100297	2576	0.05	2966.90	1338.67	0.37	12876	16635	4700
	3	7.50	16	0.00001	79420	2561	0.05	3033.40	1375.46	0.37	13465	17204	4920
	4	7.50	20	0.00001	77270	2552	0.06	3232.87	1459.42	0.37	15121	19549	5518
	5	16.28	8	0.00004	24844	2575	0.05	2911.21	1309.37	0.37	12297	16049	4483
	6	16.28	12	0.00008	12939	2571	0.05	3058.65	1369.24	0.38	13431	17751	4891
	7	16.28	16	0.00011	9395	2557	0.05	3148.96	1422.21	0.37	14401	18599	5255
	8	16.28	20	0.00012	8620	2573	0.05	2982.24	1347.30	0.37	12998	16763	4745
	9	27.30	8	0.00006	16345	2530	0.06	3036.13	1370.78	0.37	13231	17091	4829
	10	27.30	12	0.00021	4997	2598	0.06	2982.18	1344.78	0.37	13101	16953	4782
	11	27.30	16	0.00023	4575	2549	0.06	3149.44	1419.24	0.37	14290	18559	5212
	12	27.30	20	0.00025	4141	2585	0.06	3131.23	1411.20	0.37	14391	18616	5254
	13	43.90	8	0.00017	6167	2543	0.05	2874.26	1309.54	0.37	12111	15286	4431
	14	43.90	12	0.00032	3237	2568	0.06	2906.64	1318.47	0.37	12415	15852	4536
	15	43.90	16	0.00050	2052	2570	0.06	2982.24	1345.56	0.37	12952	16760	4727
	16	43.90	20	0.00056	1863	2595	0.05	3070.11	1385.10	0.37	13888	17953	5069

After preparing the raw data in Table 6.1, the value of r was calculated between ROP and MSE and other parameters. Table 6.2 presents those values. For a better illustration, the results of Table 6.2 have been also graphically demonstrated in Figure 6.1 and Figure 6.2.

Table 6.2 The calculated values of r between ROP and MSE and other measured parameters

Parameter	*WOB* (kg)	*RPM* (REV/s)	ρ (Kg/m³)	φ (-)	*Vp* (m/s)	*Vs* (m/s)	v_{dyn} (-)	E_{dyn} (MPa)	K_{dyn} (MPa)	G_{dyn} (MPa)	*ROP* (m/s)
ROP *(m/s)*	0.45	0.79	-0.46	0.49	-0.51	-0.51	-0.10	-0.50	-0.47	-0.49	-
MSE *(MPa)*	-0.36	-0.59	0.31	-0.31	0.20	0.24	0.28	0.26	0.19	0.26	-0.5

Figure 6.1 The calculated values of r between *ROP* and other parameters.

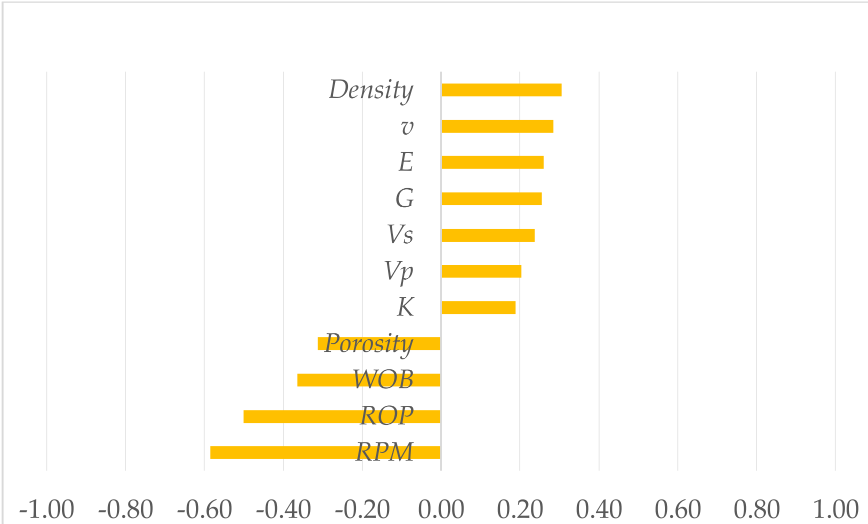

Figure 6.2 The calculated values of *r* between *MSE* and other parameters.

As illustrated in Figure 6.1, ROP values correlate most strongly and positively with RPM, followed by a moderate positive correlation with WOB. These findings confirm that increasing rotation speed and weight on bit generally enhances drilling speed. Porosity also shows a positive correlation with ROP, implying that rocks with higher porosity tend to allow faster drilling—likely due to their lower mechanical resistance. In contrast, ROP exhibits negative correlations with several rock properties, including wave velocities, elastic moduli, and density. The closeness in the magnitude of these negative correlations suggests that these parameters, which reflect the rock's stiffness and structural integrity, collectively contribute to reduced drill-ability.

Figure 6.2 highlights that MSE is negatively correlated with both RPM, ROP and WOB, indicating that increased operational input reduces the energy required per unit volume of rock removed. Porosity, again, exhibits a negative correlation with MSE, reinforcing the idea that less compact, more porous rocks demand less mechanical energy for drilling. Meanwhile, moderate positive correlations were observed between MSE and several mechanical parameters such as density, elastic moduli, and Poisson's ratio. The similarity in these values suggests that stiffer, denser rocks require more energy to fracture, which is consistent with the inverse relationship observed for ROP.

It should be noted that the strong negative correlation between MSE and ROP, with a Pearson's correlation coefficient of r=-0.50, confirms that drilling with a higher ROP leads to more efficient rock removal and a lower mechanical specific energy. In simpler terms, when drilling is more effective (i.e., higher ROP), less energy is consumed per unit volume of rock, and thus MSE decreases. This reinforces the concept that MSE serves as a performance indicator for drilling efficiency—where lower MSE values are associated with favorable drilling conditions and more responsive formations. Understanding this relationship is critical for real-time optimization in drilling operations, as monitoring MSE can indirectly reflect changes in ROP and help adjust operational parameters accordingly.

Overall, these findings clearly manifest the complex interplay between operational parameters and inherent rock properties. While drilling inputs like RPM and WOB are controllable and can be optimized in real time, the mechanical and physical features of the rock are fixed and must be understood beforehand. The statistical trends observed here emphasize the value of pre-drilling rock characterization as a predictive tool.

6.2. Dimensional Analysis

6.2.1. Formulation Criteria

In the previous section, the influence of different parameters on ROP and MSE was identified using Pearson's correlation technique. In this section, dimensional analysis is applied to develop empirically-based equations that maintain dimensional integrity while predicting ROP and MSE. The resulting models were constructed to meet three key criteria:

1. *Simple Practical Measurement of Input Parameters:* The chosen input parameters should be easily obtainable through standard field or laboratory measurements, ensuring practical application in real-world drilling scenarios. To be useful in real-world drilling operations, the input variables in the models must be easily and reliably measurable in the field or lab. Parameters that require complex or expensive testing reduce the practicality of the model. By focusing on readily available data, such as WOB, RPM, density, and porosity, the equations can be implemented effectively in operational workflows and decision-making.
2. *Inclusion of Minimum Essential Input Parameters:* The formulations should include a well-balanced set of essential parameters, minimizing complexity while maximizing predictive accuracy. Using only the most influential and necessary

parameters avoids overfitting and enhances the generalizability of the model. Including too many variables can introduce redundancy and obscure the underlying relationships, while a focused selection—guided by statistical correlation—improves model efficiency and interpretability. This approach ensures the model remains both robust and easy to calibrate with limited data.

3. *Dimensional Consistency of the Equation:* Each equation must be dimensionally coherent to ensure physical validity. Ensuring dimensional consistency in empirical equations is fundamental to maintaining physical validity. An equation that is dimensionally consistent allows for comparisons and predictions that are independent of the units used, making it universally applicable. This principle also helps detect errors in formulation and ensures that the relationships among variables reflect real-world physical behavior.

6.2.2. Selected parameters

In this section, the selection process of different contributing factors is elaborated. The contributing parameters, whose influence on ROP and MSE were assessed through Pearson's technique, can be sorted as follows:

1) Drilling parameters (WOB, RPM)
2) Rock physical parameters (density and porosity)
3) Rock mechanical parameters (*Vp*, *Vs*, and dynamic elastic parameters)

The drilling parameters including WOB and RPM showed a high Pearson's correlation coefficient with ROP and MSE. These two parameters directly represent the mechanical input delivered by the drilling rig, and their influence on both ROP and MSE is fundamental and well-established in drilling mechanics. Practically, WOB and RPM are straightforward to monitor and adjust in real-time, fully meeting the requirements of Criterion 1 (Simple Practical Measurability). Moreover, from the perspective of Criterion 2 (Inclusion of Minimum Essential Parameters), these two variables are independent, non-redundant, and directly linked to operational inputs, ensuring that the model captures the most impactful controllable factors without unnecessary complexity. Their inclusion in the empirical equations enhances the model's clarity, robustness, and practical relevance, making it useful not only for prediction but also for real-time drilling optimization. Accordingly, WOB and RPM were selected as essential inputs in the formulation of ROP and MSE predictive models.

The physical properties of the rocks, e.g. density and porosity, are fundamental to understanding and predicting drilling behavior. These parameters directly reflect the internal structure, compaction, and material composition of the rock, which influence both its mechanical strength and the ease with which it can be penetrated. Density is closely tied to the rock's mass per unit volume and serves as a proxy for its overall strength and stiffness, while porosity represents the void space within the rock matrix, often correlating with mechanical weakness and drill-ability. From a practical perspective, both parameters are easily and routinely measurable in laboratory or field conditions, satisfying Criterion 1 (Simple Practical Measurability). In addition, they are independent and non-redundant, making them valuable for maintaining model clarity and efficiency in line with Criterion 2 (Inclusion of Minimum Essential Parameters). Including density and porosity thus ensures that the empirical models capture the inherent geological variability of formations, enhancing both the physical relevance and the predictive accuracy of the ROP and MSE equations.

Among the rock mechanical parameters considered, e.g. *Vp*, *Vs*, and dynamic elastic moduli, only *Vp* was retained in the final empirical model. This decision is grounded in both Criterion 1 (Simple Practical Measurability) and Criterion 2 (Inclusion of Minimum Essential Parameters). In the subsequent paragraphs, the selection process of the rock mechanical parameters are described.

While dynamic elastic parameters provide valuable insight into rock stiffness and strength, they are inherently derived from a combination of wave velocities and density, making them redundant when those base parameters are already included. Their measurement also typically requires advanced laboratory instrumentation and controlled stress conditions, which limits their practical application in field settings. Furthermore, dynamic moduli, measured during real-time drilling operations, are generally higher than their static counterparts due to the influence of the drilling process and the frequency-dependent nature of the material's response. As such, they do not accurately reflect the rock's static mechanical behavior under typical drilling conditions. Additionally, the real-time measurement of these dynamic properties during drilling is often difficult and may introduce additional uncertainties due to environmental factors and the complexity of the rock formations. Therefore, while dynamic elastic moduli could be useful for other geophysical studies, their inclusion in the ROP model would add unnecessary complexity without providing more accurate results.

Similarly, although *Vs* is useful for characterizing shear behavior, its measurement is more complex and less stable than *Vp*, especially in heterogeneous or fractured formations. It is noteworthy that shear wave velocity is commonly measured through dipole shear wave logging methods, although its application remains relatively limited in practice [Bukar et al., 2019]. Furthermore, its availability and reliability may be compromised by factors such as missing data from older wells, poor data storage, suboptimal logging conditions, remote well locations, or limitations in logging technology (Olutoki et al., 2024). In contrast, *Vp* is not only easier, cheaper, and more reliable to measure in both lab and field environments, but also serves as a direct and independent indicator of rock competence (Azadpour et al., 2020; A. E. Haque et al., 2023). Retaining *Vp* allows the model to incorporate mechanical behavior without overcomplicating the formulation, ensuring that it remains both physically representative and operationally applicable. Therefore, *Vp* was selected as the sole mechanical property for inclusion in the empirical modeling of ROP and MSE.

In the end, the parameters retained for empirical formulation of ROP and MSE include *WOB*, *RPM*, density, porosity, and *Vp*. These five variables were selected based on a balanced consideration of statistical significance, physical relevance, and practical measurability. Together, they represent a comprehensive yet concise set of inputs that capture both the operational and geological factors influencing drilling performance. By excluding redundant or impractically measured variables, the resulting models are designed to remain dimensionally consistent, interpretable, and suitable for real-time application in diverse drilling scenarios.

As well as the selected parameters through Pearson's technique, additional variables were considered based on theoretical understanding and physical relevance to ensure a comprehensive formulation. The experimental setup used in this research involved a single coring bit with an outer diameter of 44 mm and inner diameter of 38 mm. From a modeling perspective, excluding such geometrically critical parameters would result in an empirical formulation that is incomplete when applied to wider operational scenarios involving variable bit sizes. To address this issue, bit outer diameter, D, as well as the ratio of bit's outer diameter to inner diameter, λ, were considered in formulations. As a result, the formulations can be applied to broader geometries, expanding its range of applications. On a positive note, those geometrical parameters are controllable in bit design and selection process. Including them in the models provides engineers with a direct lever for optimizing performance through tool choice.

Several studies have shown that bit diameter has a reciprocal relationship with ROP and a direct influence on MSE when all other conditions, e.g. rock type, WOB, and RPM, are held constant (Alwaar et al., 2025; Teale, 1965). This behavior is physically intuitive: a larger bit must remove more rock per unit depth, which increases the mechanical work required and consequently slows down the rate of penetration. In contrast, smaller diameter bits remove less rock per revolution, allowing for faster progression in the axial direction under the same energy input (Macpherson, 2025; Stoxreiter et al., 2019).

The inclusion of bit diameter in the ROP and MSE formulations is fully justified when assessed against the three core criteria used in this study; firstly, bit diameter is among the most straightforward parameters to measure in any drilling system. Whether in laboratory testing or field operations, bit diameter is readily available, constant for a given run, and unambiguous (Maurer, 1962; Teale, 1965). Therefore, it strongly satisfies Criterion 1. Secondly, bit diameter is both geometrically essential and physically non-redundant. It cannot be derived from any other input parameter and has a distinct, well-documented influence on drilling performance. Its effect is not captured by WOB, RPM, or rock properties alone (Tou, 1988; Jiao et al., 2024). Thirdly, bit diameter has a straightforward unit, meter (m), which makes it easy to incorporate into dimensional formulations without added complexity. Unlike compound units such as density (kg/m^3), the simplicity of diameter's unit facilitates cleaner dimensional expressions and enhances the clarity of the overall model structure.

Furthermore, incorporating the outer-to-inner diameter ratio of a coring bit into empirical models improves their predictive capability by accounting for the bit’s geometric influence on drilling performance. This ratio affects both the volume of rock removed per revolution and the structural strength of the bit, which in turn impact ROP and MSE. Including it allows the model to differentiate between bit designs, enhancing accuracy, scalability, and practical relevance for optimizing drilling operations. Moreover, considering this ratio provides engineers with a direct parameter for bit selection and design adjustments.

6.2.3. Formulation development

Dimensional analysis refer to a technique utilized to derive relationships between physical quantities by examining their fundamental dimensions, namely length ($\dot{L}$), mass ($\dot{M}$), and time ($\dot{T}$). Every measurable physical parameter can be described using these three basic dimensions. For example, velocity has the dimension of $[\dot{L}][\dot{T}]^{-1}$, force is $[\dot{M}][\dot{L}][\dot{T}]^{-2}$, and energy is $[\dot{M}][\dot{L}]^{2}[\dot{T}]^{-2}$. The core principle behind dimensional analysis is dimensional homogeneity, which states that all terms in a physically meaningful equation must have the same dimensional form. This principle ensures that the relationship holds true regardless of the specific units (e.g., SI, and Imperial units systems) used for measurement.

This approach aligns directly with Criterion 3 (Dimensional consistency), which requires that all empirical formulations be physically valid and unit-independent. By enforcing dimensional consistency through dimensional analysis, the resulting equations are not only theoretically sound but also more robust and universally applicable. In the previous section, the selected parameters for formulating of ROP and MSE were:

I. *WOB:* $[\dot{M}]$
II. *RPM:* $[1/\dot{T}]$
III. φ: [Dimensionless]
IV. ρ : $[\dot{M}/\dot{L}^3]$
V. V_p : $[\dot{L}/\dot{T}]$
VI. D : $[\dot{L}]$
VII. λ : [Dimensionless]

Given these parameters, the relationship between ROP and the selected variables can be expressed as:

$$ROP = WOB^a \times RPM^b \times \varphi^c \times D^d \times \rho^e \times {V_p}^f \times \lambda^k \quad (6.1)$$

where, a, b, c, d, e, and f are dimensionless exponents which may take any real values, determined through dimensional balancing, empirical calibration, and laboratory experiments. Furthermore, λ represents the ratio of outer diameter to inner diameter of the coring bit (dimensionless), and k is a constant (dimensionless).

By substituting the fundamental dimensions of each parameter into the equation and ensuring dimensional consistency, the following relation is obtained:

$$\dot{L}/\dot{T} = \left(\dot{M}\right)^a \times \left(1/\dot{T}\right)^b \times (1)^c \times \left(\dot{L}\right)^d \times \left(\dot{M}/\dot{L}^3\right)^e \times \left(\dot{L}/\dot{T}\right)^f \times (1)^k \tag{6.2}$$

The above relation, once simplified, can be rearranged to reflect the dimensions of mass, time, and length as follows:

$$\dot{L}/\dot{T} = \dot{M}^{(a+e)} \times \dot{T}^{(-b-f)} \times \dot{L}^{(d-3e+f)} \tag{6.3}$$

For the above equation to be dimensionally consistent, the exponents of $\dot{M}$, $\dot{T}$, and $\dot{L}$ must be equal on both sides, resulting in the following system of equations:

$$\begin{cases} a + e = 0 \\ -b - f = -1 \\ d - 3e + f = 1 \end{cases} \tag{6.4}$$

Once the above system of equations is solved, the values of the exponents *a, b, d, e,* and *f* are determined.

Additionally, note that in Eq. (6.2), the term of $(1)^c$ and $(1)^k$ are dimensionless quantities, so they do not affect dimensional analysis. That's why the exponents c and k do not appear in Eq. (6.3). Dimensional analysis alone cannot determine c and k. They can be determined experimentally using log-log regression or curve fitting based on laboratory experiments.

The following subsection outlines the procedure used to solve the system of equations in Eq. (6.4). This is followed by a section detailing the method for determining the exponents *c* and *k* using experimental data.

6.2.3.1. Determination of exponents a, b, d, e, and f

The determination process was initiated by calculating the exponent *a;* this exponent belongs to parameter *WOB* in Eq. (6.1). For this purpose, using the raw data presented in Table 6.1, the variation of ROP with WOB was plotted for all rock types. Figures (6.3), (6.4), (6.5) and (6.6) depict the corresponding variation of ROP with WOB under four RPM values for Szydłowiec-Śmiłów, Wola Komborska, Tumlin sandstone, and Morawica marble, respectively. The ROP-WOB plotting was done for four RPM conditions including 7.50, 16.28, 27.30, and 43.90 REV/s.

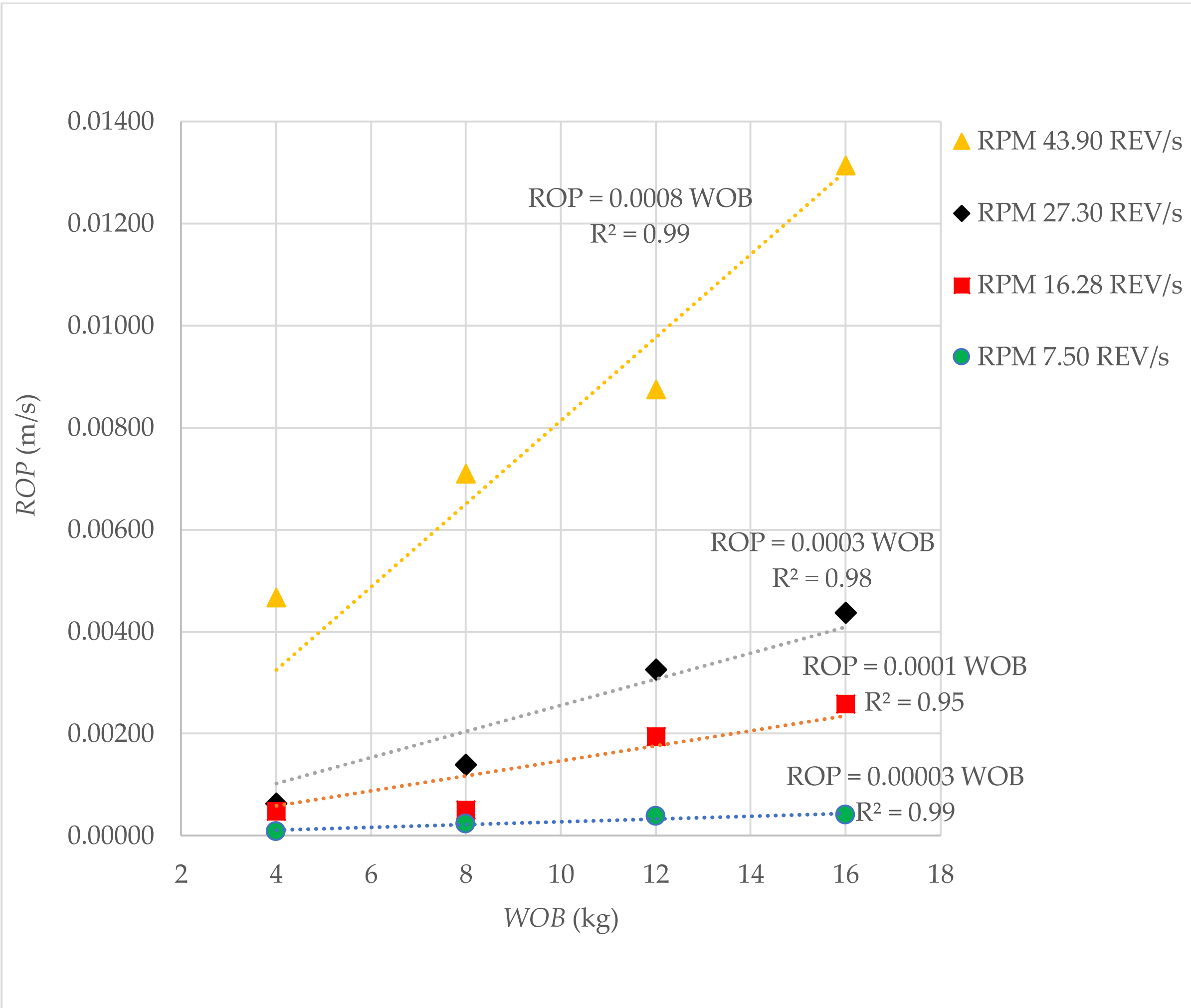

Figure 6.3 The variations of ROP with WOB under four RPM values for Szydłowiec-Śmiłów sandstone.

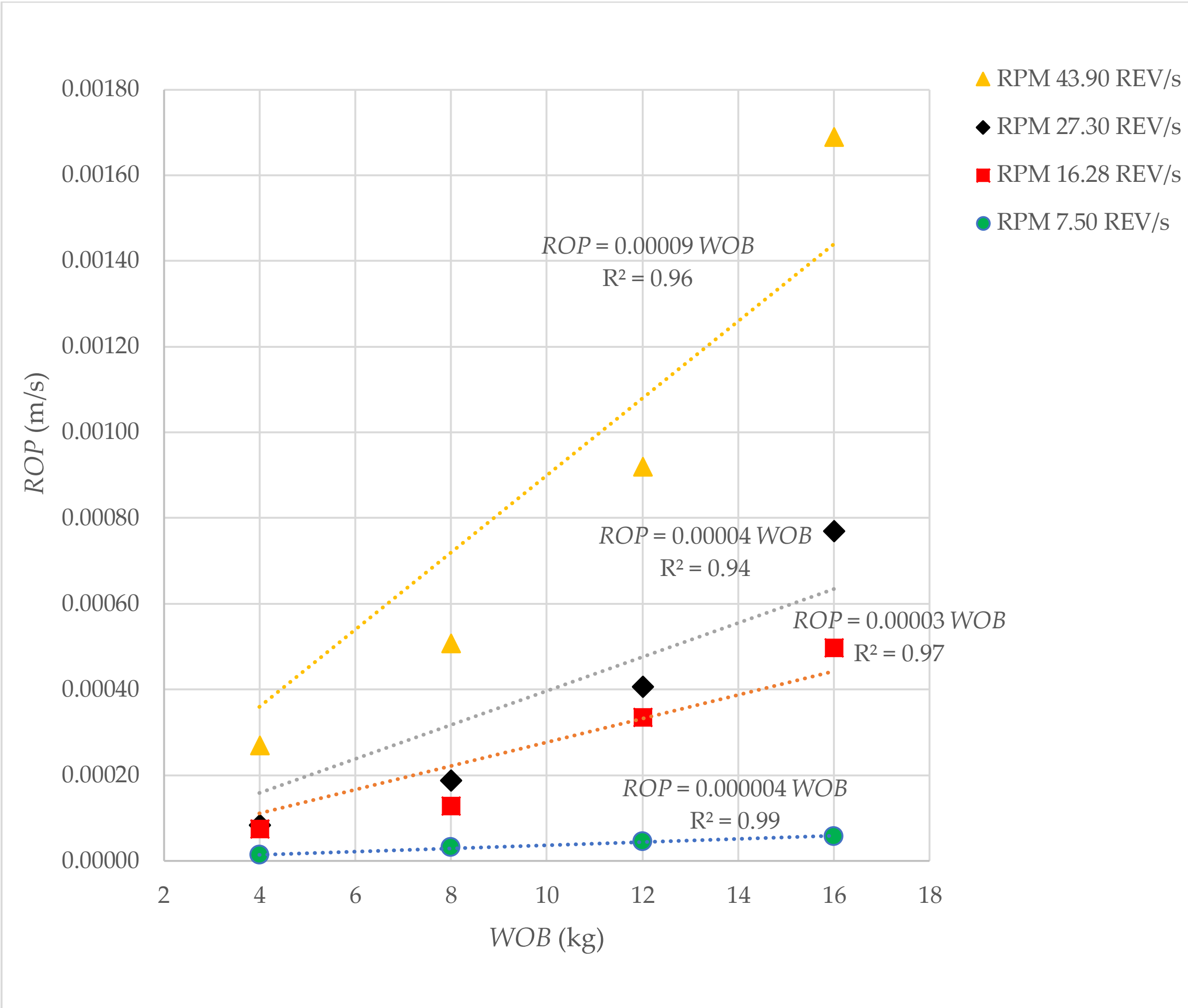

Figure 6.4 The variations of ROP with WOB under four RPM values for Wola Komborska sandstone.

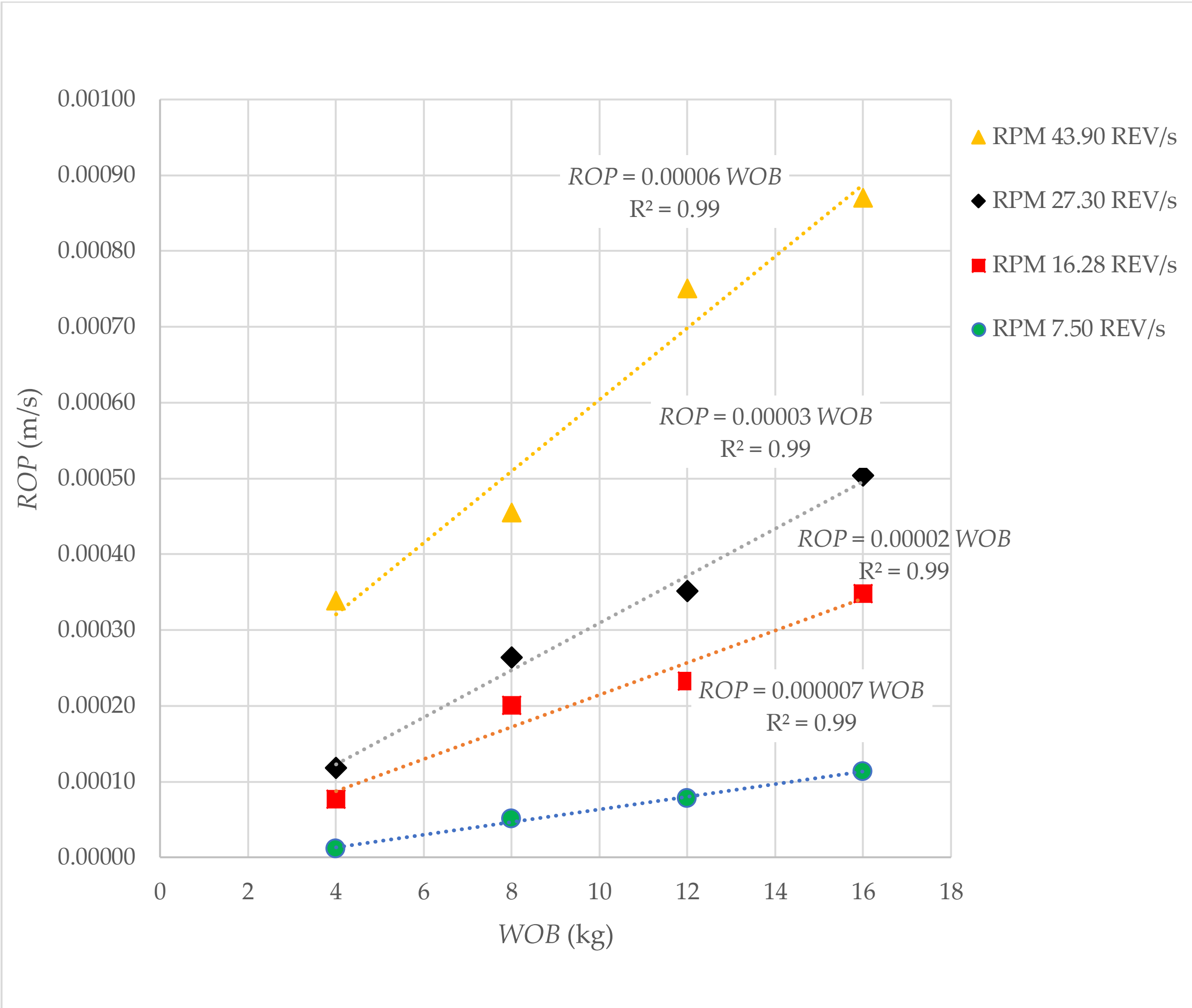

Figure 6.5 The variations of ROP with WOB under four RPM values for Tumlin sandstone.

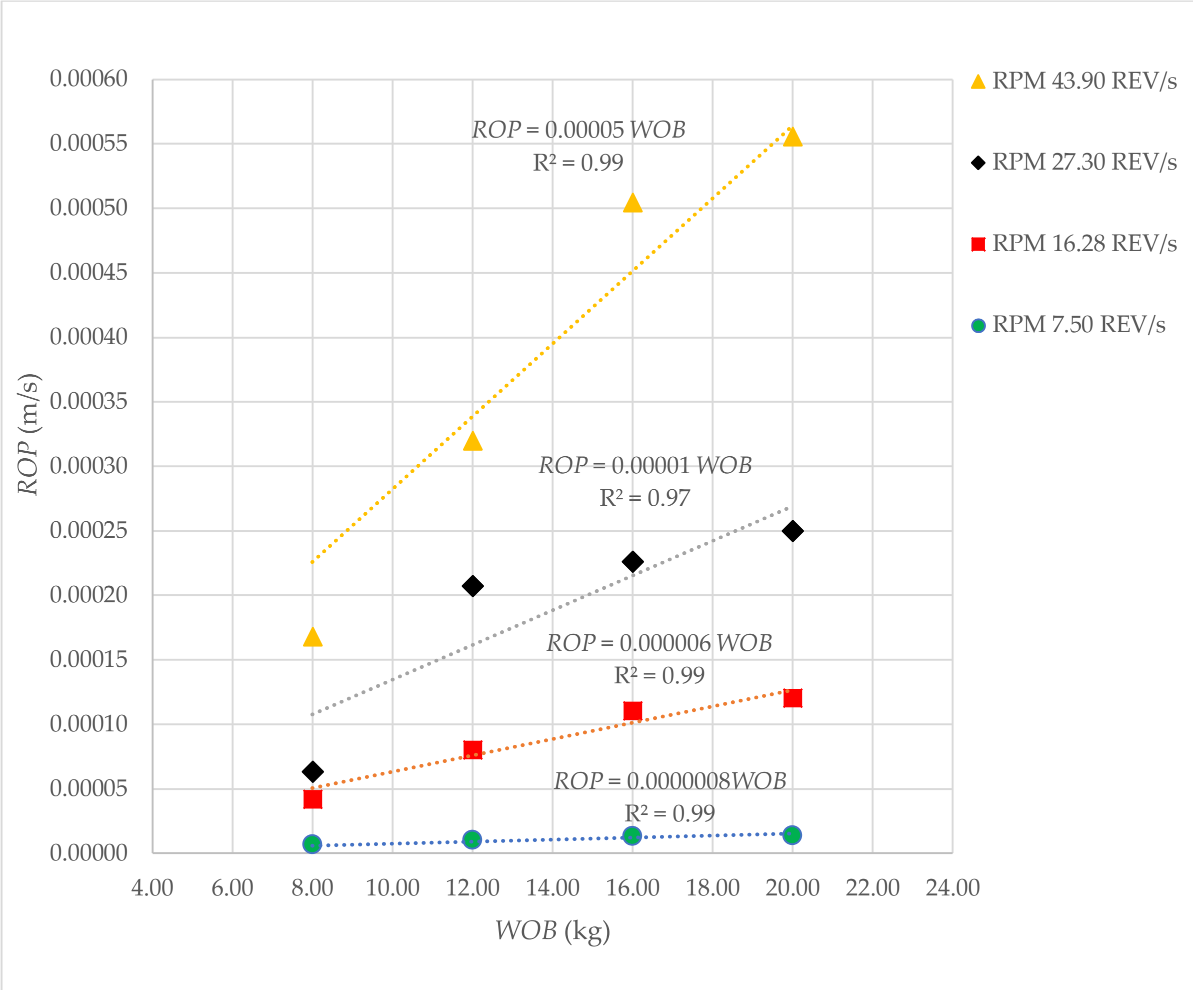

Figure 6.6 The variations of ROP with WOB under four RPM values for Morawica marble.

As shown in Figures 6.3 through 6.6, a direct relationship exists between ROP and WOB across all tested rock types and for various RPM values. Specifically, at a constant RPM, ROP consistently increases with increasing WOB. This upward trend is well-approximated by a linear relationship, as indicated by high coefficients of determination (R^2>0.95) for all cases. These strong correlations demonstrate both the accuracy and reliability of the linear fits. Therefore, it is reasonable to conclude that the exponent a in Eq. (6.1) can be taken as 1, reflecting a linear dependency of ROP on WOB.

The second exponent, b, corresponds to the parameter RPM. To determine b, the same method used for exponent a was applied. Using the raw data presented in Table 6.1, the variation of ROP with RPM was plotted for each rock type. Figures 6.7 through 6.10 show the resulting ROP–RPM curves for Szydłowiec-Śmiłów sandstone, Wola Komborska sandstone, Tumlin sandstone, and Morawica Marble, respectively. For the sandstone samples, the curves were generated under four RPM conditions including 4, 8, 12, and 16 kg. In the case of marble, the applied WOB values were 8, 12, 16, and 20 kg.

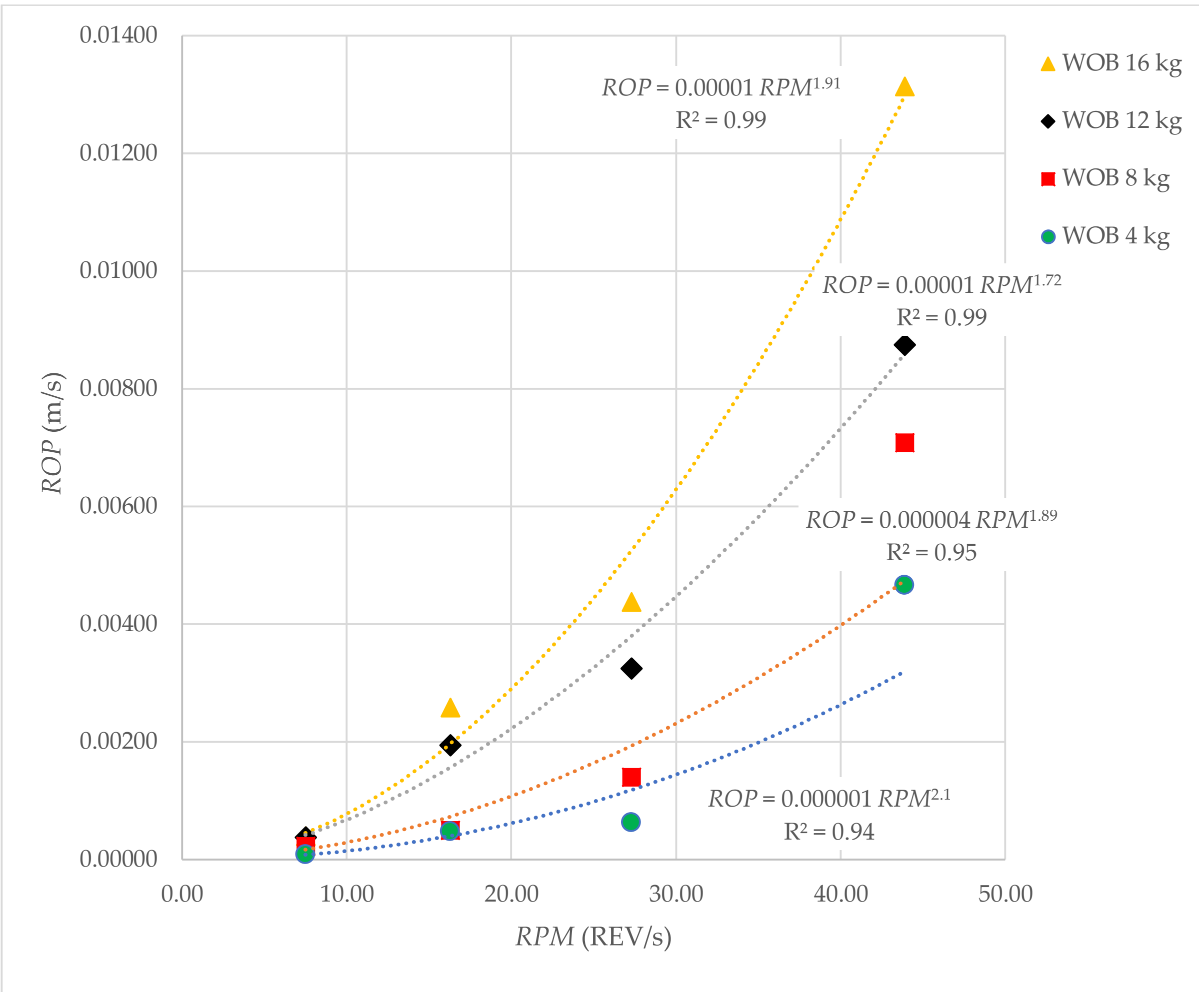

Figure 6.7 The variations of ROP with RPM under four WOB values for Szydłowiec-Śmiłów sandstone.

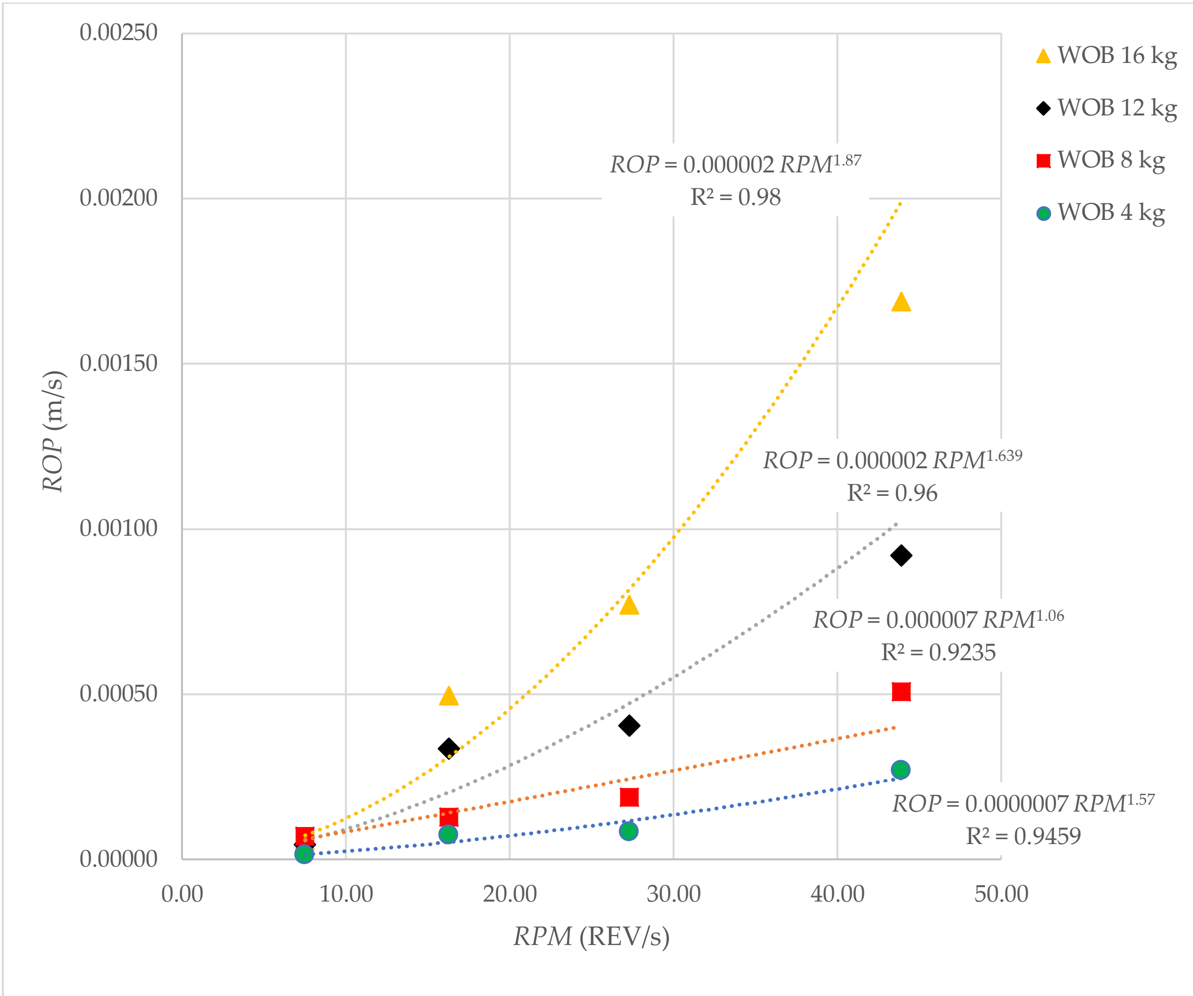

Figure 6.8 The variations of ROP with RPM under four WOB values for Wola Komborska sandstone.

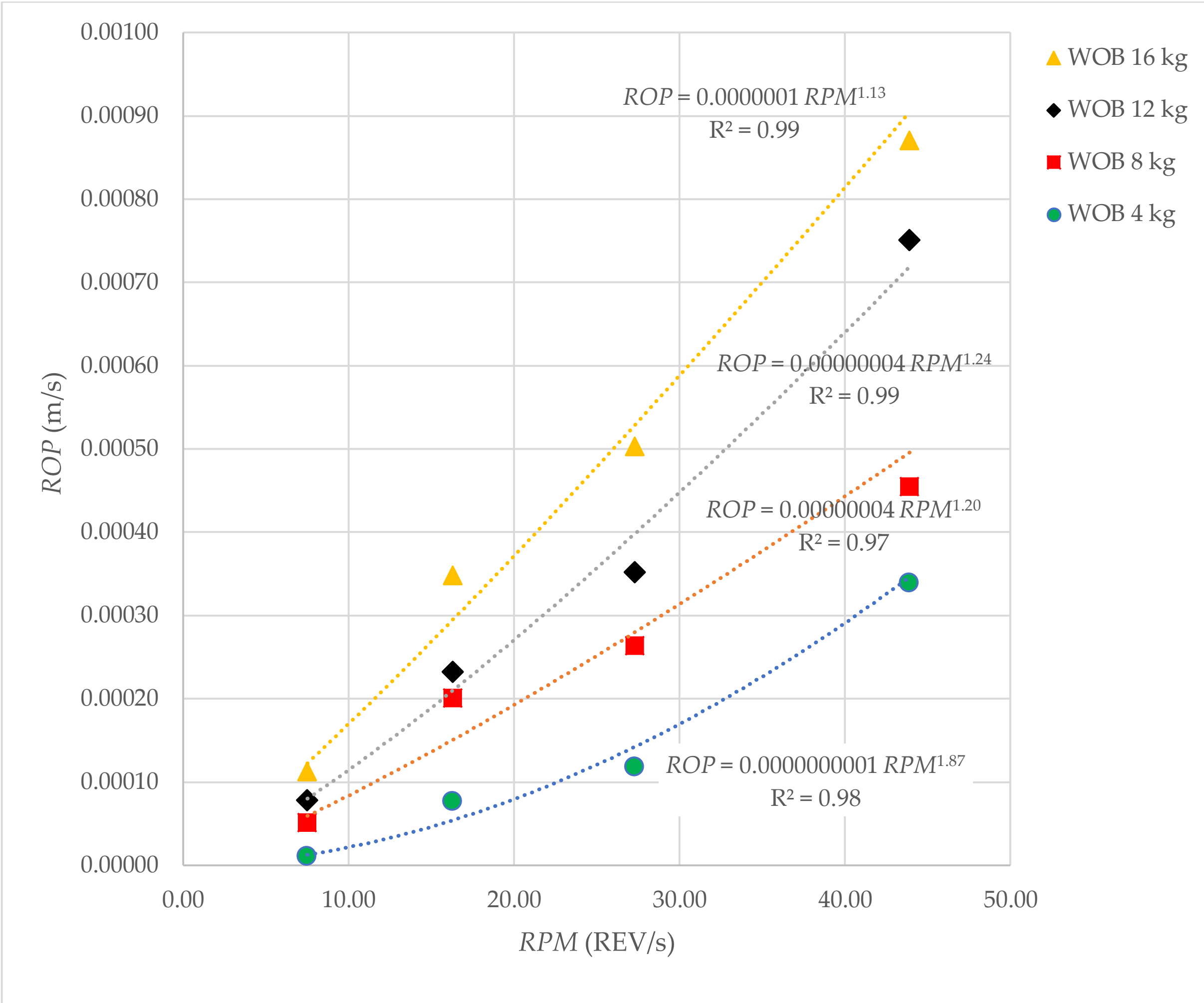

Figure 6.9 The variations of ROP with RPM under four WOB values for Tumlin sandstone.

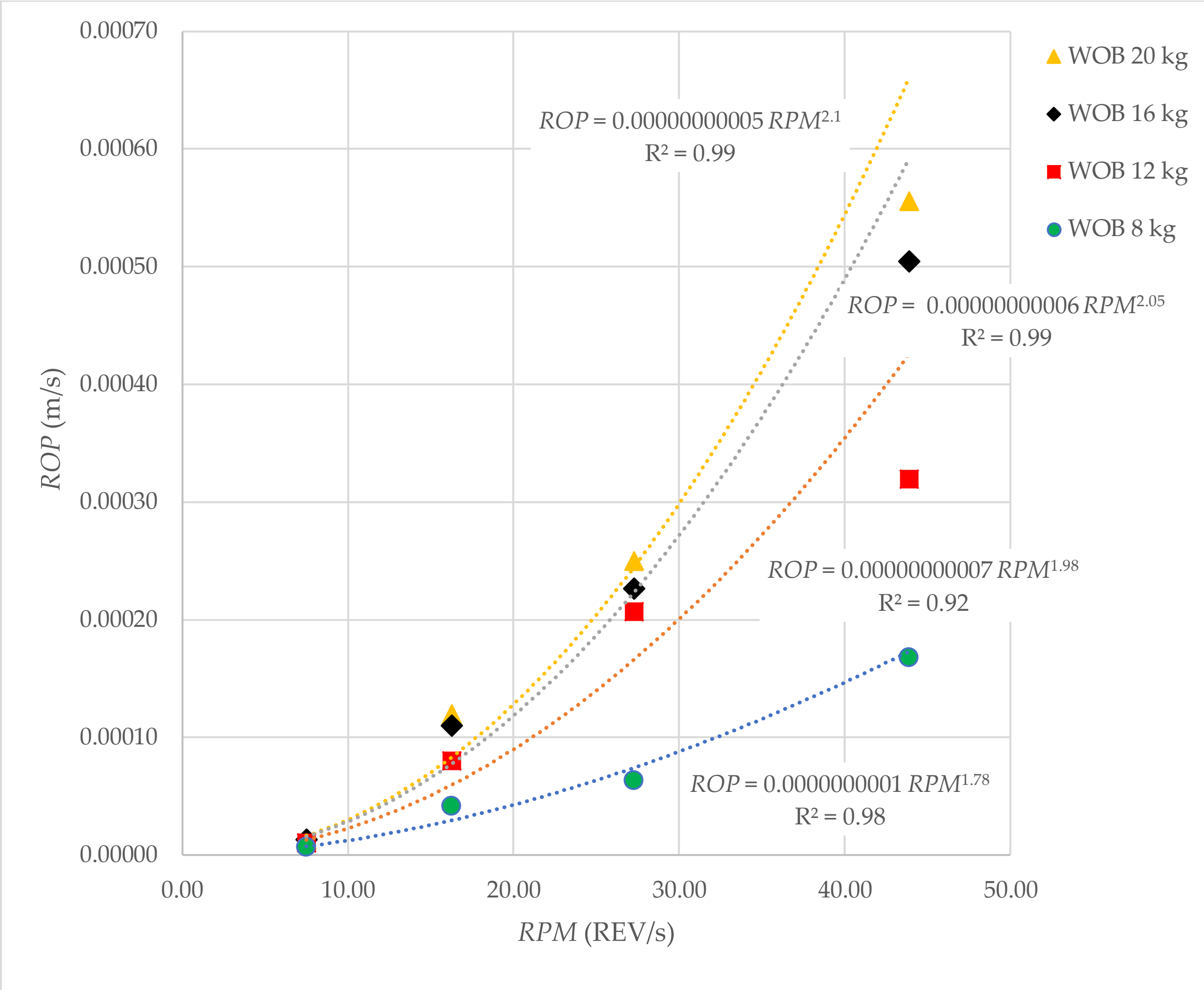

Figure 6.10 The variations of ROP with RPM under four WOB values for Morawica marble.

According to Figures 6.7, 6.8, 6.9, and 6.10, *ROP* can be appropriately modeled as a power function of *RPM*. The high coefficients of determination (R^2 values between 0.92 and 1.00) across all fitted models confirm the reliability and robustness of the power-law approximation.

The extracted exponent values representing the power relationship between *ROP* and *RPM* range from approximately 1.06 to 2.10, with the majority of values clustering between 1.7 and 2.1. This consistent trend across various data points suggests that *ROP* exhibits a near-quadratic dependence on *RPM*. Although a few exponents fall slightly below 1.5, these are relatively fewer and are mostly related to Tumlin sandstone, which is likely related to its structural heterogeneity. Given the predominance of values close to 2, it is reasonable to model the *ROP*–*RPM* relationship as a second-degree power function, i.e., $ROP \propto RPM^2$, which simplifies analysis while maintaining strong fidelity to the observed data behavior.

Now, with the exponents $a = 1$, and $b = 2$, the system of equations in Eq. (6.4) can be solved as follows:

$$a + e = 0, \Rightarrow e = -1$$

$$-b - f = -1, \Rightarrow f = -1$$

$$d - 3e + f = 1, \Rightarrow d = -1$$

Therefore, the ROP formulation established in Eq. (6.1) can be rewritten as follows:

$$ROP = \lambda^k \times WOB^1 \times RPM^2 \times \varphi^c \times D^{-1} \times \rho^{-1} \times {V_p}^{-1} \tag{6.5}$$

The remaining unknown variables, including k and c, will be determined in the following subsection.

6.2.3.2. Determination of constants k and c

The values of the k and c cannot be determined through dimensional analysis, as they do not affect the dimensional balance of the equation. Instead, these parameters should be obtained empirically through the application of experimental data. Therefore, this was done through log-log regression analysis.

This section outlines the step-by-step calculation method used to determine the parameters c and k in the empirical ROP model.

The established empirical model for ROP in Eq. (6.5) can be rearranged as:

$$ROP = \lambda^k \times \varphi^c \times WOB^1 \times RPM^2 \times D^{-1} \times \rho^{-1} \times {V_p}^{-1} \tag{6.6}$$

If both sides of the expression are transformed using a natural logarithm, the resulting form of the equation is obtained as follow:

$$ln(ROP) = k.ln(\lambda) + c \cdot ln(\varphi) + ln(WOB) + 2ln(RPM) - ln(D) - ln(\rho) - ln(Vp) \tag{6.7}$$

Rewriting the above equation by grouping all known terms into a single variable X yields:

$$X = c \cdot ln(\varphi) + k.ln(\lambda) \tag{6.8}$$

where

$$X = ln(ROP) - ln(WOB) - 2ln(RPM) + ln(D) + ln(\rho) + ln(Vp) \tag{6.9}$$

In the next step, using the experimental data provided in Table 6.1, for each laboratory experiment (64 in total), the values of X were computed. Moreover, the corresponding values of φ were assigned, yielding 64 equations of the form:

$$X_i = c \cdot ln(\varphi_i) + k.ln(\lambda) \quad \text{for} \quad i = 1,2,3,\dots,64 \tag{6.10}$$

This represents a system of 64 linear equations with two unknowns, including c and k.

To isolate and solve for c, the following two-steps operations were executed:

I. The first 32 of the 64 equations were multiplied by -1, as follows:

$$-X_1 = -c \cdot ln(\varphi_1) - k.ln(\lambda)$$
$$-X_2 = -c \cdot ln(\varphi_2) - k.ln(\lambda)$$
$$\vdots$$
$$\vdots$$
$$-X_{32} = -c \cdot ln(\varphi_{32}) - k.ln(\lambda)$$

Where X_1, X_2, …, and X_{32} represent the X values for 1st, 2th, …, and 32th laboratory experiment, respectively. Similarly, φ_1, φ_2, …, and φ_{32} represent the φ values for 1st, 2th,…, and 32th laboratory experiment, respectively.

II. Then, all 64 equations were summed, resulting in the elimination of terms of $k.ln(\lambda)$. This yielded:

$$-\sum_{i=1}^{32} X_i + \sum_{i=33}^{64} X_i = c\left(-\sum_{i=1}^{32} \ln(\varphi_i) + \sum_{i=33}^{64} \ln(\varphi_i)\right) \tag{6.11}$$

This produced the final formula for calculating c:

$$c = \frac{\sum_{i=33}^{64} X_i - \sum_{i=1}^{32} X_i}{\sum_{i=33}^{64} \ln(\varphi_i) - \sum_{i=1}^{32} \ln(\varphi_i)} \tag{6.12}$$

Once c was determined, k was calculated by solving for term $k.ln(\lambda)$ in the linear form equation as follows:

$$k.ln(\lambda) = X_i - c \cdot ln(\varphi_i) \qquad \text{for } i = 1,2,3,\dots,64 \tag{6.13}$$

Taking the average over all 64 tests yields:

$$k = \frac{\frac{1}{64} \times \sum_{i=1}^{64} [X_i - c \cdot ln(\varphi_i)]}{ln(\lambda)} \qquad \text{for } i = 1,2,3,\dots,64 \tag{6.14}$$

Considering $\lambda = 1.16$, the above equation can be simplified as follows:

$$k = \frac{\sum_{i=1}^{64} [X_i - c \cdot ln(\varphi_i)]}{64 \times ln(1.16)} \qquad \text{for } i = 1,2,3,\dots,64 \tag{6.15}$$

Based on the computational procedure described above, the values of c and k were determined to be approximately 1.7 and -2, respectively.

The computed porosity exponent of $c = 1.7$ demonstrates the significant influence of porosity on the rate of penetration during drilling. This value indicates that ROP increases more than linearly with porosity, highlighting that more porous rocks tend to be drilled more easily and rapidly. A higher exponent suggests that even small increases in porosity can lead to relatively large improvements in drilling efficiency. This is consistent with the physical behavior of porous rocks, which generally exhibit lower mechanical strength and higher permeability, allowing the drill bit to fracture and remove material more readily. The exponent value of 1.7 not only validates the inclusion of porosity as a key predictive parameter in the ROP model but also quantifies its relative weight compared to other factors such as WOB and RPM.

The value of k, which was obtained as -2, also demonstrates that the ratio of bit's outer diameter to the inner diameter is an important geometrical factor influencing coring drilling performance. This ratio affects both the mechanical efficiency of rock removal and the structural stiffness of the coring bit. A higher ratio, corresponding to thinner bit walls, reduces the volume of rock that must be removed per revolution, potentially increasing ROP, but may also increase the risk of bit deformation. Conversely, a lower ratio, corresponding to thicker bit walls, reduces ROP although the bit is more resistant.

6.2.3.3. ROP formulation

Based on the descriptions provided in the above subsections, the ROP formulation presented in Eq. (6.1) becomes:

$$ROP = \frac{WOB \times RPM^2 \times \varphi^{1.7}}{\rho \times V_p \times D \times \lambda^2} \tag{6.16}$$

The equation offers several key advantages. First, it maintains dimensional consistency, ensuring that the physical relationships among variables are preserved regardless of the units used. Second, it is built exclusively from measurable and commonly available parameters including WOB, RPM, porosity, density, compressional wave velocity, and bit geometry, making it highly practical for field applications. The use of porosity with a data-calibrated exponent enhances the model's sensitivity to lithological variability, allowing it to adapt to different rock types and formation conditions.

Additionally, by incorporating both operational (WOB and RPM) and geological (φ, ρ, and V_p) inputs, the model strikes a balance between controllable and intrinsic factors, which is essential for real-time drilling optimization. The simplicity of the expression, combined with its strong empirical backing, makes it efficient for implementation in both manual calculations and automated drilling software.

6.2.4. Development of MSE formulation

When a drilling rig starts to drill a rock, the drill-bit breaks the rock through a rotary and percussive mechanism. The mechanical specific energy consumption associated with the drilling rig is equivalent to the work done. The work done in rotary and percussive mechanisms can be formulated as follows:

$$W_{total} = W_{rotation} + W_{percussion} \tag{6.17}$$

where W_{total} indicates the total work done by the drilling rig, $W_{rotation}$ represents the work in rotary mechanism, and $W_{percussion}$ indicates the work done during percussion mechanism.

The $W_{rotation}$ relies on the rotational speed of the drill bit. For a certain drilling time, t, $W_{rotation}$ can be determined using the following expression:

$$W_{rotation} = P \times t \tag{6.18}$$

where $P_{rotation}$ represents the Power of the drilling rig, computed as follows:

$$P = w \times T \tag{6.19}$$

where w indicates angular velocity of the drill-bit, and T represents Torque.

The parameter w can be stated with respect to *RPM*, as follows:

$$w = \frac{2\pi}{60} \times RPM \tag{6.20}$$

Replacing Eqs. (6.19) and (6.20) in Eq. (6.18), it gets:

$$W_{rotation} = \frac{2\pi}{60} \times RPM \times T \times t \tag{6.21}$$

On the other side, $W_{percussion}$ is the work done by the force on the bit, F. For a certain drilling time, t, the vertical movement of the drilling bit is equivalent to the height (length) of the drilled rock. The height of the drilled rock is computed as follows:

$$h = ROP.t \tag{6.22}$$

where h represents the height of the drilled rock.

Thus, $W_{percussion}$ can be calculated as:

$$W_{percussion} = F.ROP.t \tag{6.23}$$

The volume of rock removed through drilling is also computed as follows:

$$V_{drilled} = A.ROP.t \tag{6.24}$$

Where, A donates the cross-sectional area of the drill-bit.

The mechanical specific energy is expressed as the work done to break and displace a unit volume of the rock. Hence, combining Eqs. (6.17), (6.21), (6.23), and (6.24), it yields:

$$MSE = \frac{F.ROP.t}{A.ROP.t} + \frac{(\frac{2\pi}{60})\times RPM \times T \times t}{A.ROP.t} \tag{6.25}$$

Consequently, the above formula is simplified as follows:

$$MSE = \frac{F}{A} + \frac{2\pi \times T \times RPM}{60 \times A \times ROP} \tag{6.26}$$

The key shortcoming of Eq. (6.26) lies in the absence of rock parameters in the evaluation of MSE.

Now, let's consider Eq. (6.26) specifically for coring bits. For coring bits, Eq. (6.26) can be rewritten as follows:

$$MSE = \frac{F}{A_{net}} + \frac{2\pi \times T \times RPM}{60 \times A_{net} \times ROP} \tag{6.27}$$

where A_{net} represents the area of the non-hollow cross section of the coring bit, which can be calculated using Eq. (4.5).

In the current research, the conducted coring drilling tests showed that the energy consumed by the percussive mechanism (the term $\frac{F}{A_{net}}$ in Eq. (6.27)) was very significantly negligible compared to that consumed by the rotary mechanism. This means that the MSE can be defined solely in terms of the rotary energy. Taking this into account, and incorporating Eqs. (4.5) and (6.16) in Eq. (6.27), it yields:

$$MSE = \frac{0.13 \times \lambda^4 \times T \times \rho \times V_p}{(\lambda^2 - 1)\times D \times WOB \times RPM \times \varphi^{1.7}} \tag{6.28}$$

The above MSE formulation offers several significant advantages. Most notably, it integrates critical rock-dependent parameters, including ρ, V_p, and φ, which are entirely absent in Eq. (6.26). This enhancement allows the new equation to better reflect the mechanical resistance of the rock being drilled, making it more responsive to lithological variations.

Additionally, Eq. (6.28) maintains a balanced representation of both operational inputs (such as torque, RPM, and WOB) and formation characteristics, making it suitable for performance monitoring, bit wear analysis, and real-time drilling optimization. Ultimately, this equation represents a meaningful step forward in linking drilling mechanics with formation properties, enhancing its predictive capability and field relevance.

In the following chapter, the developed formulations for ROP and MSE, presented in Eqs. (6.16) and (6.28), are subjected to validation and performance evaluation. These formulations are applied to laboratory drilling data collected from laboratory experiments to assess their accuracy and robustness. By comparing the models' outputs with observed values, the effectiveness of the derived ROP and MSE formulations in capturing real drilling behavior will be critically examined. This validation step is essential for confirming the practical applicability and reliability of the models for various rock and operational conditions.

Chapter 7:

Validation of ROP and MSE Models

7.1. Validation process

In the previous chapter, two empirical equations were developed for modeling ROP and MSE, presented in Eqs. (6.16) and (6.28), respectively. Additionally, the raw laboratory data used for model development and evaluation was provided in Table 6.1, which contains the measured (actual) values of ROP and MSE obtained from laboratory drilling experiments. For each rock type, 16 drilling tests were performed, yielding 16 corresponding ROP and MSE data points. As a result, 64 drilling tests were performed, yielding 64 corresponding ROP and MSE data points for the evaluation process.

In this chapter, the measured values of ROP and MSE presented in Table 6.1 are compared with the corresponding values obtained from the Eqs. (6.16) and (6.28), respectively. This comparison allows for an assessment of how accurately the developed models reflect the actual drilling behavior observed in the laboratory conditions.

To validate the capability of the developed models, both qualitative and quantitative methods are employed. Graphical comparisons, such as scatter plots of predicted versus measured values, are used to visually assess the consistency between the models and the experimental results. Additionally, standard statistical metrics including R^2, *MAPE*, and *RMSE* are calculated to quantitatively evaluate the accuracy of the results.

A high level of alignment between the predicted and measured data would confirm the validity and robustness of the proposed models for use in similar lithological conditions. Furthermore, the inclusion of rock-specific parameters such as porosity, density, and compressional wave velocity in the models is expected to enhance their adaptability across different rock types. The following sections present the results of the validation process in detail, offering insight into the performance and limitations of the developed ROP and MSE formulations.

7.2. ROP Model Validation

This section presents the validation of the ROP model derived in Eq. (6.16). The predicted ROP values are computed using the known input variables from each drilling test and are then compared against the measured values from Table 6.1. The validation was conducted both individually for each rock type and collectively across all rock samples, offering an in-depth assessment of the model's accuracy and generalizability.

7.2.1. ROP Model validation for Szydłowiec-Śmiłów sandstone

Table 7.1 presents the values of real ROP, predicted ROP, and the corresponding evaluation metrics including R^2, *MAPE*, and *RMSE* for Szydłowiec-Śmiłów sandstone. For better illustration, Figure 7.1 depicts the comparison between real and predicted ROP values across the 16 drilling tests. Additionally, Figure 7.2 provides a scatter diagram illustrating the relationship between measured and predicted ROP, offering a visual confirmation of the model's accuracy and consistency for this rock.

Table 7.1 Measured and predicted ROP values with evaluation metrics for Szydłowiec-Śmiłów sandstone.

Test number	Real *ROP* (m/s)	Predicted *ROP* (m/s)	R^2	*MAPE*	*RMSE*
1	0.00008	0.00008	0.98	28%	0.0009
2	0.00023	0.00015			
3	0.00038	0.00023			
4	0.00040	0.00031			
5	0.00048	0.00038			
6	0.00050	0.00073			
7	0.00194	0.00104			
8	0.00258	0.00145			
9	0.00063	0.00103			
10	0.00140	0.00195			
11	0.00325	0.00332			
12	0.00438	0.00397			
13	0.00467	0.00302			
14	0.00709	0.00607			
15	0.00875	0.00807			
16	0.01314	0.01070			

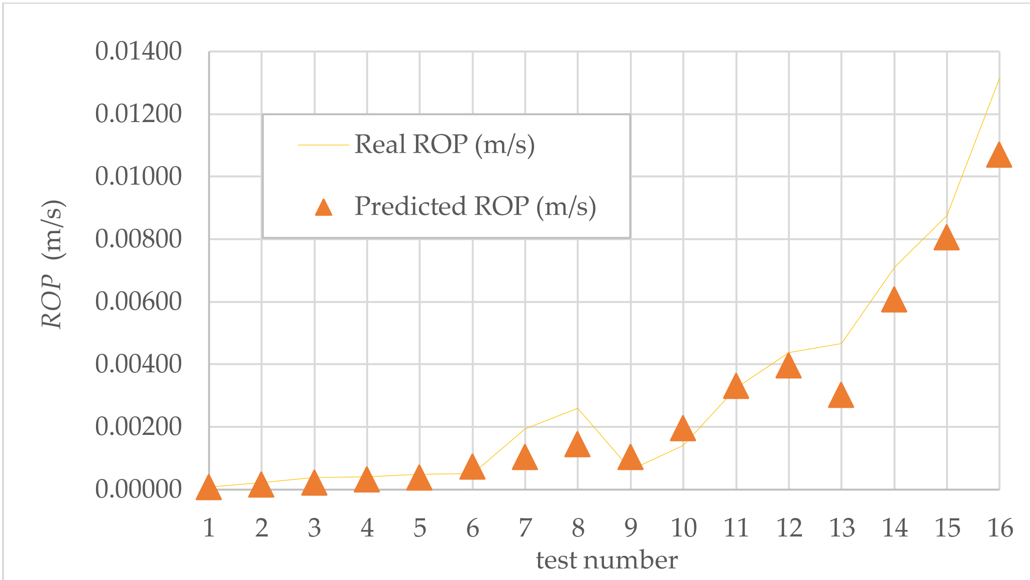

Figure 7.1 Real vs. predicted ROP across 16 laboratory tests for Szydłowiec-Śmiłów sandstone.

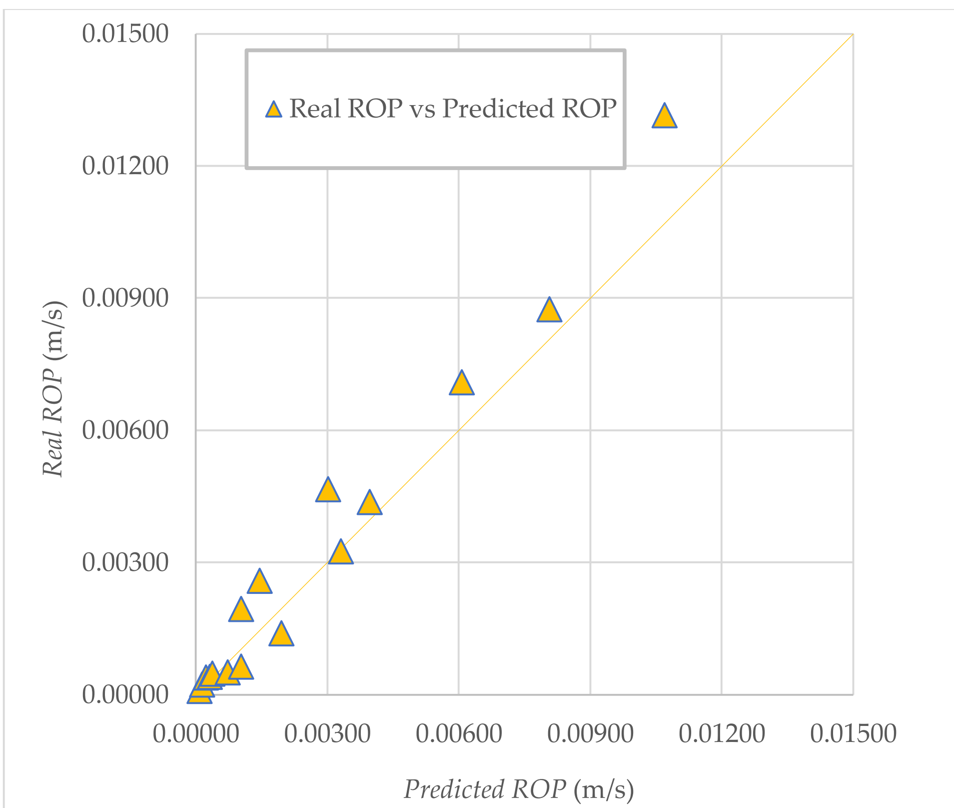

Figure 7.2 Correlation between real and predicted ROP for Szydłowiec-Śmiłów sandstone.

The findings displayed in Table 7.1, along with Figures 7.1 and 7.2, offer a clear evaluation of the ROP model's performance for Szydłowiec-Śmiłów sandstone. The comparison between measured and predicted ROP values across 16 drilling tests shows strong agreement, both numerically and visually. The model achieves a high coefficient of determination (R^2 = 0.98), indicating that it explains 98% of the variation observed in the measured data. Additionally, the *MAPE* of 28% and the RMSE of 0.0009 m/s demonstrate that the model maintains reasonable accuracy across a range of drilling conditions. It is noteworthy that a *MAPE* of 28% is considered moderately accurate in many engineering applications, especially when dealing with complex, variable systems like rock drilling.

Figure 7.1 illustrates how closely the predicted ROP values align with the pattern observed in the measured values for each test. The alignment confirms that the model effectively captures the dynamic behavior of ROP in response to changing input parameters. Figure 7.2 further reinforces this finding, as the data points are tightly clustered around the line of perfect correlation, showing minimal deviation and no systematic over- or underestimation.

In summary, the results confirm that the ROP model developed in Eq. (6.16) is highly effective for predicting penetration rate in Szydłowiec-Śmiłów sandstone formation. Its strong predictive performance, supported by both statistical metrics and graphical comparison, suggests that the model is suitable for application in predicting ROP values.

7.2.2. ROP Model validation for Wola Komborska sandstone

Table 7.2 displays the measured and predicted ROP values for Wola Komborska sandstone, along with the associated evaluation metrics: R^2, *MAPE*, and *RMSE*. To support the numerical results, Figure 7.3 illustrates the comparison between measured and predicted ROP across all 16 drilling tests. Furthermore, Figure 7.4 presents a scatter plot highlighting the correlation between real and predicted ROP values for Wola Komborska sandstone.

Table 7.2 Real and predicted ROP values with evaluation metrics for Wola Komborska rock.

Test number	Real *ROP* (m/s)	Predicted *ROP* (m/s)	R^2	*MAPE*	*RMSE*
1	0.00001	0.00001	0.88	38%	0.0002
2	0.00003	0.00003			
3	0.00005	0.00004			
4	0.00006	0.00005			
5	0.00007	0.00006			
6	0.00013	0.00013			
7	0.00033	0.00012			
8	0.00050	0.00024			
9	0.00008	0.00017			
10	0.00019	0.00032			
11	0.00041	0.00053			
12	0.00077	0.00067			
13	0.00027	0.00047			
14	0.00051	0.00090			
15	0.00092	0.00142			
16	0.00169	0.00184			

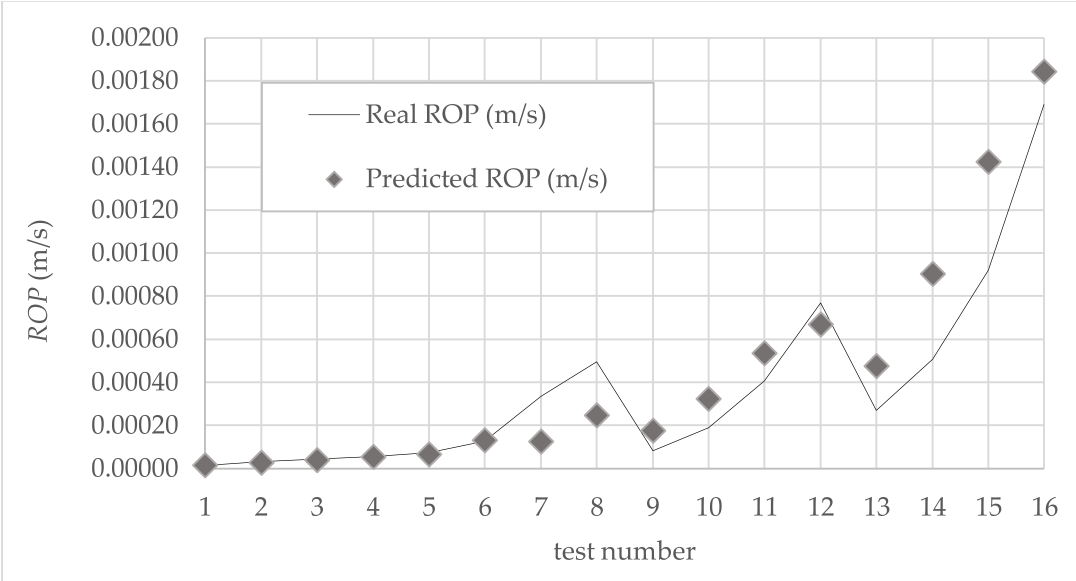

Figure 7.3 Real vs. predicted ROP across 16 laboratory tests for Wola Komborska sandstone.

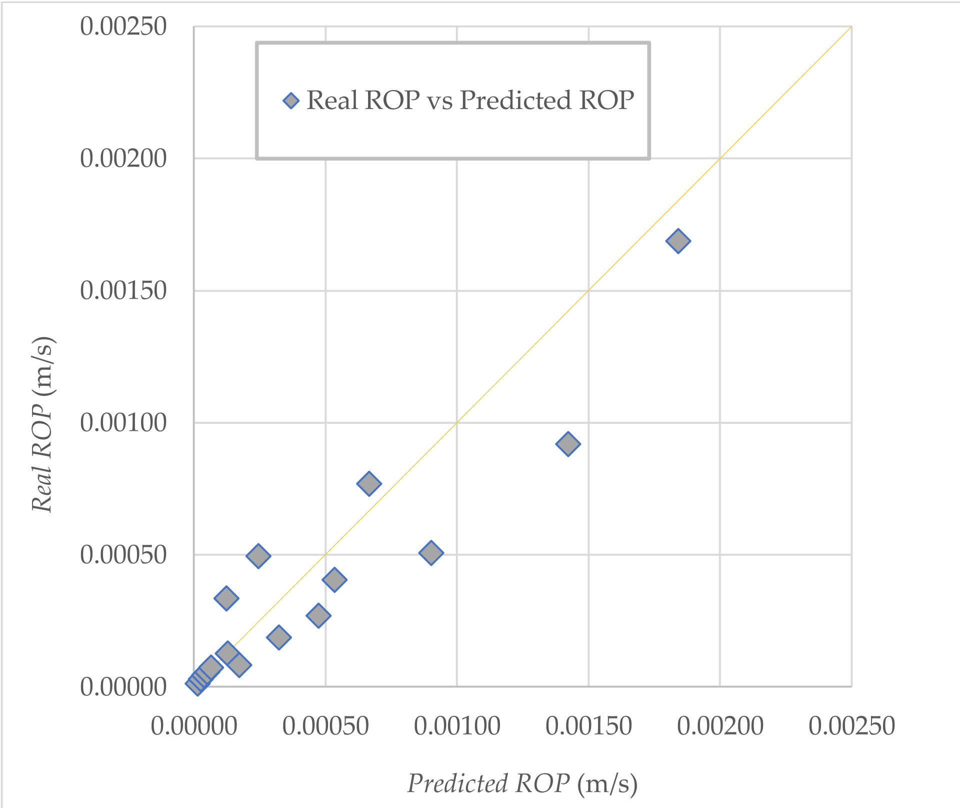

Figure 7.4 Correlation between real and predicted ROP for Wola Komborska sandstone.

The model validation for Wola Komborska sandstone, as shown in Table 7.2 and Figures 7.3 and 7.4, provides further insight into the performance of the developed ROP formulation. The value of R^2 which is 0.88 demonstrates a relatively marked correlation between measured and predicted ROP data, though not as high as the $R^2 = 0.98$ observed for Szydłowiec-Śmiłów sandstone. This reduction suggests that the model captures the general drilling behavior of Wola Komborska sandstone, but with slightly less accuracy, possibly due to increased internal variability or less uniform mineralogical structure.

The *MAPE* of 38% also exceeds the 28% reported for Szydłowiec-Śmiłów sandstone, indicating a higher average deviation in the results. This is reflected visually in Figure 7.3, where the predicted ROP values are consistent with the overall trend of the measured values but with more noticeable fluctuations. Particularly in mid-range test cases, some over- and underestimations are evident. Nevertheless, the *RMSE* of 0.0002 m/s remains low, confirming that the absolute errors are still small in magnitude.

Figure 7.4 presents the correlation between predicted and real ROP values for Wola Komborska sandstone. Despite the data points being mostly distributed along the line of perfect prediction, the spread is wider compared to Szydłowiec-Śmiłów sandstone (Figure 7.2), reinforcing the interpretation that Wola Komborska sandstone's behavior introduces slightly more uncertainty into the model's outputs.

In summary, the ROP model performs well for Wola Komborska sandstone but with reduced precision compared to its performance on Szydłowiec-Śmiłów sandstone. These findings emphasize the importance of accounting for lithological variability, and suggest that additional geological parameters or localized adjustments may improve model accuracy for more complex formations.

7.2.3. ROP Model validation for Tumlin sandstone

Table 7.3 presents the real and predicted ROP values for Tumlin sandstone, accompanied by key evaluation metrics including R^2, *MAPE*, and *RMSE*. To complement comparative analysis, Figure 7.5 provides a visual comparison of real versus predicted ROP across all 16 drilling tests for Tumlin sandstone. Additionally, Figure 7.6 shows a scatter plot that illustrates the correlation between the actual and predicted ROP values.

Table 7.3 Measured and predicted ROP values with evaluation metrics for Tumlin sandstone.

Test number	Real *ROP* (m/s)	Predicted *ROP* (m/s)	R^2	*MAPE*	*RMSE*
1	0.00001	0.00002	0.95	22%	0.0001
2	0.00005	0.00004			
3	0.00008	0.00006			
4	0.00011	0.00009			
5	0.00008	0.00007			
6	0.00020	0.00016			
7	0.00023	0.00016			
8	0.00035	0.00029			
9	0.00012	0.00020			
10	0.00026	0.00034			
11	0.00035	0.00030			
12	0.00050	0.00042			
13	0.00034	0.00032			
14	0.00046	0.00049			
15	0.00075	0.00088			
16	0.00087	0.00086			

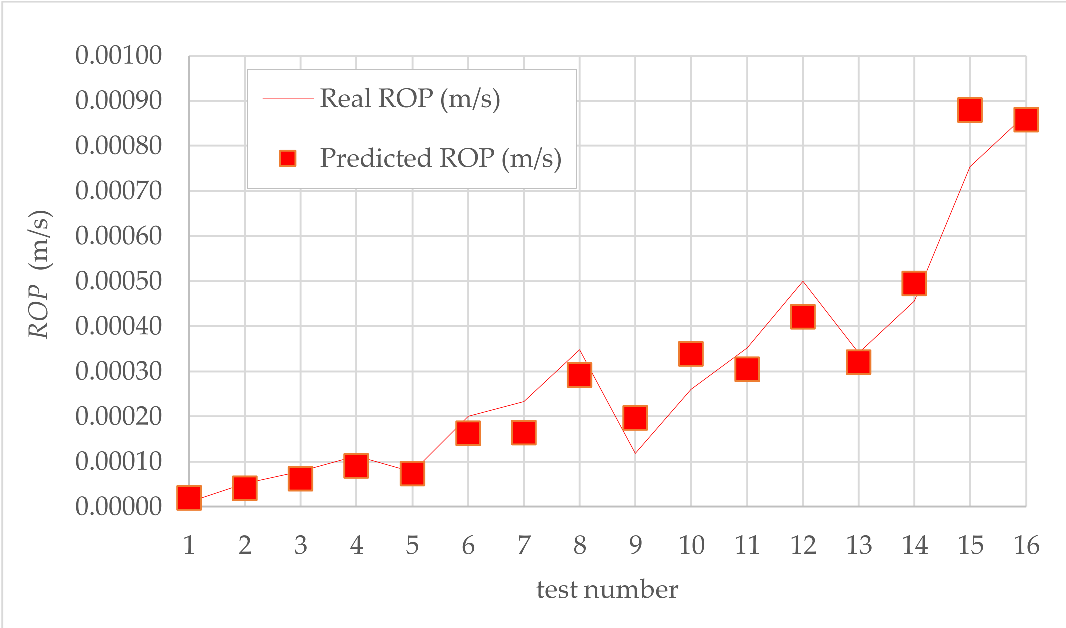

Figure 7.5 Real vs. predicted ROP across 16 laboratory tests for Tumlin sandstone.

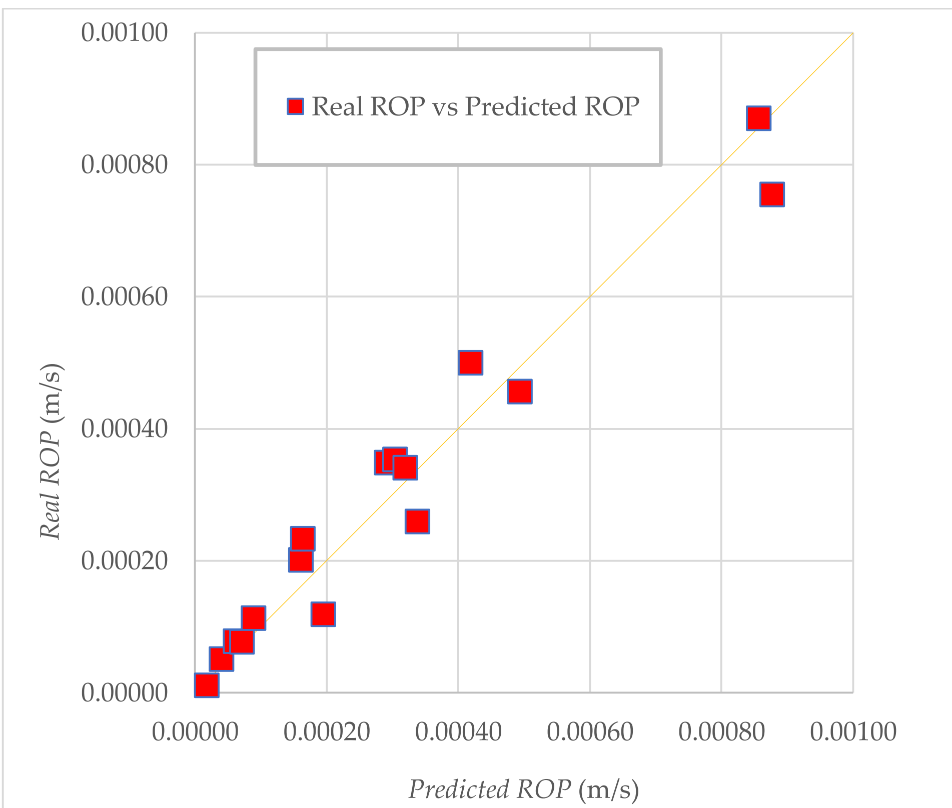

Figure 7.6 Correlation between real and predicted ROP for Tumlin sandstone.

The validation results for Tumlin sandstone, as presented in Table 7.3 and Figures 7.5 and 7.6, indicate that the ROP model performs well for this rock type, with an R^2 of 0.95. This high value reflects a significant connection between the measured and predicted ROP values and confirms that the model effectively captures the drilling behavior of Tumlin sandstone. The *MAPE* of 22% suggests a relatively low average deviation, indicating that the predictions are accurate and consistent across the test range. Furthermore, the *RMSE* of 0.0001 m/s highlights that the absolute differences between measured and predicted values remain small.

Figure 7.5 illustrates the conformity of the predicted ROP values with the measured ones over the 16 drilling tests. The model successfully replicates the increasing trend of ROP, with only minor under- or overestimations in a few tests. The scatter plot in Figure 7.6 further supports this finding, showing that the majority of the data points are positioned near the line of perfect agreement, reinforcing the model's precision for Tumlin sandstone.

When compared to the previous cases, Tumlin sandstone yields slightly better performance than Wola Komborska sandstone (which had an R^2 of 0.88 and *MAPE* of 38%), and is closer in accuracy to Szydłowiec-Śmiłów sandstone (which achieved R^2 = 0.98 and *MAPE* = 28%). It can be inferred that the model generalizes effectively across diverse rock types and achieves superior results in specific formations, notably the Tumlin sandstone.

In conclusion, the findings validate the applicability and robustness of the developed ROP formulation for Tumlin sandstone. The combination of high correlation, low prediction error, and strong trend alignment confirms that the model is reliable and robust for this rock type under laboratory drilling conditions.

7.2.4. ROP Model validation for Morawica marble

Table 7.4 presents the real and predicted ROP values for Morawica marble, accompanied by key evaluation metrics including R^2, *MAPE*, and *RMSE*. To complement comparative analysis, Figure 7.7 provides a visual comparison of real versus predicted ROP across all 16 drilling tests for Morawica marble. Additionally, Figure 7.7 shows a scatter plot that illustrates the correlation between the actual and predicted ROP values.

Table 7.4 Measured and predicted ROP values with evaluation metrics for Morawica marble.

Test number	Real *ROP* (m/s)	Predicted *ROP* (m/s)	R^2	*MAPE*	*RMSE*
1	0.00001	0.00001	0.96	25%	0.00004
2	0.00001	0.00001			
3	0.00001	0.00001			
4	0.00001	0.00002			
5	0.00004	0.00003			
6	0.00008	0.00005			
7	0.00011	0.00006			
8	0.00012	0.00008			
9	0.00006	0.00012			
10	0.00021	0.00019			
11	0.00023	0.00020			
12	0.00025	0.00025			
13	0.00017	0.00026			
14	0.00032	0.00040			
15	0.00050	0.00052			
16	0.00056	0.00057			

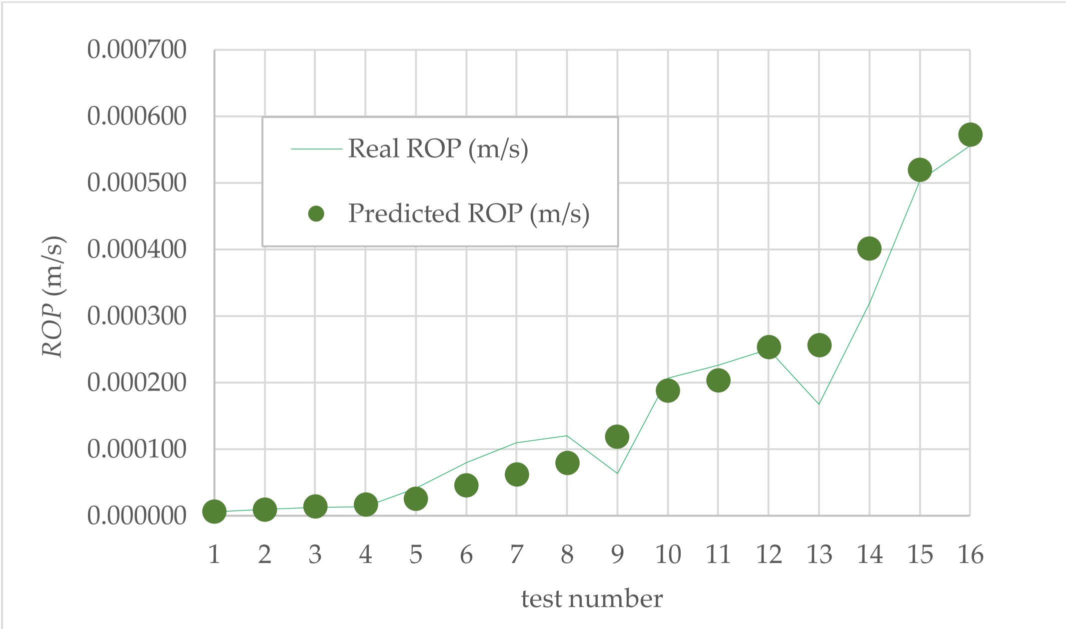

Figure 7.7 Real vs. predicted ROP across 16 laboratory tests for Morawica marble.

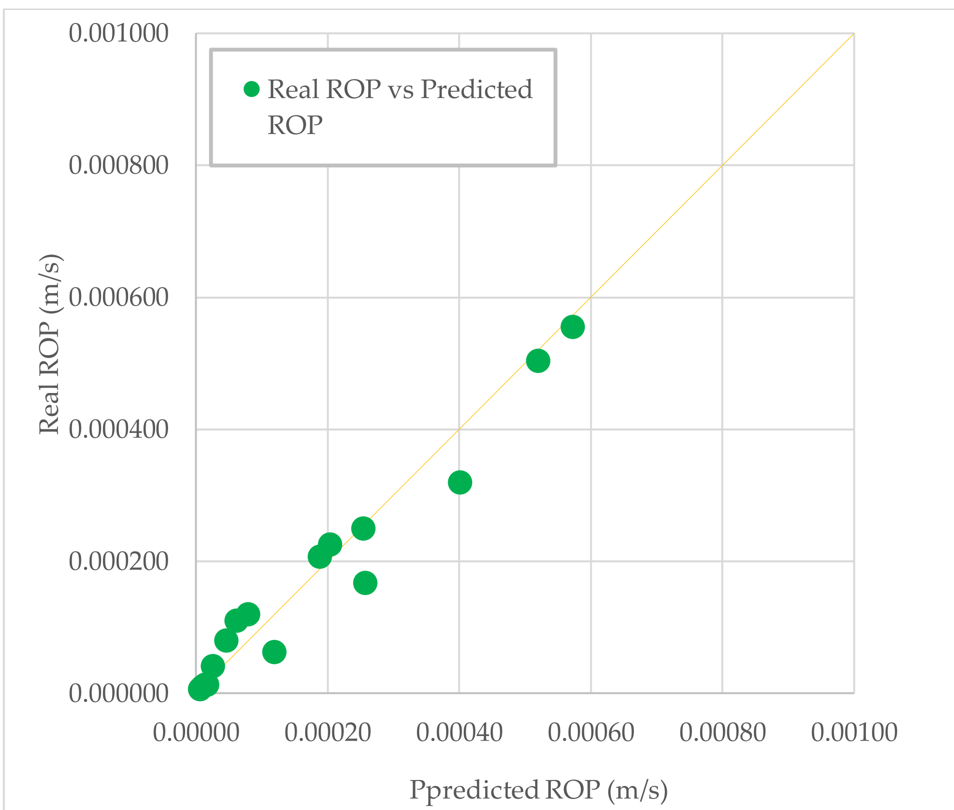

Figure 7.8 Correlation between real and predicted ROP for Morawica marble.

According to Table 7.4, and Figures 7.7 and 7.8, the developed ROP model exhibited a strong predictive performance for Morawica marble. The model achieved a coefficient of determination (R^2=0.96), indicating excellent agreement between the real and predicted ROP values. The *MAPE* of 25% and *RMSE* of 0.00004 m/s further confirm the model's accuracy for this rock type, particularly given the very low magnitude of ROP values observed in the tests.

Furthermore, Figure 7.7 shows that the predicted ROP values closely follow the real measurements across all 16 drilling tests. Despite the extremely small values involved, the model successfully replicated the trend and captured the progressive increase in ROP as drilling parameters varied. Figure 7.8 also reinforces this outcome, as the scatter plot reveals a tight clustering of data points around the line of perfect prediction, reflecting minimal dispersion and systematic error.

When compared with previous rocks, the model's performance for Morawica marble is very competitive. Although Szydłowiec-Śmiłów sandstone showed the highest overall accuracy (R^2 = 0.98, *MAPE* = 28%), Morawica marble follows closely with R^2 = 0.96 and a lower *MAPE* of 25%, suggesting slightly better relative accuracy. It also outperforms Wola Komborska sandstone (R^2 = 0.88, *MAPE* = 38%) and is on par with or slightly better than Tumlin sandstone (R^2 = 0.95, *MAPE* = 22%), particularly in handling low ROP values with precision.

In conclusion, the results confirm that the developed ROP model is highly effective for Morawica marble. Its ability to deliver reliable results in cases of low-penetration-rate conditions highlights its robustness and adaptability across a range of lithological environments tested under laboratory conditions.

7.2.5. Comparison of ROP Model efficiency for individual Rock types

Figure 7.9 shows the predicted and experimental ROP values for each individual rock type. Note that this figure is a combination of Figures 7.1, 7.3, 7.5, and 7.7. This combined plot allows for a direct visual comparison of model performance across all four rock types. It is evident that the model consistently tracks the trend of the real ROP values for each rock, though the degree of accuracy varies depending on lithological characteristics. The plot highlights the model's adaptability and its capacity to maintain reasonable accuracy across different formations. Overall, Figure 7.9 reinforces the reliability of the ROP formulation developed in Eq. (6.16), validating its general applicability for a wide range of rock types encountered in controlled laboratory drilling conditions.

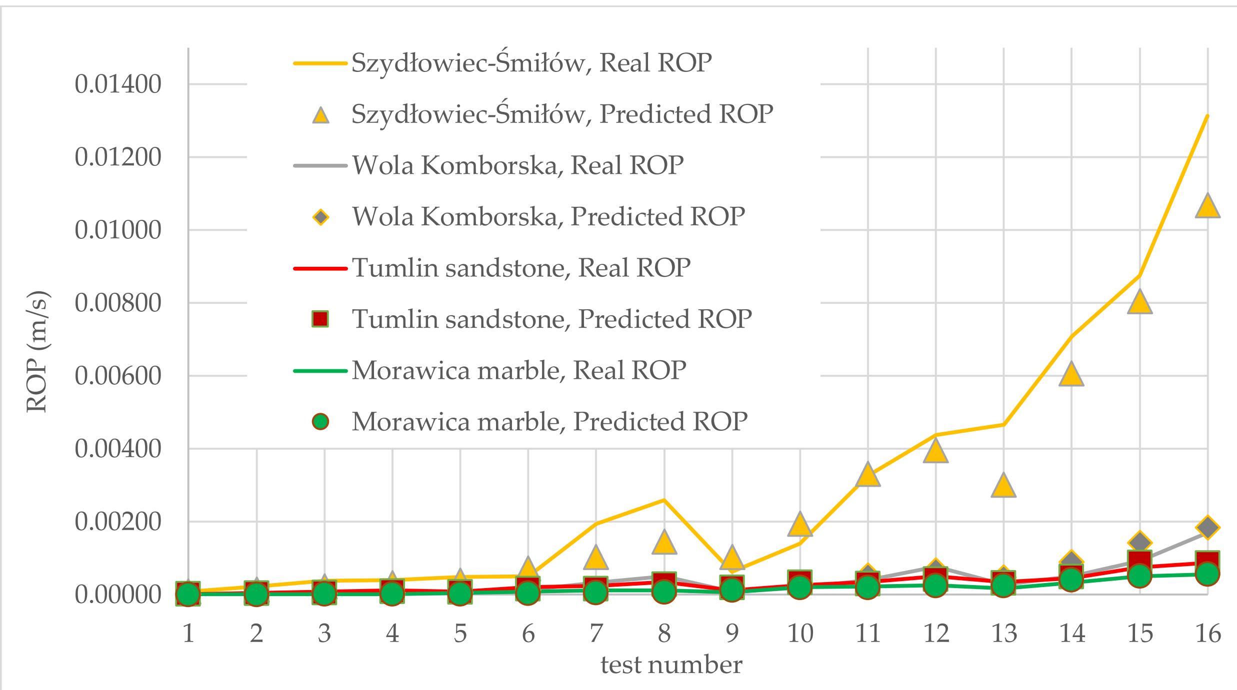

Figure 7.9 Comparison of measured and predicted ROP values across all Rock types.

Figure 7.9 also highlights that among the four rocks tested, Szydłowiec–Śmiłów sandstone exhibited relatively high ROP values, indicating that this formation is more drillable under the given conditions. Wola Komborska sandstone showed more variability in ROP and slightly lower overall values, likely due to its internal heterogeneity. Tumlin sandstone presented a consistent trend with moderately high ROP values, reflecting uniform but resistant properties. In contrast, Marble recorded the lowest ROP values, confirming its compact and crystalline structure, which naturally resists penetration. These differences align with expectations based on lithological characteristics and demonstrate the model's robustness across formations with varying mechanical behavior. The consistency in computation accuracy across this diverse dataset reinforces the generalizability of the ROP model and its suitability for analyzing a wide range of sedimentary and metamorphic rocks.

7.2.6. ROP Model validation for all Rock types

To comprehensively assess the performance of the developed ROP model across various rock types, the real and predicted values compiled in Tables 7.1 through 7.4 were aggregated into a single dataset. This consolidated approach enabled the calculation of overall performance metrics. An R^2 value of 0.98 reflects the high accuracy attained by the model, indicating a strong linear relationship between the predicted and real values of ROP. The *MAPE* was determined to be 28%, which reflects a reasonably low level of relative error, and the *RMSE* was found to be 0.00046, suggesting a minimal average deviation between predicted and real values.

Figure 7.10 provides a direct visual comparison between the real and predicted ROP values for all 64 coring tests. The figure evidently illustrates how the predicted values closely follow the actual measurements, offering a qualitative validation of the model's effectiveness across diverse drilling scenarios.

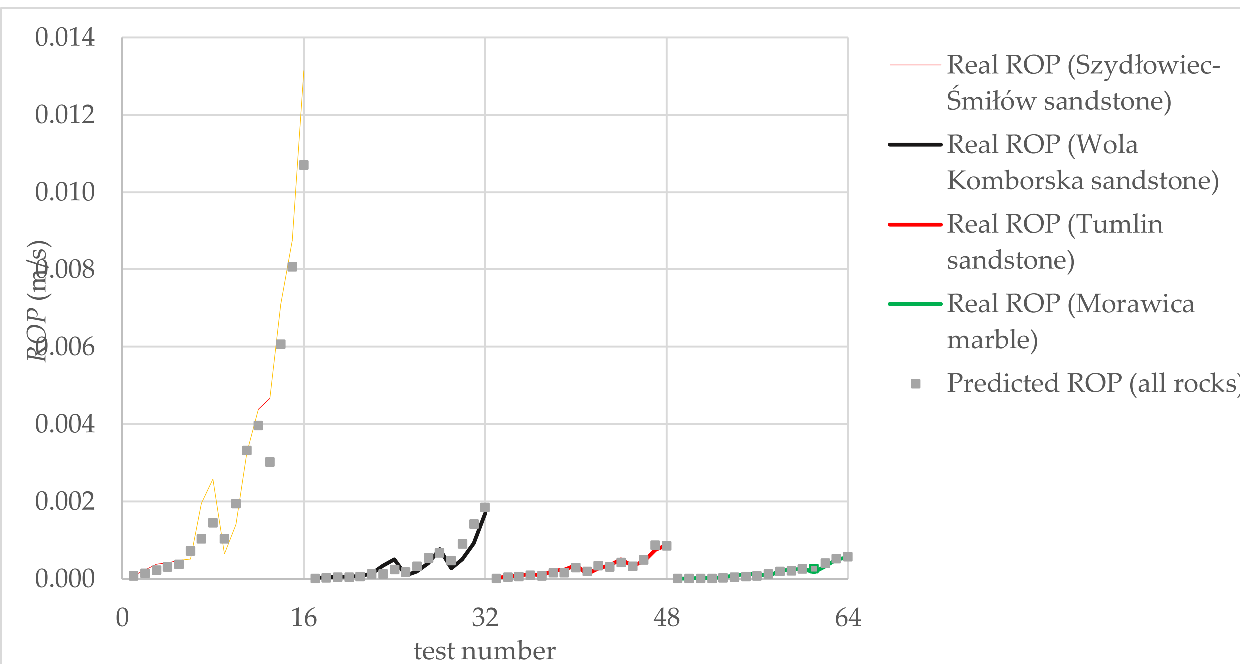

Figure 7.10 Real vs. predicted ROP values across all 64 drilling tests.

In addition, Figure 7.11 presents a scatter plot that illustrates the correlation between actual and predicted ROP values. This visualization demonstrates the strength of the model's predictive capabilities, as data points closely aligning along the diagonal line would suggest a high level of agreement between predicted and actual results. Together, these figures visually reinforce the robustness and reliability of the model across different rock types tested.

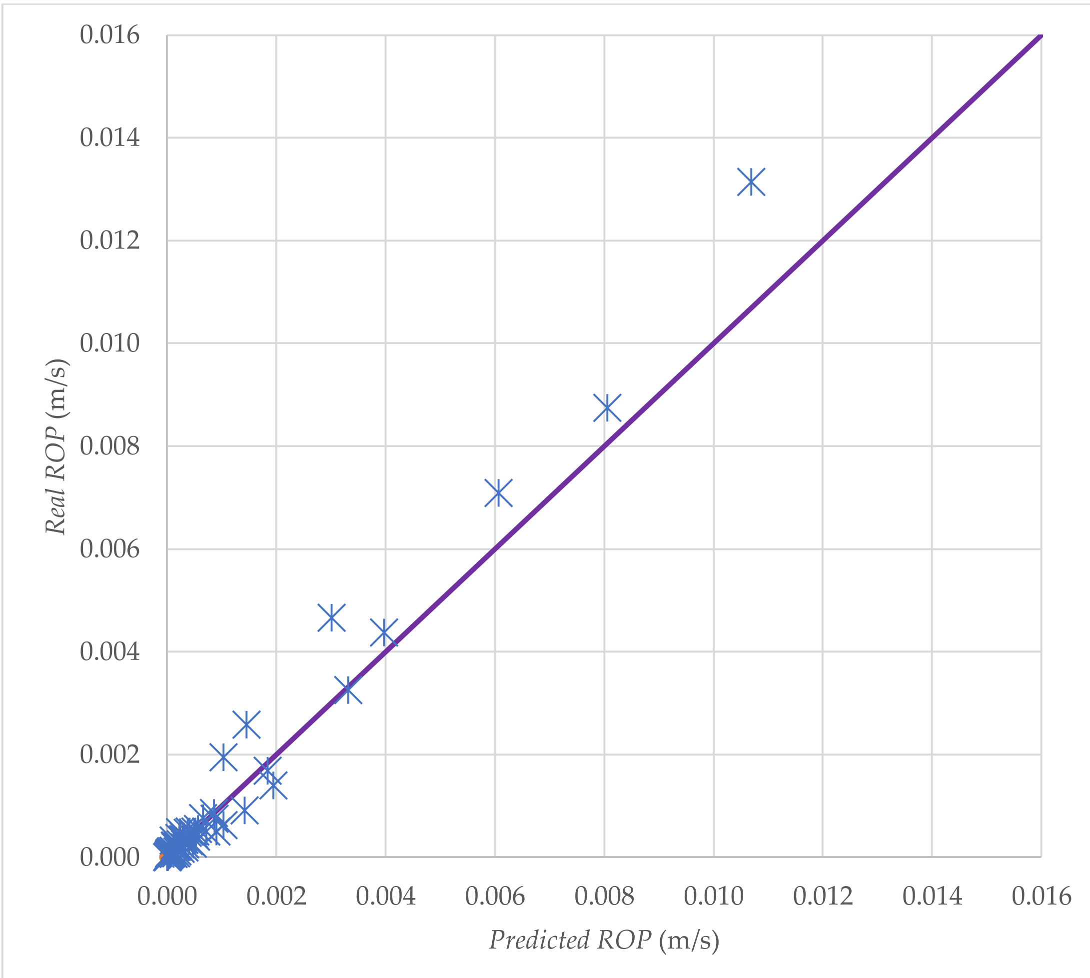

Figure 7.11 Correlation between real and predicted ROP for all rock types.

7.3. MSE Model Validation

To assess the reliability and accuracy of the derived MSE model presented in Eq. (6.28), a comprehensive validation process was carried out. This involved calculating the predicted MSE values for various coring tests using the input parameters specified in Eq. (6.28). The predicted values were then systematically compared with the corresponding actual MSE values listed in Table 6.1.

The validation was performed in two stages: first, individually for each rock type to evaluate the model's ability to capture lithology-specific behavior; and second, collectively across all rock samples to assess its overall performance and generalizability. This two-level validation framework provides a robust evaluation, demonstrating both the model's effectiveness in distinct lithologies and its broader applicability across diverse rock formations.

7.3.1. MSE Model validation for Szydłowiec-Śmiłów sandstone

The performance of the MSE model for Szydłowiec-Śmiłów sandstone was evaluated through a detailed comparison between the real and predicted MSE values across 16 coring tests. Table 7.5 summarizes these results, listing both the real and predicted MSE values alongside key performance metrics including R^2, *RMSE*, and *MAPE*. The R^2 value of 0.94 indicates a strong correlation between the estimated and real data, thereby corroborating the model's robustness and accuracy. The *MAPE* value of 35% reflects moderate error, while an *RMSE* of 837 MPa suggests some deviations in individual predictions, particularly in cases with large MSE values.

Table 7.5 Real and predicted MSE values with evaluation metrics for Szydłowiec-Śmiłów rock.

Test number	Real *MSE* (MPa)	Predicted *MSE* (MPa)	R^2	*MAPE*	*RMSE*
1	12360	12330	0.94	35%	837
2	4567	6974			
3	2724	4568			
4	2567	3289			
5	2168	2710			
6	2070	1428			
7	533	997			
8	401	712			
9	1639	1002			
10	741	530			
11	319	313			
12	237	261			
13	222	343			
14	146	171			
15	118	129			
16	79	97			

Figure 7.12 also provides a visual comparison of the real and predicted MSE values across all 16 tests. This figure helps illustrate how closely the model's output aligns with the experimental data. The general trend shows reasonable agreement, though some variance is observed in certain tests, particularly where predicted values tend to overestimate MSE in lower ranges. To further support the validation, Figure 7.13 presents a scatter plot illustrating the correlation between real and predicted MSE values for Szydłowiec-Śmiłów sandstone. The clustering of data points near the diagonal line confirms a generally strong agreement, reinforcing the R^2 result from the tabulated metrics. However, a few points deviate from the ideal fit, suggesting areas where the model may benefit from refinement or adjustment to better accommodate specific rock behaviors. Together, these results indicate that the MSE model demonstrates good predictive performance for Szydłowiec-Śmiłów sandstone, though with some room for improvement in accurately capturing variations in lower MSE ranges.

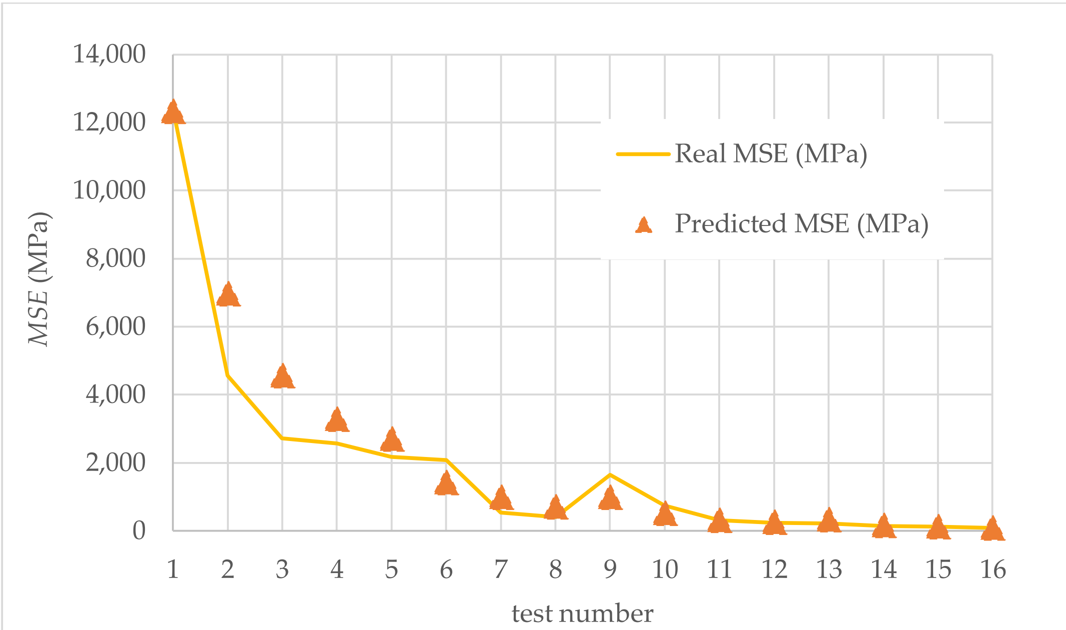

Figure 7.12 Real vs. predicted MSE across 16 coring tests for Szydłowiec-Śmiłów sandstone.

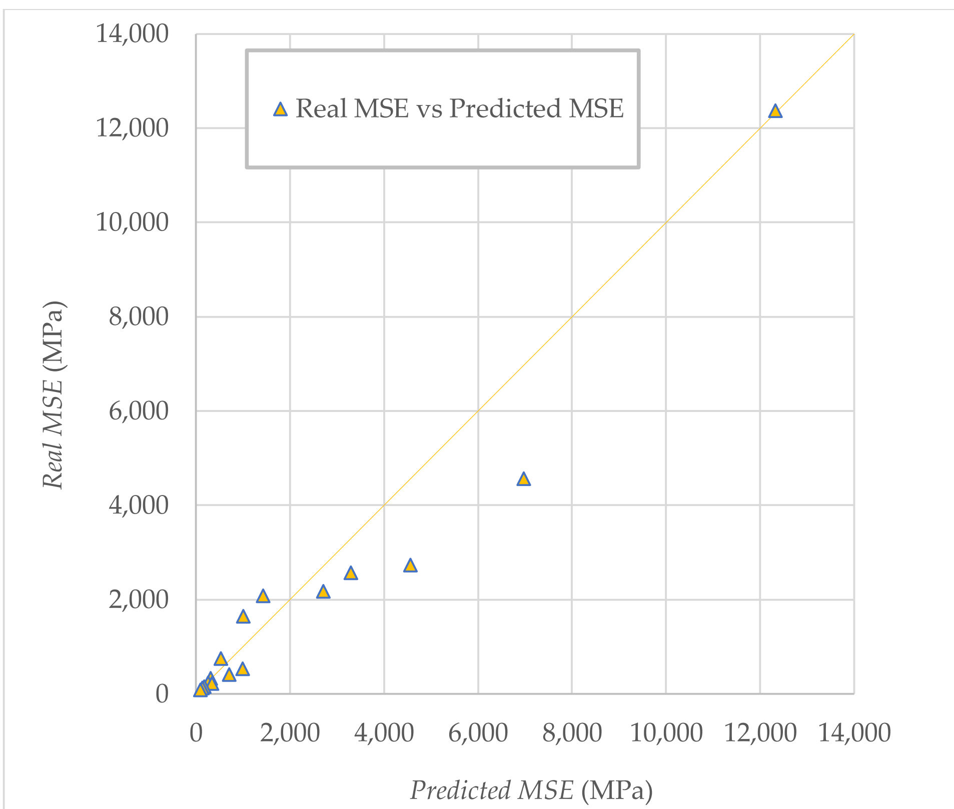

Figure 7.13 Correlation between real and predicted MSE for Szydłowiec-Śmiłów sandstone.

7.3.2. MSE Model validation for Wola Komborska sandstone

The MSE model was validated for Wola Komborska sandstone using data from 16 coring tests. Table 7.6 lists the real and predicted MSE values, along with the evaluation metrics: R^2, *MAPE*, and RMSE. The model achieved a high R^2 of 0.98, implying a strong correlation between real and predicted values. This suggests that the model performs well in capturing the energy demands associated with drilling through Wola Komborska sandstone. The *MAPE* was 38%, pointing to a moderate level of relative error in the results. Meanwhile, the *RMSE* was 4007 MPa, reflecting the average absolute deviation between predicted and real MSE values. The larger *RMSE* may be attributed to notable errors in tests involving extreme MSE values.

Table 7.6 Real and predicted MSE values with evaluation metrics for Wola Komborska rock.

Test number	Real *MSE* (MPa)	Predicted *MSE* (MPa)	R^2	*MAPE*	*RMSE*
1	66182	77264	0.98	38%	4007
2	33558	39138			
3	22983	26482			
4	18308	20128			
5	14049	16079			
6	8108	7982			
7	3092	8388			
8	2086	4232			
9	12390	5972			
10	5505	3212			
11	2552	1939			
12	1344	1554			
13	3849	2182			
14	2042	1146			
15	1125	728			
16	613	563			

Figure 7.14 provides a visual comparison of real versus predicted MSE across the 16 tests. The majority of the predicted values closely follow the real values, though noticeable discrepancies occur, particularly at lower MSE levels where the model tends

to overestimate. Furthermore, Figure 7.15 presents a scatter plot illustrating the relation between real and predicted MSE values. The majority of the data points align well with the ideal correlation line, reinforcing the high R^2 value. However, there are a few outliers. The results confirm that the model performs reliably for Wola Komborska sandstone, with strong predictive capability and consistent trends, though some refinements may enhance accuracy in low-MSE scenarios.

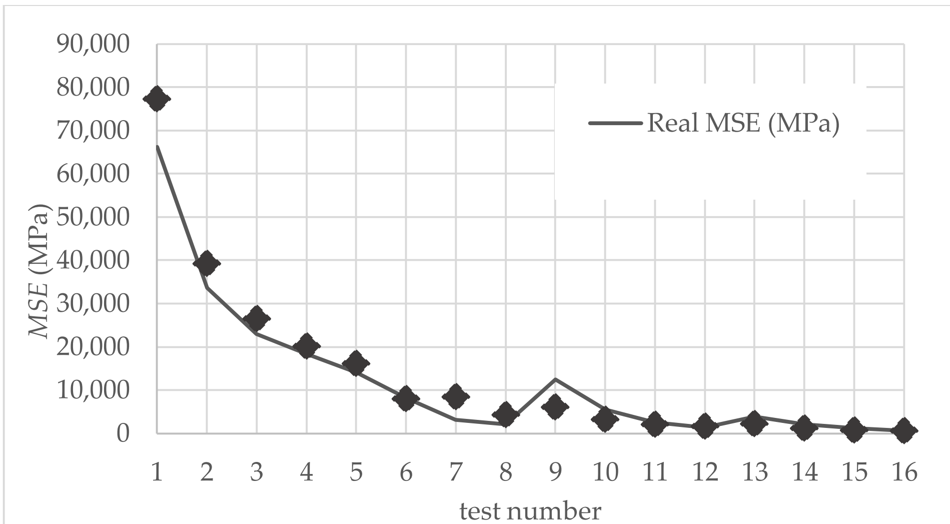

Figure 7.14 Real vs. predicted MSE across 16 coring tests for Wola Komborska sandstone.

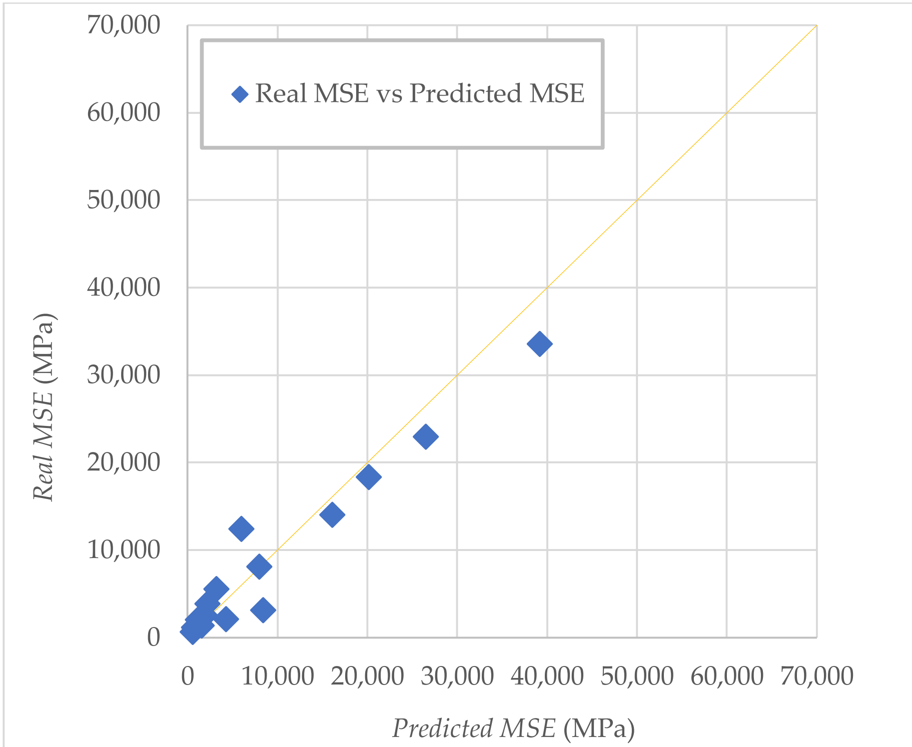

Figure 7.15 Correlation between real and predicted MSE for Wola Komborska sandstone.

7.3.3. MSE Model validation for Tumlin sandstone

Table 7.7 summarizes the real and predicted MSE values along with the associated evaluation metric for Tumlin sandstone. The model obtained an R^2 of 0.93, implying a strong correlation between real and predicted MSE values, confirming that this model is generally capable of capturing the energy behavior associated with drilling through Tumlin sandstone. Additionally, the *MAPE* was 21%, suggesting relatively low average percentage error in the results. More than this, the *RMSE* was 9858 MPa, which reflects the average magnitude of the prediction error. The higher *RMSE*, particularly when compared to Szydłowiec-Śmiłów and Wola Komborska sandstones, can be partially attributed to substantial structural non-homogeneity of Tumlin sandstone.

Table 7.7 Measured and predicted MSE values with evaluation metrics for Tumlin sandstone.

Test number	Real *MSE* (MPa)	Predicted *MSE* (MPa)	R^2	*MAPE*	*RMSE*
1	95081	56454	0.93	21%	9858
2	20262	25365			
3	13269	16743			
4	9166	11523			
5	13495	14333			
6	5155	6406			
7	4451	6317			
8	2971	3554			
9	8725	5285			
10	3990	3062			
11	2933	3398			
12	2070	2466			
13	3039	3232			
14	2269	2094			
15	1372	1179			
16	1190	1208			

Figure 7.16 shows the comparison of real versus predicted MSE values across all 16 tests for Tumlin sandstone. While the overall trend indicates fair alignment, some underestimations are evident in several high MSE cases, particularly for test 1. Despite this, the predicted values generally follow the shape and scale of the real data. Moreover, Figure 7.17 presents a scatter plot of real against predicted MSE values. Most observations fall near the ideal line, supporting the validity and accuracy of the model.

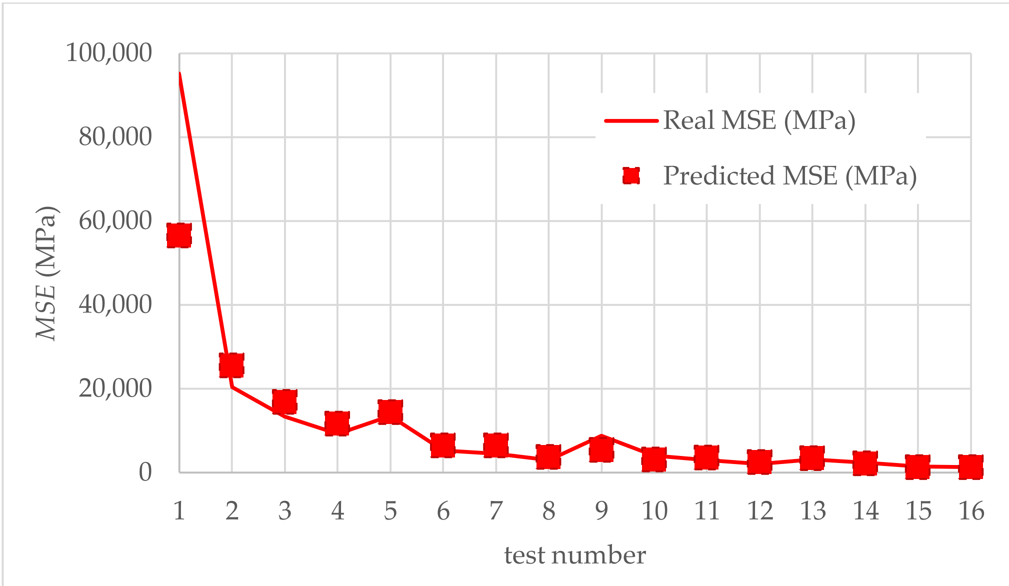

Figure 7.16 Real vs. predicted MSE across 16 coring tests for Tumlin sandstone.

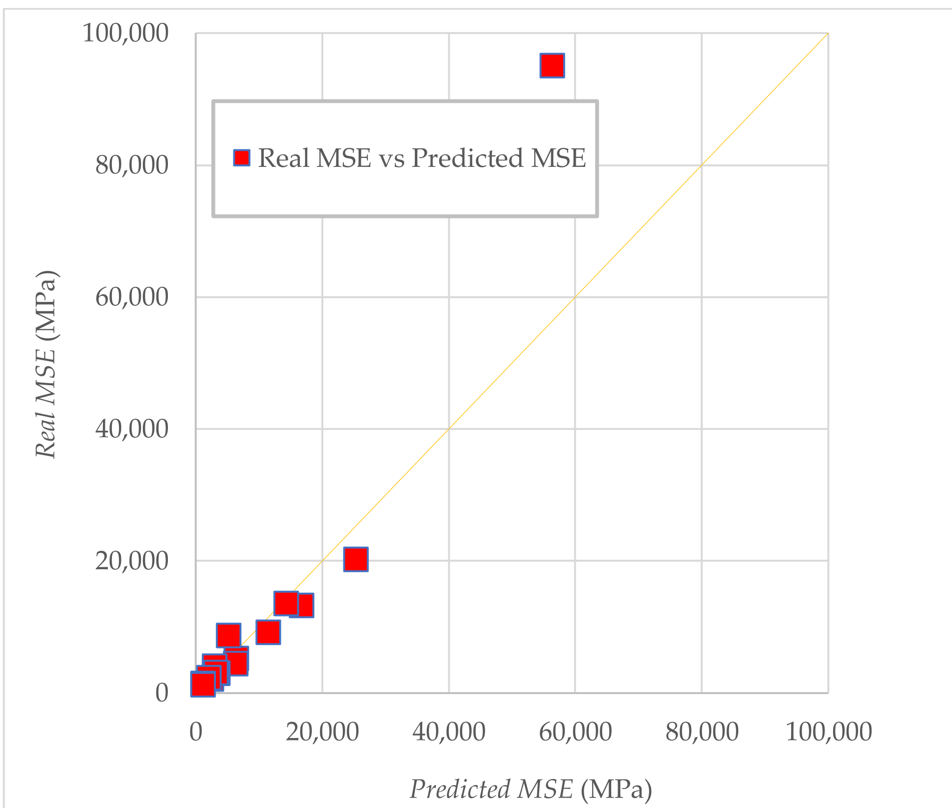

Figure 7.17 Correlation between real and predicted MSE for Tumlin sandstone.

7.3.4. MSE Model validation for Morawica marble

Table 7.8 presents both the actual and predicted MSE values, along with the corresponding evaluation metrics for Morawica marble. The model exhibited strong predictive performance, with an R^2 value of 0.98, highlighting a high degree of correlation between the measured and estimated results. This suggests that the model effectively captures the drilling energy characteristics of Morawica marble. The *MAPE*, recorded at 27%, indicates a reasonably low average percentage error, while the *RMSE* of 7044 MPa reflects the overall accuracy of the model's estimates.

Table 7.8 Measured and predicted MSE values with evaluation metrics for Morawica marble.

Test number	Real *MSE* (MPa)	Predicted *MSE* (MPa)	R^2	*MAPE*	*RMSE*
1	160552	158980	0.98	27%	7044
2	100297	104655			
3	79420	73174			
4	77270	60967			
5	24844	40396			
6	12939	22333			
7	9395	16718			
8	8620	13076			
9	16345	8700			
10	4997	5507			
11	4575	5089			
12	4141	4076			
13	6167	4031			
14	3237	2577			
15	2052	1992			
16	1863	1808			

Figure 7.18 presents a comparison between the real and predicted MSE values across 16 coring tests for Morawica marble. The predicted values closely follow the overall trend and magnitude of the real measurements, indicating that the model can reasonably capture the material's mechanical response during drilling. This alignment suggests that the model effectively accounts for the input parameters influencing MSE under the conditions tested.

In addition, Figure 7.19 shows a scatter plot that contrasts the measured MSE with the predicted vales. The clustering of most data points near the ideal diagonal line demonstrates a strong correlation and confirms the model's general reliability. These results collectively suggest that the MSE model performs well for Morawica marble.

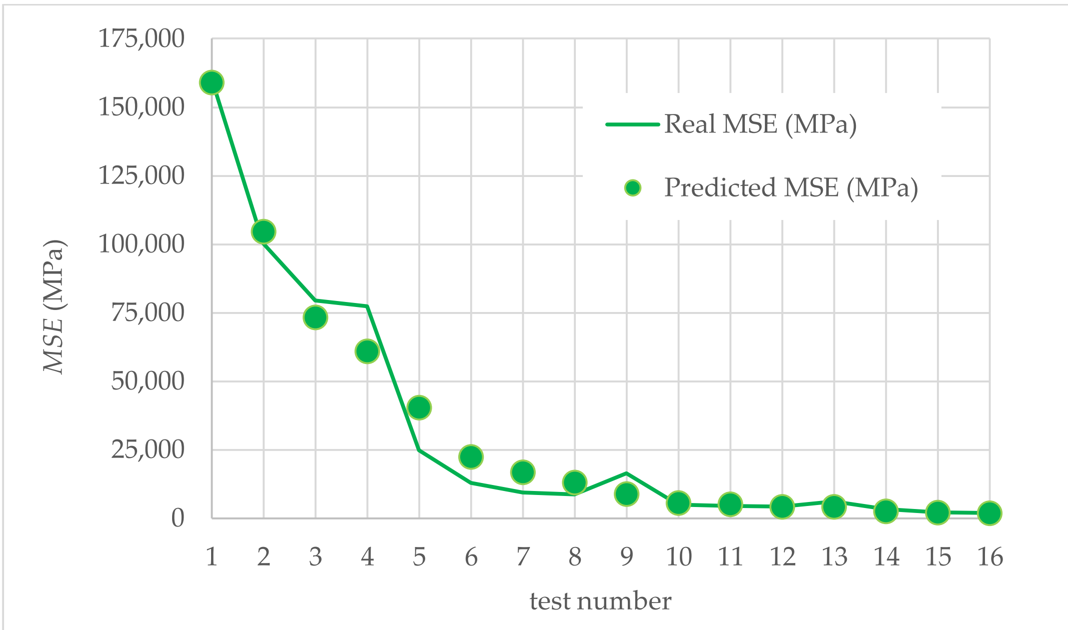

Figure 7.18 Real vs. predicted MSE across 16 coring tests for Morawica marble.

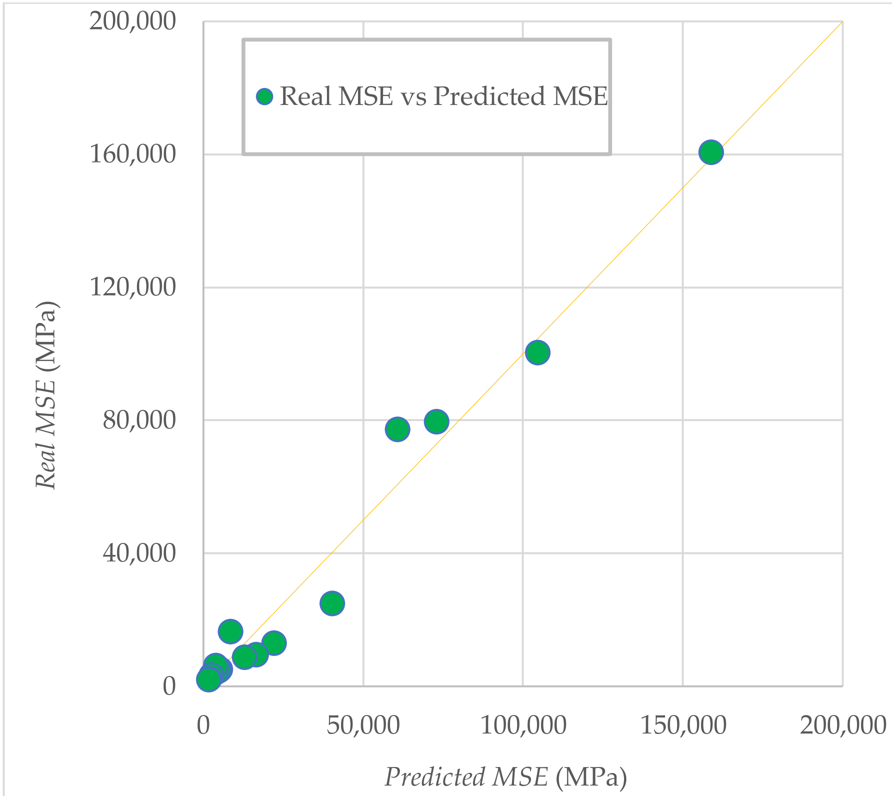

Figure 7.19 Correlation between real and predicted MSE for Morawica marble.

7.3.5. Comparison of MSE Model efficiency for individual Rock types

Figure 7.20 provides a comparative illustration of the real and predicted MSE values for all rock types studied, offering a clear assessment of the model's performance across different geological materials. Figure 7.20 demonstrates that the MSE model performs reliably across a diverse range of lithologies, capturing both the magnitude and trend of mechanical energy requirements. The figure validates the model's robustness to varying geological conditions encountered in drilling operations.

The figure also illustrates not only how well the model tracks the measured data but also highlights significant differences in MSE magnitude among the rock types. Among the rocks analyzed, Szydłowiec-Śmiłów exhibited the lowest MSE values, indicating that it requires the least mechanical energy for drilling. On the opposite, marble shows the highest MSE values. The MSE values for marble are significantly higher than those of the other rocks, especially in the initial tests conducted under lower RPM and WOB conditions. Comparing Wola Komborska sandstone and Tumlin sandstone, the MSE values of both rocks are similar under higher WOB and RPM values. Having said this, there are some discrepancies particularly related to initial tests conducted under lower RPM and WOB conditions.

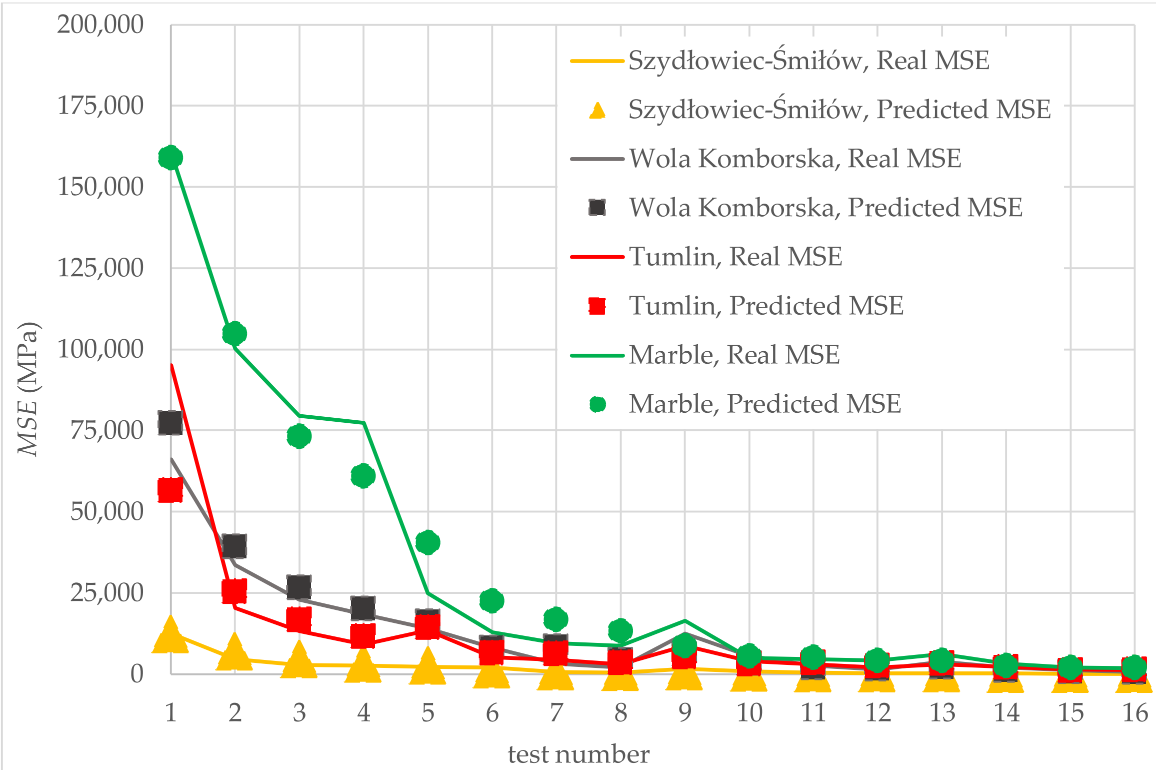

Figure 7.20 Comparison of measured and predicted MSE values across all Rock types.

7.3.6. MSE Model validation for all Rock types

To thoroughly evaluate the performance of the developed MSE model for various rock types, the actual and predicted values presented in Tables 7.5 through 7.8 were consolidated into a single dataset. This comprehensive dataset enabled the calculation of overall performance metrics.

The model exhibited high predictive accuracy, with $R^2 = 0.95$, indicating a significant linear correlation exists between the estimated and real MSE values. The *MAPE* was calculated to be 30%, reflecting a moderate level of relative error, while the *RMSE* was 6395, suggesting a relatively low deviation between predicted and actual values.

Figure 7.21 offers a visual representation contrasting actual and predicted MSE values for all 64 coring tests. The close alignment of the predicted data points with the actual measurements highlights the model's strong predictive performance and offers qualitative evidence of its reliability across diverse drilling conditions.

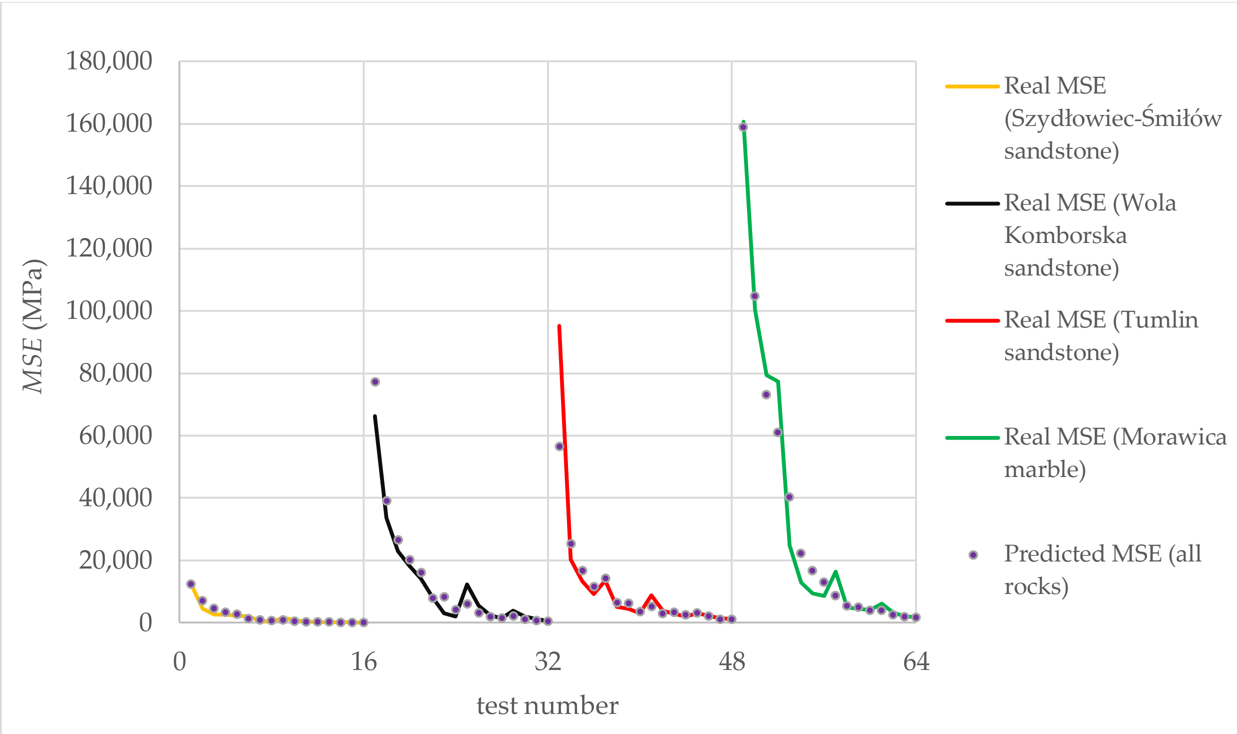

Figure 7.21 Real vs. predicted MSE values across all 64 coring tests.

Moreover, Figure 7.22 provides a scatter plot comparing real MSE values with those predicted by the model. The clustering of data points near the diagonal line indicates a strong agreement between the two sets of values, underscoring the model's robustness and consistency across different rock types.

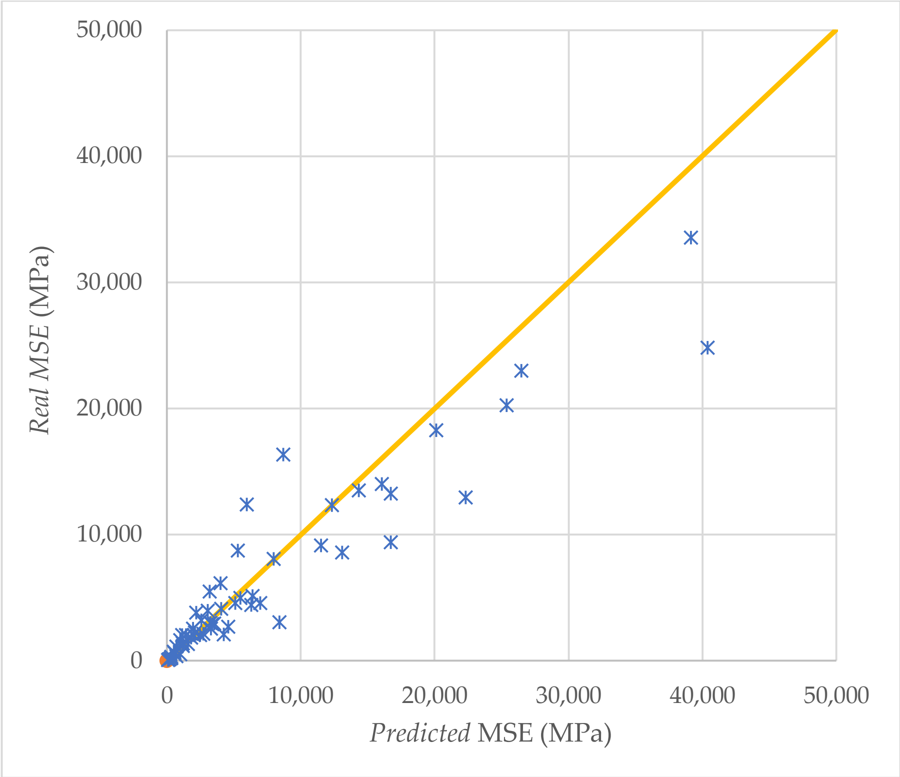

Figure 7.22 Correlation between real and predicted MSE for all rock types.

Chapter 8:

Conclusions

In this study, laboratory experiments were performed on four distinct Polish rock types to develop new empirical formulations for predicting ROP and MSE in coring drilling operations. Consequently, two novel ROP and MSE formulas, respectively presented in Eq. (6.16) and Eq. (6.28), were obtained. Those formulas incorporate operational parameters (WOB and RPM), rocks' properties (φ, ρ, and V_p), and core bit geometry (D, and λ), all of which can be easily measured at drilling sites.

By combining both adjustable parameters such as operational parameters and non-adjustable parameters (e.g. rocks' properties), the new ROP and MSE models provide a balanced approach with the purpose of real-time optimization of drilling. The inclusion of rock-dependent parameters in those new formulations marks a significant advancement, addressing a gap that existed in earlier models in the literature.

According to the results obtained, the major conclusions can be outlined as follows:

1. The strongest positive influence on ROP was observed from RPM, followed by WOB, as confirmed by Pearson correlation coefficients. Specifically, ROP showed a strong positive correlation of r=0.79 with RPM and a moderate positive correlation of r=0.45 with WOB, indicating that increases in rotation speed and weight on bit both significantly enhance core drilling penetration rates.
2. With increasing dynamic elastic moduli of the rocks, the bit penetration rate decreased. This finding reflected the inverse relationship between those parameters and ROP. Having said this, actual drill-ability appeared to be strongly influenced by rock type, and physical properties such as density and porosity.
3. Furthermore, rock's density exhibited an indirect relationship with ROP, and a direct relations with MSE. This confirms the previous investigations reports expressing that denser rocks are commonly harder to be drilled.
4. Amongst the four different rock types, Szydłowiec–Śmiłów sandstone showed the highest ROP values and the least MSE values as it possesses lower density and higher porosity than others. On the opposite side, Morawica marble exhibited the highest resistance to core drilling, with the lowest ROP and highest MSE among all tested formations.
5. As presented in Sections 7.2.6 and 7.3.6, defining a good set of criteria for development of new ROP and MSE formulations can guarantee the robustness and accuracy of the obtained models. Three main criteria including; simple practical measurement of input parameters, inclusion of minimum set of essential input parameters, and 'dimensional consistency of the developed formulas can be

regarded as the fundamental pillars for establishment of future ROP and MSE predictive models.

6. Using Pearson's correlation coefficient, six parameters including *WOB*, *RPM*, density, porosity, *Vp*, and bit diameter were selected for formulating ROP and MSE models. Together, they represent a comprehensive concise set of input parameters that capture both the operational and geological factors influencing drilling performance.
7. The new ROP model presented in Eq. (6.16) has a straightforward, easy-to-interpret, and dimensionally consistent formulation. The input parameters are commonly available, independent and non-redundant which avoids the models' complexity, and need for additional, unnecessary measurements.
8. Rock's porosity was shown to influence ROP nonlinearly, with an exponent value of approximately 1.7 obtained through dimensional analysis technique and log-log regression analysis approach. The use of porosity with this data-calibrated exponent enhances the model's sensitivity to lithological variability, allowing it to adapt to different rock types and formation conditions.
9. The developed MSE formulation possesses the advantages of the novel ROP model. It is dimensionally consistent, simple, and easy-to-compute. More particularly, it integrates operational parameters as well as the rock's parameters which turns it to a more reliable predictive model for estimating the energy needed to drill through different rocks.
10. The new ROP model achieved excellent fit to the laboratory data by yielding an R^2 of 0.98. Furthermore, the *MAPE* was determined as 28%, which reflected a reasonably low level of relative error. Additionally, the *RMSE* was found to be 0.00046, suggesting a minimal average deviation in the model results. Together, those findings corroborated the robustness and accuracy of the new ROP model.
11. The new MSE model also showed a strong agreement with the laboratory results (R^2=0.95). The *MAPE* was computed as 30%, indicating a moderate degree of slight error, while the *RMSE* was 6395, reflecting a nearly low deviation in the results. Those desirable statistical metrics confirmed the MSE model's accuracy and reliability.
12. The simplicity of the new ROP and MSE formulations, combined with their strong empirical backing, makes them practical for ROP and MSE computation in laboratory coring drilling operations.

Nomenclature

Symbol	Description	Unit
A	Cross-sectional area of the drill-bit	m^2
AFR	Actual mass rate of cuttings exiting the wellbore	kg/s
A_{bed}	Area of the cuttings bed accumulation at bottom-hole	m^2
A_{net}	Area of the non-hollow cross section of the coring bit	m^2
A_{well}	Cross-sectional area of wellbore	m^2
C_c	Constant for cuttings concentration	-
CCS	Confined compressive strength of rock	Pa
D	Bit diameter	m
$\acute{E}$	Energy consumed by the drilling machine	J
E	Young's modulus	Pa
ECD	Equivalent circulating density	kg/m^3
E_{dyn}	Dynamic Young's modulus	Pa
E_m	Drilling's mechanical efficiency	Pa
E_f	Drilling efficiency	-
E_S	Specific energy	Pa
F	Force on the bit	N
$\acute{F}$	Frictional force	N
F_{Jet}	Fluid motion force beneath the bit	N
F_{Jc}	Critical jet force	N
G	Shear modulus	Pa

G_{dyn}	Dynamic shear modulus	Pa
H	Formation hardness	Pa
HCE	Hole Cleaning Efficiency	-
HP	Hydraulic power	kW
IFR	Ideal mass rate of cuttings expected	kg/s
K	Bulk modulus	Pa
K'	Proportionality constant that incorporates the rock strength	Pa
K_{dyn}	Dynamic bulk modulus	Pa
M	Mass	kg
N	normal force	N
P	power of drilling machine	W
P_e	effective pressure for cutting removal	Pa
Q	flow rate	m^3/s
R	Determination coefficient	-
ROP	Rate of penetration	m/s
RPM	Rotary speed	m/s
RPM_c	Critical RPM	rev/s
S	Rock strength	Pa
SG	Specific gravity	N/m^3
T	Torque	N.m
TVD	True vertical depth	m
UCS	Unconfined compressive strength of rock	MPa

V	Total volume of rock sample	m^3
V_{Actual}	Actual volume of cuttings removal	m^3
$V_{drilled}$	The volume of rock removed through drilling (for all drilling bit types)	m^3
$V_{critical}$	Critical volume for cuttings removal	m^3
V_{net}	The removed net volume of the rock by coring bit	m^3
V_p	Compressional wave velocity	m/s
V_s	Share wave velocity	m/s
V_V	Volume of rock's pores	m^3
WOB	Weight on Bit	kg
WOB_b	Weight on the bit at the bottom-hole for inclined wellbores	kg
WOB_0	Threshold weight on the bit	kg
W_f	Bit wear function	-
$W_{percussion}$	Work done during percussion mechanism	J
$W_{rotation}$	Work done in rotary mechanism	J
W_{total}	Total work done by the drilling rig	J
X	Composite logarithmic term	-
X_i	Composite logarithmic term calculated for the *i*-th coring drilling test	-
a	Exponent of *WOB*	-
a'	First coefficient in Warren's ROP models	-
a_1	First Constant in Bourgoyne and Young's model and Osgouei's model	-
a_2	Second Constant in Bourgoyne and Young's model and Osgouei's model	-
a_3	Third Constant in Bourgoyne and Young's model and Osgouei's model	-

a_4	Forth Constant in Bourgoyne and Young's model and Osgouei's model	-
a_5	Fifth Constant in Bourgoyne and Young's model and Osgouei's model	-
a_6	Sixth Constant in Bourgoyne and Young's model and Osgouei's model	-
a_7	Seventh Constant in Bourgoyne and Young's model and Osgouei's model	-
a_8	Eighth Constant in Bourgoyne and Young's model and Osgouei's model	-
a_9	Ninth Constant in Osgouei's model	-
a_{10}	Tenth Constant in Osgouei's model	-
a_{11}	Eleventh Constant in Osgouei's model	-
b	Exponent for *RPM*	-
b'	Second coefficient in Warren's ROP models	-
b_5	Exponent in Bingham's ROP model	-
b_7	Exponent in Gale and Woods' ROP model	-
c	Exponent of porosity	-
c'	Third coefficient in Warren's ROP model	-
c_1	Constant determined by the specific geometric characteristics of drill bit	-
d	Exponent of bit diameter	-
d_{bd}	Bit earing's diameter	m
d_C	Depth of cut	m
e	Exponent of density	-
f	Exponent of P-wave velocity	-
f_c	Chip hold-down function	-
f_1	First factor in Bourgoyne and Young's model	-

f_2	Second factor in Bourgoyne and Young's model	-
f_3	Third factor in Bourgoyne and Young's model	-
f_4	Fourth factor in Bourgoyne and Young's model	-
f_5	Fifth factor in Bourgoyne and Young's model	-
f_6	Sixth factor in Bourgoyne and Young's model	1/s
f_7	Seventh factor in Bourgoyne and Young's model	-
f_8	Eighth factor in Bourgoyne and Young's model	-
f_1'	First factor in Osgouei's model	-
f_2'	Second factor in Osgouei's model	-
f_3'	Third factor in Osgouei's model	-
f_4'	Fourth factor in Osgouei's model	-
f_5'	Fifth factor in Osgouei's model	-
f_6'	Sixth factor in Osgouei's model	1/s
f_7'	Seventh factor in Osgouei's model	-
f_8'	Eighth factor in Osgouei's model	-
f_9'	Ninth factor in Osgouei's model	-
f_{10}'	Tenth factor in Osgouei's model	-
f_{11}'	Eleventh factor in Osgouei's model	-
g	Gravitational acceleration	m/s^2
g_p	Gradient of pore fluid pressure	MPa/m
h	Height of the drilled hole in the rock	m
h_f	Fractional bit tooth's dullness	m

i	Number (index) of the drilling test	-
k	Constant related to the ratio of bit's outer diameter to inner diameter	-
K''	Proportionality coefficient in Maurer's ROP model	-
$\dot{L}$	Dimension of length	-
$\dot{M}$	Dimension of mass	-
p	pressure	Pa
p_p	pore fluid pressure	Pa
r	Pearson's correlation coefficient	-
t	Time	s
$\dot{T}$	Dimension of time	s
x	Arbitrary variable	-
y	Arbitrary variable	-
$\bar{x}$	Means of variable x	-
$\bar{y}$	Means of variable y	-
x_i	Value of the x for the i-th data point	-
y_i	Value of the y for the i-th data point	-
β	Normal force per unit length on a two-dimensional cutter	N/m
γ	Specific weight of the rock	N/m³
γ'	Proportion between the inner and outer radius of coring bit	-
γ_b	Bottom-hole inclination constant	-
γ_f	Fluid specific gravity	N/m³
γ_w	Specific weight of the water	N/m³

ϵ	Strain	-
ϵ_{axial}	Strain in the axial direction	-
$\epsilon_{lateral}$	Strain in the lateral direction	-
ϵ_{xy}	Shear strain	-
ζ	Shear force per unit length on a two-dimensional cutter	N/m
λ	The ratio of outer diameter to inner diameter of the coring bit	-
μ	Drilling fluid's dynamic viscosity	Pa.s
μ_b	Friction coefficient of the bit	-
μ_s	Drill string sliding coefficient	-
v	Poisson's ratio of rock	-
v'	Mud's kinematic viscosity	m^2/s
v_{dyn}	Dynamic Poisson's ratio	-
ρ	Density of rock *density*	kg/m^3
ρ_f	Fluid density	kg/m^3
ρ_m	Mud density	kg/m^3
ρ_w	Density of water	kg/m^3
σ	Stress	Pa
σ_{axial}	Axial stress	Pa
τ_{xy}	Shear stress	Pa
φ	Rock's porosity	-
ω	Angular velocity	Rad/s

References:

1. Abdulmalek, A.S.; Salaheldin, E.; Abdulazeez, A.; Mohammed, M.; Abdulwahab, Z.A.; Mohamed, I.M. Prediction of rate of penetration of deep and tight formation using support vector machine. In Proceeding of the SPE Kingdom of Saudi Arabia Annual Technical Symposium and Exhibition, Dammam, Saudi Arabia, 23 April 2018. https://doi.org/10.2118/192316-MS
2. Abtahi, A. Bit wear analysis and optimization for vibration assisted rotary drilling (VARD) using impregnated diamond bits, Doctoral dissertation, Memorial University of Newfoundland, 2011.
3. Ahmed, O.; Adeniran, A.; Samsuri, A. Rate of penetration prediction utilizing hydromechanical specific energy. Drilling, 2018, 105-131. http://dx.doi.org/10.5772/intechopen.76903
4. Akin, S. and Karpuz, C. Estimating drilling parameters for diamond bit drilling operations using artificial neural networks. International Journal of Geomechanics, *8*(1), pp.68-73. 2008. https://doi.org/10.1061/(ASCE)1532-3641(2008)8:1(68)
5. Allawi, R.H.; Al-Mudhafar, W.J.; Abbas, M.A.; Wood, D.A. Leveraging Boosting Machine Learning for Drilling Rate of Penetration (ROP) Prediction Based on Drilling and Petrophysical Parameters. Artif. Intell. Geosci. 2025, 100121. https://doi.org/10.1016/j.aiig.2025.100121.
6. Almomen, H.; Mahmoud, A.A.; Elkatatny, S.; Abdulraheem, A. Predicting the Rate of Penetration while Horizontal Drilling through Unconventional Reservoirs Using Artificial Intelligence. ACS Omega 2024, 9, 49719–49727. https://doi.org/10.1021/acsomega.4c08006.
7. Al Hamlawi, I.T.; Creegan, A.; Baptista, L.R.; Azizuddin, K.M. MSE Based Drilling Optimizer Project for Large National Drilling Contractor. In Proceedings of the Day 3 Wed, November 17, 2021; SPE: Abu Dhabi, UAE, December 2021; http://dx.doi.org/10.2118/207736-MS
8. Al-Betairi, E.A.; Moussa. M.M.; Al-Otaibi, S. Multiple regression approach to optimize drilling operations in the Arabian Gulf area. SPE drilling engineering 1988 3(01), 83-88. https://doi.org/10.2118/13694-PA
9. Alum, M.A.; Egbon, F. Semi-analytical models on the effect of drilling fluid properties on rate of penetration (ROP). Procededing of the Nigeria Annual International Conference and Exhibition,Abuja, Nigeria, Julay 2011. https://doi.org/10.2118/150806-MS
10. Alwaar, A.; Futhiez, I.; Abugharara, A.; Zhang, Y.; Butt, S. Influence of Drilling Along Pilot Holes on Drilling Performance and Effective Rock Strength. Appl. Sci. 2025, 15, 32. https://doi.org/10.3390/app15010032
11. Amanullah, M.; Al-Arfaj, M.K.; Al-Abdullatif, Z. Preliminary Test Results of Nano-based Drilling Fluids for Oil and Gas Field Application, SPE/IADC Drilling Conference and Exhibition, Amsterdam, The Netherlands, March 2011. https://doi.org/10.2118/139534-MS
12. Amar, K.; Ibrahim, A. Rate of Penetration Prediction and Optimization Using Advances in Artificial Neural Networks, a Comparative Study: In Proceedings of the 4th International Joint Conference on Computational Intelligence; SciTePress - Science and Technology Publications: Barcelona, Spain, 2012; pp. 647–652.
13. Anemangely, M.; Ramezanzadeh, A.; Tokhmechi, B. Determination of constant coefficients of Bourgoyne and Young drilling rate model using a novel evolutionary algorithm. Journal of Mining and Environment, 2017, 8(4), 693-702. https://doi.org/10.22044/jme.2017.842
14. Anemangely, M.; Ramezanzadeh, A.; Tokhmechi, B.; Molaghab, A.; Mohammadian, A. Drilling rate prediction from petrophysical logs and mud logging data using an optimized multilayer perceptron neural network. Journal of Geophysics and Engineering. 2018, 1;15 (4):1146-59. https://doi.org/10.1088/1742-2140/aaac5d
15. Angelini, E.; Ludovici, A. CDS evaluation model with neural networks. J Serv Sci Manage 2009; 2(1):15. https://doi.org/10.4236/jssm.2009.21003.

16. Arehart, R.A. Drill-Bit Diagnosis with Neural Networks. SPE Computer Applications 1990, 2, 24–28, https://doi.org/10.2118/19558-PA
17. Armenta, M. Identifying Inefficient Drilling Conditions Using Drilling-Specific Energy. In Proceedings of the All Days; SPE: Denver, Colorado, USA, September 2008, https://doi.org/10.2118/116667-MS
18. Arnø, M.L.; Godhavn, J.-M.; Aamo, O.M. Classification of Drilled Lithology in Real-Time Using Deep Learning with Online Calibration. SPE Drilling and Completion 2021, 26-37, https://doi.org/10.2118/204093-PA
19. Asanlou, Morteza. مهندسی حفاری [Drilling Engineering]. Tehran: Islamic Azad University, 1991.
20. Azadpour, M., Reza, M., Javaherian, A., Shabani, M. Rock physics model-based prediction of shear wave velocity utilizing machine learning technique for a carbonate reservoir, southwest Iran. J. Petrol. Sci. Eng. 2020. https://doi.org/10.1016/j.petrol.2020.107864.
21. Bahari, A.; Baradaran Seyed, A. Drilling cost optimization in a hydrocarbon field by combination of comparative and mathematical methods. Pet. Sci. 2009, 6, 451–463. https://doi.org/10.1007/s12182-009-0069-x
22. Bai, K.; Jin, S.; Zhang, Z.; Dai, S. Drilling Rate of Penetration Prediction Based on CBT-LSTM Neural Network. Sensors 2024, 24, 6966. https://doi.org/10.3390/s24216966.
23. Bani Mustafa, A.; Abbas, A.K.; Alsaba, M.; Alameen, M. Improving Drilling Performance through Optimizing Controllable Drilling Parameters. J. Pet. Explor. Prod. Technol. 2021, 11, 1223–1232. https://doi.org/10.1007/s13202-021-01116-2
24. Basarir, H., Tutluoglu, L. and Karpuz, C. Penetration rate prediction for diamond bit drilling by adaptive neuro-fuzzy inference system and multiple regressions. Engineering Geology, *173*, 1-9. 2014, https://doi.org/10.1016/j.enggeo.2014.02.006
25. Bataee, M.; Irawan, S.; Kamyab, M. Artificial neural network model for prediction of drilling rate of penetration and optimization of parameters. Journal of the Japan Petroleum Institute. 2014: 57(2):65-70. https://doi.org/10.1627/jpi.57.65
26. Bello, O.; Teodoriu, C.; Yaqoob, T.; Oppelt, J.; Holzmann, J.; Obiwanne, A. Application of artificial intelligence techniques in drilling system design and operations: a state of the art review and future research pathways. In proceedings of SPE Nigeria Annual International Conference and Exhibition, Lagos, Nigeria, August 2016. https://doi.org/10.2118/184320-MS
27. Bilgesu, H.I.; Tetrick, L.T.; Altmis, U.; Mohaghegh, S.; Ameri, S. A New Approach for the Prediction of Rate of Penetration (ROP) Values. In Proceedings of the SPE Annual Technical Conference and Exhibition: Lexington, Kentucky, USA, October 1997, https://doi.org/10.2118/39231-MS
28. Bilim, N. and Karakaya, E. Penetration rate prediction models for core drilling. Mining, Metallurgy and Exploration, 38(1) 359-366. 2021, https://doi.org/10.1007/s42461-020-00322-6
29. Bingham, M.G. A New Approach to Interpreting Rock Drill-Ability, Petroleum Pub. Co: Oklahoma, USA, 1965
30. Bodaghi, A.; Ansari, H.R.; Gholami, M. Optimized support vector regression for drillingrate of penetration estimation. Open Geosciences 2015 7(1), 870-879. https://doi.org/10.1515/geo-2015-0054
31. Bond, D.F. The optimization of PDC bit selection using sonic velocity profiles present in the Timor Sea. SPEDE 1990, 5, 135-142.
32. Bourgoyne, A.T., Jr.; Chenevert, M.E.; Milheim, K.K.; Young, F.S., Jr. Applied Drilling Engineering; Society of Petroleum Engineers: Richardson, TX, USA, 1986.
33. Bourgoyne, A.T.; Young, F.S. A Multiple Regression Approach to Optimal Drilling and Abnormal Pressure Detection. Society of Petroleum Engineers Journal. 1974, 14, 371–384, https://doi.org/10.2118/4238-PA

34. Bukar, I., Adamu, M.B., Hassan, U. A machine learning approach to shear sonic log prediction. In: Society of Petroleum Engineers - SPE Nigeria Annual International Conference and Exhibition 2019, https://doi.org/10.2118/198764-MS
35. Chen, P.; Miska, S.; Yu, M.; Ozbayoglu, E. Modeling of Cutting Rock: From PDC Cutter to PDC Bit—Modeling of PDC Bit. SPE Journal 26(6), 2021, 3444-3464, https://doi.org/10.2118/205342-PA
36. Chen, X.; Yang, J.; Gao, D. Drilling Performance Optimization Based on Mechanical Specific Energy Technologies. 2018 http://dx.doi.org/10.5772/intechopen.75827
37. De Oliveira, L.S.R.; Nascimento, A.; Mantegazini, D.Z.; Nascimento, N. Drilling optimization of petroleum wells: A data analysis of the drilling fluid flow-rate influence in ROP. Latin American Journal of Energy Research. 2021. 8(1), .59-66, https://doi.org/10.21712/lajer.2021.v8.n1.p59-66
38. Detournay, E., Richard, T. and Shepherd, M., 2008. Drilling response of drag bits: Theory and experiment. International Journal of Rock Mechanics and Mining Sciences, 45(8), 1347-1360. https://doi.org/10.1016/j.ijrmms.2008.01.010
39. Dunlop, J.; Isangulov, R.; Aldred, W.D.; Sanchez, H.A.; Flores, J.L.; Herdoiza, J.A.; Belaskie, J.; Luppens, J.C. Increased rate of penetration through automation. In proceeding of SPE/IADC Drilling Conference and Exhibition. Amsterdam, Netherlands, March 2011, http://dx.doi.org/10.2118/139897-MS
40. Dupriest, F.E.; Koederitz, W.L. Maximizing Drill Rates with Real-Time Surveillance of Mechanical Specific Energy. In Proceedings of the SPE Annual Technical Conference and Exhibition: Amsterdam, Netherlands, February 2005, https://doi.org/10.2118/92194-MS
41. Dupriest, F.; Lai, S.; Behounek, M.; Pastusek, P.; Cutts, C.; Best, B.; Cook, B.; Bassarath, W.; Collins, J.; Kamyab, M.; Moore, D. Standardization of Mechanical Specific Energy Equations and Nomenclature. SPE Drill. Complet. 2023, 38, 73–89. https://doi.org/10.2118/208777-MS.
42. Eckel, J.R. Microbit studies of the effect of fluid properties and hydraulics on drilling rate. J Pet Technol, 1967, 19(04): 541–546. https://doi.org/10.2118/1520-PA
43. Edalatkhah, S.; Rasoul, R.; Hashemi, A. Bit selection optimization using artificial intelligence systems. Pet Sci Technol, 2010 28(18):1946–1956, https://doi.org/10.1080/10916460903160818
44. Elkatatny, S. Development of a new rate of penetration model using self-adaptive differential evolution-artificial neural network. Arab J Geosci, (12)19, 2019. https://doi.org/10.1007/s12517-018-4185-z
45. Elkatatny, S. New approach to optimize the rate of penetration using artificial neural network. Arabian J Sci Eng, 2018; 43(11):6297–6304. https://doi.org/10.1007/s13369-017-3022-0
46. Fjaer, E.; Holt, R.M.; Horsrud, P.; Raaen, A.M.; Risnes, R. Petroleum Related Rock Mechanics, 2nd ed.; Elsevier: Amsterdam, The Netherlands, 2008.
47. Flood, V. Density of Rocks and Soils. Published 14 March 2023. Available online: https://chem.libretexts.org/Ancillary_Materials/Exemplars_and_Case_Studies/Exemplars/Geology/Density_of_Rocks_and_Soils (accessed on 11 May 2025).
48. Galle, H.B.; Woods, E.M. Best Constant Weight and Rotary Speed for Rotary Rock Bits, Hughes Tool Company, New York, USA, 1963.
49. Gan, C., Cao, W., Wu, M., Liu, K.Z., Chen, X., Hu, Y. and Ning, F. Two-level intelligent modeling method for the rate of penetration in complex geological drilling process. Applied Soft Computing, 2019 80, 592-602. https://doi.org/10.1016/j.asoc.2019.04.020
50. Gidh, Y.; Purwanto, A.; Bits, S. Artificial Neural Network Drilling Parameter Optimization System Improves ROP by Predicting/Managing Bit Wear. In Proceedings of the All Days; SPE: Utrecht, Netherlands, March 2012; https://doi.org/10.2118/149801-MS
51. Goebel, T.; Molina, R.V.; Vilalta, R.; Gupta, K.D. Landmark Graphics Corp, Method and system for predicting a drill string stuck pipe event. 2014, https://www.google.com/patents/US8752648

52. Gong, D.; Zu, Y.; Zhou, Z.; Jia, M.; Liu, J.; Hu, Y. Research on the Prediction of Drilling Rate in Geological Core Drilling Based on the BP Neural Network. Appl. Sci. 2024, 14, 9959. https://doi.org/10.3390/app14219959
53. Gradziński, R. and Uchman, A. Trace fossils from interdune deposits—an example from the Lower Triassic aeolian Tumlin Sandstone, central Poland. Palaeogeography, Palaeoclimatology, Palaeoecology, 1994. 108(1-2), pp.121-138. https://doi.org/10.1016/0031-0182(94)90025-6
54. Great Drill Bit. Factors Affecting the Roller Bit Drilling. Published August 2022. Available online: https://www.greatdrillbit.com/factors-affecting-the-roller-bit-drilling.html (accessed on 11 May 2025).
55. Graham, J.W.; Muench, N.L. Analytical determination of optimum bit weight and rotary speed combinations. In Proceeding of the In Fall meeting of the Society of Petroleum Engineers of AIME. Dallas, Texas, USA. October 1959. https://doi.org/10.2118/1349-G
56. Gupta, R.; Bhui, U.K. Transforming Oil Well Drilling: Prediction of Real-Time Rate of Penetration with Novel Machine Learning Approach in Varied Lithological Formations. J. Energy Resour. Technol. Part B: Subsurface Energy Carbon Capture 2025, 1, 011003. https://doi.org/10.1115/1.4066015.
57. Hamrick, T.R. Optimization of operating parameters for minimum mechanical specific energy in drilling. West Virginia University, USA, 2011. https://doi.org/10.33915/etd.3059
58. Haque, A.E., Siddiqui, A.N., Hermana, M., Olutoki, J.O. Determining the optimum drilling spots using geomodeling for multilayered reservoirs, Taranaki Basin, New Zealand. Petroleum and Coal 63 (1), 278e283. 2023. https://doi.org/ 10.1142/9781786345882_0006.
59. Hareland, G.; Rampersad, P.R. Drag-bit model including wear. In Proceeding of the SPE Latin America/Caribbean Petroleum Engineering Conference. Buenos Aires, Argentina, April 1994. https://doi.org/10.2118/26957-MS
60. Hareland, G.; Wu, A.; Rashidi, B.; James, J.A. A new drilling rate model for tricone bits and its application to predict rock compressive strength. In Proceeding of the 44th US Rock Mechanics Symposium and 5th US-Canada Rock Mechanics Symposium, Salt Lake City, Utah, 27 June 2010.
61. Hart, D.J.; Wang, H.F. Laboratory Measurements of a Complete Set of Poroelastic Moduli for Berea Sandstone and Indiana Limestone. J. Geophys. Res. 1995, 100, 17741–17751. https://doi.org/10.1029/95JB01242
62. Hassan, A.; Al-Majed, A.; Elkatatny, S.; Mahmoud, M.; Abdulraheem, A.; Nader, M.; Abughaban, M.; Khamis, M. Developing an efficient drilling system by coupling torque modelling with mechanical specific energy. In proceeding of SPE Kingdom of Saudi Arabia Annual Technical Symposium and Exhibition. April 2018, https://doi.org/10.2118/192251-MS
63. Hegde, C.; Daigle, H.; Millwater, H.; Gray, K. Analysis of Rate of Penetration (ROP) Prediction in Drilling Using Physics-Based and Data-Driven Models. Journal of Petroleum Science and Engineering. 2017, 159, 295–306. doi:10.1016/j.petrol.2017.09.020
64. Hegde, C.; Gray, K.E. Use of Machine Learning and Data Analytics to Increase Drilling Efficiency for Nearby Wells. Journal of Natural Gas Science and Engineering, 2017, 40, 327–335. https://doi.org/10.1016/j.jngse.2017.02.019
65. Hegde, C.; Soares, C.; Gray, K. September. Rate of penetration (ROP) modeling using hybrid models: deterministic and machine learning. In Proceeding of the Unconventional Resources Technology Conference, Houston, Texas, USA, 23-25 July 2018. https://doi.org/10.15530/urtec-2018-2896522.
66. Hinton, G.E.; Osindero. S.; The, Y.W. A fast learning algorithm for deep belief nets. Neural Comput, 2006; 18(7): 1527–1554. https://doi.org/10.1162/neco.2006.18.7.1527
67. Holdaway, K.R. Harness oil and gas big data with analytics: Optimize exploration and production with data-driven models: John Wiley and Sons, 2014; ISBN 978-1-118-77931-6

68. Hopmann, U.; Algrain, M.C. Diesel Engine Electric Turbo Compound Technology. SAE Technical Paper No. 2003-01-2294, 2003. https://doi.org/10.4271/2003-01-2294
69. Hoseinie, S.H.; Aghababaei, H.; Pourrahimian, Y. Development of a new classification system for assessing of rock mass drillability index (RDi). International Journal of Rock Mechanics and Mining Sciences, 2008, 45(1), 1-10. https://doi.org/10.1016/j.ijrmms.2007.04.001
70. Hossain ME, Al-Majed AA. Fundamentals of Sustainable Drilling Engineering. wiley; 2015: 374-412. https://doi.org/10.1002/9781119100300
71. Howarth, D.F. Experimental study on the relationship between rock texture and mechanical performance. Trans. Inst. Min. Metall. Sect. A, 1986, 95: 41–45
72. Huang, G.; Hamzah, S.K.; Patel, P.; Ramachandran, T.; Shankhyan, A.; Karthikeyan, A.; Thatoi, D.N.; Gupta, D.; AbdulAmeer, S.; Alwan, M.; Abdulali, Z.S. Data-Driven Prediction of Rate of Penetration (ROP) in Drilling Operations Using Advanced Machine Learning Models. J. Pet. Explor. Prod. Technol. 2025, 15, 121. https://doi.org/10.1007/s13202-025-02018-3.
73. Hu, W.; Zhang, J.; Xu, B.; Zhu, H. Numerical Simulation and Experimental Study of Hole Cleaning. Tunn. Undergr. Space Technol. 2024, 147, 105697. https://doi.org/10.1016/j.tust.2024.105697
74. Jaeger, J.C.; Cook, N.G.W.; Zimmerman, R.W. Fundamentals of Rock Mechanics, 4th ed.; Wiley-Blackwell: Hoboken, NJ, USA, 2007. http://dx.doi.org/10.1017/CBO9780511735349
75. Jahanbakhshi, R.; Keshavarzi, R.; Jafarnezhad, A. Real-time prediction of rate of penetration during drilling operation in oil and gas wells. In Proceeding of the 46th US Rock Mechanics/Geomechanics Symposium, USA, Chicago, Illinois, USA, 24 June 2012.
76. Jiao, S.; Li, W.; Li, Z.; Gai, J.; Zou, L.; Su, Y. Hybrid Physics–Machine Learning Models for Predicting Rate of Penetration in the Halahatang Oil Field, Tarim Basin. Sci. Rep. 2024, 14, 5957. https://doi.org/10.1038/s41598-024-56640-y.
77. Kahraman, S. Estimating the Penetration Rate in Diamond Drilling in Laboratory Works Using the Regression and Artificial Neural Network Analysis. Neural Process Lett, 2016, 43, 523–535. https://doi.org/10.1007/s11063-015-9424-7
78. Khalilidermani, M.; Knez, D. A Survey of Application of Mechanical Specific Energy in Petroleum and Space Drilling. Energies 2022, 15(14), 3162, https://doi.org/10.3390/en15093162
79. Khalilidermani, M.; Knez, D. A Survey on the Shortcomings of the Current Rate of Penetration Predictive Models in Petroleum Engineering. Energies 2023, 16, 4289. https://doi.org/10.3390/en16114289
80. Khalilidermani, M.; Knez, D.; Zamani, M.A.M. Empirical Correlations between the Hydraulic Properties Obtained from the Geoelectrical Methods and Water Well Data of Arak Aquifer. Energies 2021, 14, 5415, doi:10.3390/en14175415.
81. Kilb, J.; Brame, B.; Anderson, K. Finally, a Low Cost and Autonomous Method of Generating Corrected Mechanical Specific Energy for Improved Decision Making, Drilling Performance, and Rock Property Characterization. In Proceedings of the SPE Annual Technical Conference and Exhibition, Houston, TX, USA, 2022, https://doi.org/10.2118/210195-MS.
82. Knez, D.; Khalilidermani, M. A Review of Different Aspects of Off-Earth Drilling. Energies. 2021, 14, 7351, https://doi.org/10.3390/en14217351
83. Kuesel, T.R.; King, E.H.; Bickel, J.O. Tunnel engineering handbook. Springer Science and Business Media. USA, 2012
84. Kumar, S.; Murthy, V.M.S.R. Experimental studies on drill penetration rate prediction in coal measure rocks through Cerchar hardness index tests. J. Mines Metals Fuels, 2014a, 62(4), 88–95. https://doi.org/10.1016/j.ijmst.2021.05.010

85. Kumar, S.; Murthy, V.M.S.R. Predicting penetration rate for rotary blast hole drills in surface coal mines—an approach. Proceedings of the 6th National Seminar on Surface Mining (NSSM), Indian School of Mines, Dhanbad, 10–11 January (2014)b
86. Liang, H.; Chen, H.; Guo, J.; Bai, J.; Jiang, Y. Research on lithology identification method based on mechanical specific energy principle and machine learning theory, Expert Systems with Applications, 2022, 189, 116142. https://doi.org/10.1016/j.eswa.2021.116142
87. Lippmann, R.P. An introduction to computing with neural nets. IEEE Assp Mag, 1987; 4(2): 4–22. https://doi.org/10.1109/MASSP.1987.1165576.
88. Lu, N.; Zhang, B.; Wang, T.; Fu, Q. Modeling Research on the Extreme Hydraulic Extension Length of Horizontal Well: Impact of Formation Properties, Drilling Bit, and Cutting Parameters. J. Pet. Explor. Prod. Technol. 2021, 11, 123–135. https://doi.org/10.1007/s13202-021-01106-4
89. Macpherson, J.D. Mechanical Specific Energy: Derivation, Understanding and Relationship to Formation Strength. In Proceedings of the SPE/IADC Drilling Conference and Exhibition, Stavanger, Norway, March 2025; p. D021S015R002. https://doi.org/10.2118/223707-PA.
90. Mahdi, D.S. Predicting Drilling Rate of Penetration Using Artificial Neural Networks. In Proceeding of the 4th International Conference on Engineering Sciences (ICES 2020), Kerbala, Iraq, 5th-6th December 2020. DOI 10.1088/1757-899X/1067/1/012150
91. Maidla, E.E.; Ohara. S. Field Verification of Drilling Models and Computerized Selection off Drill Bit, WOB, and Drillstring Rotation. In Proceeding of the SPE Drilling Engineering. USA, Septamper, 1991. 1;6(03):189-95. https://doi.org/10.2118/19130-PA
92. Majidi, R.; Albertin, M.; Last, N. Pore-Pressure Estimation by Use of Mechanical Specific Energy and Drilling Efficiency. SPE Drilling and Completion 2017, 32, 097–104, https://doi.org/10.2118/178842-PA
93. Mantha, B.; Samuel, R. ROP optimization using artificial intelligence techniques with statistical regression coupling. In Proceeding of the SPE Annual Technical Conference and Exhibition, Dubai, UAE, 26-28 September 2016, SPE-181382-MS. https://doi.org/10.2118/181382-MS
94. Maurer, W.C. The "Perfect - Cleaning" Theory of Rotary Drilling. J. Pet. Technol. 1962, 14, 1270–1274. https://doi.org/10.2118/408-PA
95. Ma, Z.; Hsu, M.; Hu, H.; Wang, T.; Zhou, X.; Li, G.; Tian, S. Hybrid Strategies for Interpretability of Rate of Penetration Prediction: Automated Machine Learning and SHAP Interpretation. In Proceedings of the ARMA US Rock Mechanics/Geomechanics Symposium, Austin, TX, USA, June 2024; p. D022S020R008. https://doi.org/10.56952/ARMA-2024-0315.
96. Mendes, J.R.P.: Fonseca, T.C.: Serapião, A. Applying a genetic neuro-model reference adaptive controller in drilling optimization. World oil, 2007, 29-36. https://orcid.org/0000-0001-9728-7092
97. Meng, H.; Lin, B.; Jin, Y. Stop Using Black-Box Models: Application of Explainable Artificial Intelligence for Rate of Penetration Prediction. SPE J. 2024, 29, 6640–6654. https://doi.org/10.2118/223622-PA.
98. Miedema, S.A. Calculation of the Cutting Forces When Cutting Water Saturated Sand, Delft University of Technology, 1987.
99. Minghui, W.; Gensheng, L.; Huaizhong, S.; Shuaishuai, S.; Zhaokun, L.; Yi, Z. Theories and Applications of Pulsed-Jet Drilling With Mechanical Specific Energy. SPE Journal. 2016, 21, 303–310, https://doi.org/10.2118/174550-PA
100. Miska, S.Z.; Mitchell, R.F.; Ozbayoglu, E.M. Drilling Engineering: Advanced Applications and Technology. 1st ed. New York: McGraw Hill. 2022.
101. Mitchell, R.F.; Miska, S.Z. Fundamentals of Drilling Engineering; Society of Petroleum Engineers: Richardson, TX, USA, 2011. https://doi.org/10.2118/9781555632076
102. Moazzeni, A.R.; Khamehchi, E. Rain optimization algorithm (roa): a new metaheuristic method for drilling optimization solutions. J Pet Sci Eng, 2020, 195:107512, https://doi.org/10.1016/j.petrol.2020.107512

103. Mohammadinia, F.; Ranjbar, A.; Ghazi, F.; Hosseini, S.T. Rate of Penetration Prediction in Drilling Operations: A Comparative Study of AI Models and Meta-Heuristic Approaches. J. Pet. Explor. Prod. Technol. 2025, 15, 115. https://doi.org/10.1007/s13202-025-02020-9.
104. Monjezi, M.; Dehghani, H. Evaluation of effect of blasting pattern parameters on back break using neural networks. Int J Rock Mech Min Sci, 2008; 45(8):1446–53. https://doi.org/10.1016/j.ijrmms.2008.02.007.
105. Mostafaei, K.; Maleki, Sh.; Mahmoudi, M.Z.A.; Knez, D. Risk management prediction of mining and industrial projects by support vector machine. Resources Policy, 2022, 78: 102819. http://dx.doi.org/10.1016/j.resourpol.2022.102819
106. Motahhari, H.R.; Hareland, G.; James, J.A. Improved drilling efficiency technique using integrated PDM and PDC bit parameters. Journal of Canadian Petroleum Technology. 2010, 1;49(10):45-52. https://doi.org/10.2118/141651-PA
107. Niyazi, B. Determination of drillability of some natural stones and their association with rock properties. Scientific research and Essays, 2011. 6(2): 382-387. https://doi.org/10.5897/SRE10.878
108. Noshi, C.I; Schubert, J.J. The role of machine learning in drilling operations; a review. In Proceedings of the SPE/AAPG Eastern Regional Meeting, Pittsburgh, Pennsylvania, USA, October 2018. https://doi.org/10.2118/191823-18ERM-MS
109. Olutoki, J.O.; Zhao, J.; Siddiqui, N.A.; Elsaadany, M.; Haque, A.E.; Akinyemi, O.D.; Said, A.H.; Zhao, Z. Shear wave velocity prediction: A review of recent progress and future opportunities. Energy Geoscience 2024, 1, 100338. https://doi.org/10.1016/j.engeos.2024.100338.
110. Osgouei, R.E. Rate of Penetration Estimation Model for Directional and Horizontal Wells, Middle East Technical University: Ankara, Turkey, 2007. https://hdl.handle.net/11511/17004
111. Paiaman, A.M.; Al-Askari, M.G.; Salmani, B.; Al-Anazi, B.D.; Masihi, M. Effect of drilling fluid properties on rate of penetration. Nafta, 2009, 60(3), 129-134.
112. Paone, J.; Madson, D.; Bruce, W.E. Drillability studies-laboratory percussive drilling, US Department of the Interior, Bureau of Mines. USA, 1969. No. 7300-7309.
113. Pathankar, G.B.; Misra, A. Critical appraisal of the Protodyakonov Index. Int. J. Rock Mech. Min. Sci. 1976, 13(8), 249–251, https://doi.org/10.1016/0148-9062(76)91545-X
114. Peña-Gutiérrez, J.; Sabirov, A. Automated Estimation of Mechanical Specific Energy as a Tool for Stratigraphic Interpretation during Real-Time Drilling Operations. In Proceedings of the International Petroleum Technology Conference, Dhahran, Saudi Arabia, February 2024; IPTC-24448. https://doi.org/10.2523/IPTC-24448-EA.
115. Perrin, V.P.; Mensa-Wilmot, G.; Alexander, W.L. Drilling index-a new approach to bit performance evaluation. In Proceeding of the SPE/IADC drilling conference, Amsterdam, Netherlands, March, 1997. https://doi.org/10.2118/37595-MS
116. Pessier, R.C.; Fear, M.J. Quantifying Common Drilling Problems with Mechanical Specific Energy and a Bit-Specific Coefficient of Sliding Friction. In Proceedings of the All Days; SPE: Washington, D.C., October 1992; https://doi.org/10.2118/24584-MS
117. Pollock, J.; Stoecker-Sylvia, Z.; Veedu, V.; Panchal, N.; Elshahawi, H. Machine learning for improved directional drilling. In proceeding of Offshore Technology Conference. Houston, Texas, USA, 30 April – 3 May 2018. https://doi.org/10.4043/28633-MS
118. Protodyakonov, M.M. Mechanical properties and drillability of rocks. In Proceedings of the 5th Symposium Rock Mechanics, 103–118, University of Minnesota, Minnesota, USA, 1963.
119. Rabia, H. Oil Well Drilling Engineering: Principles and Practice; Graham and Trotman: London, UK, 1985.

120. Rafatian, N.; Miska, S.; Ledgerwood, L.W.. W.; Ahmed, R.; Yu, M.; Takach, N. Experimental Study of MSE of a Single PDC Cutter Interacting With Rock Under Simulated Pressurized Conditions. SPE Drilling and Completion 2010, 25, 10–18, https://doi.org/10.2118/119302-PA
121. Ramsey, M.S. Bit Hydraulics. In Practical Wellbore Hydraulics and Hole Cleaning, TX, USA, 2019
122. Reza, M.R.; Alcocer, C.F. A unique computer simulation model well drilling: Part I-the reza drilling model. In Proceeding in the SPE California Regional Meeting.Oakland, California, USA, April 1986. https://doi.org/10.2118/15108-MS
123. Rice, J.R. Elasticity of Fluid-Infiltrated Porous Solids (Poroelasticity). Stress 1998, 2(2).
124. Rodgers, J.L.; Nicewander, W.A. Thirteen Ways to Look at the Correlation Coefficient. Am. Stat. 1988, 42, 59–66. https://doi.org/10.1080/00031305.1988.10475524
125. Roseke Engineering Ltd. How to Calculate Specific Gravity. Published 19 December 2013. Available online: https://www.roseke.com/how-to-calculate-specific-gravity (accessed on 11 May 2025).
126. Sahood, T.; Myers, M.T.; Hathon, L.; Unomah, G.C. Quantifying the Mechanical Specific Energy (MSE) with Differential Wellbore Pressure for Real-Time Well Automation. In Proceedings of the Offshore Technology Conference, Houston, TX, USA, April 2024; p. D011S014R008. https://doi.org/10.4043/35336-MS.
127. Shi, X.; Liu, G.; Gong, X.; Zhang, J.; Wang, J.; Zhang, H. An efficient approach for real-time prediction of rate of penetration in offshore drilling. Mathematical Problems in Engineering, 2016. http://dx.doi.org/10.1155/2016/3575380
128. Shigley, J.E.; Mischke, C.R; Saunders, H. Mechanical Engineering Design, 4th ed.; McGraw-Hill: New York, NY, USA, 1985. https://doi.org/10.1115/1.3258702
129. Skalle, P. Exercises in Drilling Fluid Engineering; Bookboon.com: London, UK, 2015.
130. Słonka, Ł.; Krzywiec, P. Seismic Characteristics and Development of the Upper Jurassic Carbonate Buildups from the Miechów Trough (Southern Poland). Geosciences 2020, 10, 239. https://doi.org/10.3390/geosciences10060239
131. Sobhi, I.; Dobbi, A.; Hachana, O. Prediction and analysis of penetration rate in drilling operation using deterministic and metaheuristic optimization methods. J Petrol Explor Prod Technol, 2022, 12, 1341–1352. https://doi.org/10.1007/s13202-021-01394-w
132. Song, X.; Li, G.; Xu, Z.; Shah, S. Fundamentals of Horizontal Wellbore Cleanout: Theory and Applications of Rotary Jetting Technology; Gulf Professional Publishing: Cambridge, MA, USA, 2022.
133. Stelzer, C. Drillpipe Failure and its Prediction Doctoral dissertation, University of Leoben, Leoben, Austria,2007
134. Stoxreiter, T.; Portwood, G.; Gerbaud, L.; Seibel, O.; Essl, S.; Plank, J.; Hofstätter, H. Full-Scale Experimental Investigation of the Performance of a Jet-Assisted Rotary Drilling System in Crystalline Rock. Int. J. Rock Mech. Min. Sci. 2019, 115, 87–98. https://doi.org/10.1016/j.ijrmms.2019.01.011
135. Strzeboński, P. Late Cretaceous-Early Palaeogene sandy-to-gravelly debris flows and their sediments in the Silesian Basin of the Alpine Tethys (Western Outer Carpathians, Istebna Formation). Geological Quarterly, 59. 2015, https://doi.org/10.7306/gq.1183
136. Sultan, M.A. and Al-Kaabi, A.U. Application of neural network to the determination of well-test interpretation model for horizontal wells. In Proceeding of the SPE Asia Pacific Oil and Gas Conference and Exhibition. Melbourne, Australia, October 2002. https://doi.org/10.2118/77878-MS
137. Tandanand, S.; Unger, H.F. Drillability determination: a drillability index for percussion drills, US Department of the Interior, Bureau of Mines. Uniwersytet Michigan, USA, 1975. (Vol. 8073).A.G.
138. Teale, R. The Concept of Specific Energy in Rock Drilling. Int. J. Rock Mech Min. 1965, 2, 57–73. https://doi.org/10.1016/0148-9062(65)90022-7
139. Tian, L.; Chen, M.; Zheng, Z.; Zhu, Z.; Song, X.; Yang, D.; Pan, T. Real-Time Monitoring Model of PDC Bit Wear Based on GRU Neural Network. In Proceedings of the ARMA US Rock

Mechanics/Geomechanics Symposium, Atlanta, GA, USA, June 2023; ARMA-2023. https://doi.org/10.56952/ARMA-2023-0195.
140. Tou, S.K.W. Application of Dimensional & Regression Analysis in Oil Drill Bit Data. Comput. Geotech. 1988, 6, 49–64. https://doi.org/10.1016/0266-352X(88)90055-9
141. Trenchlesspedia. Weight on Bit (WOB). Published 30 August 2018; Updated 5 July 2023. Available online: https://trenchlesspedia.com/definition/3650/weight-on-bit-wob (accessed on 11 May 2025).
142. Trivedi, A.S.; Clarkson, C.R.; Shor, R.J. Accounting for Hydraulics and Vibration in MSE Calculations to Estimate Formation Properties. In Proceedings of the Day 3 Thu, March 05, 2020; SPE: Galveston, Texas, USA, February 25 2020; https://doi.org/10.2118/199672-MS
143. Wamsley, W.H., Jr.; Ford, R. Introduction to Roller-Cone and Polycrystalline Diamond Drill Bits. In Petroleum Engineering Handbook; Volume 2; pp. 221–264; 2006. https://doi.org/10.2118/9781555631147-ch05
144. Wang, G.; Dong, M.; Wang, Z.; Ren, T.; Xu, S. Removing Cuttings from Inclined and Horizontal Wells: Numerical Analysis of the Required Drilling Fluid Rheology and Flow Rate. J. Nat. Gas Sci. Eng. 2022, 102, 104544. https://doi.org/10.1016/j.jngse.2022.104544
145. Wang, H.F. Theory of Linear Poroelasticity with Applications to Geomechanics and Hydrogeology; Princeton University Press: Oxford, UK, 2000.
146. Warren, T.M. Drilling Model for Soft-Formation Bits. Journal of Petroleum Technology 1981, 33, 963–970. https://doi.org/10.2118/8438-PA
147. Warren, T.M. Factors Affecting Torque for a Roller Cone Bit. J. Pet. Technol. 1984, 36, 1500–1508, https://doi.org/10.2118/11994-PA
148. Waśkowska, A., Cieszkowski, M., Golonka, J. and Kowal-Kasprzyk, J. Paleocene sedimentary record of ridge geodynamics in Outer Carpathian basins (Subsilesian Unit), 2014, https://www.doi.org/10.2478/geoca-2014-0003
149. Nic, M.; Hovorka, L.; Jirat, J.; Kosata, B.; Znamenacek, J. IUPAC Compendium of Chemical Terminology—The Gold Book; International Union of Pure and Applied Chemistry: Research Triagle Park, NC, USA, 2005.
150. Wiśniowski, R.; Knez, D.; Hytroś, Ł. Drillability and Mechanical Specific Energy Analysis on the Example of Drilling in the Pomeranian Basin. drill 2015, 32, 201, http://dx.doi.org/10.7494/drill.2015.32.L201
151. Yavari, H.; Sabah, M.; Khosravanian, R.; Wood, D. Application of an adaptive neuro-fuzzy inference system and mathematical rate of penetration models to predicting drilling rate. Iranian Journal of Oil and Gas Science and Technology, 2018, 7(3): 73-100. https://doi.org/10.22050/ijogst.2018.83374.1391
152. Yin, H.; Cui, H.; Gao, J. Research on Pore Pressure Detection While Drilling Based on Mechanical Specific Energy. Processes 2022, 10, 1481. https://doi.org/10.3390/pr10081481
153. Youcefi, M.R.; Hadjadj, A.; Bentriou, A.; Boukredera, F.S. Rate of penetration modeling using hybridization extreme learning machine and whale optimization algorithm. Earth Sci Inform, 2020, 13(4), 51–68. https://doi.org/10.1007/s12145-020-00524-y
154. Zhang, J.J. Applied Petroleum Geomechanics, Vol. 1; Gulf Professional Publishing: Cambridge, MA, USA, 2019. https://doi.org/10.1016/C2017-0-01969-9
155. Zoback, M.D. Reservoir Geomechanics; Cambridge University Press: Cambridge, UK, 2007. https://doi.org/10.1017/CBO9780511586477

Appendix

The appendix is provided to present supplementary data and detailed experimental results that support the analyses discussed in the main body of this dissertation. This additional material is included to ensure transparency and to allow verification of the empirical formulations developed in the study.

(AVS data)

Sample	Hydrostatic stress (MPa)	Time of flight (µs)			Wave speed (m/s)			υ_u	E_u (MPa)	K_u (MPa)	G_u (MPa)
		P-wave	S1-wave	S2 -wave	P-wave	S1-wave	S2-wave				
S1	5.0	57.6	121.0	121.0	1157	501	501	0.385	1409	2039	509
	10.0	57.2	119.0	119.0	1170	513	513	0.381	1475	2066	534
	15.0	56.4	117.0	117.0	1197	526	526	0.380	1549	2158	561
	20.0	56.0	115.0	115.0	1210	539	539	0.376	1625	2187	590
	25.0	55.6	115.0	114.0	1224	539	546	0.378	1648	2246	598
	30.0	54.4	112.0	112.0	1269	561	561	0.379	1761	2417	639
	35.0	52.0	104.0	104.0	1368	628	628	0.367	2188	2732	800
	40.0	44.8	88.0	88.0	1787	825	825	0.364	3774	4640	1383
	45.0	41.2	79.0	79.0	2111	1003	1003	0.354	5528	6321	2041
	50.0	40.8	77.8	77.8	2154	1032	1032	0.351	5844	6533	2163
	55.0	40.6	77.4	77.4	2176	1043	1043	0.351	5962	6672	2206
	60.0	40.4	77.0	77.0	2199	1053	1053	0.351	6083	6815	2251
	65.0	40.2	76.6	76.6	2222	1064	1064	0.351	6207	6963	2297
	70.0	40.0	76.0	76.0	2246	1080	1080	0.350	6392	7083	2368
S2	5.0	58.1	122.9	122.9	1129	484	484	0.387	1378	2041	497
	10.0	56.2	117.9	117.9	1190	514	514	0.386	1550	2257	559
	15.0	55.6	114.8	114.8	1211	534	534	0.379	1670	2299	606
	20.0	55.1	112.3	112.3	1228	552	552	0.373	1774	2337	646
	25.0	53.3	106.0	106.0	1296	602	602	0.362	2094	2538	769
	30.0	49.9	97.6	97.6	1450	686	686	0.356	2704	3126	997
	35.0	47.0	90.5	90.5	1618	778	778	0.350	3460	3839	1282
	40.0	45.1	86.2	86.2	1744	846	846	0.346	4081	4426	1516
	45.0	42.7	81.0	81.0	1940	945	945	0.344	5093	5450	1894
	50.0	41.4	77.9	77.9	2069	1017	1017	0.341	5883	6149	2194
	55.0	41.2	77.2	77.2	2090	1035	1035	0.337	6074	6229	2271
	60.0	41.2	76.7	76.7	2090	1048	1048	0.332	6200	6153	2327
	65.0	41.2	76.4	76.4	2090	1056	1056	0.329	6278	6106	2363
	70.0	41.2	76.2	76.2	2090	1061	1061	0.326	6332	6074	2387

To be continued

Sample	Hydrostatic stress (MPa)	Time of flight (µs)			Wave speed (m/s)			v_u	E_u (MPa)	K_u (MPa)	G_u (MPa)
		P-wave	S1-wave	S2 -wave	P-wave	S1-wave	S2-wave				
S3	5.0	58.3	122.9	122.9	1148	495	495	0.385	1415	2059	511
	10.0	57.0	119.2	119.2	1190	518	518	0.383	1544	2202	558
	15.0	56.4	117.2	117.2	1211	530	530	0.381	1617	2268	585
	20.0	55.9	115.0	115.0	1228	546	546	0.377	1705	2313	619
	25.0	54.1	109.9	109.5	1296	584	587	0.372	1955	2545	713
	30.0	52.1	104.3	104.3	1382	632	632	0.368	2274	2863	831
	35.0	48.4	94.9	94.9	1570	735	735	0.360	3055	3630	1123
	40.0	45.1	87.6	87.6	1787	842	842	0.357	4005	4677	1475
	45.0	41.8	80.0	80.0	2070	991	991	0.351	5521	6187	2043
	50.0	41.4	78.8	78.8	2111	1020	1020	0.348	5832	6388	2164
	55.0	41.2	78.3	78.3	2133	1032	1032	0.347	5972	6506	2217
	60.0	41.1	77.7	77.7	2144	1048	1048	0.343	6134	6519	2283
	65.0	41.0	77.4	77.4	2156	1056	1056	0.342	6223	6577	2318
	70.0	40.9	77.1	77.1	2168	1064	1064	0.341	6316	6635	2354
S4	5.0	58.0	123.0	123.0	1144	489	489	0.388	1359	2027	489
	10.0	57.2	120.6	120.6	1170	503	503	0.387	1436	2110	518
	15.0	55.6	116.0	116.0	1224	532	532	0.383	1605	2294	580
	20.0	54.4	113.0	113.0	1269	553	553	0.383	1733	2459	627
	25.0	50.0	102.0	102.0	1463	647	647	0.378	2363	3239	857
	30.0	48.0	96.0	96.0	1573	713	713	0.371	2853	3675	1041
	35.0	46.0	91.0	91.0	1700	779	779	0.367	3398	4259	1243
	40.0	44.8	88.0	88.0	1787	825	825	0.364	3803	4677	1394
	45.0	43.0	83.0	83.0	1935	915	915	0.356	4648	5379	1714
	50.0	41.6	79.0	79.0	2069	1003	1003	0.347	5540	6015	2057
	55.0	41.6	78.0	78.0	2069	1027	1027	0.336	5770	5880	2159
	60.0	41.6	77.6	77.6	2069	1037	1037	0.332	5866	5822	2202
	65.0	41.6	77.4	77.4	2069	1043	1043	0.330	5914	5793	2224
	70.0	41.6	77.0	77.0	2069	1053	1053	0.325	6013	5733	2269

To be continued

Sample	Hydrostatic stress (MPa)	Time of flight (μs)			Wave speed (m/s)			v_u	E_u (MPa)	K_u (MPa)	G_u (MPa)
		P-wave	S1-wave	S2 -wave	P-wave	S1-wave	S2-wave				
S5	5.0	58.4	122.0	122.0	1119	489	489	0.382	1400	1976	506
	10.0	58.0	119.0	119.0	1131	507	507	0.374	1496	1984	544
	15.0	57.8	116.0	116.0	1137	526	526	0.364	1600	1957	586
	20.0	54.8	109.2	109.2	1239	576	576	0.362	1913	2316	702
	25.0	49.6	96.0	96.0	1466	705	705	0.350	2841	3154	1052
	30.0	49.2	95.0	95.0	1487	717	717	0.349	2938	3236	1089
	35.0	48.8	93.0	93.0	1509	743	743	0.340	3132	3268	1168
	40.0	44.4	83.0	83.0	1797	904	904	0.330	4611	4528	1733
	45.0	44.2	82.0	82.0	1812	925	925	0.324	4797	4544	1811
	50.0	41.0	75.6	75.6	2107	1078	1078	0.322	6517	6119	2464
	55.0	40.0	73.0	73.0	2219	1156	1156	0.314	7445	6658	2834
	60.0	40.0	72.8	72.8	2219	1163	1163	0.311	7512	6616	2866
	65.0	40.0	72.8	72.8	2219	1163	1163	0.311	7512	6616	2866
	70.0	40.0	72.8	72.8	2219	1163	1163	0.311	7512	6616	2866
S6	5.0	57.8	122.8	122.8	1151	490	490	0.389	1415	2128	509
	10.0	56.8	120.0	120.0	1183	507	507	0.388	1511	2242	544
	15.0	54.6	115.0	115.0	1261	539	539	0.388	1711	2551	616
	20.0	52.4	109.0	109.0	1350	584	584	0.385	2004	2902	724
	25.0	52.0	104.0	104.0	1368	628	628	0.367	2285	2853	836
	30.0	49.2	96.6	96.6	1505	706	706	0.359	2872	3395	1057
	35.0	48.8	94.0	94.0	1527	738	738	0.348	3114	3404	1156
	40.0	44.4	84.0	84.0	1818	896	896	0.340	4558	4740	1701
	45.0	44.0	82.8	82.8	1850	919	919	0.336	4788	4869	1792
	50.0	41.2	77.0	77.0	2111	1053	1053	0.334	6273	6309	2351
	55.0	40.8	76.0	76.0	2154	1080	1080	0.332	6588	6537	2473
	60.0	40.8	75.0	75.0	2154	1109	1109	0.320	6877	6361	2605
	65.0	40.8	74.8	74.8	2154	1114	1114	0.317	6936	6324	2633
	70.0	40.8	74.6	74.6	2154	1120	1120	0.315	6996	6287	2661

To be continued

Sample	Hydrostatic stress (MPa)	Time of flight (µs)			Wave speed (m/s)			v_u	E_u (MPa)	K_u (MPa)	G_u (MPa)
		P-wave	S1-wave	S2 -wave	P-wave	S1-wave	S2-wave				
S7	5.0	58.0	122.8	122.8	1144	490	490	0.388	1399	2076	504
	10.0	56.4	118.7	118.7	1197	515	515	0.386	1542	2263	556
	15.0	55.1	115.3	115.3	1243	537	537	0.385	1677	2434	605
	20.0	53.6	111.0	111.0	1298	568	568	0.382	1871	2634	677
	25.0	52.0	104.0	104.0	1368	628	628	0.367	2261	2824	827
	30.0	49.3	96.7	96.7	1500	705	705	0.358	2832	3331	1042
	35.0	46.8	90.3	90.3	1650	790	790	0.351	3539	3964	1310
	40.0	44.6	85.0	85.0	1803	877	877	0.345	4344	4664	1615
	45.0	43.0	81.4	81.4	1940	949	949	0.342	5076	5372	1891
	50.0	41.4	77.9	77.9	2090	1030	1030	0.339	5965	6193	2227
	55.0	41.1	77.1	77.1	2122	1051	1051	0.337	6200	6354	2318
	60.0	41.1	76.2	76.2	2122	1076	1076	0.327	6441	6208	2427
	65.0	41.1	76.0	76.0	2122	1081	1081	0.325	6496	6175	2452
	70.0	41.1	75.9	75.9	2122	1084	1084	0.323	6526	6157	2466
S8	5.0	58.8	123.9	123.9	1135	490	490	0.386	1378	2008	497
	10.0	57.3	118.9	118.9	1181	520	520	0.380	1546	2148	560
	15.0	56.2	114.8	114.8	1219	547	547	0.374	1707	2253	621
	20.0	52.8	106.6	106.6	1351	611	611	0.371	2128	2753	776
	25.0	50.1	99.5	99.5	1475	681	681	0.365	2627	3233	963
	30.0	49.7	97.5	97.5	1496	703	703	0.358	2788	3278	1027
	35.0	47.2	91.9	91.9	1641	776	776	0.356	3389	3919	1250
	40.0	45.0	85.3	85.3	1792	882	882	0.340	4324	4511	1613
	45.0	44.7	84.3	84.3	1815	901	901	0.337	4501	4592	1684
	50.0	41.0	76.5	76.5	2153	1079	1079	0.332	6439	6394	2417
	55.0	40.4	74.6	74.6	2221	1132	1132	0.324	7048	6685	2661
	60.0	40.4	74.0	74.0	2221	1151	1151	0.316	7235	6570	2748
	65.0	40.4	73.9	73.9	2221	1154	1154	0.315	7266	6550	2763
	70.0	40.4	73.6	73.6	2221	1163	1163	0.311	7363	6489	2808

To be continued

Sample	Hydrostatic stress (MPa)	Time of flight (µs)			Wave speed (m/s)			v_u	E_u (MPa)	K_u (MPa)	G_u (MPa)
		P-wave	S1-wave	S2 -wave	P-wave	S1-wave	S2-wave				
S9	5.0	57.8	122.8	122.8	1151	490	490	0.389	1402	2108	505
	10.0	55.4	116.0	116.0	1232	532	532	0.385	1649	2392	595
	15.0	53.6	111.0	111.0	1300	568	568	0.382	1875	2646	679
	20.0	50.0	102.0	102.0	1463	647	647	0.378	2426	3324	880
	25.0	49.6	101.0	101.0	1484	657	657	0.378	2501	3415	908
	30.0	49.2	98.0	98.0	1505	690	690	0.367	2732	3427	999
	35.0	45.0	89.0	89.0	1772	809	809	0.368	3765	4761	1376
	40.0	44.8	86.0	86.0	1787	859	859	0.350	4184	4641	1550
	45.0	44.4	85.0	85.0	1818	877	877	0.348	4356	4788	1615
	50.0	40.4	76.0	76.0	2199	1080	1080	0.341	6570	6888	2450
	55.0	40.2	75.0	75.0	2222	1109	1109	0.334	6887	6929	2581
	60.0	40.2	74.0	74.0	2222	1139	1139	0.322	7198	6740	2723
	65.0	40.2	73.8	73.8	2222	1145	1145	0.319	7263	6701	2752
	70.0	40.2	73.2	73.2	2222	1164	1164	0.311	7459	6578	2845
S10	5.0	56.7	118.9	118.9	1132	489	489	0.385	1431	2077	516
	10.0	56.1	116.3	116.3	1150	505	505	0.381	1521	2124	551
	15.0	55.2	112.7	112.7	1181	529	529	0.374	1663	2205	605
	20.0	53.2	108.0	108.0	1254	565	565	0.373	1890	2478	688
	25.0	48.6	96.3	96.3	1465	676	676	0.365	2694	3319	987
	30.0	47.4	93.1	93.1	1530	715	715	0.360	3005	3585	1104
	35.0	46.2	89.7	89.7	1605	761	761	0.355	3390	3895	1251
	40.0	43.6	83.4	83.4	1792	865	865	0.348	4356	4781	1616
	45.0	42.6	80.6	80.6	1874	920	920	0.341	4903	5147	1828
	50.0	40.5	75.6	75.6	2088	1040	1040	0.335	6243	6297	2338
	55.0	40.0	73.7	73.7	2144	1092	1092	0.325	6823	6497	2575
	60.0	40.0	73.5	73.5	2144	1100	1100	0.321	6908	6444	2614
	65.0	40.0	73.4	73.4	2144	1103	1103	0.320	6935	6428	2626
	70.0	40.0	73.2	73.2	2144	1108	1108	0.318	6988	6395	2651

To be continued

Sample	Hydrostatic stress (MPa)	Time of flight (μs)			Wave speed (m/s)			v_u	E_u (MPa)	K_u (MPa)	G_u (MPa)
		P-wave	S1-wave	S2 -wave	P-wave	S1-wave	S2-wave				
S11	5.0	59.5	126.0	126.0	1151	495	495	0.387	1429	2100	515
	10.0	58.9	123.7	123.7	1170	508	508	0.384	1503	2157	543
	15.0	57.6	120.3	120.3	1211	529	529	0.382	1629	2299	589
	20.0	56.8	117.6	117.6	1240	546	546	0.379	1734	2397	628
	25.0	54.0	111.3	110.8	1344	593	597	0.378	2054	2808	745
	30.0	52.3	106.2	106.2	1421	637	637	0.374	2348	3111	854
	35.0	50.0	99.6	99.6	1534	704	704	0.367	2849	3565	1042
	40.0	45.9	90.4	90.4	1787	825	825	0.364	3913	4812	1434
	45.0	43.0	83.0	83.0	2023	959	959	0.355	5247	6034	1936
	50.0	42.1	80.4	80.4	2111	1017	1017	0.349	5879	6478	2179
	55.0	42.0	79.6	79.6	2123	1035	1035	0.344	6060	6478	2254
	60.0	41.9	79.2	79.2	2134	1045	1045	0.342	6173	6520	2299
	65.0	41.8	78.9	78.9	2146	1053	1053	0.341	6262	6578	2334
	70.0	41.7	78.4	78.4	2157	1067	1067	0.338	6409	6606	2394
S12	5.0	58.2	122.8	122.8	1138	490	490	0.386	1390	2035	501
	10.0	56.0	117.4	117.4	1210	523	523	0.385	1582	2296	571
	15.0	55.6	115.6	115.6	1224	535	535	0.382	1652	2332	598
	20.0	55.0	113.2	113.2	1246	552	552	0.378	1753	2394	636
	25.0	52.0	104.0	104.0	1368	628	628	0.367	2249	2809	823
	30.0	49.4	96.8	96.8	1495	704	704	0.358	2806	3285	1033
	35.0	45.0	87.0	87.0	1772	842	842	0.354	4007	4582	1479
	40.0	44.8	86.0	86.0	1787	859	859	0.350	4158	4612	1540
	45.0	42.0	80.0	80.0	2029	979	979	0.348	5397	5923	2002
	50.0	41.6	78.8	78.8	2069	1008	1008	0.345	5697	6109	2118
	55.0	41.4	78.2	78.2	2090	1022	1022	0.343	5856	6205	2181
	60.0	41.4	77.4	77.4	2090	1043	1043	0.334	6053	6088	2268
	65.0	41.4	77.2	77.2	2090	1048	1048	0.332	6103	6058	2291
	70.0	41.4	77.2	77.2	2090	1048	1048	0.332	6103	6058	2291

To be continued

Sample	Hydrostatic stress (MPa)	Time of flight (µs)			Wave speed (m/s)			v_u	E_u (MPa)	K_u (MPa)	G_u (MPa)
		P-wave	S1-wave	S2 -wave	P-wave	S1-wave	S2-wave				
S13	5.0	58.8	125.0	125.0	1120	478	478	0.389	1254	1878	451
	10.0	57.2	120.4	120.4	1170	504	504	0.386	1394	2036	503
	15.0	56.4	115.8	115.8	1197	534	534	0.376	1550	2080	563
	20.0	56.0	113.2	113.2	1210	552	552	0.369	1649	2093	602
	25.0	55.6	110.0	110.0	1224	576	576	0.358	1783	2089	656
	30.0	51.2	100.0	100.0	1405	668	668	0.354	2388	2725	882
	35.0	50.0	96.0	96.0	1463	713	713	0.344	2704	2893	1006
	40.0	46.0	87.6	87.6	1700	832	832	0.343	3674	3892	1368
	45.0	44.0	83.2	83.2	1850	911	911	0.340	4400	4579	1642
	50.0	41.6	78.0	78.0	2069	1027	1027	0.336	5576	5681	2086
	55.0	41.4	77.2	77.2	2090	1048	1048	0.332	5782	5738	2170
	60.0	41.4	77.0	77.0	2090	1053	1053	0.330	5830	5709	2192
	65.0	41.4	76.6	76.6	2090	1064	1064	0.325	5928	5650	2237
	70.0	41.4	76.2	76.2	2090	1075	1075	0.320	6027	5588	2283
S14	5.0	57.5	121.9	121.9	1148	490	490	0.389	1345	2015	484
	10.0	56.6	119.3	119.3	1177	505	505	0.387	1429	2109	515
	15.0	54.7	114.6	114.6	1243	536	536	0.386	1607	2347	580
	20.0	53.0	110.1	110.1	1310	569	569	0.384	1809	2593	654
	25.0	50.6	102.2	102.2	1416	638	638	0.373	2255	2954	821
	30.0	48.3	95.6	95.6	1539	710	710	0.365	2777	3429	1017
	35.0	47.0	91.8	91.8	1614	759	759	0.358	3160	3710	1163
	40.0	44.3	85.3	85.3	1803	861	861	0.352	4046	4570	1496
	45.0	43.2	82.4	82.4	1893	917	917	0.347	4577	4971	1700
	50.0	41.2	77.5	77.5	2090	1028	1028	0.340	5721	5976	2134
	55.0	41.0	76.5	76.5	2111	1054	1054	0.334	5984	6015	2243
	60.0	41.0	75.8	75.8	2111	1073	1073	0.326	6167	5905	2326
	65.0	41.0	75.6	75.6	2111	1078	1078	0.323	6219	5873	2350
	70.0	41.0	75.3	75.3	2111	1087	1087	0.320	6297	5825	2385

To be continued

Sample	Hydrostatic stress (MPa)	Time of flight (μs)			Wave speed (m/s)			υ_u	E_u (MPa)	K_u (MPa)	G_u (MPa)
		P-wave	S1-wave	S2 -wave	P-wave	S1-wave	S2-wave				
S15	5.0	59.5	126.9	126.9	1151	490	490	0.389	1395	2098	502
	10.0	57.7	121.8	121.8	1207	520	520	0.386	1564	2295	564
	15.0	55.7	116.6	116.6	1281	554	554	0.385	1776	2574	641
	20.0	52.6	108.6	108.6	1407	616	616	0.382	2190	3081	792
	25.0	52.2	105.6	105.6	1426	643	643	0.373	2370	3100	863
	30.0	50.5	100.2	100.2	1505	698	698	0.363	2775	3379	1018
	35.0	48.0	94.0	94.0	1650	774	774	0.359	3402	4019	1252
	40.0	45.7	87.3	87.3	1803	877	877	0.345	4328	4646	1609
	45.0	45.3	86.1	86.1	1834	898	898	0.342	4526	4783	1686
	50.0	41.7	78.4	78.4	2155	1067	1067	0.338	6360	6534	2377
	55.0	41.4	77.3	77.3	2188	1094	1094	0.333	6674	6669	2503
	60.0	41.4	76.3	76.3	2188	1124	1124	0.321	6971	6488	2639
	65.0	41.4	76.1	76.1	2188	1130	1130	0.318	7032	6450	2667
	70.0	41.4	75.6	75.6	2188	1142	1142	0.313	7158	6371	2726
S16	5.0	60.8	129.1	129.1	1139	489	489	0.387	1388	2042	500
	10.0	59.8	125.6	125.6	1170	509	509	0.383	1496	2140	541
	15.0	58.9	122.1	122.1	1197	530	530	0.378	1617	2210	587
	20.0	58.5	119.6	119.6	1210	546	546	0.372	1708	2232	622
	25.0	58.1	117.8	117.3	1224	558	561	0.368	1790	2261	654
	30.0	55.0	110.4	110.4	1337	614	614	0.366	2155	2683	789
	35.0	53.1	104.2	104.2	1416	671	671	0.355	2548	2936	940
	40.0	47.1	91.4	91.4	1744	829	829	0.354	3887	4442	1435
	45.0	44.0	84.1	84.1	1980	957	957	0.348	5159	5645	1914
	50.0	42.6	80.8	80.8	2111	1030	1030	0.344	5957	6362	2216
	55.0	42.4	80.2	80.2	2133	1045	1045	0.342	6127	6464	2283
	60.0	42.3	79.8	79.8	2144	1053	1053	0.341	6216	6520	2317
	65.0	42.2	79.4	79.4	2156	1064	1064	0.339	6333	6561	2364
	70.0	42.1	78.9	78.9	2168	1077	1077	0.336	6481	6587	2426

To be continued

Sample	Hydrostatic stress (MPa)	Time of flight (μs)			Wave speed (m/s)			v_u	E_u (MPa)	K_u (MPa)	G_u (MPa)
		P-wave	S1-wave	S2 -wave	P-wave	S1-wave	S2-wave				
W1	5.0	41.2	101.0	101.0	2360	736	736	0.446	3648	11292	1261
	10.0	39.0	93.1	93.1	2658	839	839	0.445	4740	14272	1640
	15.0	36.2	83.6	83.6	3162	1012	1012	0.443	6880	20116	2384
	20.0	34.9	79.2	79.2	3461	1117	1117	0.442	8382	24027	2907
	25.0	34.0	76.6	76.6	3693	1190	1190	0.442	9514	27382	3299
	30.0	33.4	73.4	73.4	3890	1295	1295	0.438	11234	30055	3907
	35.0	32.6	71.1	71.1	4146	1384	1384	0.437	12828	34106	4463
	40.0	32.4	69.6	69.6	4228	1448	1448	0.434	14001	35148	4883
	45.0	32.1	68.6	68.6	4352	1492	1492	0.433	14861	37224	5184
	50.0	32.0	68.1	68.1	4397	1518	1518	0.432	15373	37901	5366
	55.0	31.9	67.1	67.1	4444	1566	1566	0.429	16330	38407	5713
	60.0	31.9	67.1	67.1	4444	1566	1566	0.43	16330	38407	5713
	65.0	31.9	67.1	67.1	4444	1566	1566	0.43	16330	38407	5713
	70.0	31.9	67.1	67.1	4444	1566	1566	0.43	16330	38407	5713
W2	5.0	39.9	96.0	96.0	2258	713	713	0.44	3424	10300	1185
	10.0	38.9	92.0	92.0	2386	765	765	0.44	3937	11450	1364
	15.0	35.6	80.8	80.8	2937	961	961	0.44	6202	17228	2154
	20.0	34.4	76.6	76.6	3206	1064	1064	0.44	7582	20436	2636
	25.0	33.6	74.0	74.0	3415	1139	1139	0.44	8684	23140	3021
	30.0	32.8	71.0	71.0	3652	1239	1239	0.43	10272	26306	3579
	35.0	32.2	69.0	69.0	3853	1317	1317	0.43	11592	29204	4042
	40.0	31.8	67.6	67.6	4000	1378	1378	0.43	12671	31384	4422
	45.0	31.6	66.8	66.8	4078	1415	1415	0.43	13353	32524	4664
	50.0	31.4	66.2	66.2	4158	1444	1444	0.43	13908	33814	4858
	55.0	31.2	65.4	65.4	4242	1485	1485	0.43	14693	35087	5137
	60.0	31.2	65.4	65.4	4242	1485	1485	0.43	14693	35087	5137
	65.0	31.2	65.4	65.4	4242	1485	1485	0.43	14693	35087	5137
	70.0	31.2	65.4	65.4	4242	1485	1485	0.43	14693	35087	5137

To be continued

Sample	Hydrostatic stress (MPa)	Time of flight (μs)			Wave speed (m/s)			v_u	E_u (MPa)	K_u (MPa)	G_u (MPa)
		P-wave	S1-wave	S2 -wave	P-wave	S1-wave	S2-wave				
W3	5.0	40.0	98.0	98.0	2193	673	673	0.45	3041	9733	1050
	10.0	36.8	87.0	87.0	2645	822	822	0.45	4526	14119	1564
	15.0	34.8	80.4	80.4	3037	947	947	0.45	6009	18592	2078
	20.0	33.6	76.4	76.4	3333	1044	1044	0.45	7293	22370	2522
	25.0	32.8	74.2	74.2	3565	1106	1106	0.45	8190	25664	2831
	30.0	32.4	71.2	71.2	3694	1203	1203	0.44	9655	27131	3351
	35.0	31.6	68.8	68.8	3981	1294	1294	0.44	11174	31527	3877
	40.0	31.6	67.4	67.4	3981	1354	1354	0.43	12178	31038	4244
	45.0	31.2	66.4	66.4	4141	1400	1400	0.44	13031	33670	4539
	50.0	31.2	66.0	66.0	4141	1419	1419	0.43	13376	33502	4666
	55.0	31.2	65.0	65.0	4141	1470	1470	0.43	14297	33048	5006
	60.0	31.2	65.0	65.0	4141	1470	1470	0.43	14297	33048	5006
	65.0	31.2	65.0	65.0	4141	1470	1470	0.43	14297	33048	5006
	70.0	31.2	65.0	65.0	4141	1470	1470	0.43	14297	33048	5006
W4	5.0	42.7	107.5	107.5	2244	682	682	0.45	3110	10199	1073
	10.0	39.0	94.8	94.8	2713	832	832	0.45	4630	14875	1599
	15.0	36.7	85.6	85.6	3122	990	990	0.44	6535	19492	2263
	20.0	35.3	80.5	80.5	3431	1107	1107	0.44	8163	23424	2831
	25.0	34.6	77.7	77.7	3609	1184	1184	0.44	9319	25767	3236
	30.0	34.1	75.3	75.3	3739	1256	1256	0.44	10467	27432	3643
	35.0	33.2	72.7	72.7	4029	1350	1350	0.44	12091	31890	4207
	40.0	33.2	71.5	71.5	4029	1394	1394	0.43	12855	31516	4488
	45.0	32.8	70.1	70.1	4192	1453	1453	0.43	13965	34089	4877
	50.0	32.8	69.9	69.9	4192	1463	1463	0.43	14142	34002	4942
	55.0	32.8	69.4	69.4	4192	1488	1488	0.43	14609	33771	5116
	60.0	32.8	69.4	69.4	4192	1488	1488	0.43	14609	33771	5116
	65.0	32.8	69.4	69.4	4192	1488	1488	0.43	14609	33771	5116
	70.0	32.8	69.4	69.4	4192	1488	1488	0.43	14609	33771	5116

To be continued

Sample	Hydrostatic stress (MPa)	Time of flight (μs)			Wave speed (m/s)			υ_u	E_u (MPa)	K_u (MPa)	G_u (MPa)
		P-wave	S1-wave	S2 -wave	P-wave	S1-wave	S2-wave				
W5	5.0	42.8	106.6	106.6	2182	677	677	0.45	3044	9534	1052
	10.0	38.6	92.4	92.4	2711	851	851	0.45	4803	14672	1662
	15.0	36.2	82.6	82.6	3159	1032	1032	0.44	7050	19653	2448
	20.0	34.8	77.7	77.7	3472	1158	1158	0.44	8849	23586	3078
	25.0	34.4	75.2	75.2	3591	1233	1233	0.43	10007	24962	3491
	30.0	33.9	73.7	73.7	3718	1285	1285	0.43	10870	26692	3795
	35.0	33.0	71.1	71.1	4001	1383	1383	0.43	12577	30925	4391
	40.0	33.0	70.4	70.4	4001	1410	1410	0.43	13060	30686	4569
	45.0	32.6	69.1	69.1	4160	1470	1470	0.43	14184	33133	4964
	50.0	32.4	68.9	68.9	4242	1480	1480	0.43	14397	34633	5031
	55.0	32.4	68.3	68.3	4242	1506	1506	0.43	14879	34395	5210
	60.0	32.4	68.3	68.3	4242	1506	1506	0.43	14879	34395	5210
	65.0	32.4	68.3	68.3	4242	1506	1506	0.43	14879	34395	5210
	70.0	32.4	68.3	68.3	4242	1506	1506	0.43	14879	34395	5210
W6	5.0	41.1	100.9	100.9	2195	682	682	0.45	3125	9736	1080
	10.0	38.2	88.0	88.0	2578	855	855	0.44	4882	13161	1697
	15.0	35.5	78.8	78.8	3059	1044	1044	0.43	7256	18340	2530
	20.0	34.1	74.4	74.4	3400	1168	1168	0.43	9068	22600	3164
	25.0	33.5	71.6	71.6	3570	1263	1263	0.43	10571	24642	3700
	30.0	32.9	69.7	69.7	3761	1335	1335	0.43	11809	27307	4135
	35.0	32.3	68.1	68.1	3971	1403	1403	0.43	13056	30489	4569
	40.0	32.0	66.8	66.8	4048	1463	1463	0.42	14155	31393	4967
	45.0	31.6	65.8	65.8	4208	1516	1516	0.43	15192	33984	5329
	50.0	31.4	65.6	66.2	4292	1526	1497	0.43	15148	35666	5300
	55.0	31.4	65.1	65.1	4292	1552	1552	0.42	15922	35282	5588
	60.0	31.4	65.1	65.1	4292	1552	1552	0.42	15922	35282	5588
	65.0	31.4	65.1	65.1	4292	1552	1552	0.42	15922	35282	5588
	70.0	31.4	65.1	65.1	4292	1552	1552	0.42	15922	35282	5588

To be continued

Sample	Hydrostatic stress (MPa)	Time of flight (μs)			Wave speed (m/s)			υ_u	E_u (MPa)	K_u (MPa)	G_u (MPa)
		P-wave	S1-wave	S2 -wave	P-wave	S1-wave	S2-wave				
W7	5.0	42.5	106.5	106.5	2212	678	678	0.45	3059	9846	1056
	10.0	39.7	93.8	93.8	2549	829	829	0.44	4551	12836	1579
	15.0	37.5	86.8	86.8	2897	946	946	0.44	5926	16562	2057
	20.0	35.9	79.0	79.0	3209	1122	1122	0.43	8282	19826	2895
	25.0	34.6	73.9	73.9	3529	1277	1277	0.42	10692	23647	3752
	30.0	33.9	72.1	72.1	3718	1343	1343	0.42	11827	26260	4150
	35.0	33.3	70.4	70.4	3925	1410	1410	0.43	13041	29340	4573
	40.0	32.8	69.1	69.1	4078	1470	1470	0.43	14169	31615	4971
	45.0	32.6	68.3	68.3	4160	1508	1508	0.42	14900	32830	5230
	50.0	32.4	67.8	68.3	4242	1534	1506	0.43	15161	34310	5315
	55.0	32.4	67.8	67.8	4242	1534	1534	0.42	15424	34179	5413
	60.0	32.4	67.8	67.8	4242	1534	1534	0.42	15424	34179	5413
	65.0	32.4	67.8	67.8	4242	1534	1534	0.42	15424	34179	5413
	70.0	32.4	67.8	67.8	4242	1534	1534	0.42	15424	34179	5413
W8	5.0	40.8	99.2	99.2	2154	676	676	0.45	3066	9339	1061
	10.0	37.6	88.0	88.0	2577	825	825	0.44	4557	13285	1579
	15.0	34.4	78.0	78.0	3206	1027	1027	0.44	7058	20566	2446
	20.0	33.2	74.0	74.0	3529	1139	1139	0.44	8666	24868	3005
	25.0	32.4	70.0	70.0	3784	1277	1277	0.44	10856	28146	3781
	30.0	32.0	69.0	69.0	3925	1317	1317	0.44	11554	30353	4021
	35.0	31.6	67.0	67.0	4078	1405	1405	0.43	13116	32439	4578
	40.0	31.6	67.4	67.4	4078	1387	1387	0.43	12790	32599	4458
	45.0	31.2	66.4	66.4	4242	1434	1434	0.44	13687	35363	4767
	50.0	31.2	66.0	66.0	4242	1454	1454	0.43	14048	35186	4900
	55.0	31.2	65.0	65.0	4242	1506	1506	0.43	15015	34709	5258
	60.0	31.2	65.0	65.0	4242	1506	1506	0.43	15015	34709	5258
	65.0	31.2	65.0	65.0	4242	1506	1506	0.43	15015	34709	5258
	70.0	31.2	65.0	65.0	4242	1506	1506	0.43	15015	34709	5258

To be continued

Sample	Hydrostatic stress (MPa)	Time of flight (µs)			Wave speed (m/s)			υ_u	E_u (MPa)	K_u (MPa)	G_u (MPa)
		P-wave	S1-wave	S2 -wave	P-wave	S1-wave	S2-wave				
W9	5.0	39.6	98.0	98.0	2295	690	690	0.45	3241	10878	1117
	10.0	36.4	87.0	87.0	2781	842	842	0.45	4825	15946	1664
	15.0	34.4	77.8	77.8	3206	1032	1032	0.44	7217	20799	2502
	20.0	33.2	73.0	73.0	3529	1170	1170	0.44	9251	24960	3216
	25.0	32.8	70.4	70.4	3652	1262	1262	0.43	10708	26334	3738
	30.0	32.4	69.2	69.2	3784	1309	1309	0.43	11522	28252	4023
	35.0	31.6	67.0	67.0	4078	1405	1405	0.43	13286	32859	4637
	40.0	31.6	66.4	66.4	4078	1434	1434	0.43	13805	32603	4829
	45.0	31.2	65.0	65.0	4242	1506	1506	0.43	15210	35158	5326
	50.0	31.2	65.0	65.0	4242	1506	1506	0.43	15210	35158	5326
	55.0	31.2	65.0	65.0	4242	1506	1506	0.43	15210	35158	5326
	60.0	31.2	65.0	65.0	4242	1506	1506	0.43	15210	35158	5326
	65.0	31.2	65.0	65.0	4242	1506	1506	0.43	15210	35158	5326
	70.0	31.2	65.0	65.0	4242	1506	1506	0.43	15210	35158	5326
W10	5.0	40.8	99.8	99.8	2154	670	670	0.45	3040	9459	1051
	10.0	37.2	88.0	88.0	2642	825	825	0.45	4612	14208	1595
	15.0	36.0	86.0	86.0	2857	859	859	0.45	5012	16806	1728
	20.0	34.8	76.0	76.0	3111	1080	1080	0.43	7818	19017	2731
	25.0	33.2	70.4	70.4	3529	1262	1262	0.43	10635	24192	3727
	30.0	32.8	69.2	69.2	3652	1309	1309	0.43	11442	25877	4011
	35.0	32.0	67.0	67.0	3925	1405	1405	0.43	13190	29905	4623
	40.0	31.6	66.4	66.4	4078	1434	1434	0.43	13764	32505	4815
	45.0	31.6	66.0	66.0	4078	1454	1454	0.43	14125	32326	4949
	50.0	31.2	65.0	65.0	4242	1506	1506	0.43	15164	35054	5310
	55.0	31.2	65.0	65.0	4242	1506	1506	0.43	15164	35054	5310
	60.0	31.2	65.0	65.0	4242	1506	1506	0.43	15164	35054	5310
	65.0	31.2	65.0	65.0	4242	1506	1506	0.43	15164	35054	5310
	70.0	31.2	65.0	65.0	4242	1506	1506	0.43	15164	35054	5310

To be continued

Sample	Hydrostatic stress (MPa)	Time of flight (μs)			Wave speed (m/s)			v_u	E_u (MPa)	K_u (MPa)	G_u (MPa)
		P-wave	S1-wave	S2 -wave	P-wave	S1-wave	S2-wave				
W11	5.0	42.0	103.8	103.8	2173	675	675	0.45	3081	9622	1065
	10.0	38.5	91.8	91.8	2611	824	824	0.44	4583	13823	1586
	15.0	35.7	82.7	82.7	3122	987	987	0.44	6582	19744	2279
	20.0	34.4	78.4	78.4	3431	1091	1091	0.44	8037	23817	2783
	25.0	33.5	74.9	74.9	3675	1191	1191	0.44	9565	27143	3318
	30.0	33.1	72.8	72.8	3809	1260	1260	0.44	10679	28980	3712
	35.0	32.5	70.5	70.5	4029	1350	1350	0.44	12237	32277	4258
	40.0	32.5	70.0	70.0	4029	1370	1370	0.43	12595	32102	4390
	45.0	32.0	68.9	68.9	4192	1417	1417	0.44	13478	34824	4695
	50.0	32.0	68.4	68.4	4192	1437	1437	0.43	13834	34650	4825
	55.0	32.0	67.4	67.4	4192	1488	1488	0.43	14787	34180	5178
	60.0	32.0	67.4	67.4	4192	1488	1488	0.43	14787	34180	5178
	65.0	32.0	67.4	67.4	4192	1488	1488	0.43	14787	34180	5178
	70.0	32.0	67.4	67.4	4192	1488	1488	0.43	14787	34180	5178
W12	5.0	39.8	98.4	98.4	2270	685	685	0.45	3165	10523	1091
	10.0	38.4	87.6	87.6	2456	832	832	0.44	4617	11875	1608
	15.0	35.6	77.8	77.8	2937	1032	1032	0.43	7080	16746	2476
	20.0	34.0	73.2	73.2	3307	1164	1164	0.43	8999	21220	3148
	25.0	33.2	69.6	69.6	3529	1293	1293	0.42	11051	23770	3884
	30.0	32.4	67.6	67.6	3784	1378	1378	0.42	12558	27392	4411
	35.0	32.0	66.8	66.8	3925	1415	1415	0.43	13260	29605	4652
	40.0	31.6	65.0	65.0	4078	1506	1506	0.42	14982	31613	5271
	45.0	31.2	64.0	64.0	4242	1562	1562	0.42	16123	34267	5671
	50.0	31.2	64.0	65.0	4242	1562	1506	0.42	15585	34535	5469
	55.0	31.2	64.0	64.0	4242	1562	1562	0.42	16123	34267	5671
	60.0	31.2	64.0	64.0	4242	1562	1562	0.42	16123	34267	5671
	65.0	31.2	64.0	64.0	4242	1562	1562	0.42	16123	34267	5671
	70.0	31.2	64.0	64.0	4242	1562	1562	0.42	16123	34267	5671

To be continued

Sample	Hydrostatic stress (MPa)	Time of flight (μs)			Wave speed (m/s)			v_u	E_u (MPa)	K_u (MPa)	G_u (MPa)
		P-wave	S1-wave	S2 -wave	P-wave	S1-wave	S2-wave				
W13	5.0	40.7	100.0	100.0	2264	699	699	0.45	3284	10381	1134
	10.0	39.5	92.2	92.2	2421	799	799	0.44	4258	11628	1479
	15.0	36.3	81.3	81.3	2937	997	997	0.43	6616	16939	2305
	20.0	34.8	76.6	76.6	3257	1114	1114	0.43	8252	20767	2878
	25.0	34.0	73.3	73.3	3472	1216	1216	0.43	9808	23396	3429
	30.0	33.1	70.7	70.7	3718	1309	1309	0.43	11356	26774	3972
	35.0	32.6	69.3	69.3	3889	1366	1366	0.43	12377	29321	4329
	40.0	32.2	67.6	67.6	4039	1442	1442	0.43	13765	31413	4823
	45.0	31.9	66.7	66.7	4160	1488	1488	0.43	14665	33297	5140
	50.0	31.8	66.4	66.9	4200	1503	1475	0.43	14692	34075	5144
	55.0	31.7	66.0	66.0	4242	1523	1523	0.43	15356	34577	5384
	60.0	31.7	66.0	66.0	4242	1523	1523	0.43	15356	34577	5384
	65.0	31.7	66.0	66.0	4242	1523	1523	0.43	15356	34577	5384
	70.0	31.7	66.0	66.0	4242	1523	1523	0.43	15356	34577	5384
W14	5.0	43.1	106.1	106.1	2111	667	667	0.44	2970	8936	1028
	10.0	38.7	91.7	91.7	2642	842	842	0.44	4735	13945	1640
	15.0	36.7	85.8	85.8	2984	946	946	0.44	5972	17831	2068
	20.0	35.4	78.5	78.5	3263	1112	1112	0.43	8207	20799	2861
	25.0	34.3	74.4	74.4	3529	1233	1233	0.43	10053	24115	3514
	30.0	33.9	72.9	72.9	3652	1285	1285	0.43	10919	25745	3820
	35.0	33.0	70.4	70.4	3925	1383	1383	0.43	12632	29730	4419
	40.0	32.8	69.7	69.7	4001	1410	1410	0.43	13145	30887	4599
	45.0	32.6	69.0	69.0	4078	1444	1444	0.43	13772	32015	4821
	50.0	32.1	68.2	68.2	4242	1480	1480	0.43	14491	34859	5064
	55.0	32.1	67.7	67.7	4242	1506	1506	0.43	14977	34619	5244
	60.0	32.1	67.7	67.7	4242	1506	1506	0.43	14977	34619	5244
	65.0	32.1	67.7	67.7	4242	1506	1506	0.43	14977	34619	5244
	70.0	32.1	67.7	67.7	4242	1506	1506	0.43	14977	34619	5244

To be continued

Sample	Hydrostatic stress (MPa)	Time of flight (μs)			Wave speed (m/s)			v_u	E_u (MPa)	K_u (MPa)	G_u (MPa)
		P-wave	S1-wave	S2 -wave	P-wave	S1-wave	S2-wave				
W15	5.0	42.4	105.9	105.9	2224	683	683	0.45	3133	10028	1082
	10.0	38.8	93.5	93.5	2679	834	834	0.45	4660	14489	1611
	15.0	36.0	82.8	82.8	3206	1030	1030	0.44	7091	20550	2458
	20.0	34.6	77.8	77.8	3529	1154	1154	0.44	8898	24755	3089
	25.0	33.9	74.1	74.1	3718	1269	1269	0.43	10713	27062	3735
	30.0	33.5	72.9	72.9	3855	1313	1313	0.43	11465	29110	3996
	35.0	32.8	70.6	70.6	4078	1405	1405	0.43	13116	32439	4578
	40.0	32.8	70.4	70.4	4078	1410	1410	0.43	13207	32394	4611
	45.0	32.4	69.1	69.1	4242	1470	1470	0.43	14345	35040	5010
	50.0	32.4	68.9	68.9	4242	1480	1480	0.43	14529	34950	5077
	55.0	32.4	68.3	68.3	4242	1506	1506	0.43	15015	34709	5258
	60.0	32.4	68.3	68.3	4242	1506	1506	0.43	15015	34709	5258
	65.0	32.4	68.3	68.3	4242	1506	1506	0.43	15015	34709	5258
	70.0	32.4	68.3	68.3	4242	1506	1506	0.43	15015	34709	5258
W16	5.0	41.6	100.4	100.4	2069	664	664	0.44	2953	8583	1024
	10.0	37.2	86.0	86.0	2642	859	859	0.44	4943	13929	1715
	15.0	34.8	77.8	77.8	3111	1032	1032	0.44	7123	19192	2476
	20.0	33.6	73.8	73.8	3415	1145	1145	0.44	8752	23036	3046
	25.0	33.2	72.0	72.0	3529	1204	1204	0.43	9661	24458	3368
	30.0	32.8	70.4	70.4	3652	1262	1262	0.43	10598	26065	3700
	35.0	32.0	68.0	68.0	3925	1360	1360	0.43	12306	30077	4297
	40.0	32.0	67.4	67.4	3925	1387	1387	0.43	12770	29848	4469
	45.0	31.6	66.4	66.4	4078	1434	1434	0.43	13664	32269	4780
	50.0	31.2	66.0	66.0	4242	1454	1454	0.43	14085	35277	4913
	55.0	31.2	65.0	65.0	4242	1506	1506	0.43	15054	34799	5271
	60.0	31.2	65.0	65.0	4242	1506	1506	0.43	15054	34799	5271
	65.0	31.2	65.0	65.0	4242	1506	1506	0.43	15054	34799	5271
	70.0	31.2	65.0	65.0	4242	1506	1506	0.43	15054	34799	5271

To be continued

Sample	Hydrostatic stress (MPa)	Time of flight (μs)			Wave speed (m/s)			υ_u	E_u (MPa)	K_u (MPa)	G_u (MPa)
		P-wave	S1-wave	S2 -wave	P-wave	S1-wave	S2-wave				
T1	5.0	36.4	72.0	72.0	3179	1376	1376	0.385	12687	18346	4581
	10.0	36.2	70.0	70.0	3221	1460	1460	0.371	14134	18241	5155
	15.0	36.0	69.0	69.0	3265	1505	1505	0.365	14971	18491	5484
	20.0	35.2	67.6	67.6	3453	1574	1574	0.369	16422	20860	5999
	25.0	34.8	66.8	66.8	3556	1617	1617	0.370	17330	22158	6327
	30.0	34.4	65.8	65.8	3664	1673	1673	0.368	18541	23457	6775
	35.0	34.2	65.2	65.2	3721	1709	1709	0.366	19314	24082	7068
	40.0	34.0	64.8	64.8	3780	1734	1734	0.367	19882	24871	7274
	45.0	34.0	64.6	64.6	3780	1746	1746	0.364	20136	24730	7380
	50.0	34.0	64.4	64.4	3780	1759	1759	0.362	20394	24585	7488
	55.0	33.8	63.8	63.8	3840	1799	1799	0.359	21286	25246	7829
	60.0	33.8	63.2	63.2	3840	1840	1840	0.35	22138	24760	8193
	65.0	33.8	63.2	63.2	3840	1840	1840	0.35	22138	24760	8193
	70.0	33.8	63.2	63.2	3840	1840	1840	0.35	22138	24760	8193
T2	5.0	38.1	76.0	76.0	2619	1131	1131	0.39	8513	12366	3073
	10.0	37.4	75.4	75.4	2733	1149	1149	0.39	8828	13699	3170
	15.0	36.8	73.0	73.0	2839	1226	1226	0.39	9996	14529	3608
	20.0	36.0	70.0	70.0	2993	1338	1338	0.38	11816	15774	4296
	25.0	35.6	69.6	69.6	3077	1354	1354	0.38	12149	16852	4402
	30.0	35.4	68.4	68.4	3121	1406	1406	0.37	13030	17042	4747
	35.0	35.2	67.6	67.6	3165	1443	1443	0.37	13685	17383	4999
	40.0	35.1	66.4	66.4	3188	1502	1502	0.36	14705	17175	5417
	45.0	35.0	65.6	65.6	3212	1545	1545	0.35	15454	17122	5726
	50.0	34.8	64.4	64.4	3259	1612	1612	0.34	16698	17174	6240
	55.0	34.6	63.4	63.4	3308	1674	1674	0.33	17859	17302	6724
	60.0	34.4	62.8	62.8	3359	1713	1713	0.32	18650	17686	7042
	65.0	34.4	62.8	62.8	3359	1713	1713	0.32	18650	17686	7042
	70.0	34.4	62.8	62.8	3359	1713	1713	0.32	18650	17686	7042

To be continued

Sample	Hydrostatic stress (MPa)	Time of flight (μs)			Wave speed (m/s)			υ_u	E_u (MPa)	K_u (MPa)	G_u (MPa)
		P-wave	S1-wave	S2 -wave	P-wave	S1-wave	S2-wave				
T3	5.0	38.0	76.4	76.4	2455	1044	1044	0.39	6720	10157	2418
	10.0	37.4	74.8	74.8	2547	1088	1088	0.39	7296	10894	2627
	15.0	36.8	73.0	73.0	2645	1142	1142	0.39	8028	11670	2898
	20.0	35.8	70.0	70.0	2828	1247	1247	0.38	9519	13149	3450
	25.0	35.4	69.0	69.0	2908	1286	1286	0.38	10119	13877	3670
	30.0	35.0	68.2	68.2	2993	1319	1319	0.38	10654	14734	3862
	35.0	34.8	68.0	68.0	3037	1327	1327	0.38	10811	15261	3912
	40.0	34.6	67.8	67.8	3083	1336	1336	0.38	10972	15813	3963
	45.0	34.4	66.2	66.2	3130	1410	1410	0.37	12110	15865	4411
	50.0	34.4	65.0	65.0	3130	1470	1470	0.36	13037	15348	4799
	55.0	34.4	63.0	63.0	3130	1584	1584	0.33	14789	14321	5569
	60.0	34.2	62.0	62.0	3178	1647	1647	0.32	15862	14392	6025
	65.0	34.0	61.4	61.4	3228	1688	1688	0.31	16599	14702	6327
	70.0	34.0	61.0	61.0	3228	1716	1716	0.30	17044	14417	6540
T4	5.0	37.6	76.0	76.0	2638	1106	1106	0.39	7497	11724	2690
	10.0	36.8	75.0	75.0	2774	1135	1135	0.40	7932	13153	2834
	15.0	36.2	73.2	73.2	2886	1192	1192	0.40	8729	14158	3124
	20.0	35.6	70.6	70.6	3007	1284	1284	0.39	10073	15056	3628
	25.0	35.4	70.4	70.4	3050	1292	1292	0.39	10211	15566	3671
	30.0	35.2	69.6	69.6	3094	1324	1324	0.39	10699	15915	3854
	35.0	35.0	70.0	70.0	3139	1308	1308	0.40	10493	16658	3761
	40.0	34.8	69.6	69.6	3185	1324	1324	0.40	10758	17181	3854
	45.0	34.6	69.2	69.2	3233	1340	1340	0.40	11033	17728	3951
	50.0	34.4	68.0	68.0	3282	1392	1392	0.39	11857	18019	4264
	55.0	34.4	68.0	68.0	3282	1392	1392	0.39	11857	18019	4264
	60.0	34.4	68.0	68.0	3282	1392	1392	0.39	11857	18019	4264
	65.0	34.0	65.0	65.0	3386	1542	1542	0.37	14323	18246	5231
	70.0	34.0	65.0	65.0	3386	1542	1542	0.37	14323	18246	5231

To be continued

Sample	Hydrostatic stress (MPa)	Time of flight (μs)			Wave speed (m/s)			υ_u	E_u (MPa)	K_u (MPa)	G_u (MPa)
		P-wave	S1-wave	S2 -wave	P-wave	S1-wave	S2-wave				
T5	5.0	38.1	78.0	78.0	3036	1247	1247	0.40	9693	15906	3466
	10.0	37.2	75.2	75.4	3208	1339	1332	0.40	11086	17619	3973
	15.0	36.8	72.8	73.0	3290	1429	1421	0.38	12527	18083	4524
	20.0	36.0	69.2	70.0	3469	1589	1551	0.37	15059	19489	5491
	25.0	35.6	69.4	69.6	3566	1580	1570	0.38	15233	20967	5523
	30.0	35.4	68.2	68.4	3617	1641	1630	0.37	16339	21199	5957
	35.0	35.2	67.2	67.6	3669	1695	1673	0.37	17263	21564	6316
	40.0	35.2	66.0	66.4	3669	1766	1741	0.35	18518	20854	6848
	45.0	35.0	65.2	65.6	3723	1816	1790	0.35	19504	21212	7241
	50.0	34.8	64.0	64.4	3778	1897	1869	0.33	21081	21259	7897
	55.0	34.6	63.2	63.4	3835	1955	1940	0.33	22409	21487	8449
	60.0	34.4	62.4	62.8	3893	2017	1985	0.32	23556	21866	8920
	65.0	34.4	62.2	62.8	3893	2033	1985	0.32	23711	21771	8992
	70.0	34.4	62.2	62.8	3893	2033	1985	0.32	23711	21771	8992
T6	5.0	39.2	80.2	80.2	2765	1149	1149	0.40	8181	13073	2931
	10.0	38.8	78.0	78.0	2829	1211	1211	0.39	9034	13426	3255
	15.0	37.6	74.0	74.0	3037	1342	1342	0.38	11026	15146	3999
	20.0	36.8	72.0	72.0	3194	1419	1419	0.38	12311	16686	4470
	25.0	36.6	71.0	71.0	3235	1461	1461	0.37	13001	16925	4738
	30.0	36.4	70.0	70.0	3278	1505	1505	0.37	13748	17155	5031
	35.0	35.6	67.2	67.2	3462	1645	1645	0.35	16277	18593	6010
	40.0	34.8	64.0	64.0	3667	1841	1841	0.33	20042	19818	7526
	45.0	34.4	63.0	63.0	3779	1912	1912	0.33	21562	20879	8119
	50.0	34.4	62.4	62.4	3779	1958	1958	0.32	22405	20359	8509
	55.0	34.4	62.4	62.4	3779	1958	1958	0.32	22405	20359	8509
	60.0	34.2	61.8	61.8	3837	2005	2005	0.31	23429	20792	8927
	65.0	34.2	61.8	61.8	3837	2005	2005	0.31	23429	20792	8927
	70.0	34.2	61.8	61.8	3837	2005	2005	0.31	23429	20792	8927

To be continued

Sample	Hydrostatic stress (MPa)	Time of flight (μs)			Wave speed (m/s)			υ_u	E_u (MPa)	K_u (MPa)	G_u (MPa)
		P-wave	S1-wave	S2 -wave	P-wave	S1-wave	S2-wave				
T7	5.0	38.0	76.4	76.4	2695	1145	1145	0.39	8387	12677	3018
	10.0	37.2	74.0	74.0	2830	1220	1220	0.39	9488	13859	3423
	15.0	36.8	73.0	73.0	2903	1254	1254	0.39	10020	14564	3616
	20.0	36.6	70.0	70.0	2941	1368	1368	0.36	11729	14154	4306
	25.0	34.6	65.4	65.4	3383	1591	1591	0.36	15810	18569	5821
	30.0	34.0	64.0	64.0	3543	1674	1674	0.36	17478	20286	6443
	35.0	33.6	63.0	63.0	3659	1738	1738	0.35	18824	21518	6950
	40.0	32.8	61.0	61.0	3913	1884	1884	0.35	22025	24334	8163
	45.0	32.6	60.4	60.4	3982	1932	1932	0.35	23121	25023	8589
	50.0	32.4	60.0	60.0	4054	1966	1966	0.35	23940	25946	8892
	55.0	32.4	60.0	60.0	4054	1966	1966	0.35	23940	25946	8892
	60.0	32.4	59.4	59.4	4054	2019	2019	0.34	25037	25299	9377
	65.0	32.4	59.4	59.4	4054	2019	2019	0.34	25037	25299	9377
	70.0	32.4	59.4	59.4	4054	2019	2019	0.34	25037	25299	9377
T8	5.0	37.8	76.0	76.0	2455	1041	1041	0.39	6876	10439	2473
	10.0	37.4	74.8	74.8	2516	1075	1075	0.39	7311	10917	2633
	15.0	36.6	72.8	72.8	2647	1135	1135	0.39	8148	12060	2936
	20.0	35.8	70.0	70.0	2793	1231	1231	0.38	9539	13177	3458
	25.0	35.4	69.0	69.0	2872	1270	1270	0.38	10140	13907	3678
	30.0	35.0	68.2	68.2	2956	1303	1303	0.38	10677	14766	3870
	35.0	34.8	68.0	68.0	3000	1311	1311	0.38	10835	15293	3920
	40.0	34.6	67.8	67.8	3045	1320	1320	0.38	10995	15847	3971
	45.0	34.4	66.2	66.2	3092	1392	1392	0.37	12136	15899	4420
	50.0	34.4	65.0	65.0	3092	1452	1452	0.36	13065	15380	4809
	55.0	34.4	63.0	63.0	3092	1564	1564	0.33	14821	14351	5581
	60.0	34.2	62.0	62.0	3140	1627	1627	0.32	15896	14422	6038
	65.0	34.0	61.4	61.4	3189	1668	1668	0.31	16634	14733	6340
	70.0	34.0	61.0	61.0	3189	1695	1695	0.30	17080	14448	6554

To be continued

Sample	Hydrostatic stress (MPa)	Time of flight (μs)			Wave speed (m/s)			υ_u	E_u (MPa)	K_u (MPa)	G_u (MPa)
		P-wave	S1-wave	S2 -wave	P-wave	S1-wave	S2-wave				
T9	5.0	38.0	78.6	78.6	2395	964	964	0.40	5975	10299	2129
	10.0	37.4	76.2	76.2	2484	1023	1023	0.40	6705	10938	2398
	15.0	36.2	73.0	73.0	2685	1115	1115	0.40	7942	12710	2845
	20.0	35.8	71.0	71.0	2759	1180	1180	0.39	8857	13173	3191
	25.0	35.6	70.0	70.0	2797	1216	1216	0.38	9373	13401	3388
	30.0	35.4	68.6	68.6	2837	1270	1270	0.37	10160	13502	3696
	35.0	35.2	67.4	67.4	2878	1321	1321	0.37	10917	13638	3994
	40.0	35.0	66.8	66.8	2920	1347	1347	0.36	11347	13978	4157
	45.0	34.8	66.0	66.0	2963	1385	1385	0.36	11946	14250	4391
	50.0	34.6	65.0	65.0	3008	1434	1434	0.35	12747	14432	4711
	55.0	34.4	64.0	64.0	3053	1488	1488	0.34	13628	14593	5068
	60.0	34.2	63.0	63.0	3101	1545	1545	0.33	14596	14728	5468
	65.0	34.0	62.0	62.0	3150	1607	1607	0.32	15664	14829	5916
	70.0	33.8	61.0	61.0	3200	1675	1675	0.31	16843	14888	6421
T10	5.0	39.4	80.2	80.2	2376	998	998	0.39	6492	10099	2331
	10.0	38.6	78.0	78.0	2486	1052	1052	0.39	7200	11006	2588
	15.0	38.0	76.0	76.0	2575	1106	1106	0.39	7937	11699	2861
	20.0	37.2	73.0	73.0	2704	1198	1198	0.38	9258	12635	3360
	25.0	35.6	69.2	69.2	3007	1340	1340	0.38	11566	15555	4202
	30.0	35.0	67.4	67.4	3139	1420	1420	0.37	12937	16763	4717
	35.0	34.8	66.6	66.6	3185	1458	1458	0.37	13609	17105	4976
	40.0	34.4	65.2	65.2	3282	1531	1531	0.36	14929	17899	5485
	45.0	34.2	64.4	64.4	3333	1576	1576	0.36	15760	18252	5811
	50.0	33.6	62.8	62.8	3496	1674	1674	0.35	17721	19855	6557
	55.0	32.8	61.0	61.0	3739	1800	1800	0.35	20461	22605	7583
	60.0	32.4	59.6	59.6	3874	1912	1912	0.34	22913	23708	8556
	65.0	32.4	59.4	59.4	3874	1929	1929	0.34	23259	23502	8711
	70.0	32.4	59.0	59.0	3874	1965	1965	0.33	23968	23074	9032

To be continued

Sample	Hydrostatic stress (MPa)	Time of flight (μs)			Wave speed (m/s)			v_u	E_u (MPa)	K_u (MPa)	G_u (MPa)
		P-wave	S1-wave	S2 -wave	P-wave	S1-wave	S2-wave				
T11	5.0	42.8	88.6	88.6	2372	991	991	0.39	6567	10365	2355
	10.0	41.4	85.0	85.0	2537	1065	1065	0.39	7584	11822	2722
	15.0	40.6	82.0	82.0	2642	1136	1136	0.39	8592	12628	3098
	20.0	39.0	78.0	78.0	2881	1247	1247	0.38	10341	14947	3734
	25.0	38.2	76.0	76.0	3018	1311	1311	0.38	11423	16352	4128
	30.0	37.4	74.0	74.0	3168	1383	1383	0.38	12684	17965	4588
	35.0	37.2	72.0	72.0	3208	1462	1462	0.37	14042	17854	5129
	40.0	36.8	70.0	70.0	3290	1551	1551	0.36	15667	18287	5772
	45.0	36.2	68.0	68.0	3423	1651	1651	0.35	17646	19393	6543
	50.0	35.6	66.0	66.0	3566	1766	1766	0.34	20014	20552	7481
	55.0	35.0	64.0	64.0	3723	1897	1897	0.32	22877	21746	8635
	60.0	34.6	63.0	63.0	3835	1970	1970	0.32	24605	22870	9315
	65.0	34.6	63.0	63.0	3835	1970	1970	0.32	24605	22870	9315
	70.0	34.6	63.0	63.0	3835	1970	1970	0.32	24605	22870	9315
T12	5.0	36.0	72.2	72.2	2993	1254	1254	0.39	10430	16331	3742
	10.0	35.0	69.4	69.4	3212	1363	1363	0.39	12288	18654	4420
	15.0	33.8	66.2	66.2	3520	1513	1513	0.39	15103	22225	5445
	20.0	33.6	65.2	65.2	3577	1567	1567	0.38	16134	22665	5840
	25.0	33.6	65.0	65.0	3577	1578	1578	0.38	16342	22553	5924
	30.0	33.4	64.2	64.2	3636	1624	1624	0.38	17272	23095	6279
	35.0	33.2	63.2	63.2	3697	1687	1687	0.37	18531	23507	6770
	40.0	33.2	62.6	62.6	3697	1726	1726	0.36	19300	23077	7092
	45.0	33.0	62.0	62.0	3761	1768	1768	0.36	20205	23738	7438
	50.0	33.0	61.2	61.2	3761	1827	1827	0.35	21370	23068	7941
	55.0	32.8	61.4	61.4	3826	1812	1812	0.36	21174	24422	7811
	60.0	32.6	60.4	60.4	3894	1889	1889	0.35	22871	24753	8496
	65.0	32.6	60.4	60.4	3894	1889	1889	0.35	22871	24753	8496
	70.0	32.4	60.0	60.0	3964	1922	1922	0.35	23681	25665	8795

To be continued

Sample	Hydrostatic stress (MPa)	Time of flight (µs)			Wave speed (m/s)			υ_u	E_u (MPa)	K_u (MPa)	G_u (MPa)
		P-wave	S1-wave	S2 -wave	P-wave	S1-wave	S2-wave				
T13	5.0	36.2	72.0	72.0	2953	1261	1261	0.39	10645	15905	3834
	10.0	35.2	69.0	70.0	3165	1380	1338	0.39	12345	18215	4450
	15.0	34.0	66.0	66.0	3465	1523	1523	0.38	15434	21473	5591
	20.0	33.8	65.4	65.4	3520	1555	1555	0.38	16078	22086	5831
	25.0	33.6	65.0	65.0	3577	1578	1578	0.38	16550	22840	6000
	30.0	33.6	64.0	64.0	3577	1636	1636	0.37	17654	22234	6454
	35.0	33.4	63.0	63.0	3636	1700	1700	0.36	18941	22585	6962
	40.0	33.2	62.6	62.6	3697	1726	1726	0.36	19546	23371	7183
	45.0	33.0	61.8	61.8	3761	1782	1782	0.36	20750	23876	7656
	50.0	32.8	61.4	61.4	3826	1812	1812	0.36	21444	24733	7910
	55.0	32.8	61.4	61.4	3826	1812	1812	0.36	21444	24733	7910
	60.0	32.6	60.4	61.0	3894	1889	1842	0.35	22667	25354	8389
	65.0	32.6	60.4	60.4	3894	1889	1889	0.35	23162	25068	8604
	70.0	32.6	60.4	60.4	3894	1889	1889	0.35	23162	25068	8604
T14	5.0	39.2	80.0	80.0	2682	1119	1119	0.39	8360	13210	2997
	10.0	38.8	78.0	78.0	2743	1174	1174	0.39	9154	13605	3298
	15.0	37.8	74.2	74.2	2909	1294	1294	0.38	11036	14906	4008
	20.0	37.6	73.0	73.0	2945	1338	1338	0.37	11730	15043	4281
	25.0	36.6	71.0	71.0	3137	1416	1416	0.37	13174	17150	4801
	30.0	36.4	70.0	70.0	3179	1460	1460	0.37	13931	17383	5098
	35.0	35.4	67.2	67.2	3404	1595	1595	0.36	16557	19611	6090
	40.0	34.4	64.0	64.0	3664	1785	1785	0.34	20505	21958	7626
	45.0	34.2	63.0	63.0	3721	1854	1854	0.33	21963	22161	8227
	50.0	34.2	62.4	62.4	3721	1898	1898	0.32	22833	21634	8622
	55.0	34.0	61.8	61.8	3780	1944	1944	0.32	23883	22120	9046
	60.0	34.0	61.8	61.8	3780	1944	1944	0.32	23883	22120	9046
	65.0	33.8	61.0	61.0	3840	2009	2009	0.31	25343	22402	9662
	70.0	33.8	61.0	61.0	3840	2009	2009	0.31	25343	22402	9662

To be continued

Sample	Hydrostatic stress (MPa)	Time of flight (µs)			Wave speed (m/s)			υ_u	E_u (MPa)	K_u (MPa)	G_u (MPa)
		P-wave	S1-wave	S2 -wave	P-wave	S1-wave	S2-wave				
T15	5.0	38.1	76.0	76.0	2619	1131	1131	0.39	8513	12366	3073
	10.0	37.4	75.4	75.4	2733	1149	1149	0.39	8828	13699	3170
	15.0	36.8	73.0	73.0	2839	1226	1226	0.39	9996	14529	3608
	20.0	36.0	70.0	70.0	2993	1338	1338	0.38	11816	15774	4296
	25.0	35.6	69.6	69.6	3077	1354	1354	0.38	12149	16852	4402
	30.0	35.4	68.4	68.4	3121	1406	1406	0.37	13030	17042	4747
	35.0	35.2	67.6	67.6	3165	1443	1443	0.37	13685	17383	4999
	40.0	35.1	66.4	66.4	3188	1502	1502	0.36	14705	17175	5417
	45.0	35.0	65.6	65.6	3212	1545	1545	0.35	15454	17122	5726
	50.0	34.8	64.4	64.4	3259	1612	1612	0.34	16698	17174	6240
	55.0	34.6	63.4	63.4	3308	1674	1674	0.33	17859	17302	6724
	60.0	34.4	62.8	62.8	3359	1713	1713	0.32	18650	17686	7042
	65.0	34.4	62.8	62.8	3359	1713	1713	0.32	18650	17686	7042
	70.0	34.4	62.8	62.8	3359	1713	1713	0.32	18650	17686	7042
T16	5.0	36.4	72.0	72.0	3179	1376	1376	0.38	12687	18346	4581
	10.0	36.2	70.0	70.0	3221	1460	1460	0.37	14134	18241	5155
	15.0	36.0	69.0	69.0	3265	1505	1505	0.37	14971	18491	5484
	20.0	35.2	67.6	67.6	3453	1574	1574	0.37	16422	20860	5999
	25.0	34.8	66.8	66.8	3556	1617	1617	0.37	17330	22158	6327
	30.0	34.4	65.8	65.8	3664	1673	1673	0.37	18541	23457	6775
	35.0	34.2	65.2	65.2	3721	1709	1709	0.37	19314	24082	7068
	40.0	34.0	64.8	64.8	3780	1734	1734	0.37	19882	24871	7274
	45.0	34.0	64.6	64.6	3780	1746	1746	0.36	20136	24730	7380
	50.0	34.0	64.4	64.4	3780	1759	1759	0.36	20394	24585	7488
	55.0	33.8	63.8	63.8	3840	1799	1799	0.36	21286	25246	7829
	60.0	33.8	63.2	63.2	3840	1840	1840	0.35	22138	24760	8193
	65.0	33.8	63.2	63.2	3840	1840	1840	0.35	22138	24760	8193
	70.0	33.8	63.2	63.2	3840	1840	1840	0.35	22138	24760	8193

To be continued

Sample	Hydrostatic stress (MPa)	Time of flight (μs)			Wave speed (m/s)			v_u	E_u (MPa)	K_u (MPa)	G_u (MPa)
		P-wave	S1-wave	S2 -wave	P-wave	S1-wave	S2-wave				
M1	5.0	38.0	75.8	75.8	2573	1111	1111	0.385	8740	12704	3155
	10.0	37.6	75.0	75.0	2634	1134	1134	0.386	9110	13344	3286
	15.0	37.4	74.4	74.4	2666	1152	1152	0.385	9392	13637	3390
	20.0	35.6	69.5	69.5	3015	1330	1330	0.379	12457	17194	4516
	25.0	35.3	68.7	68.7	3077	1363	1363	0.378	13071	17864	4742
	30.0	35.0	68.5	68.5	3143	1371	1371	0.382	13280	18822	4803
	35.0	34.8	67.7	67.7	3188	1406	1406	0.379	13932	19229	5051
	40.0	34.7	67.1	67.1	3212	1434	1434	0.375	14454	19349	5254
	45.0	34.5	66.1	66.1	3260	1482	1482	0.370	15372	19659	5612
	50.0	34.3	65.1	65.1	3309	1534	1534	0.363	16385	19952	6010
	55.0	33.8	64.1	64.1	3437	1595	1595	0.363	17706	21510	6496
	60.0	33.7	63.9	63.9	3464	1606	1606	0.36	17966	21862	6591
	65.0	33.6	63.6	63.6	3492	1624	1624	0.36	18356	22152	6739
	70.0	33.6	63.6	63.6	3492	1624	1624	0.36	18356	22152	6739
M2	5.0	37.5	74.7	74.7	2413	1037	1037	0.39	7678	11309	2768
	10.0	37.2	74.2	74.2	2456	1053	1053	0.39	7919	11733	2854
	15.0	36.8	73.2	73.2	2517	1081	1081	0.39	8345	12310	3008
	20.0	34.9	68.4	68.4	2874	1247	1247	0.38	11095	15939	4008
	25.0	34.7	67.6	67.6	2916	1279	1279	0.38	11637	16283	4213
	30.0	34.5	67.2	67.2	2958	1295	1295	0.38	11941	16783	4322
	35.0	34.3	66.6	66.6	3002	1321	1321	0.38	12400	17229	4493
	40.0	34.1	65.7	65.7	3047	1365	1365	0.37	13197	17523	4801
	45.0	33.9	64.9	64.9	3094	1403	1403	0.37	13899	17900	5071
	50.0	33.7	63.9	63.9	3142	1453	1453	0.36	14843	18177	5441
	55.0	33.4	63.1	63.1	3215	1501	1501	0.36	15786	18900	5800
	60.0	33.1	62.0	62.0	3300	1569	1569	0.35	17174	19599	6342
	65.0	33.1	62.0	62.0	3300	1569	1569	0.35	17174	19599	6342
	70.0	33.1	62.0	62.0	3300	1569	1569	0.35	17174	19599	6342

To be continued

Sample	Hydrostatic stress (MPa)	Time of flight (μs)			Wave speed (m/s)			υ_u	E_u (MPa)	K_u (MPa)	G_u (MPa)
		P-wave	S1-wave	S2 -wave	P-wave	S1-wave	S2-wave				
M3	5.0	39.0	78.0	78.0	2485	1076	1076	0.38	8208	11853	2964
	10.0	38.7	77.2	77.2	2529	1098	1098	0.38	8546	12256	3088
	15.0	38.2	76.1	76.1	2607	1127	1127	0.38	9013	13055	3254
	20.0	36.2	71.3	71.3	2950	1288	1288	0.38	11741	16623	4247
	25.0	36.0	70.4	70.4	2992	1320	1320	0.38	12304	16971	4461
	30.0	35.8	70.0	70.0	3035	1337	1337	0.38	12620	17480	4574
	35.0	35.6	69.4	69.4	3079	1362	1362	0.38	13097	17931	4751
	40.0	35.4	68.4	68.4	3124	1407	1407	0.37	13922	18224	5071
	45.0	35.2	67.5	67.5	3171	1446	1446	0.37	14649	18602	5351
	50.0	35.0	66.5	66.5	3219	1497	1497	0.36	15622	18877	5735
	55.0	34.6	65.2	65.2	3306	1569	1569	0.35	17066	19588	6298
	60.0	34.6	65.2	65.2	3306	1569	1569	0.35	17066	19588	6298
	65.0	34.5	65.0	65.0	3332	1580	1580	0.35	17326	19904	6394
	70.0	34.5	65.0	65.0	3332	1580	1580	0.35	17326	19904	6394
M4	5.0	39.0	78.1	78.1	2649	1145	1145	0.38	9270	13433	3347
	10.0	38.7	77.3	77.3	2704	1169	1169	0.39	9657	14007	3486
	15.0	38.3	76.5	76.5	2760	1193	1193	0.39	10063	14596	3633
	20.0	36.4	71.4	71.4	3123	1371	1371	0.38	13235	18488	4793
	25.0	36.1	70.6	70.6	3178	1405	1405	0.38	13879	19050	5034
	30.0	35.8	70.3	70.3	3235	1418	1418	0.38	14164	19859	5128
	35.0	35.6	69.5	69.5	3282	1450	1450	0.38	14784	20328	5361
	40.0	35.5	68.7	68.7	3318	1488	1488	0.37	15515	20551	5645
	45.0	35.3	67.8	67.8	3367	1533	1533	0.37	16417	20926	5995
	50.0	35.1	66.7	66.7	3418	1587	1587	0.36	17503	21236	6423
	55.0	34.6	65.5	65.5	3532	1656	1656	0.36	19013	22490	6995
	60.0	34.6	65.4	65.4	3546	1662	1662	0.36	19160	22686	7048
	65.0	34.4	65.1	65.1	3574	1678	1678	0.36	19517	23017	7182
	70.0	34.4	65.1	65.1	3574	1678	1678	0.36	19517	23017	7182

To be continued

Sample	Hydrostatic stress (MPa)	Time of flight (µs)			Wave speed (m/s)			v_u	E_u (MPa)	K_u (MPa)	G_u (MPa)
		P-wave	S1-wave	S2 -wave	P-wave	S1-wave	S2-wave				
M5	5.0	37.7	75.1	75.1	2381	1027	1027	0.39	7527	10980	2716
	10.0	37.4	74.4	74.4	2424	1046	1046	0.39	7804	11382	2816
	15.0	37.1	73.7	73.7	2469	1065	1065	0.39	8099	11807	2923
	20.0	35.1	68.8	68.8	2834	1231	1231	0.38	10803	15479	3904
	25.0	34.9	68.0	68.0	2875	1262	1262	0.38	11327	15810	4102
	30.0	34.7	67.6	67.6	2916	1278	1278	0.38	11621	16291	4207
	35.0	34.5	67.0	67.0	2959	1303	1303	0.38	12064	16720	4372
	40.0	34.3	66.1	66.1	3003	1347	1347	0.37	12833	17002	4669
	45.0	34.1	65.3	65.3	3049	1384	1384	0.37	13511	17364	4930
	50.0	33.9	64.3	64.3	3096	1433	1433	0.36	14419	17629	5287
	55.0	33.6	63.4	63.4	3169	1481	1481	0.36	15371	18334	5650
	60.0	33.5	63.3	63.3	3194	1492	1492	0.36	15592	18630	5730
	65.0	33.5	63.3	63.3	3194	1492	1492	0.36	15592	18630	5730
	70.0	33.5	63.3	63.3	3194	1492	1492	0.36	15592	18630	5730
M6	5.0	38.0	76.0	76.0	2515	1080	1080	0.39	8318	12262	2999
	10.0	37.8	75.4	75.4	2545	1097	1097	0.39	8575	12532	3093
	15.0	37.6	75.0	75.0	2577	1109	1109	0.39	8760	12855	3159
	20.0	35.4	69.6	69.6	2979	1293	1293	0.38	11893	17080	4297
	25.0	35.2	68.8	68.8	3022	1325	1325	0.38	12473	17449	4516
	30.0	35.0	68.4	68.4	3066	1342	1342	0.38	12799	17984	4633
	35.0	34.8	67.8	67.8	3111	1369	1369	0.38	13291	18461	4816
	40.0	34.6	66.8	66.8	3158	1415	1415	0.37	14144	18775	5145
	45.0	34.4	66.0	66.0	3206	1454	1454	0.37	14896	19179	5434
	50.0	34.2	65.0	65.0	3256	1506	1506	0.36	15906	19476	5831
	55.0	34.0	64.6	64.6	3307	1528	1528	0.36	16377	20113	6002
	60.0	33.8	64.2	64.2	3360	1551	1551	0.36	16869	20781	6181
	65.0	33.8	64.2	64.2	3360	1551	1551	0.36	16869	20781	6181
	70.0	33.8	64.2	64.2	3360	1551	1551	0.36	16869	20781	6181

To be continued

Sample	Hydrostatic stress (MPa)	Time of flight (μs)			Wave speed (m/s)			υ_u	E_u (MPa)	K_u (MPa)	G_u (MPa)
		P-wave	S1-wave	S2 -wave	P-wave	S1-wave	S2-wave				
M7	5.0	38.8	77.4	77.4	2571	1117	1117	0.38	8828	12653	3190
	10.0	38.2	76.4	76.4	2663	1145	1145	0.39	9302	13655	3354
	15.0	38.0	75.6	75.6	2695	1169	1169	0.38	9675	13904	3495
	20.0	36.4	70.8	70.8	2980	1336	1336	0.37	12540	16624	4562
	25.0	36.0	70.0	70.0	3061	1368	1368	0.38	13166	17577	4787
	30.0	35.6	70.0	70.0	3147	1368	1368	0.38	13245	18936	4787
	35.0	35.4	69.0	69.0	3191	1411	1411	0.38	14039	19253	5092
	40.0	35.4	68.8	68.8	3191	1420	1420	0.38	14197	19167	5157
	45.0	35.2	67.6	67.6	3237	1476	1476	0.37	15250	19370	5570
	50.0	35.0	66.6	66.6	3285	1526	1526	0.36	16225	19646	5955
	55.0	34.2	64.8	64.8	3488	1625	1625	0.36	18390	22107	6754
	60.0	34.2	64.8	64.8	3488	1625	1625	0.36	18390	22107	6754
	65.0	34.0	64.2	64.2	3543	1661	1661	0.36	19182	22692	7057
	70.0	34.0	64.2	64.2	3543	1661	1661	0.36	19182	22692	7057
M8	5.0	38.4	76.6	76.6	2427	1051	1051	0.38	7869	11363	2842
	10.0	38.0	75.8	75.8	2485	1073	1073	0.39	8203	11940	2960
	15.0	37.6	74.8	74.8	2546	1101	1101	0.38	8641	12517	3120
	20.0	35.6	70.0	70.0	2902	1262	1262	0.38	11335	16205	4097
	25.0	35.4	69.2	69.2	2943	1293	1293	0.38	11880	16548	4303
	30.0	35.2	68.8	68.8	2986	1310	1310	0.38	12187	17048	4413
	35.0	35.0	68.2	68.2	3029	1335	1335	0.38	12649	17493	4585
	40.0	34.8	67.2	67.2	3074	1379	1379	0.37	13450	17785	4895
	45.0	34.6	66.4	66.4	3120	1417	1417	0.37	14155	18160	5166
	50.0	34.4	65.4	65.4	3168	1467	1467	0.36	15100	18435	5537
	55.0	34.0	64.0	64.0	3268	1543	1543	0.36	16627	19298	6129
	60.0	34.0	64.0	64.0	3268	1543	1543	0.36	16627	19298	6129
	65.0	34.0	64.0	64.0	3268	1543	1543	0.36	16627	19298	6129
	70.0	34.0	64.0	64.0	3268	1543	1543	0.36	16627	19298	6129

To be continued

Sample	Hydrostatic stress (MPa)	Time of flight (μs)			Wave speed (m/s)			υ_u	E_u (MPa)	K_u (MPa)	G_u (MPa)
		P-wave	S1-wave	S2 -wave	P-wave	S1-wave	S2-wave				
M9	5.0	38.7	77.3	77.3	2470	1069	1069	0.38	8006	11583	2891
	10.0	38.3	76.5	76.5	2530	1091	1091	0.39	8347	12174	3012
	15.0	37.9	75.5	75.5	2592	1120	1120	0.39	8795	12766	3175
	20.0	35.8	70.6	70.6	2957	1285	1285	0.38	11555	16557	4176
	25.0	35.6	69.8	69.8	3000	1317	1317	0.38	12115	16911	4388
	30.0	35.4	69.4	69.4	3043	1334	1334	0.38	12430	17426	4500
	35.0	35.2	68.7	68.7	3088	1360	1360	0.38	12904	17885	4676
	40.0	35.0	67.7	67.7	3134	1405	1405	0.37	13727	18186	4995
	45.0	34.8	66.9	66.9	3181	1444	1444	0.37	14451	18573	5273
	50.0	34.6	65.9	65.9	3230	1495	1495	0.36	15424	18857	5655
	55.0	34.3	64.5	64.5	3320	1568	1568	0.36	16869	19590	6218
	60.0	34.3	64.5	64.5	3320	1568	1568	0.36	16869	19590	6218
	65.0	34.3	64.5	64.5	3320	1568	1568	0.36	16869	19590	6218
	70.0	34.3	64.5	64.5	3320	1568	1568	0.36	16869	19590	6218
M10	5.0	37.8	75.5	75.5	2425	1041	1041	0.39	7815	11521	2817
	10.0	37.5	74.9	74.9	2469	1058	1058	0.39	8067	11965	2907
	15.0	37.1	73.9	73.9	2531	1086	1086	0.39	8502	12556	3065
	20.0	35.1	69.0	69.0	2893	1254	1254	0.38	11314	16288	4087
	25.0	34.9	68.2	68.2	2935	1286	1286	0.38	11870	16642	4297
	30.0	34.7	67.8	67.8	2978	1303	1303	0.38	12182	17156	4409
	35.0	34.5	67.2	67.2	3022	1328	1328	0.38	12654	17615	4584
	40.0	34.3	66.2	66.2	3068	1373	1373	0.37	13472	17918	4900
	45.0	34.1	65.4	65.4	3115	1412	1412	0.37	14193	18307	5177
	50.0	33.9	64.5	64.5	3164	1463	1463	0.36	15163	18593	5558
	55.0	33.7	63.7	63.7	3227	1507	1507	0.36	16044	19189	5896
	60.0	33.4	62.6	62.6	3308	1572	1572	0.35	17381	19863	6418
	65.0	33.4	62.6	62.6	3308	1572	1572	0.35	17381	19863	6418
	70.0	33.4	62.6	62.6	3308	1572	1572	0.35	17381	19863	6418

To be continued

Sample	Hydrostatic stress (MPa)	Time of flight (µs)			Wave speed (m/s)			v_u	E_u (MPa)	K_u (MPa)	G_u (MPa)
		P-wave	S1-wave	S2 -wave	P-wave	S1-wave	S2-wave				
M11	5.0	39.5	79.3	79.3	2585	1115	1115	0.39	8778	12803	3167
	10.0	39.2	78.5	78.5	2623	1135	1135	0.38	9095	13163	3284
	15.0	38.8	77.8	77.8	2681	1156	1156	0.39	9446	13769	3409
	20.0	36.6	72.3	72.3	3065	1334	1334	0.38	12553	17896	4538
	25.0	36.4	71.5	71.5	3109	1368	1368	0.38	13160	18276	4768
	30.0	36.2	71.0	71.0	3154	1385	1385	0.38	13501	18830	4890
	35.0	36.0	70.4	70.4	3200	1412	1412	0.38	14015	19323	5081
	40.0	35.8	69.3	69.3	3247	1459	1459	0.37	14906	19645	5426
	45.0	35.6	68.5	68.5	3297	1499	1499	0.37	15691	20060	5728
	50.0	35.3	67.4	67.4	3347	1552	1552	0.36	16744	20363	6143
	55.0	35.0	66.5	66.5	3419	1602	1602	0.36	17779	21083	6539
	60.0	34.9	66.3	66.3	3446	1613	1613	0.36	18034	21423	6632
	65.0	34.9	66.1	66.1	3460	1619	1619	0.36	18176	21598	6684
	70.0	34.9	66.1	66.1	3460	1619	1619	0.36	18176	21598	6684
M12	5.0	37.8	75.8	75.8	2545	1086	1086	0.39	8463	12688	3047
	10.0	37.6	75.4	75.4	2577	1097	1097	0.39	8644	13016	3111
	15.0	37.2	74.4	74.4	2642	1126	1126	0.39	9111	13665	3280
	20.0	35.2	69.2	69.2	3022	1309	1309	0.38	12265	17697	4429
	25.0	35.0	68.4	68.4	3066	1342	1342	0.38	12871	18085	4659
	30.0	34.8	68.0	68.0	3111	1360	1360	0.38	13212	18649	4780
	35.0	34.6	67.4	67.4	3158	1387	1387	0.38	13727	19152	4971
	40.0	34.4	66.4	66.4	3206	1434	1434	0.37	14620	19485	5317
	45.0	34.2	65.6	65.6	3256	1474	1474	0.37	15409	19911	5620
	50.0	34.0	64.6	64.6	3307	1528	1528	0.36	16469	20226	6036
	55.0	33.8	64.2	64.2	3360	1551	1551	0.36	16965	20899	6215
	60.0	33.2	62.0	62.0	3529	1688	1688	0.35	19906	22386	7363
	65.0	33.2	62.0	62.0	3529	1688	1688	0.35	19906	22386	7363
	70.0	33.2	62.0	62.0	3529	1688	1688	0.35	19906	22386	7363

To be continued

Sample	Hydrostatic stress (MPa)	Time of flight (µs)			Wave speed (m/s)			v_u	E_u (MPa)	K_u (MPa)	G_u (MPa)
		P-wave	S1-wave	S2 -wave	P-wave	S1-wave	S2-wave				
M13	5.0	38.6	77.0	77.0	2370	1028	1028	0.38	7439	10702	2687
	10.0	38.4	76.2	76.2	2398	1049	1049	0.38	7733	10890	2798
	15.0	37.8	75.2	75.2	2485	1076	1076	0.38	8161	11774	2947
	20.0	36.0	70.6	70.6	2789	1224	1224	0.38	10528	14701	3813
	25.0	35.8	69.8	69.8	2828	1254	1254	0.38	11024	14999	4001
	30.0	35.6	69.4	69.4	2867	1270	1270	0.38	11303	15439	4101
	35.0	35.4	68.8	68.8	2908	1294	1294	0.38	11723	15827	4258
	40.0	35.2	67.8	67.8	2950	1336	1336	0.37	12448	16074	4540
	45.0	35.0	67.0	67.0	2993	1372	1372	0.37	13086	16397	4786
	50.0	34.8	66.0	66.0	3037	1419	1419	0.36	13939	16627	5123
	55.0	34.4	64.6	64.6	3130	1492	1492	0.35	15313	17368	5659
	60.0	34.4	64.6	64.6	3130	1492	1492	0.35	15313	17368	5659
	65.0	34.2	64.2	64.2	3178	1514	1514	0.35	15772	17922	5827
	70.0	34.2	64.2	64.2	3178	1514	1514	0.35	15772	17922	5827
M14	5.0	38.9	77.7	77.7	2385	1035	1035	0.38	7618	10939	2752
	10.0	38.5	76.8	76.8	2441	1059	1059	0.38	7973	11468	2880
	15.0	38.1	75.9	75.9	2500	1084	1084	0.38	8353	12027	3017
	20.0	36.4	71.1	71.1	2785	1236	1236	0.38	10802	14696	3921
	25.0	36.1	70.3	70.3	2842	1266	1266	0.38	11325	15263	4114
	30.0	35.8	70.1	70.1	2902	1273	1273	0.38	11502	16077	4165
	35.0	35.6	69.3	69.3	2943	1306	1306	0.38	12060	16412	4377
	40.0	35.5	68.7	68.7	2964	1331	1331	0.37	12496	16501	4548
	45.0	35.3	67.7	67.7	3007	1375	1375	0.37	13279	16753	4854
	50.0	35.1	66.7	66.7	3051	1422	1422	0.36	14136	16990	5192
	55.0	34.5	65.0	65.0	3193	1504	1504	0.36	15777	18432	5812
	60.0	34.5	65.0	65.0	3193	1504	1504	0.36	15777	18432	5812
	65.0	34.3	64.5	64.5	3243	1532	1532	0.36	16353	18967	6029
	70.0	34.3	64.5	64.5	3243	1532	1532	0.36	16353	18967	6029

To be continued

Sample	Hydrostatic stress (MPa)	Time of flight (µs)			Wave speed (m/s)			υ_u	E_u (MPa)	K_u (MPa)	G_u (MPa)
		P-wave	S1-wave	S2 -wave	P-wave	S1-wave	S2-wave				
M15	5.0	38.2	76.2	76.2	2426	1049	1049	0.39	7833	11356	2828
	10.0	37.8	75.4	75.4	2485	1071	1071	0.39	8169	11939	2947
	15.0	37.4	74.4	74.4	2547	1100	1100	0.39	8610	12524	3107
	20.0	35.4	69.6	69.6	2908	1262	1262	0.38	11330	16272	4093
	25.0	35.2	68.8	68.8	2950	1294	1294	0.38	11883	16623	4303
	30.0	35.0	68.4	68.4	2993	1310	1310	0.38	12193	17133	4413
	35.0	34.8	67.8	67.8	3037	1336	1336	0.38	12662	17588	4588
	40.0	34.6	66.8	66.8	3083	1381	1381	0.37	13475	17887	4902
	45.0	34.4	66.0	66.0	3130	1419	1419	0.37	14191	18271	5177
	50.0	34.2	65.0	65.0	3178	1470	1470	0.36	15153	18554	5555
	55.0	33.9	63.8	63.8	3254	1536	1536	0.36	16458	19124	6066
	60.0	33.9	63.8	63.8	3254	1536	1536	0.36	16458	19124	6066
	65.0	33.9	63.8	63.8	3254	1536	1536	0.36	16458	19124	6066
	70.0	33.9	63.8	63.8	3254	1536	1536	0.36	16458	19124	6066
M16	5.0	38.5	77.1	77.1	2501	1076	1076	0.39	8337	12225	3007
	10.0	38.1	76.4	76.4	2561	1096	1096	0.39	8648	12859	3116
	15.0	37.8	75.4	75.4	2608	1122	1122	0.39	9056	13298	3266
	20.0	36.0	70.4	70.4	2935	1293	1293	0.38	11965	16566	4336
	25.0	35.7	69.6	69.6	2995	1325	1325	0.38	12558	17209	4555
	30.0	35.4	69.4	69.4	3059	1334	1334	0.38	12763	18129	4615
	35.0	35.2	68.6	68.6	3104	1368	1368	0.38	13391	18526	4853
	40.0	35.0	67.9	67.9	3128	1396	1396	0.38	13905	18649	5054
	45.0	34.8	66.9	66.9	3175	1442	1442	0.37	14792	18954	5399
	50.0	34.6	65.9	65.9	3223	1493	1493	0.36	15774	19239	5785
	55.0	34.1	64.8	64.8	3347	1552	1552	0.36	17035	20731	6249
	60.0	33.8	63.7	63.7	3431	1620	1620	0.36	18484	21469	6813
	65.0	33.7	63.4	63.4	3458	1638	1638	0.36	18863	21744	6958
	70.0	33.7	63.4	63.4	3458	1638	1638	0.36	18863	21744	6958